3-2005

Tensile Stress Rupture Behavior of a Woven Ceramic Matrix Composite in Humid Environments at Intermediate Temperature

Kevin J. LaRochelle

TENSILE STRESS RUPTURE BEHAVIOR OF A WOVEN CERAMIC MATRIX COMPOSITE IN HUMID ENVIRONMENTS AT INTERMEDIATE TEMPERATURE

DISSERTATION

Kevin J. LaRochelle, Major, USAF

AFIT/DS/ENY/05-01

DEPARTMENT OF THE AIR FORCE
AIR UNIVERSITY

AIR FORCE INSTITUTE OF TECHNOLOGY

Wright-Patterson Air Force Base, Ohio

APPROVED FOR PUBLIC RELEASE; DISTRIBUTION UNLIMITED

AFIT/DS/ENY/05-01

TENSILE STRESS RUPTURE BEHAVIOR OF A WOVEN CERAMIC MATRIX

COMPOSITE IN HUMID ENVIRONMENTS AT INTERMEDIATE

TEMPERATURE

DISSERTATION

Presented to the Faculty

Graduate School of Engineering and Management

Air Force Institute of Technology

Air University

Air Education and Training Command

in Partial Fulfillment of the Requirements for the

Degree of Doctor of Philosophy

Kevin J. LaRochelle, BS, MS

Major, USAF

March 2005

TENSILE STRESS RUPTURE BEHAVIOR OF A WOVEN CERAMIC MATRIX

COMPOSITE IN HUMID ENVIRONMENTS AT INTERMEDIATE

TEMPERATURE

Kevin J. LaRochelle, BS, MS
Major, USAF

Approved:

Date

_____   _____
Shankar Mall (Chairman)

_____   _____
Larry W. Burggraf (Member)

_____   _____
Alan V. Lair (Member)

_____   _____
William F. Bailey (Dean's Representative)

Accepted:

_____   _____
Robert A. Calico, Jr.   Date
Dean, Graduate School of Engineering and Management

AFIT/DS/ENY/05-01

Abstract

Ceramic matrix composite (CMC) materials offer high strength and toughness, low density, high thermal conductivity, and erosion resistance in harsh environments like that of an aircraft combustor liner. CMCs manufactured with silicon carbide fiber reinforcement in a silicon carbide matrix (SiC/SiC) maintain their strength and toughness at low and high temperatures; however, they experience embrittlement at intermediate temperatures (450-900°C). This study focused on moisture and intermediate temperature effects on the embrittlement phenomenon and stress-rupture life of the SiC/SiC CMC made of Sylramic^{TM} fibers with an in-situ layer of boron nitride (Syl-iBN), boron nitride interphase (BN), and SiC matrix (Syl-iBN/BN/SiC). This study modeled the strength degradation behavior of Syl-iBN/BN/SiC in these environments.

An environmental apparatus was designed and validated to test Syl-iBN/BN/SiC specimens in test environments involving intermediate temperatures of 550°C or 750°C with controlled moisture contents of 0.0, 0.2, or 0.6 atm partial pressure of water vapor, pH$_2$O, at each temperature. Stress rupture strength degradation was temperature and pH$_2$O dependent. The CMC strengths at 100 hrs at 550°C with 0.0, 0.2, or 0.6 atm pH$_2$O were 75%, 65% and 51% of the monotonic room temperature tensile strength, respectively. At 750°C, the corresponding strengths were 67%, 51%, and 49%, respectively. Field Emission Scanning Electron Microscopy (FESEM) analysis showed that the amount of pesting by glass formations increased with time, temperature, and pH$_2$O leading to embrittlement. Total embrittlement times for 550°C were estimated to be greater than 63 hrs for 0.0 atm pH$_2$O, greater than 38 hrs for 0.2 atm pH$_2$O, and between 8 and 71 hrs for 0.6 atm pH$_2$O. Corresponding estimated embrittlement times for the 750°C were greater than 83 hrs, between 13 and 71 hrs, and between 1 and 6 hrs.

A time-dependent, phenomenological, Monte Carlo-type simulation of composite failure was developed. Using material properties, damage characteristics, failure mechanisms, and estimated total embrittlement times, derived from stress rupture test and microscopic data, the model successfully simulated the stress rupture behavior. The modeling results simulated the

total embrittlement times for the 550°C cases to be 300 hrs, 100 hrs, and 25 hrs for 0.0, 0.2, and 0.6 atm pH$_2$O, respectively. The corresponding embrittlement times for the 750°C cases were 300 hrs, 20 hrs, and 3 hrs. These modeling results fell within the experimentally observed, or estimated, embrittlement times.

A detailed sensitivity analysis on the variables used in the proposed model was conducted. The model was most sensitive to variation in the ultimate strength of the CMC at room temperature, the ultimate strength of the CMC at elevated temperature, and the reference strength of a fiber. The model was least sensitive to variation in the modulus of elasticity for the matrix and the modulus of elasticity for the fiber. The sensitivity analysis showed that realistic parameter variation captured the scatter in the experimental data, thus showing model robustness in simulating the mechanics of CMC failure under stress rupture conditions. The modeling results showed that the stress ruptures curves generated by variation in the total embrittlement time simulate the trends in the experimental data. No other variable in the model could generate this result. It is obvious from the data that the Syl-iBN/BN/SiC CMC material experiences severe stress rupture strength degradation when exposed to intermediate temperatures. The resulting analysis showed that the degree of degradation increases with temperature, moisture content level, and exposure time.

Acknowledgments

There are so many people that I would like to thank and acknowledge but I have such little space. I would like to express my sincere appreciation to my faculty advisor. Without his knowledge, support, and patience, the outcome would have been a lot different. Many thanks go to my friends and co-workers in AFRL/PR, AFRL/PRT, AFRL/PRTP, NASA Glenn Research Center, AFIT, and AFRL/ML. Without their continued support and encouragement this endeavor would have never become a reality. To my parents, who I think are more excited about this than I am, thanks for the support and love. To Liberty, Freedom, Thor, and Cleo, thanks for keeping my blood pressure down. To Mr. Basie, Mr. Armstrong, Mr. Goodman, Mr. Calloway, and all the others, thanks for keeping my feet tapping and my fingers trucking. To my wife, thanks for always believing I could finish, even when I didn't, and for taking care of everything on the home front. I am truly blessed and grateful to have you. Finally and most importantly, thanks to all who kept me in their prayers and thank you, Lord, for answering them.

Kevin J. LaRochelle

Table of Contents

List of Figures

List of Tables

TENSILE STRESS RUPTURE BEHAVIOR OF A WOVEN CERAMIC MATRIX COMPOSITE IN HUMID ENVIRONMENTS AT INTERMEDIATE TEMPERATURE

I. Introduction

Scientists and engineers are constantly developing new materials to meet the ever increasing demands of new applications and environments, such as, rocket engines, turbo-machinery, heat exchangers, automobile engines, and aircraft engines. These new materials must be designed to have superior structural, mechanical, and durability characteristics. Since the early 1980s, researchers have studied continuous fiber-reinforced ceramic matrix composites (CMCs) [1,2] by investing tremendous effort and money to gain an understanding how CMCs can be used in applications where the material requirements exceed those of the current materials.

In the combustor liner application, the material must be able to handle extreme temperatures, high pressures, and harsh combustion environments. This application is of great importance to the United States Air Force, NASA, and the civilian aircraft industry [3] and is the focus of this research. The Air Force Research Laboratory has a number of programs (e.g. High Temperature Combustor Liner with Pratt & Whitney) with the objective of designing an aircraft engine combustor liner (Figure 1 [4,5]) that can sustain a maximum surface temperature of 1300°C with a near stoichiometric fuel-air ratio in the combustion zone. The higher operating temperatures and overall fuel-air ratios will allow aircraft to reach higher speeds and operate more efficiently [6]. A CMC combustor liner will also have weight benefits compared to the current nickel based superalloy liner.
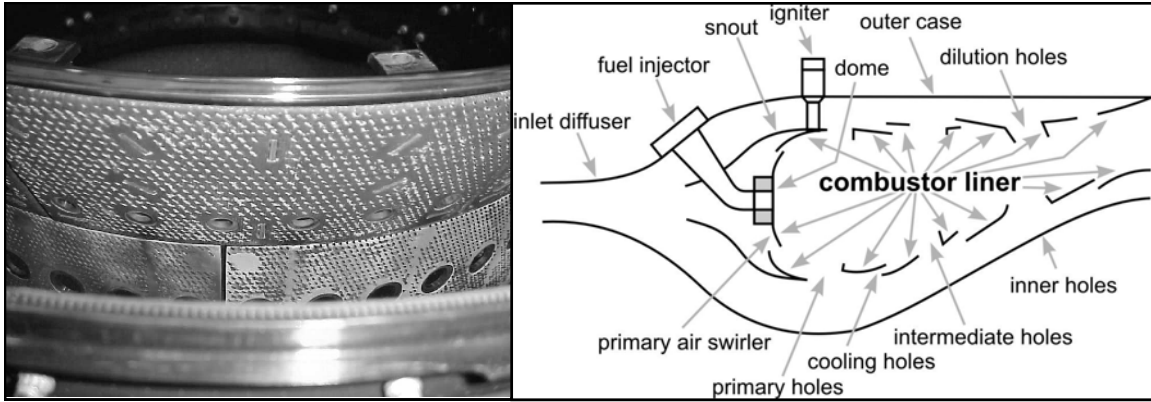
Figure 1: The Combustor Liner Application [4,5]

The High Speed Research (HSR) and the Enabling Propulsion Materials (EPM) programs at NASA looked at eleven materials for different applications in the High Speed Civil Transport (HSCT). They determined that the non-oxide SiC/SiC CMC has the most promise for high temperature, high oxidation applications [3] such as the combustor liner. Despite the tremendous advantages, CMC materials have unique challenges that must be overcome before they become a viable alternative to metals. One such challenge is CMC embrittlement.

Embrittlement

Embrittlement occurs when the composite constituents are altered due to the exposure to harsh environments causing degradation in the composite's material strength, toughness, and damage tolerance. Embrittlement of SiC/SiC CMCs has been referred to as oxidation embrittlement of the fiber/matrix interphase and is well documented in previous studies [7,8,9]. From this previous work it is understood that through-the-thickness cracks caused by applied and thermal stresses allow the environment into the interior of the specimen to attack load bearing fibers and lead to CMC embrittlement depending on the temperature of the environment.

SiC/SiC CMCs work effectively in the lower ($<450^{o}$C) and the higher ($>900^{o}$C) temperature ranges but experience embrittlement at the intermediate temperature range [10,11,12]. Heredia et al [13] summarized the problem, "It has the characteristics of a classical pest phenomenon. It occurs most rapidly at intermediate temperatures and drastically changes the structural performance of the material." Pesting occurs when the environment attacks the

fibers and the interphase material resulting in the fibers becoming solidified to each other and the matrix by a glass substance. This is problematic at intermediate temperatures because the interphase oxidizes and the oxidation by-product reacts with surrounding material to form glass. The moisture from the combustion process, approximately 10% by volume [14,15], reacts with this glass, changes its composition and viscosity, and eventually solidifies it. This results in the functional interphase material being replaced by a solid brittle glass thus removing the toughness mechanisms inherent in CMCs and leading to premature failure.

In combustor liners, temperature gradients through the thickness of the liner and along the flow path within the liner cause thermal stress. Furthermore, thermal expansion mismatch at attachment points, coupled with high pressures in the combustor, contribute to the mechanical loading and overall stress on the liner. These stresses can overcome the residual compressive stresses in the CMC and cause cracks in the matrix material. Applied loads keep these cracks open, allowing the environment to penetrate inside the material. At high temperatures above $1000^{o}C$, the SiO_2 formation seals the cracks, denying the environment further access. At intermediate temperatures, the crack does not seal allowing the environment to attack the interphase material and fibers in the interior of the specimen.

Heredia et al [13] cites three reasons why CMC susceptibility to serious degradation had not been emphasized in the literature before the mid 1990s. The first reason is that tests involved heat treatments followed by room temperature mechanical tests. Testing in this manner does not provide the environmental ingress routes via matrix cracks. The second reason is that mechanical tests were performed at temperatures above the pesting temperature. The viscosity of the silicate at higher temperatures deactivates the pesting phenomenon by sealing the crack. The third reason is that mechanical tests were done in flexure where the strength degradation of embrittled regions is diminished compared to tests done in tension.

Since the mid 1990s, experiments have been conducted in an appropriate manner to address these concerns. Specimens are now tested in tension and in environments that promote the embrittlement phenomenon. Because of this, the degradation behavior of CMC materials due

to embrittlement can be properly investigated which enables material scientists to develop more robust composites to withstand, or minimize, the effects of embrittlement.

Problem Statement

The focus of this research is to investigate how stress rupture loading, intermediate temperature, and moisture affect the CMC constituents; to understand how these effects change the time dependent failure mechanisms; and to model the relationship among these factors. The CMC system used was the Sylramic^{TM} (Syl) fiber with an in-situ boron nitride (-iBN) layer, boron nitride (BN) interphase, and silicon carbide (SiC) matrix CMC system. This system, Syl-iBN/BN/SiC, is the strongest and most creep-resistant system developed to date and is akin to NASA's 01/01 material developed under the Ultra-Efficient Engine Technology (UEET) Program [16]. It is imperative to understand how the strength of this material degrades with respect to time (i.e. stress rupture behavior) and how the environment affects this degradation. Stress rupture tests show how long a material can withstand a certain load in a certain environment, which is important to aircraft engine designers.

This study investigated the correlation between CMC stress rupture degradation and the temperature and/or the moisture content of the test environment by conducting stress rupture tests in various controlled environments. Systematic observations of the failure mechanisms using Field Emissions Scanning Electron Microscopy (FESEM) showed how increased levels of moisture in the testing environment affected the matrix, interphase, and fibers. A time-based, phenomenological, Monte Carlo-type model was developed to predict the stress rupture behavior of the Syl-iBN/BN/SiC CMC at intermediate temperatures in humid conditions using individual fiber failure theory and modeling observations seen during this research. This study went beyond the previous modeling effort by Morscher and Cawley [17] for SiC/SiC composites at 815°C in ambient moisture conditions. Their study showed how ambient moisture content led to CMC embrittlement; however, they did not investigate how different levels of moisture affect stress rupture behavior either by experiments or analysis.

An investigation into how intermediate temperature, moisture, and applied stress affect the stress rupture performance is beneficial to the CMC community and combustor liner

designers in particular, since jet engine combustor liners are subjected to moisture content levels far above those of ambient laboratory environments. Previous studies dealt with CMCs at elevated temperature, under atmospheric pressure, and at laboratory moisture content levels. No studies have been reported to investigate the effects of moisture content at intermediate temperature on the stress rupture behavior of the Syl-iBN/BN/SiC CMC material. Although it is generally understood and accepted that moisture at elevated temperatures will degrade the CMC strength, the effects of moisture have not been quantified.

Approach

This research involved experiments that generated stress rupture data in various environments as well as model development to characterize the stress rupture behavior of the Syl-iBN/BN/SiC CMC system. The test environments consisted of two intermediate temperatures, 550°C and 750°C, and three moisture content levels, 0.0, 0.2, and 0.6 atm partial pressure of water vapor, pH_2O, at each temperature. A 100-hour test duration limit was used to ensure the environmental effects were investigated and to conduct as many experiments as possible.

The stress rupture testing condition was chosen for two main reasons. First, the primary failure mechanism in CMC combustor liners is stress rupture near attachment points because the material experiences thermal stress and mechanical stress there for long periods of time, perhaps hundreds to thousands of hours. Second, the igniter and cooling holes are crack initiation sites. For all stress rupture tests in this study, the applied stresses were well above matrix cracking stress thus guaranteeing the presence of cracks.

A custom environmental apparatus was built to control the environment around the specimen. A steam generator produced the desired partial pressure of water vapor by combining the appropriate amount of steam and air. A series of heating tubes and a heating chamber heated the moisture-laden air to the desired test temperature. The apparatus was designed to maintain the moisture air as a vapor and to ensure the test conditions were reached quickly to avoid specimen-soaking time.

The experimental set-up was validated prior to main research. For this purpose, experiments were conducted to verify the thermocouples were not affected by the magnetic field of the induction heater, temperature readings were accurate, and the environment was stable. These experiments also provided the temperature profile along a specimen, verifying that the failure locations were within the hot gauge length of the test specimen.

A comprehensive test plan was developed to test specimens in the various environments, including room temperature, using both monotonic tensile tests and stress rupture tests. Room temperature monotonic test data were used to verify consistent mechanical properties between all six individually manufactured panels. Other monotonic tests were conducted in the various environments and were used to investigate the effects of the test environment (i.e. the effects of temperature and/or moisture content) on modulus of elasticity of the composite, modulus of elasticity of the fibers, the matrix cracking stress, and the ultimate strength. The environmental stress rupture data demonstrated the trends in material performance as temperature and moisture were varied. Dividing the measured failure stress by the specimen's panel room temperature ultimate strength normalized the experimental data. This removed scatter associated with variation in the material properties of different panels, which is commonly seen in the CMC literature.

Immediately upon failure, the bottom portion of the specimen (i.e. the fracture surface specimen) was removed from the heating chamber to stop any further environmental attack on the exposed fracture surface. Analysis of Field Emission Scanning Electron Microscopy images of the fracture surface specimens provided evidence of the failure mechanisms and the embrittlement phenomenon. In particular, the location and amount of glass formation with respect to time and multiple fiber failures by the same crack were observed and incorporated into the model.

The upper portion of the failed specimen was not removed until the heating chamber cooled because of test equipment limitations and, therefore, could not be used for embrittlement analysis because of the additional exposure time. This specimen was machined and polished along a plane perpendicular to the fracture surface (a plane parallel to the loading direction) and

was analyzed to determine crack density. This investigation determined how the environment affected the number of cracks.

A time-based, phenomenological, Monte Carlo-type simulation of composite failure was developed in this research. The model simulates composite failure by modeling individual fiber failures as a function of time and environment. The model incorporates the effects of matrix cracking and a strength reduction factor due to the manufacturing process. The Weibull distribution of fiber strengths over the composite cross-section and the effects that embrittlement has on the strength of the composite are also included in the model. A parametric analysis was performed on material properties, theoretical parameters, damage characteristics, and experimentally determined variables used in the model to determine the sensitivity to realistic variations.

Chapter Summary

This research is the first study to characterize the behavior of the Syl-iBN/BN/SiC composite in an environment that closely simulates the jet engine combustor liner application. The layout of this document is summarized here. Chapter II provides the necessary background information to understand the mechanisms of CMC failure. Chapter III describes the methodology of the experiments and the results of the validation experiments. Chapter IV presents the experimental results. Chapter V presents the modeling effort of this research, its results, and the parameter sensitivity analysis on variables used in the model. Chapter VI is the discussion of the analysis of this research, its findings, and how it fits into the current state of the art knowledge of SiC/SiC CMC failure due to embrittlement. Chapter VII summarizes the research presented in this dissertation and includes recommendations for future work.

II. Background

CMCs are composed of chemically and/or physically distinct materials, (i.e. fibers and interphase) distributed within a separate continuous material (i.e. matrix) [18] as shown in Figure 2. Depending on the architecture and materials chosen as constituents, CMCs can offer the following benefits: high strength and toughness, low density, high thermal conductivity, and erosion resistance. The architecture can consist of short fibers randomly oriented in the matrix material (i.e. whisker), continuous fibers all orientated in the same direction (i.e. uniaxial), continuous fibers where large numbers of fibers are orientated in different directions and manufactured in layers (i.e. laminate), or continuous fibers bundled in tows that are woven together into either two dimensional or three dimensional configurations (i.e. weave). The fiber orientation determines the CMC material properties, which are prescribed by the application. The fiber and interphase material properties and interaction give CMCs the toughening that monolithic ceramics lack.
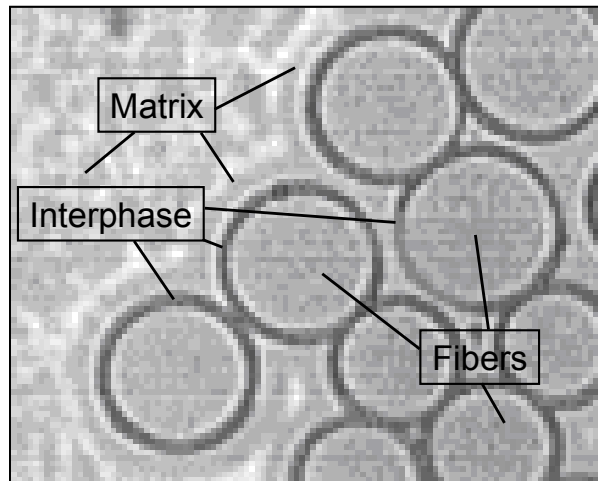
Figure 2: CMC Constituents – Polished Surface Perpendicular to Fibers

Overview of CMC Failure Behavior

CMCs possess failure mechanisms that make them more damage resistant and damage tolerant than monolithic ceramics. Prior to any damage, constituents of a CMC material share the applied load depending on the volume fractions and elastic properties of the constituents (e.g. for a material with 0.2 volume fraction of fibers in the loading direction and equivalent Modulus of Elasticity for the fibers, E_f, and the matrix, E_m, the fibers support 20% of the load and the matrix supports the remaining 80%). As thermal and/or mechanical stress in CMCs increase, damage first occurs in the form of micro-cracks in the matrix. The majority of these initial cracks form within the cross tows where there is a higher concentration of pores and matrix flaws. Other cracks start at surface flaw locations typically at the corners of the specimen. With continued loading, these micro-cracks coalesce to form larger cracks. Regardless of the source, the CMC matrix cracking stress is generally greater than the catastrophic fracture stress of the non-reinforced ceramic material [19,20] because of the additional support of the fibers.

When the applied stress exceeds the matrix cracking stress, these micro-cracks propagate until they encounter fibers that are aligned perpendicular to the crack plane and in the loading direction. As the crack opens, the fiber/matrix interphase bond fails allowing these fibers to slide, thus, relieving the stress intensity at the crack tip. The crack becomes bridged by these fibers for some distance behind the crack tip and further crack propagation stops. The number of bridging fibers needed to stop crack propagation depends on the fiber architecture (i.e. laminate, uniaxial, or weave), the loading conditions, and the crack dimensions. When a bridging fiber fails, the stress intensity factor at the crack tip increases. If enough bridging fibers fail, the crack intensity factor at the tip increase enough to that crack propagation starts again. The crack propagates until more fibers bridge the crack stopping further crack propagation. The nonlinearity of this initial stress strain response due to the fibers' influence is shown in Figure 3.
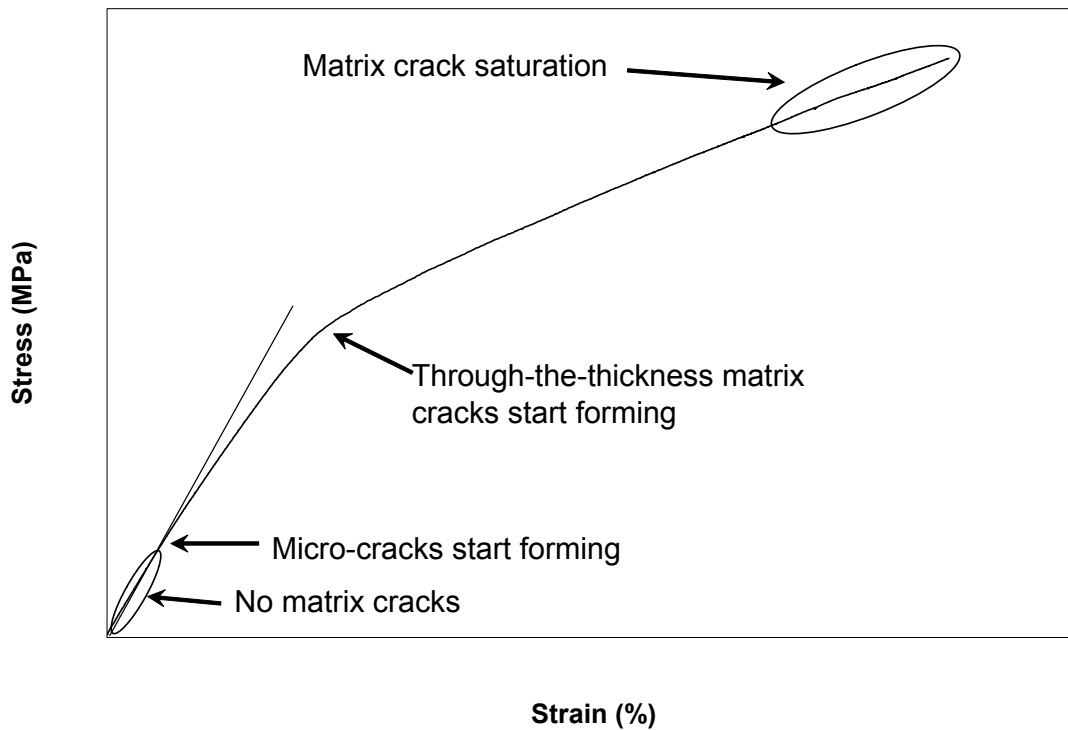
Figure 3: Typical Stress Strain Curve for a CMC Material

Under an increasing load, through-the-thickness cracks form when either one crack propagates across all the fibers or, more typically, several cracks coalesce. A "knee" in the stress strain curve as shown in Figure 3 indicates this behavior. In the presence of a through-the-thickness crack, only fibers support the load. When one fiber fails, the remaining fibers in the cross section take up the load because of global load sharing. In addition to affecting the stress on fibers, matrix cracks also affect the stress on the matrix and the location of future matrix cracks.

As shown in Figure 3, there are two extremes of matrix cracking: no matrix cracks and matrix crack saturation. The former case is when the applied stress is below the matrix cracking stress. Matrix crack saturation occurs when the applied load is high enough such that the matrix material has so many cracks that the distance between cracks is shorter than the slip transfer length, resulting in minimal load transfer via friction from the fiber to the matrix material [21].

Between these two extremes the material experiences damage in the form of both partial cracks and through-the-thickness cracks with the proportion of each depending on the loading

conditions. Figure 4 is a schematic drawing showing the load transfer and crack formation associated with a fiber bridging a crack. In a through-the thickness crack, the fiber lengths in the crack opening, u, carry the entire load. The load is transferred from the fiber to the matrix over the stress transfer length, $\delta/2$, above and below the crack [22]. If the applied load is high enough somewhere along the stress transfer region, the stress on the matrix could exceed the matrix cracking stress, σ_{MC}, and cause another crack to form [21,23]. In a material free of defects, cracks would be uniformly distributed along the gauge length at a distance equivalent to or less than the stress transfer length, $\delta/2$. In a partial crack, the bridging fiber will experience less stress because the matrix material in front of the crack tip will carry some load.
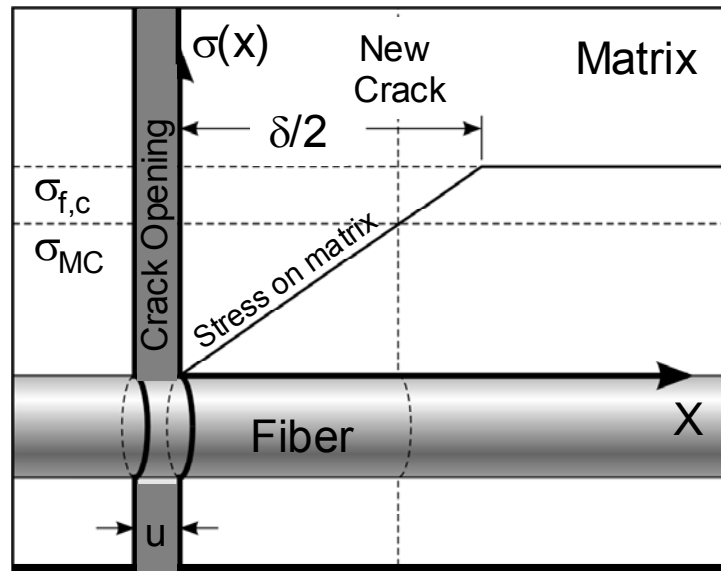
Figure 4: Location of Matrix Cracks

Due to defects in the matrix, the cracks may be very close together in some regions and farther apart in others. If the cracks are within two stress transfer regions and close enough, the stress is not completely transferred to the matrix because it is transferred back to the fiber due to the effect of the next crack, as shown in Figure 5. Another matrix crack is not formed in this situation. Conversely, if the two existing cracks are further apart but still within two stress transfer regions, a region exists where the matrix stress is higher than the matrix cracking stress causing another crack to form, as shown in Figure 6.
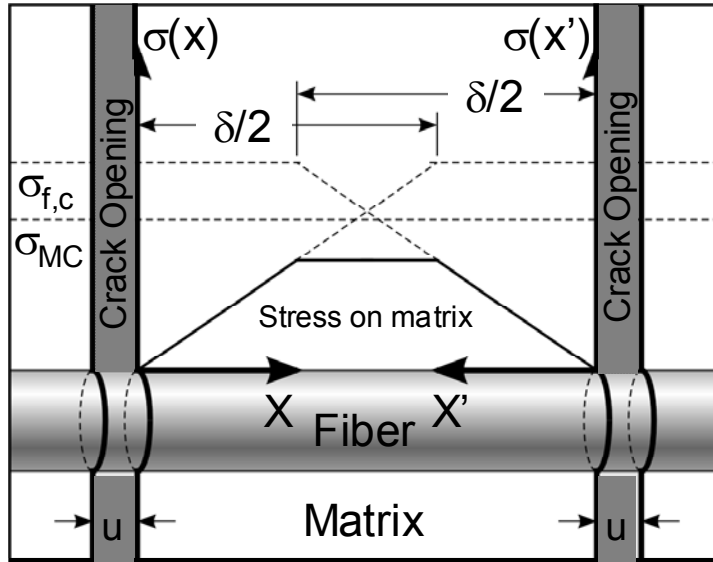
Figure 5: Two Matrix Cracks within Two Stress Transfer Regions
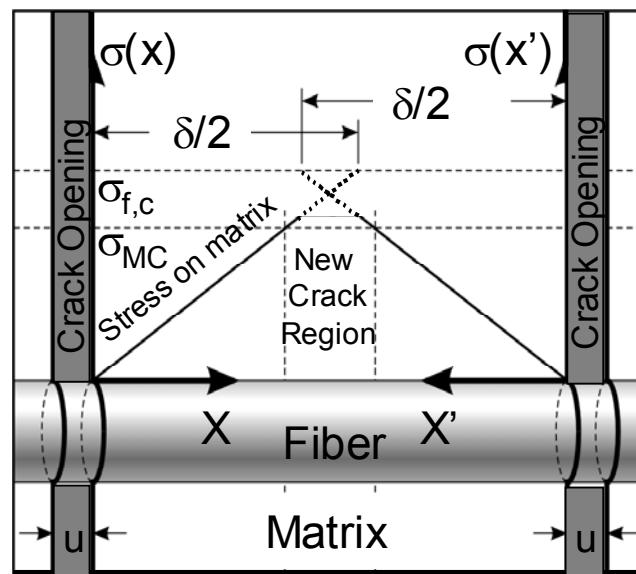
Figure 6: Stress Transfer Length Effect on Crack Location

In the case of stress rupture loading, where there is essentially monotonic loading to a predetermined applied load which is then held constant until specimen failure, the specimen will eventually reach a steady state crack density comprised of both partial and through-the-thickness cracks. Through-the-thickness and partial matrix cracks that extend to the surface of the specimen allow the environment access to the interior of the specimen. The access of the environment allows reactants (i.e. O_2 and H_2O) to attack the constituents, and thus, promote embrittlement of the CMC material. In the case of environmental attack, such as oxidation and

pesting, only the bridging fibers and interphase material in the cracked region are susceptible to stress-oxidation strength degradation and embrittlement. The fibers in the uncracked matrix region will only experience strength degradation due to temperature creep. The time and environment dependence of the fiber strength degradation for these exposed fibers is important to CMC failure.

Time and Temperature Dependence of Fiber Failure

Previous research at NASA Glenn Research Center [24,25] has shown that the time-temperature dependent fracture characteristics of the individual fibers ultimately determine the failure strength of a CMC. This environmental dependence of individual fibers must be studied to gain an understanding of CMC stress rupture failure. In response to an applied load, the atoms and defects in a material move relative to one another in a concerted time-dependent manner. This deformation is called creep and is enhanced by a temperature increase because "a temperature increase is related to an increase of the average atomic oscillations of atoms about their equilibrium positions" [26]. Under stress, this increase in oscillations results in molecular rearrangements that lead to deformation. Since creep is a thermally activated process, the creep rate is governed by the Arrhenius equation, which captures the creep dependence on temperature, and is of the form:

$$\dot{\varepsilon} = Ae^{\frac{-Q}{RT}} \tag{1}$$

where

$\dot{\varepsilon} \equiv$ strain rate
$A \equiv$ Coefficient of Creep
$Q \equiv$ activation energy of creep (J/mol)
$R \equiv$ universal gas constant (8.314 J/K•mol)
$T \equiv$ temperature (K)

The Coefficient of Creep, A, in Equation 1 has several definitions depending on the type of creep mechanism that is occurring, which depends on the class of material. For example, amorphous materials like polymers deform according to viscous creep, where as crystalline materials like ceramics deform by either diffusion flow (Nabarro-Herring Creep and Coble Creep)

or dislocation creep (Power Law Creep). Nabarro-Herring Creep and Coble Creep occur as a result of the spontaneous formation of vacancies in the material and the diffusion of these vacancies either through the crystal lattice or along the grain boundary, respectively. In these creep mechanisms, *A* is proportional to the applied stress and inversely proportional to the grain size where both are raised to powers depending on the creep mechanism. Also, it is inversely proportional to temperature.   However, this weak temperature dependence is typically ignored in time-temperature parameter derivations like the Sherby-Dorn and Larson-Miller Parameters because of the dominant temperature dependence in the exponential. Even with neglecting the weak temperature dependence, the time-temperature parameters often give reasonable results. Therefore, Larson-Miller plots derived from the Arrhenius equation (Equation 1) have been used to effectively compare CMC fibers. [26]

Larson-Miller plots, summarized in Appendix A, characterize and rank materials by graphically capturing the time and temperature dependence of fiber strength. Development of the Larson-Miller parameter assumes the activation energy of the creep failure mechanism is dependent on the applied stress. The plots use data from relatively short tests at temperatures above the service temperature to estimate the behavior for longer times at the service temperature. [26]

Figure 7 [10,27,28] is a Larson-Miller plot for four SiC fibers: Nicalon[TM] (Nic), Hi-Nicalon[TM] (HN), Sylramic[TM] (Syl), and Syl fiber with an in-situ BN layer (Syl-iBN). The relationship between fiber stress rupture strength and both time and temperature can be seen in these plots (i.e. one fiber may be more stable at a particular temperature while another is more resistant to oxidation at another temperature). When comparing the fibers, the higher the curve on a Larson-Miller plot, the more resistant the fiber is to failure. The slopes of the curves indicate the rate at which the fiber strength degrades.
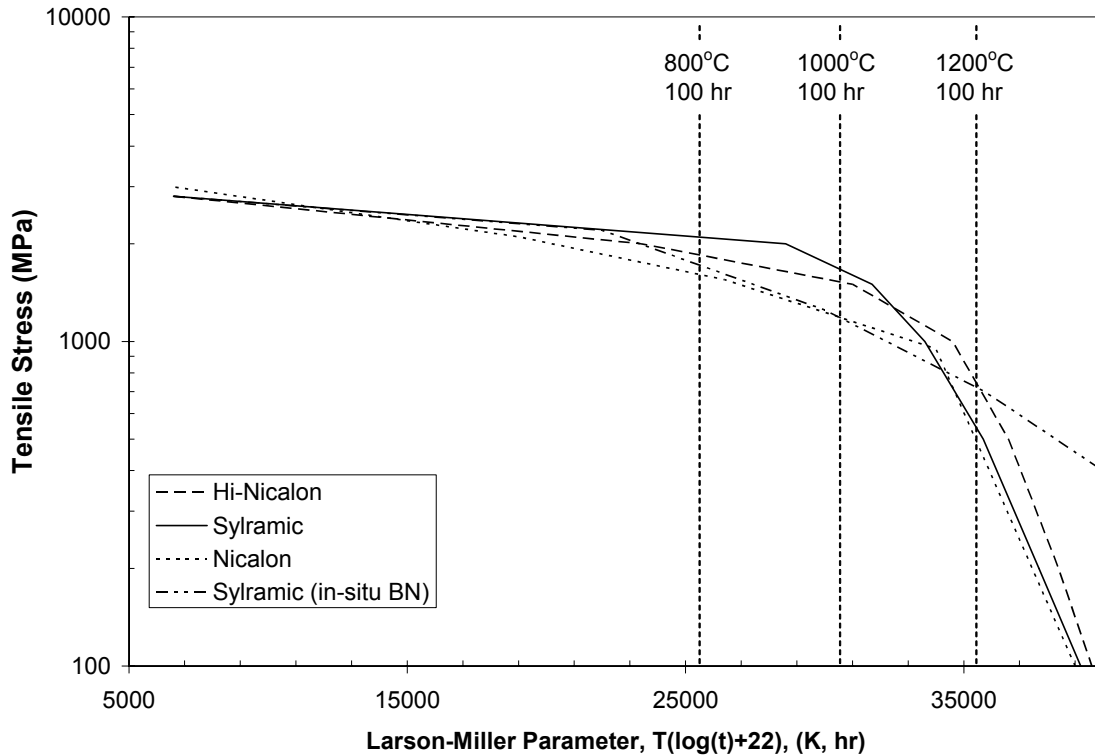
Figure 7: Larson-Miller plot for Nic, HN, Syl, and Syl-iBN fibers [10,27,28]

To isolate the effects of time, stress rupture plots are used. They show how long a material will survive at a given applied stress before catastrophic failure and can be generated by inserting the desired temperature into the Larson-Miller Parameter for existing Larson-Miller data. Figure 8 is a stress rupture plot simulation generated by using the Syl fiber curve from Figure 7 with temperature (T) equal to 550°C and 750°C. Alternately, a stress rupture plot can be created by subjecting the specimen to a constant load under constant environmental conditions until it fails and plotting the failure stress versus failure time for several specimen.
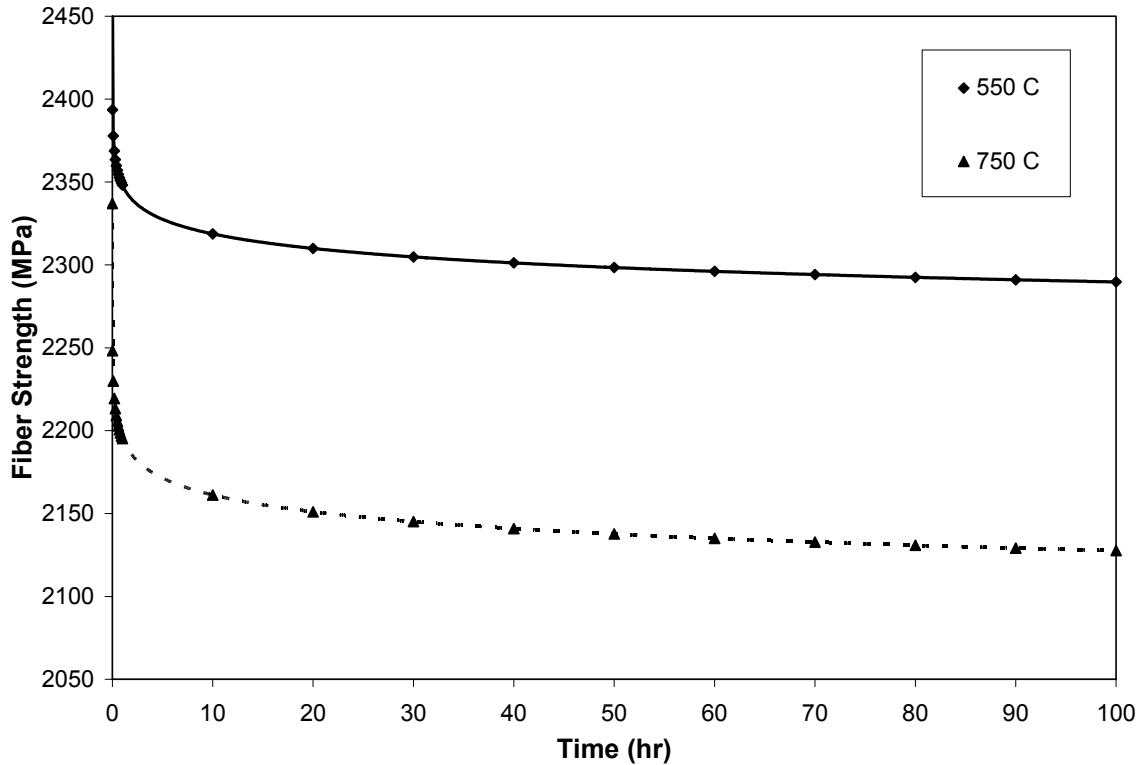
Figure 8: Schematic of Stress Rupture Plots for Syl Fiber

Principal Constituents of CMCs

The previous discussion shows the importance of constituent selection in tailoring the properties of CMCs. For a combustor liner, the CMC must have strong, creep resistant fibers. The interphase must be weak enough such that the interfacial shear properties allow matrix crack deflection and fiber/matrix sliding when initial damage occurs. The interphase must also be environmentally stable over a wide range of conditions so that once damage has occurred and the environment has access to the interphase it continues to function properly and provides a protective layer for the fibers. The matrix, while having some load carrying capacity, must provide the necessary dimensional stability, environmental durability, and thermal conductivity for the application. Selecting the appropriate materials for the constituents can attain these properties.

Endless combinations of fibers (e.g. C, SiC, and oxide fibers) and matrices (e.g. C, SiC, glasses, and oxide matrices) exist that can be manufactured to meet the demands of various

applications [29]. For example, CMCs have been manufactured using oxide fibers within oxide matrices like the Nextel 720/alumina CMC system. Other CMC systems consist of non-oxide fibers within oxide matrices, like the carbon (C)/alumina silicate CMC system. Lastly, CMCs have been manufactured with non-oxide fibers within non-oxide matrices, like the popular SiC/SiC CMC system.

Oxide fibers, by their nature, are impervious to oxidation. However, they have a temperature limitation of approximately 1000-1200°C because of limited creep resistance at high temperature controlled by the number of slip systems, the grain boundary phases, and the diffusion rates of species in the oxide [30,31]. Increasing the grain size can reduce the high creep rates, but this lowers the fiber strength. The development of interphase coatings for oxide fibers has lagged behind that of non-oxide fibers because of the poor creep resistance at elevated temperature of oxide fibers during the coating application process.

Recent work by Oak Ridge National Laboratories demonstrated that the oxide/oxide CMC Nextel 720/alumina can survive 3000 and 1000 hours at 1137°C and 1200°C, respectively, in a 10 ATM Kaiser Rig test with 10% H_2O, with no loss in strength because of the exposure [31,32]. This CMC can be used with an all-alumina based, friable insulation that allows the insulation to go to very high temperature, while keeping the oxide/oxide CMC at 1200°C [33]. Although this is a tremendous improvement in oxide/oxide CMCs, it still falls short of the desired 1300°C operating temperature of the combustor liner application. Therefore, CMCs with oxide constituents have not been considered for the combustor liner application [30] leaving non-oxide/non-oxide CMC as the best option for designers.

For a combustor liner, the CMC must have strong, creep resistant fibers. Several materials have been manufactured into fibers; however, only SiC and alumina fibers are available commercially. Although alumina is immune to oxidation, SiC has a higher maximum temperature capability and is more creep resistant than alumina at high temperature. Therefore, SiC is the most promising material for the fiber constituent.

SiC and Si_3N_4 are the most promising non-oxide materials for the matrix material in the combustor liner. Both materials demonstrate the necessary strength, thermal properties, and

erosion resistance necessary for this application. Coefficient of thermal expansion mismatch between the fibers and the matrix must be considered when choosing the fiber/matrix combination because any mismatch causes internal stress. Premature or spontaneous matrix cracking occurs if the ratio of the coefficients of thermal expansion of the matrix and the fiber is considerably less than one. Conversely, thermal debonding of the fiber/matrix occurs if the ratio is considerably greater than one. It is desirable to have this ratio as close to unity as possible to avoid either situation [34]. Therefore, SiC is the preferred choice over Si_3N_4 as the matrix material.

Another important component that affects the performance of CMCs is the interphase material. In addition to the strength of the fibers, the mechanical properties of the fiber/matrix interface will dictate the tensile axial properties of the composite material [34]. Carbon, C, has been a very popular interphase material because of its mechanical properties and low cost. However, C oxidizes and volatizes as CO and CO_2, leaving a gap between the fiber and matrix. This gap increases the gauge length exposed to the environment. Filippuzzi et al [35], using thermogravimetric analysis on specimens tested in both oxidizing and inert atmospheres, showed that SiC/C/SiC composites experience an initial weight loss in the oxidizing environments attributed to the oxidation of C. Their specimens then experienced a weight gain because of subsequent oxidation of the SiC fiber and SiC matrix forming SiO_2. The SiO_2, verified using transmission electron microscopy and electron energy loss spectroscopy, seals the composite from further C interphase oxidation.

Eckel et al [36] demonstrated that C readily oxidizes to CO and CO_2 between $800^{\circ}C$ and $1200^{\circ}C$ and that the oxidation rate was independent of the size of the pore or crack. They surmised that CMCs with C interphase cannot be fabricated with an interphase thickness small enough to stop the oxidation. Cawley [37] showed that the gap left by the oxidation of the C interphase did not affect the decoupling of the matrix and fiber but did affect the time needed to fuse the fibers together. Finally, Goto et al [38] showed that graphite readily oxidizes above $400^{\circ}C$. The oxidation susceptibility of C has led scientists to find an alternative material.

BN has been considered for use as an interphase material in CMCs since it does not oxidize as readily as C. This interest started in the early 1980s and was patented in 1985 [39]. Boron nitride has similarly effective mechanical properties as C and can withstand temperatures below 450°C and high temperatures above 900°C. The rate of oxidation is too low at temperatures below 450°C to be of any concern. The rapid formation of a surface layer of SiO_2 seals cracks and prevents the environment from attacking the BN interface at temperatures above 900°C.

Sheldon et al [40] performed thermodynamic calculations to analyze the simultaneous oxidation of BN and SiC at 1000°C. They found that at 1000°C the BN would not oxidize to form B_2O_3 until all Si has formed SiO_2 and all C has formed CO. Since the formation of SiO_2 on the crack surface seals the cracks, no B_2O_3 will form. This is why the material system works well at higher temperature. Ogbuji [41] investigated similar oxidation at 800°C using different oxidation environments. He found SiO_2 formation in place of the BN interphase. The amount of SiO_2 found was more than expected from SiC oxidation at 800°C. He attributed this to the ability of liquid B_2O_3 to dissolve the SiC matrix cladding to form a liquid borosilicate that is eutectic above 372°C. These chemical reactions alter the CMC constituents, namely the interphase, such that the CMC will fail at a reduced applied stress. This embrittlement phenomenon will be more thoroughly explained later in this chapter as it pertains to the research conducted here.

Potential CMC for Combustor Liner Application

As discussed earlier, a SiC/SiC CMC is currently the best choice for applications in high temperature and high moisture environments. The C and BN interphase materials typically are used with SiC fibers, in particular the Nic, HN, Syl, and Syl-iBN fibers. These combinations provide the best CMC material properties needed for the combustor liner application. However, C and BN have oxidation problems, especially in the intermediate temperature range that leads to CMC embrittlement.

To understand how different fibers and interphase materials are affected by embrittlement, a discussion on previous experimental results is necessary. The literature search

includes studies on SiC/SiC composites with C or BN interphases, studies where the mechanical tests resulted in cracked specimens to allow the environment into the interior of the specimen, and studies on the constituent materials. The review of the previous work will show what material is best suited for applications in intermediate temperatures with humid conditions.

Studies have looked at the Nic/SiC system with either C or BN interphase. Heredia et al [13] performed stress rupture experiments in air at 800^oC on the two-dimensional woven Nic/C/SiC CMC and found a drastic reduction in rupture strength as a function of time (i.e. it was 33% of the ultimate strength at room temperature after 12 hours). Their investigation also included a cyclic study on the Nic/C-B/magnesium aluminosilicate system at 500^oC. This system failed at a peak stress of 50% of the room temperature ultimate strength at 104 cycles. Lin and Becher [42] and Lin et al [43] investigated Nic/C/SiC at 600^oC, 900^oC, and 950^oC and found analogous behavior. Their electron microscopy indicated that the life of the CMC was controlled by the oxidation of the C interphase and the formation of glass from the oxidation of the fiber and matrix. They also stated that porosity inherent in SiC/SiC CMCs played an important role in the oxidation of the interphase.

Lara-Curzio et al [44] studied this same behavior at 425^oC and found that the oxidation of the carbon interface increased the probability of fiber failure because of the increased gauge length of the fiber exposed to the maximum stress (i.e. the length of fiber in the crack opening that does not transfer any load to the matrix). Lara-Curzio [45] studied the Nic/C/SiC system at 950^oC and found similar results. The investigation of the Nic/C/SiC system at 1000^oC by Lipetzky et al [46] found similar strength degradation and showed that above 1000^oC moisture did not influence the stress rupture behavior because cracks were sealed denying the environment access.

Steyer et al [47] determined the stress rupture properties of a Nic/C-B/SiC with an "enhanced" (B_4C-containing) Chemical Vapor Impregnation (CVI) SiC matrix at 900^oC. They found that the CMC strength degradation was dependent on the fiber strength degradation and that the enhanced composite system had marginally better performance over the nonenhanced composite. Verilli et al [48] also investigated this material in a temperature range of 500-1150^oC.

They found that the Nic/C/SiC system experienced material degradation and embrittlement

between 700-800°C. Sun et al [49] studied the stress rupture behavior in flexure mode on

Nic/BN/SiC specimens at 600°C and 900°C and found similar degradation. Morscher [50] found

similar degradation in Nic/BN/SiC minicomposites at 700°C. A minicomposite is essentially one

tow of fibers (a large number of parallel fibers used in the weave architecture) that have gone

through the manufacturing process (i.e. chemical vapor deposition and/or melt infiltrate). Lin and

Becher [51] investigated the Nic/SiC system in air. Lastly, Glime and Cawley [52] collected data

on Nic fibers while investigating stress concentrations in CMCs.

　　　The data from most of these studies are summarized in stress rupture curves in Figure 9,

Figure 10, and Figure 11 [10]. The stress in these plots was calculated by dividing the composite

stress by the volume fraction of fibers in the loading direction. This was done to allow direct

comparison with fiber data. The strength degradation, shown in Figure 9, is linear with respect to

the log of time. Similar data for the Nic/C/SiC systems is plotted in Figure 10 showing that it

failed at a much lower fiber stress compared to the as-produced fibers. The Nic/BN/SiC system

failed at a slightly lower stress compared to the as-produced Nic fibers as shown in Figure 11.

The similar slopes of the as-produced Nic fiber data and the Nic/BN/SiC experimental data

indicate that there is little or no embrittlement up to 700°C; however, between 850-1050°C

(Larson Miller Parameter of approximately 19500-25000) embrittlement is evident by the

decrease in rupture strength [10].
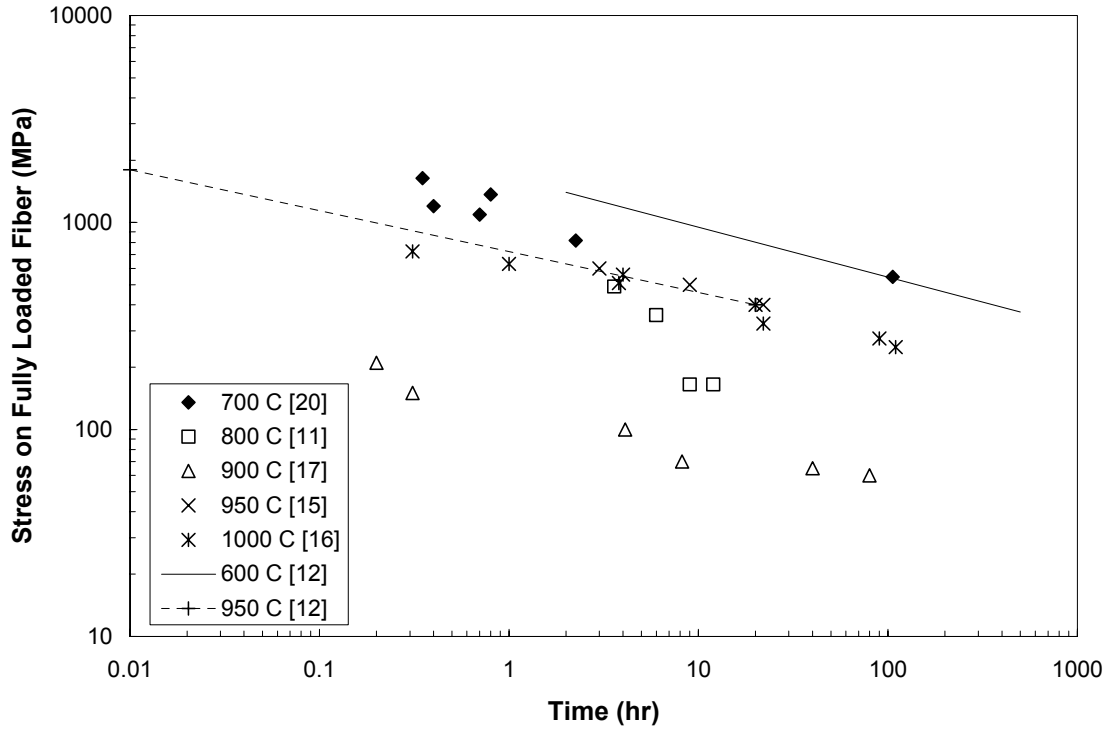
Figure 9: Stress Rupture Plot of Nic/C/SiC [10]
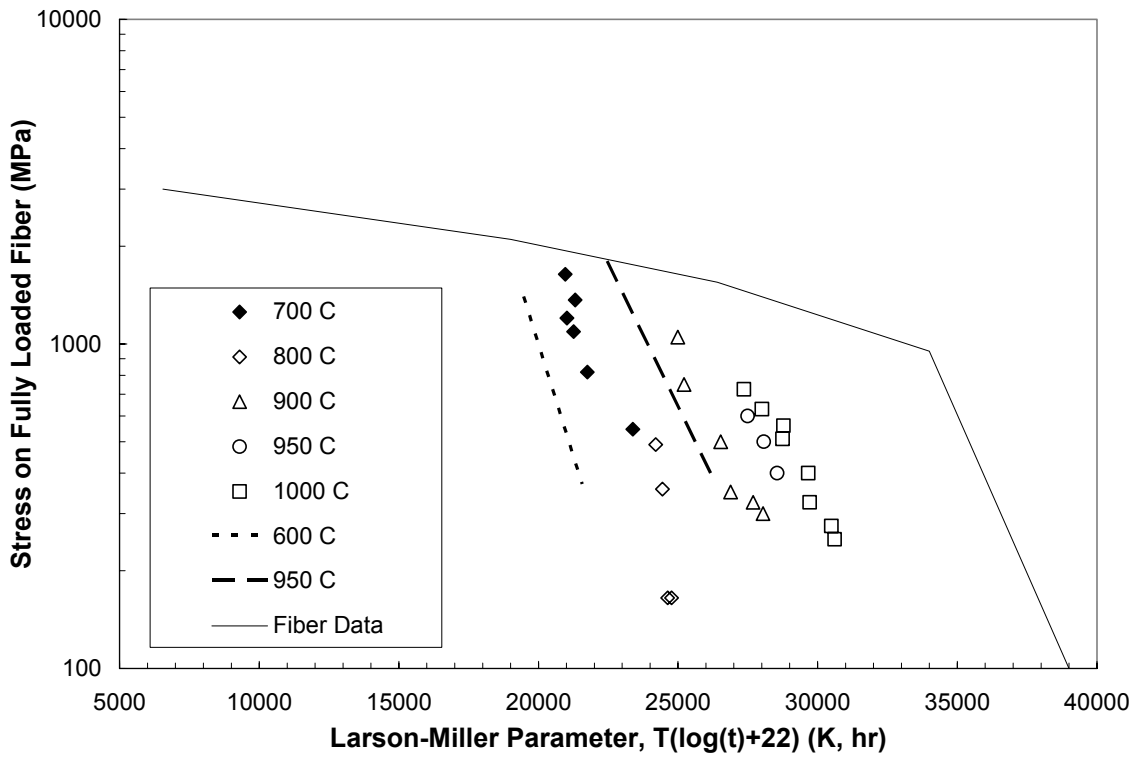
Figure 10: Larson-Miller Plot of Nic/C/SiC [10]
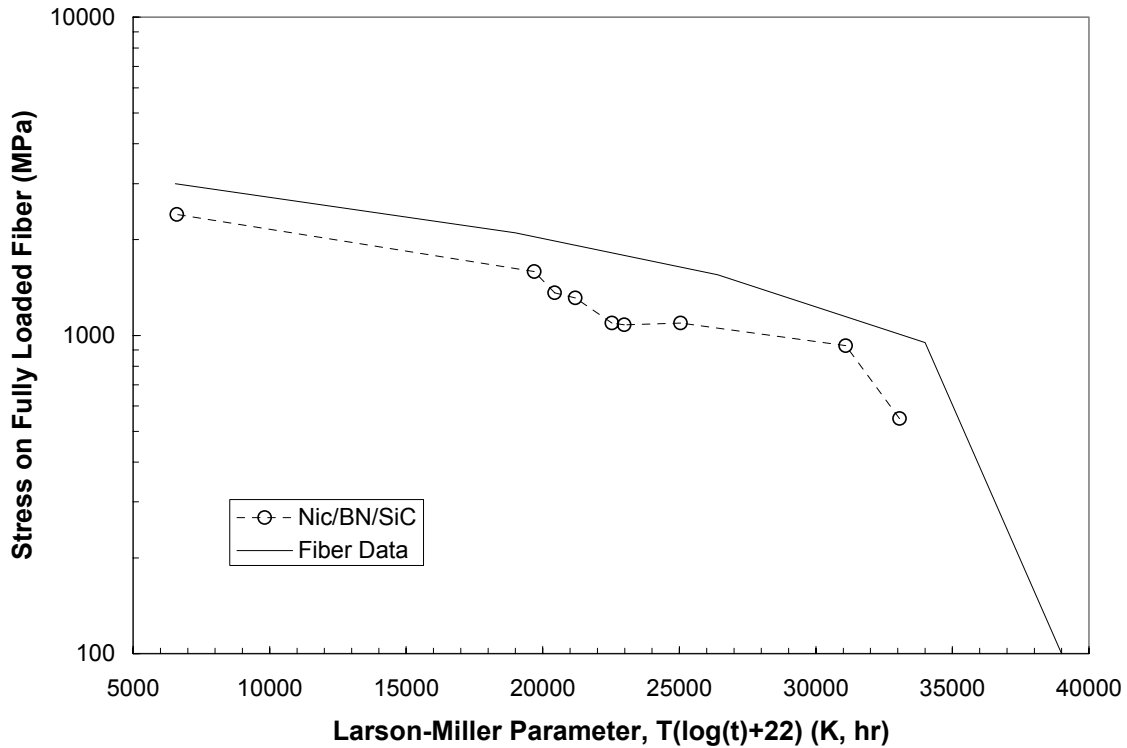
Figure 11: Larson-Miller Plot of Nic/BN/SiC [10]

Other studies have looked at the HN/SiC system using either C or BN interphase. Martinez-Fernandez and Morscher [53] investigated the behavior of HN/C/SiC minicomposites for temperatures ranging from 700-1200°C in air. They found the HN/C/SiC minicomposites outperformed the Nic/C/SiC minicomposites in the test environment but were inferior to the HN/BN/SiC minicomposites. Morscher [10,54] investigated the stress rupture behavior of HN/BN/SiC CVI matrix minicomposites and composites in air between 600-1300°C and the low-cycle fatigue behavior of HN/BN/SiC minicomposites. He found that the CMC strength degradation was attributed to the degradation of the fiber strengths caused by exposure to the test environment and reaction to the liquid by-product of the oxidation of the interphase material (i.e. the oxidation of BN to form borosilicate glass). Also, the solidification of the liquid caused the fibers to pest together, thus removing the inherent toughness of the CMC material and causing premature CMC failure.

Morscher and Cawley [17] investigated the stress rupture behavior of HN/BN/SiC MI matrix and Syl/BN/SiC MI matrix composites at 815°C in air. Morscher et al [55] investigated the

23

stress rupture behavior and low cycle fatigue behavior of the HN/BN/SiC MI matrix system. Using scanning electron microscopy, embrittled and pristine areas of the fracture surface were identified. Using electron dispersive spectroscopy (EDS), the O:C ratios were compared for the different fibers, embrittled or pulled-out. They concluded the embrittled fiber failure occurred before pulled-out fiber failure and that the bridging fibers were exposed to the environment for long periods of time. He also showed that the pulled-out fibers failed shortly after the embrittled fiber failures. From their work, the failure mechanism for these CMCs was shown as follows: the applied load causes matrix cracking, the environment attacks the interphase and embrittles fibers, the fiber strengths degrade, an embrittled fiber fails causing a cascading affect that fails the neighboring fibers that are pested together, the pristine fibers fail because of the increased load, and pristine fibers pullout.

Brewer [3] investigated the effect of moisture on low cycle fatigue at 1200°C with 0.2 and 0.9 atm pH_2O under the NASA Enabling Propulsion Materials Program. He found that at 1200°C, the life was reduced from 53 to 1.2 hours at 145 GPa with 0.2 atm pH_2O and from 1097 to 19 hours at 117 GPa with 0.9 atm pH_2O.   He also found life reductions from 4996 to 100 hours (run out time) with 0.2 atm pH_2O and to 51 hours at 105 GPa with 0.9 atm pH_2O. This work shows that moisture can affect the mechanical properties of SiC CMCs at elevated temperatures.

The data from some of the above studies with HN/SiC systems are summarized in Figure 12 and Figure 13. The slightly lesser slope of the HN/C/SiC experimental data, compared to the as-produced HN fiber data in Figure 12, indicates there is minor embrittlement occurring up to 700°C and that above 700°C more embrittlement occurs with longer times and higher temperatures. The HN/BN/SiC system failed at a similar fiber stress as the as-produced HN fibers [10], as shown in Figure 13.
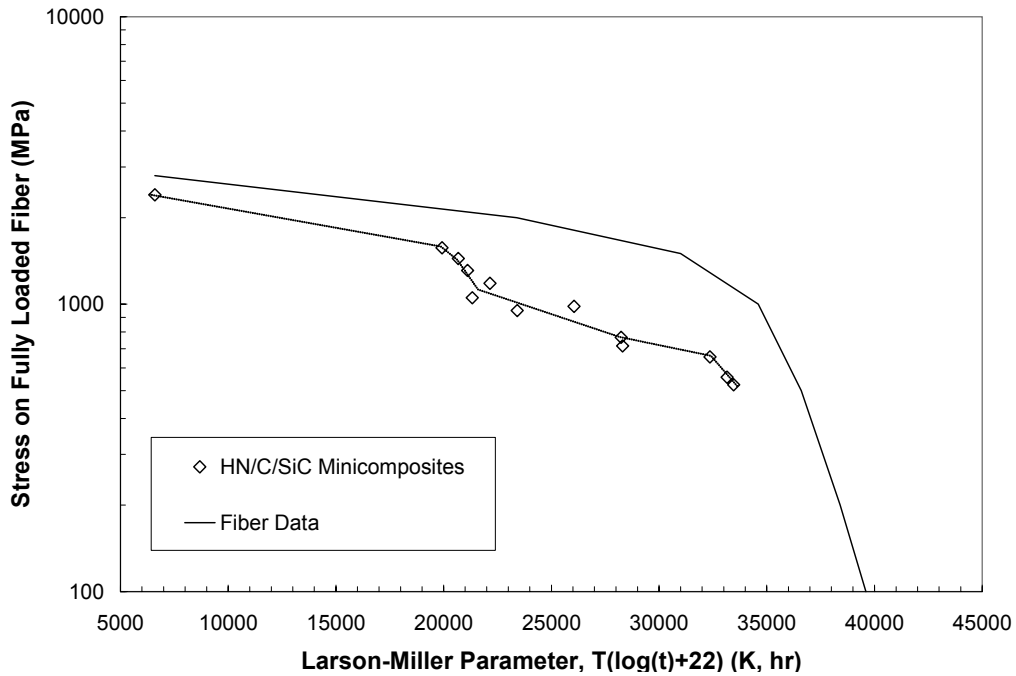
Figure 12: Larson-Miller Plot of HN/C/SiC [10]
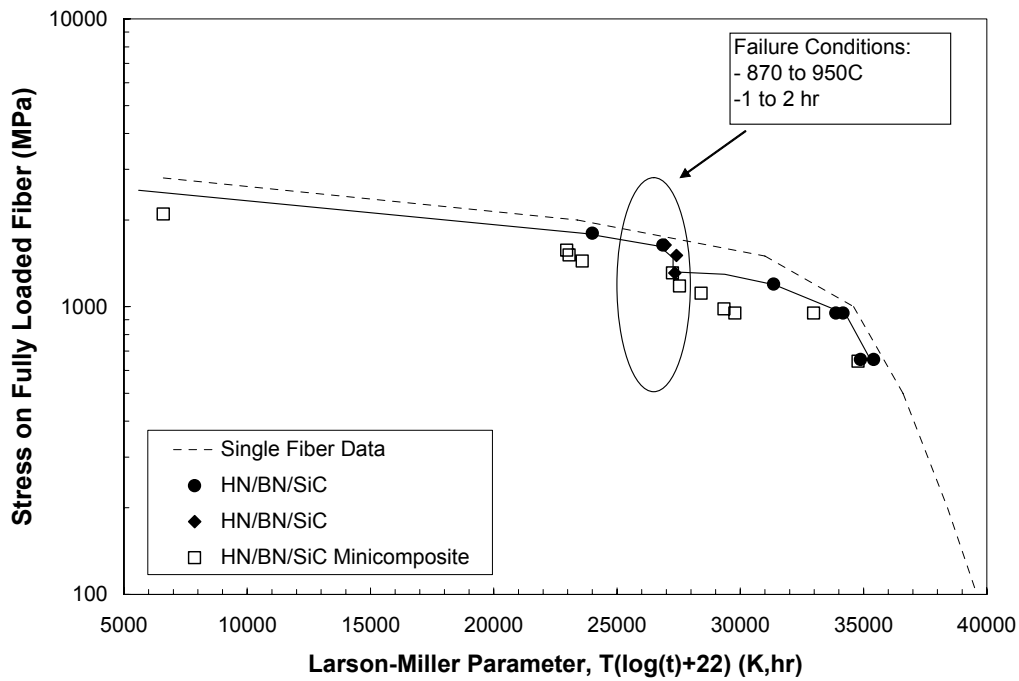
Figure 13: Larson-Miller Plot of HN/BN/SiC [10]

All of the previously mentioned studies show that embrittlement is detrimental to CMC

performance; however, none have attempted to quantify the effects of moisture in the

intermediate temperature range (i.e. the detrimental affects are not studied with respect to various

amounts of moisture content). Since combustors are exposed to both intermediate temperatures and high moisture, it is important for designers to thoroughly understand the corresponding effects on material performance. That is why this research focuses on intermediate temperature and moisture effects on a SiC/SiC CMC system.

Comparing Figure 11 to Figure 10 and Figure 13 to Figure 12 clearly shows that BN is a better performing interphase than C when used with various SiC/SiC CMCs. While BN possesses similar debonding and sliding properties as C, it is more durable in oxidizing environments. Because of this, the CMC system studied in this research will consist of Syl-iBN SiC fibers, a BN interphase, and a SiC matrix and will be denoted as Syl-iBN/BN/SiC. This research quantifies experimentally and models the effects of the different environments (temperature and moisture) on the life of the Syl-iBN/BN/SiC system subjected to stress rupture conditions. To lay the foundation for discussing this research, an understanding of gaseous diffusion and surface chemistry kinetics is discussed.

Embrittlement of SiC/BN/SiC CMCs at Intermediate Temperatures

The presence of O_2 and H_2O will severely degrade the performance of the Syl-iBN/BN/SiC material [56] if the environment has access to the load bearing fibers and the interphase material. Matrix cracks, pores, and machined edges provide ingress routes for the environment. Figure 14 [57] is a schematic drawing that illustrates environmentally assisted embrittlement of CMCs and is provided to assist the reader in the following discussion.
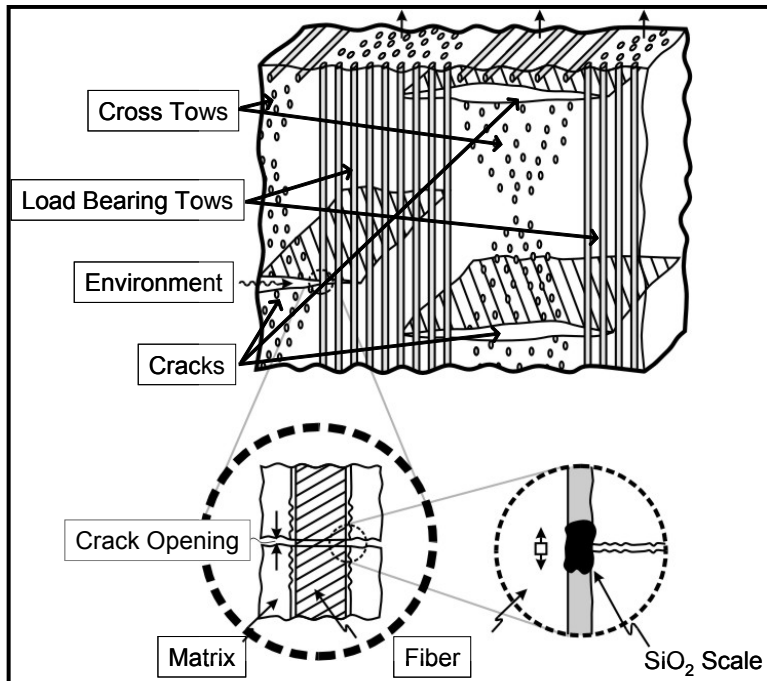
Figure 14: Model of Environmentally Assisted Embrittlement of CMCs [57]

For Syl-iBN/BN/SiC, at intermediate temperature, the major reactions are the oxidation of the BN to form B_2O_3, the formation of borosilicate glass, and the subsequent reaction with moisture to remove the boron leaving SiO_2. Above 450^oC BN rapidly oxidizes with O_2 according to the following reaction:

$$2BN(s) + \frac{3}{2}O_2(g) \rightarrow B_2O_3(l) + N_2(g) \qquad \textbf{2}$$
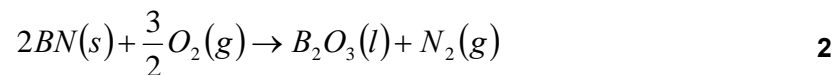
At 550^oC and 750^oC this reaction is exothermic with a ΔH_f = -739 kJ/mol and -734 kJ/mol, respectively [58]. Coffer and Economy [59] used thermogravimetric analysis, scanning electron microscopy, and mass spectrometry to verify that the BN oxidizes to form B_2O_3. They found that the reaction rate of Equation 2 at 700^oC is dependent on the crystalline structure of the BN such that larger interlayer spacing results in higher oxidation rates. They postulated that this is expected since the larger spacing correlates to less densely packed basal planes, which implies weaker atomic bonds. The BN in the Syl-iBN/BN/SiC CMCs is deposited at low temperatures resulting in large spacing. Jacobson et al [11] looked at the sensitivity of the kinetics of the BN to

boria oxidation to the crystallographic orientation, amount of porosity, and level of impurities. Using electron dispersive spectrometry they showed that the BN grains oxidized after 20 hours at $900^{o}C$. Figure 15 is an SEM image of a SiC fiber that had a BN coating applied to it and was exposed to $1000^{o}C$ air environment for 2 hours [60]. The BN has completely reacted with the O_2 and formed B_2O_3 glass.
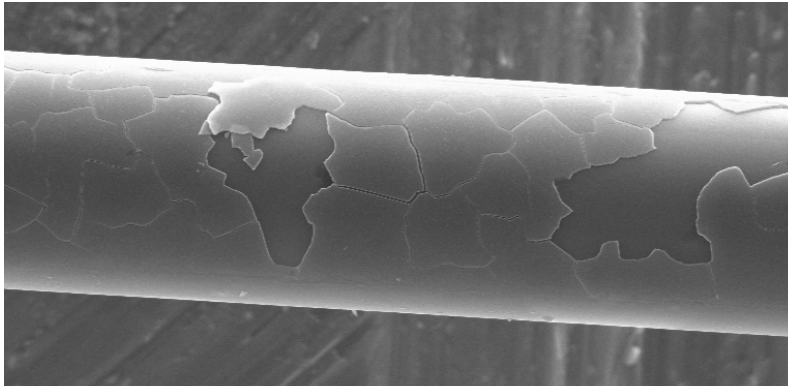
Figure 15: SiC Fiber with BN Coating after 2 hr expose to $1000^{o}C$ Air [60]

The liquid B_2O_3 product from Equation 2 can then become borosilicate glass in several ways. It can react with any SiO_2 from the oxidation of the SiC fiber and/or matrix, the oxidation of the Si that is doped into the BN, and the oxidation of any SiC the boria has dissolved. Jacobson et al [12] showed that at $700^{o}C$, $800^{o}C$, and $900^{o}C$, the BN layer on a SiC plate removed and replaced with borosilicate glass. The SiO_2 formation on the SiC plate was accelerated by the increased oxygen diffusivity of borosilicate glass compared to that of SiO_2. Ogbuji [41] reported that the phase diagrams for the $SiO_2 - B_2O_3$ system support B_2O_3 dissolving its own weight in SiO_2 at $800^{o}C$ thus resulting in borosilicate glass. Cawley [37] showed that at $700^{o}C$ it took 20 hours for SiO_2 to fill a gap of 0.1 μm left by the oxidation of C between a SiC fiber and SiC matrix.

The reaction of B_2O_3 with the SiC in the fiber and/or matrix results in borosilicate glass according to the following reaction:

$$B_2O_3(l) + SiC(s) + \frac{3}{2}O_2(g) \rightarrow B_2O_3 \cdot SiO_2(l) + CO(g) \qquad \textbf{3}$$
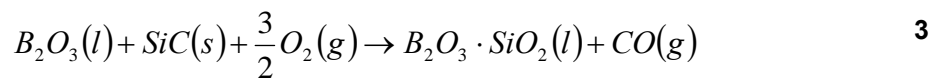
The amount of weight gain seen by Ogbuji [41] does not support the conclusion that the SiO_2

comes solely from the oxidation of the SiC fiber and matrix. He suggests the B_2O_3 dissolves the

SiC matrix and possibly the fiber, predominantly the former. The SiO_2 most probably comes from

a combination of the above sources.

The end result is that the B_2O_3 in the liquid phase above 410^oC reacts and forms

borosilicate glass. The B_2O_3 in the borosilicate glass is volatilized by moisture according to the

following reactions:

$$B_2O_3(l) + 3H_2O(g) \rightarrow 2H_3BO_3(g)$$
4

$$3B_2O_3(l) + 3H_2O(g) \rightarrow 2H_3B_3O_6(g)$$
5

$$B_2O_3(l) + H_2O(g) \rightarrow 2HBO_2(g)$$
6
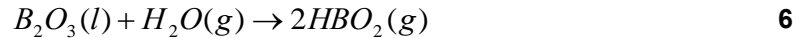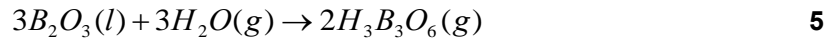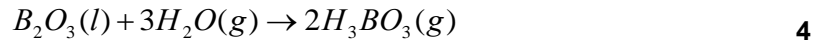
Equation 6 is the primary reaction in volatilization at the intermediate temperature studied

in the research. Coffer and Economy [59] found that the HBO_2 in Equation 6 is stable in the

gaseous form at 700^oC. Morscher et al [12] used scanning electron microscopy for imagery,

energy dispersive spectroscopy for elemental identification, Rutherford backscattering

spectroscopy for composition measurement of the B_2O_3, and wavelength dispersive spectroscopy

for boron detection. Their analysis showed the same result: that the BN was converted to liquid

B_2O_3 which then became borosilicate. Eventually the liquid solidified and was predominantly

SiO_2. Jacobson et al [11] used molecular beam mass spectrometry to identify the HBO_2

supporting the reaction in Equation 6.

The removal of boron from the borosilicate glass increases the viscosity and eventually

freezes the residual SiO_2 glass over time [10]. The viscosity of the glass is not only dependent on

the temperature but also on the amount of SiO_2 in the borosilicate glass as well as any impurities

that may be present. The resulting pesting of the fibers because of the glass formation has

detrimental effects because the attached fibers will experience local load sharing when a

neighboring fiber fails. The pesting causes embrittled fiber failure for two reasons. The first

reason is that the fiber experiences a dramatic jump in stress under local load sharing. The

second reason is that the pesting gives a path for the failure crack to propagate across.

Morscher [61] continued his investigation on the effect moisture had on the BN oxidation

by looking at ends-on oxidation specimen made with BN-based interphases fabricated at different

temperatures. He found that the lower the processing temperature of the BN interphase material

the more susceptible the BN is to oxidation. His findings, that typical BN interphases used in

CMCs have oxidation problems because the BN is processed at low temperatures around

$1000^{o}C$, support that of Coffer and Economy [59] mentioned earlier.

The changes caused by environmental attack in the constituent materials and their

interaction with each other lead to stress rupture strength degradation of Syl-iBN/BN/SiC (i.e.

embrittlement). Morscher [10] and Morscher and Cawley [17] tied all the discussion above

together to study embrittlement of SiC/SiC CMCs at $815^{o}C$ in ambient laboratory conditions. The

present research investigates similar embrittlement effects at $550^{o}C$ and $750^{o}C$ with controlled

moisture content levels of 0, 0.2, and 0.6 atm pH_2O.

Gaseous Diffusion and Surface Chemistry Kinetics of Embrittlement

Molecular diffusion is the process whereby a substance (gas, liquid, or solid)

spontaneously migrates due to the random motion of the molecules. It is caused primarily by

concentration gradients, where according to Fick's Law, the rate of molecular diffusion out a

region is proportional to the concentration in that region and vice versa. For molecular diffusion

to control a mechanism, it must be the rate determining step, or the slowest step of the

mechanism. Graham's Law,

$$\dot{D} \propto \frac{1}{\sqrt{\rho}}$$

7

states that the rate of molecular diffusion, $\dot{D}$, is inversely proportional to the square root of the

density, ρ. The rate of molecular diffusion is a function of the temperature. Higher temperatures

lead to higher molecular kinetic energy resulting in faster molecular diffusion. Eckel et al [62],

Jacobson et al [63], and Jacobson et al [64] used Chapman -Enskog theory to determine the

diffusivity of one gas in another gas, called gaseous diffusion, which is a subset of molecular diffusion. The equation from Eckel et al [62] is:

$$D_{AB} = \frac{5.9543 \times 10^{-24} \left(\frac{1}{M_A} + \frac{1}{M_B} \right)^{\frac{1}{2}} T^{\frac{3}{2}}}{\left(P \sigma_{AB}^2 \Omega_{AB} \right)}$$

8

where

$D_{AB} \equiv$ diffusivity of gas A in gas B (m^2/s)
$M_A \equiv$ molecular weight of gas A (kg/mol)
$M_B \equiv$ molecular weight of gas B (kg/mol)
$T \equiv$ temperature (K)
$P \equiv$ pressure (Pa)
$\sigma_{AB} \equiv$ effective collision diameter (m)
$\Omega_{AB} \equiv$ a tabulated integral

The diffusivity, D_{AB}, in Equation 8 can be used to estimate the time it takes a molecule of gas to diffuse to the center of a specimen in a through-the-thickness crack using the following relationship [62]:

$$\xi = \sqrt{\left(t \dot{D}_{AB} \right)}$$

9

where

$\xi \equiv$ diffusion distance (m)
$t \equiv$ time (s)

For the specimen dimensions and environmental conditions in this research, the time for a molecule to diffuse to the center of the specimen is on the order of magnitude of 10^{-2} seconds. Equations 8 and 9, assume there is no consumption of the reactants so the result is a minimum time for the reactants to reach the center of the specimen. Consumption will slow the rate of diffusion of molecules through the crack. Consumption is higher at elevated temperatures leading to a slow embrittlement front moving across the crack plane from the outside edge of the specimen towards the center.

Substances can diffuse by other means besides molecular motion. Forced diffusion is the mixing of one substance relative to one or more other substances by an externally applied force (e.g. mechanical, electrical, centrifugal, and magnetic). An example of forced diffusion is the stirring of coffee when cream is added. Without stirring it would take much longer for the cream to diffuse throughout the entire coffee mug. Typically, forced diffusion is much faster than molecular diffusion.

Surface chemistry kinetics deals with how fast a chemical reaction occurs (reaction rate), how the reaction rates can be controlled, and how a reaction proceeds from the reactant to the products. Chemical reactions are controlled by the activation energy. For a reaction to occur, two reactant molecules must collide in the correct orientation and possess a minimum amount of energy to overcome the activation energy barrier.

For surface chemistry kinetics to control a mechanism, the rate of the reaction must be the rate determining step, or the slowest step of the mechanism. The rate of the reaction is a function of the percent of molecules with the required energy to overcome the activation energy. The rate constant can be expressed as an exponential function of the ratio of the activation energy to the energy a molecule has at a given temperature. This is the foundation of the Arrhenius equation:

$$k = Ae^{-\frac{E_a}{RT}}$$

10

where k is the rate constant, A is the frequency factor which is constant for specific reactions and is a function of the probablity of collisions occuring in the correct orientation for the reaction to occur, E_a is the activation enegy, and RT is the thermal energy (molar constant multiplied by the temperature). At low temperatures, depending on the reaction, most molecules will not have enough energy to overcome the activation energy and cause the reaction. As the temperature increases, the molecules collide more frequently because they are moving faster and more of these collisions will have the energy to overcome the activation energy. Therefore, either

increasing the temperature or decreasing the activation energy through the use of catalysts will increase the rate of the reaction.

The Arrhenius equation shows how the inverse of temperture in the exponential can lead to large decreases (orders of magnitude) in the reaction rate. The magnitude of the decrease depends on the ratio of activation energy to thermal energy. Comparing the rate coefficients at different temperatures shows the effect temperature has on the reaction rate. With an activation energy of 227kJ/mol for the oxidation of BN, the ratio of the rate constants for $815^{o}C$ and $750^{o}C$ is 10; however, the ratio for $750^{o}C$ and $550^{o}C$ is 10^{3}. The temperatures used in this research covers a wide range of reaction rates for the oxidation of BN to boria.

The presence of the reactant species is also important in surface chemistry kinetics. The gaseous reactant species must come into contact with the reactant species in the condensed phase at the surface the reaction will not occur. Therefore, it is important to understand that the mobility of the reactant species in the condensed phase may control the the surface chemistry kinetics. Reactants in the condensed phase move under the influence of a concentration gradient by diffusion. As the reaction occurs at the surface, the concentration of the reactants there decreases relative to the concentration in the center of the condensed phase. Molecular diffusion will result causing reactants to move towards the surface.

The time it takes for the reactants to move through the condensed phase depends on the mean free path and is affected by the temperature, the reactant, and the condensed phase. Consider a SiC plate with a layer of borosilicate glass on it. The oxygen atoms at elevated temperatures diffuse through boria faster than it does through silica. Therefore, the rate of diffusion is dependent on the amount of silica borosilicate glass. As the borosillicate glass increases in silica content the O_2 has a harder time to diffuse. Eventually the borosilicate glass will have enough silica in it to essentially stop the O_2 from getting the the SiC plate. This will form a protective oxidation layer on the SiC plate.

Depending on the environment (i.e. temperature and pressure), a mechanism, like embrittlement, may be controlled by gaseous diffusion or by surface chemistry kinetics. The embrittlement kinetics are complex and it is extremely difficult to model each step of the

phenomenon. For gaseous diffusion controlled embrittlement, the time it takes the atoms (O_2

and/or H_2O) to enter the crack opening region and move through the crack towards the center of

the specimen is longer than the time it takes the atoms to react with the BN and/or boria. In this

case the pesting will occur on the outside edge of the specimen first and the embrittlement front

will move towards the center of the specimen, as shown in Figure 16. For surface chemistry

kinetics controlled embrittlement, the time it takes for the reactions to occur is longer compared to

the gaseous diffusion time. The atoms still diffuse through the crack opening towards the center

of the specimen; however, the reaction is slow enough to allow the entire crack to become

saturated with reactants so that when pesting occurs it affects the entire cross section uniformly,

as shown in Figure 16.

Diffusion Controlled Embrittlement

Chemical Kinetics Controlled Embrittlement
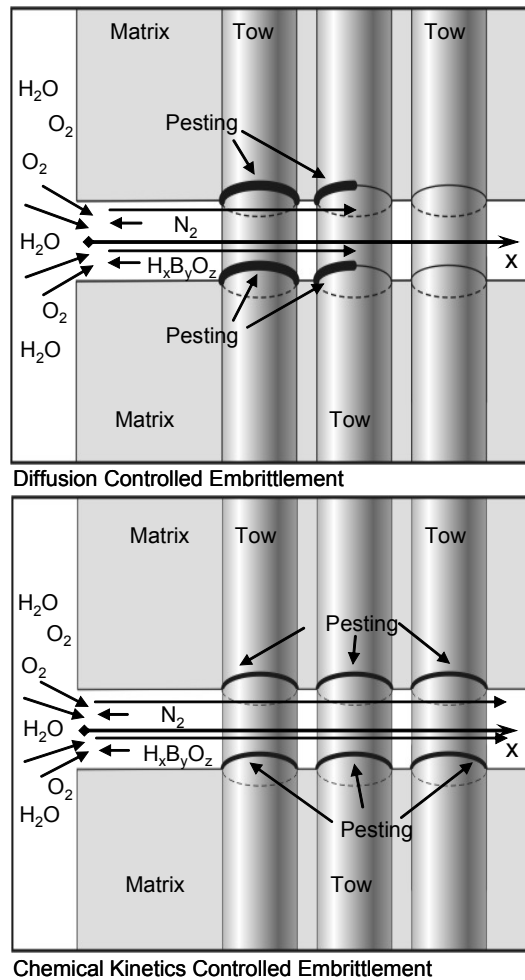
Figure 16: Embrittlement Kinetics

The kinetics of embrittlement, either gaseous diffusion controlled or surface chemistry kinetics controlled, may be different depending on the environment (i.e. the temperature, the partial pressure of the reactants, etc), testing conditions (i.e. monotonic loading, stress rupture loading, cycling, etc), material properties (i.e. fracture toughness and environmental durability of the constituent materials), or manufacturing specifications (i.e. amount of interphase material, porosity of the specimen, processing temperature of the interphase). Halbig et al [65] studied embrittlement at high temperatures, approximately 1454°C. They saw "picture frame" type embrittlement at these temperatures. They point out that in the intermediate temperature range there is a transition between the gaseous diffusion controlled embrittlement that occurs at high temperature and the surface chemistry kinetics controlled embrittlement that occurs at low temperatures and that there is an intermediate temperature at which the gaseous diffusion rate and surface chemical reaction rate are similar. They saw uniform embrittlement across the entire fracture surface of the C/SiC specimens at 700°C.

The transition leads to four possible situations concerning the controlling factors of the embrittlement phenomenon and matrix cracks. The embrittlement kinetics could be gaseous diffusion controlled within a partial matrix crack, gaseous diffusion controlled within a through-the-thickness matrix crack, surface chemistry kinetics controlled within a partial matrix crack, and surface chemistry kinetics controlled within a through-the-thickness matrix crack. Each situation will have different observable characteristics.

In the partial crack scenarios, the fracture surface for gaseous diffusion controlled and surface chemistry kinetics controlled embrittlement will look the same. The featureless glass formation and pesting will occur at the outside edge, particularly at the corners. In gaseous diffusion controlled embrittlement the glass formation will occur along the edge first because the reactions occur as soon as the O_2 and H_2O atoms enter the partial crack. In surface chemistry kinetics controlled embrittlement, the glass formation would also occur on the outside edge of the specimen because the reactions will only occur in the crack opening region which is typically on the outside edge of the specimen, again, at the corners. Morscher [66] observed featureless glass formations at the corners of the specimens he tested below the "knee" of the strain versus

strain curve of his material. The cracks formed were partial cracks since the stress was below the "knee". When embrittlement is occurring in partial cracks, the bridging fibers become embrittled and eventually one fails leading to the cascading failure of other embrittled fibers. The increased stress at the crack tip in the matrix material causes the crack to propagate further into the material, exposing more pristine fibers. These fibers bridge the crack until it stops. This process repeats until the remaining fibers and matrix can no longer support the load and the specimen fails. The last group of pristine fibers will have fiber pullout characteristics and no featureless glass around them.

In the through-the-thickness crack scenarios, gaseous diffusion controlled embrittlement will look different than surface chemistry kinetics controlled embrittlement. The fracture surface in the gaseous diffusion controlled embrittlement in a through-the-thickness crack will look like the typical "picture frame" fracture surface seen by other researchers like Morscher [66] and Heredia et al [67]. The picture frame is created because the reactants have access to the interior of the specimen along the entire specimen perimeter. As mentioned previously in the gaseous diffusion controlled embrittlement of a partial crack, the reactions occur as soon as the atoms of O_2 and H_2O enter the crack and come into contact with BN and boria. This happens uniformly along the specimen perimeter and works its way towards the center of the specimen depending on the gaseous diffusion rate and consumption of the gas.

The fracture surface in the surface chemistry kinetics controlled embrittlement will look different. Here, either the reactions do not occur fast enough or the reactants do not reach the surface fast enough, thus, allowing the O_2 and H_2O to enter the crack and saturate the interior of the specimen. This leads to uniform embrittlement across the entire fracture surface similarly to what was seen by Halbig et al [65] with C/SiC composites at intermediate temperatures.

Modeling Intermediate Temperature Stress Rupture

Models must characterize the material's performance so designers can use them to develop better performing parts for various applications. This section addresses the background information for modeling CMC failure. The model developed in this research is presented in detail in Chapter V which provides a different approach to simulate CMC failure by modeling

individual fiber failure by including probability of fiber failure, effects of matrix cracking, stress profiles along a fiber, strength reduction due to the manufacturing process, and embrittlement. It is an extension of the modeling effort by Morscher and Cawley [17], but includes several new features.

Curtin's [22] formulation provides the necessary formulation based on individual fiber theory needed to solve for the probability of fiber failure. His theory states that the probability of failure for an individual fiber, $P(\sigma,L)$, is given by the following:

$$P(\sigma, L) = 1 - e^{-\Phi(\sigma, L)}$$ **11**

$$\Phi(\sigma, L) = \int_0^L \left(\frac{1}{L_o} \right) \left(\frac{\sigma(x)}{\sigma_o} \right)^m dx$$ **12**

where

$\Phi(\sigma,L) \equiv$ the number of defects that could fail
$L \equiv$ fiber length (mm)
$L_o \equiv$ fiber reference length (mm)
$\sigma(x) \equiv$ stress along fiber length, L (MPa)
$\sigma_o \equiv$ reference strength of fiber (MPa)
$m \equiv$ Weibull parameter

Furthermore, Curtin [22] states there exists a characteristic stress, σ_c, and a characteristic gauge length, δ_c,

$$\sigma_c = \left(\sigma_o^m \cdot \tau \cdot \frac{L_o}{R} \right)^{\frac{1}{(m+1)}}$$ **13**

$$\delta_c = \frac{R \cdot \sigma_c}{\tau}$$ **14**

such that,

$$\Phi(\sigma_c, \delta_c) = 1 \qquad\qquad \textbf{15}$$

where

$\tau \equiv$ interfacial shear stress (MPa)
$R \equiv$ radius of the fiber (mm)

In short, the theory of Curtin [22] means that there exists one defect in a fiber of length δ_c that could cause failure when subjected to a stress, σ_c. To apply this theory to fibers in a CMC, the stress profiles along a fiber length need to be known. The stress profile is affected by of matrix cracking.

Matrix cracking in CMCs has been studied and modeled by several researchers [19,20,68,69,70]. Since all the applied stresses in this research were above the proportional limit, a majority of the matrix cracks will be through-the-thickness cracks. As stated earlier, the stress on the fibers bridging a through-the-thickness crack will be higher than the stress on a fiber bridging a partial crack. Therefore, the fibers in a through-the-thickness crack will fail before fibers in a partial crack, making the critical crack a through-the-thickness crack. Also, stress rupture loading is constant so crack propagation will depend on fiber failures which generally occur first in through-the-thickness cracks. Therefore, it is assumed the partial cracks did not play an important role in the failure of the specimen under the test conditions in this research. The research presented here is not concerned with developing a new approach of modeling matrix cracking; instead, it focuses on incorporating information describing the two important effects of matrix cracking: the crack opening size and the length of fiber needed to transfer the load from the fiber to the matrix, known as the stress transfer length. The number of through-the-thickness matrix cracks is also important to modeling CMC failure. Morscher and Cawley [17] showed that post test measurements can be used to accurately represent the number of cracks.

The length of fiber in the crack opening, u, can be determined using the formulation of Marshall et al [69] and is given as:

$$u = \frac{\sigma_{f,c}^2 R}{2\tau_T E_f \left(1 + \dfrac{E_f f}{E_m (1-f)}\right)} \qquad\qquad \textbf{16}$$

where

$\sigma_{f,c} \equiv$ stress on a fiber in the crack opening (MPa)
$\tau_T \equiv$ interfacial shear stress at temperature (MPa)
$E_f \equiv$ modulus of elasticity of the fiber (GPa)
$E_m \equiv$ modulus of elasticity of the matrix (GPa)
$f \equiv$ volume fraction of fibers in the loading direction

Their formulation, presented in Appendix A, provides a realistic representation of the crack opening and a computationally friendly equation to incorporate into models. It was used by Morscher and Cawley [17] and will be used in the modeling effort presented in Chapter V. The stress transfer length can be determined using the theory of Curtin [22] described above and is given by:

$$\delta = \frac{R\sigma}{\tau} \qquad \textbf{17}$$

Since fibers fail as a result of the fiber stress at a particular location being greater than the fiber strength at that same location, the stress profile along a fiber in the presence of a through-the-thickness crack must be determined and modeled. A through-the-thickness crack has a well-defined effect on the stress profile [22]. A fiber can be divided into two separate regions, the crack opening region (Region 1) and the stress transfer region (Region 2), as illustrated in Figure 17.
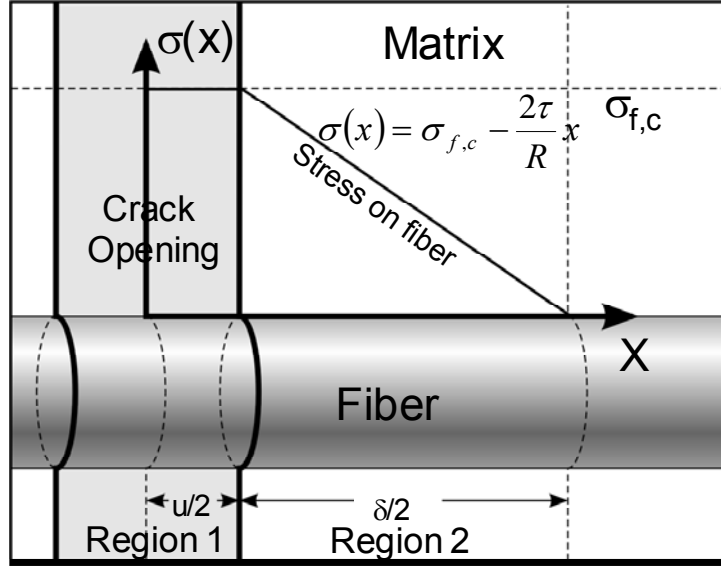
Figure 17: Stress Profile Along a Fiber in Presence of Crack

The portion of a fiber in the crack opening region (i.e. Region 1 in Figure 17) is unable to shed any load to the matrix. Therefore, the length of fiber in the crack opening region experiences a constant stress, $\sigma_{f,c}$, along its length equal to:

$$\sigma_{f,c} = \frac{\sigma_a}{f} \qquad \textbf{18}$$

where

$\sigma_a \equiv$ applied stress on CMC specimen (MPa)

The length of the fiber in the stress transfer region (i.e. Region 2 in Figure 17) experiences a non-uniform stress along it length [21,73] because the stress, $\sigma(x)$, is transferred linearly from the fiber to the matrix and equals:

$$\sigma(x) = \sigma_{f,c} - \frac{2\tau}{R} x \qquad \textbf{19}$$

Morscher and Cawley [17] used these stress profiles with the appropriate length to determine the number of defects that could fail in the two regions: the crack opening region and the stress transfer region (Φ_u and Φ_z, respectively) as:

$$\Phi_u = \left(\frac{u}{L_o}\right)\left(\frac{\sigma_{f,c}}{\sigma_o}\right)^m \qquad\qquad \textbf{20}$$

$$\Phi_z = \frac{\left(\dfrac{\sigma_{f,c}}{\sigma_c}\right)^{m+1}}{(m+1)} \qquad\qquad \textbf{21}$$

where u and $\sigma_{f,c}$ are determined from Equations 16 and 18. The reference strength, σ_o, is 2800 MPa for SiC fibers as determined by Yun and DiCarlo [27]. Morscher and Cawley [17] showed that a strength reduction factor, presented in Appendix A, exists as a result of the manufacturing process. The reduction factor represents the difference in the strength of an as-produced fiber compared to the strength of a fiber in a composite specimen as given by:

$$SR = \frac{\left[\dfrac{m(m+2)R}{2(m+1)\tau_{ult}L_o}\left(\dfrac{m+2}{m+1}\dfrac{\sigma_{ult}}{f_{init}}\right)^{m+1}\right]^{\frac{1}{m}}}{2800} \qquad\qquad \textbf{22}$$

The σ_o in Equations 20 and 21 (using Equation 13) must be multiplied by the strength reduction factor to take this phenomenon into account in the modeling CMC failure based on individual fiber failure. The 2800 in the denominator represents the σ_o in MPa for SiC fibers. The strength reduction factor only models the reduction in strength caused by the high temperatures used in the manufacturing process not the high temperatures in the environment. Environmental effects on the failure mechanisms of the individual fibers must also be incorporated into a CMC failure model.

The embrittlement phenomenon is explained thoroughly throughout the literature, and in particular, in the references sited earlier. Morscher and Cawley [17] present the only attempts at quantifying the embrittlement effects on strength degradation. The embrittlement phenomenon has been described as a 'front' starting at the outside edge of the specimen and moving towards the center of the specimen within a matrix crack, thus forming a 'picture frame' around the

41

fracture surface [13]. On the outside of the picture frame the fibers are embrittled, on the inside they are pristine. This 'picture frame' embrittlement phenomenon is the result of uniform gaseous diffusion along the crack edge of the O_2 and H_2O through the matrix crack. The diffusion of the embrittlement is a result of the O_2 and H_2O being consumed before it diffuses to the center of the specimen.

Morscher and Cawley [17] quantified this embrittlement phenomenon by calculating the 'area fraction of embrittlement' or the amount of surface area on the fracture surface that has embrittled fibers. They found that a power law relationship modeled the depth of embrittlement from the edge of the specimen as a function of time. From the depth measurement and area of embrittlement was calculated. Figure 18 [10] is a plot of their data and their equation for the 'area fraction of embrittlement'.
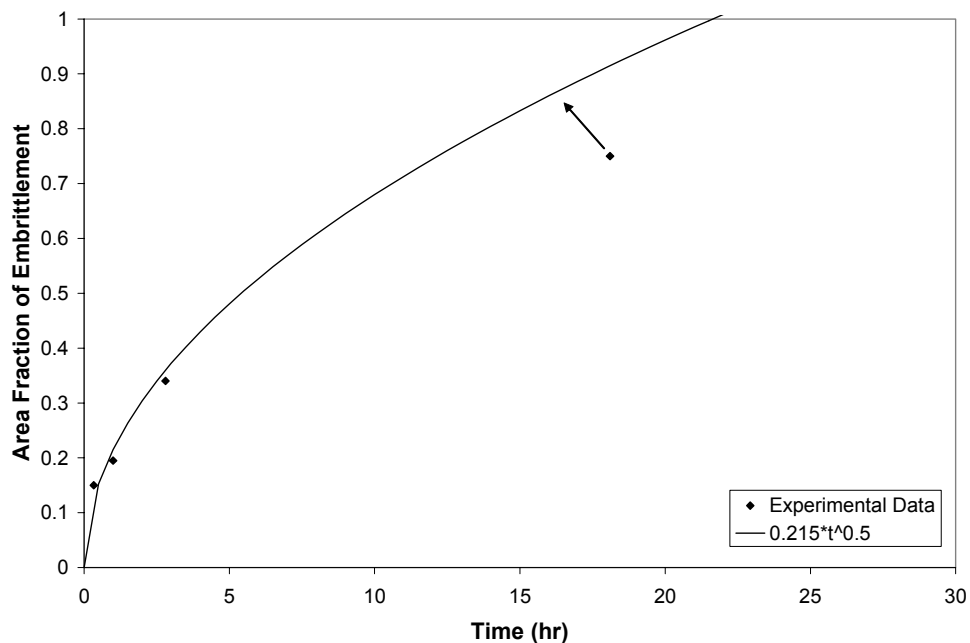
Figure 18: Depth of Embrittlement Plot from Morscher [10]

The arrow on the 18.1 hours data point indicates the area of embrittlement should have occurred in the shorter time or higher area fraction direction because the applied stress was not enough to cause a through-the-thickness matrix crack, thus limiting the access the environment had to the fracture surface [10,17]. The empirical relationship Morscher and Cawley [17] found

for the depth of embrittlement which is consistent with a gaseous diffusion controlled limiting process and is of the form:

$$x = C_{ox} t^{\frac{1}{2}}$$ **23**

where

$C_{ox} \equiv$ coefficient of oxidation
$t \equiv$ time (hr)

A goal of this research is to conduct similar measurements on the facture surfaces of specimens made of similar material, but tested in different environments. The data could then be analyzed and the coefficient of oxidation could be solved in terms of temperature and/or moisture content.

Summary

Previous studies have focused on analyzing the performance of CMCs under various environmental and loading conditions. Previous work concentrated on the Nic, HN, and Syl fiber CMC systems at high temperatures. The loading conditions in these studies were stress rupture loading in either axial or flexure loading. Currently, there is an interest in using SiC/SiC CMCs in the combustor liner application because of its promising properties and characteristics. This application involves temperatures from 450-1300°C in an extremely harsh combustion environment. The CMC family of materials experience strength degradation in these environments.

This research continues the study of the Syl-iBN/BN/SiC CMC at various environments at the intermediate temperature range and with moisture. The stress rupture curves will allow the performance of the material in the different environments to be analyzed. This study will expand on current efforts by characterizing the stress rupture performance of the Syl-iBN/BN/SiC CMC system at intermediate temperature range with various moisture content levels. This study will develop a life prediction model of the stress rupture behavior of the Syl-iBN/BN/SiC CMC system at intermediate temperatures under humid conditions.

III. Experimental Set-Up and Procedures

In this chapter, details of the experimental set-up used in this research are presented. The discussion in this chapter covers validation experiments used to verify the performance of the environmental apparatus used to control temperature and moisture content of the test environment. Test and post-test specimen specifications, as well as, the pre- and post-test procedures are explained. Lastly, the FESEM details are presented.

Experimental Test Set-Up

Figure 19 is a photograph of the entire experimental set up and a schematic of the major components of the environmental apparatus. In the left of the photo, there is the MTS frame with the environmental apparatus attached. In the center is the MTS control console. To the right of the MTS control console is the induction heater and the temperature controls. On the far right and behind the MTS control console are recirculating chillers.
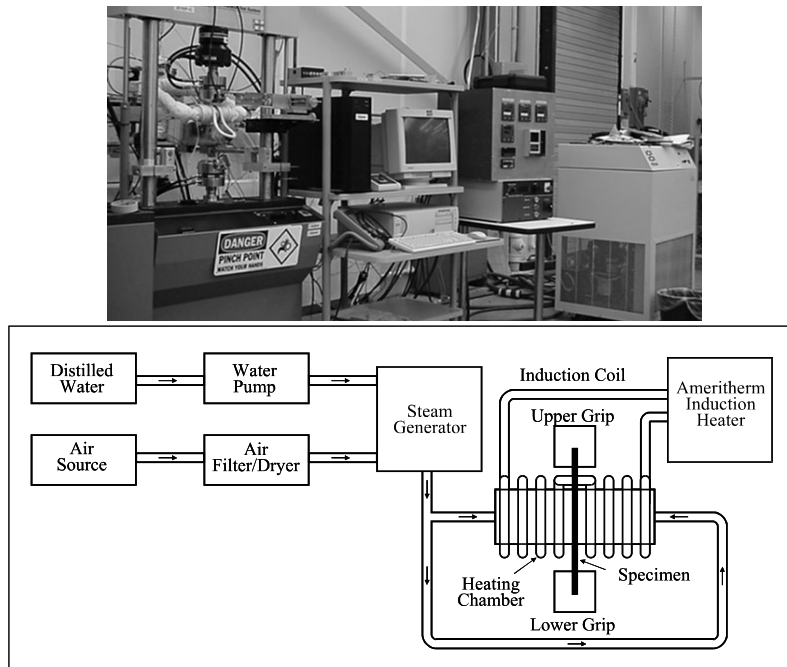
Figure 19: Experimental Test Set Up

The steam generator [71], shown in Figure 20, consisted of a stainless steel tube filled with stainless steel ball bearings heated by two Omega High Temperature Heating Tapes. The heating tapes were each controlled by a Watlow V4 Controller, a K-type thermocouple, and a solid-state relay. The tapes were wrapped around the tube in a double helix configuration to provide more uniform heating and were insulated with Coltronics WRAP-IT wet moldable felt.
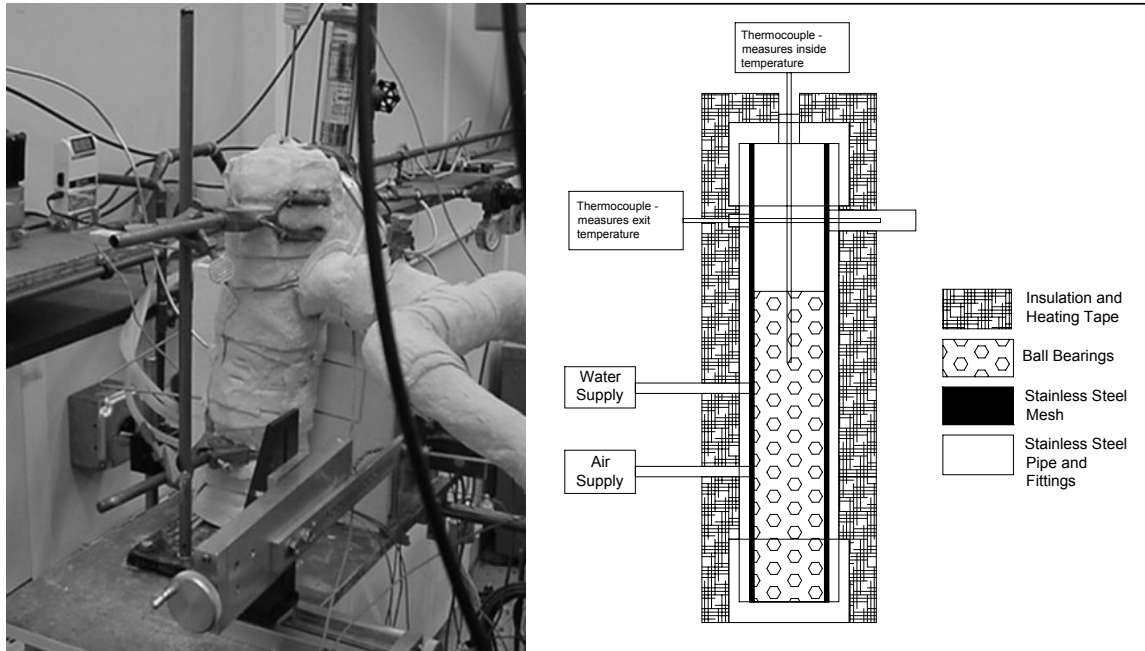
Figure 20: Steam Generator

The air came from the pressurized lines in the laboratory that passed through Coilhouse Pneumatics Air Filter Traps and a Beach Air Filter/Dryer. This removed oil, oil vapor, moisture and any particles greater than 3 microns. The airflow was controlled by a Grove Small Volume Regulator hand valve and was measured by a Mass Flowmeter, Omega Engineering, Inc. A Digital Peristaltic Pump with a Masterflex L/S Easy Load pump head, Cole-Parmer Instrument Company MIDI, pumped distilled water at a constant flow-rate through rubber tubing, Masterflex Pharmed L/S 13, and stainless steel tubing to the steam generator.

The air entered near the bottom of the steam generator while the water entered just above the air. The ball bearings provided added surface area for uniform heating and caused the air and steam to mix as they moved up inside the steam generator. The moisture content level

was calculated knowing the flow rate of the distilled water and the temperature and flow rate of the filtered/dried air. The formulation for calculating the moisture content level is presented in Appendix A.

To monitor the steam generation process, K-type thermocouples were placed at various locations throughout the steam generator. One thermocouple measured the temperature of the air before it entered the steam generator. This was needed for the calculation of the number of moles of air entering the steam generator. Another one monitored the temperature in the center of the steam generator to ensure the steam generator reached the required temperature for steam generation. To verify the steam generator was heating the moist air to the desired temperature, another thermocouple monitored the exit temperature of the steam generator.

Once the moist air was created in the steam generator, it flowed to the heating chamber through two steam tubes. Two Omega High Temperature Heating Tapes, each controlled by a Watlow V4 Controller, a K-type thermocouple, and a solid-state relay, heated these tubes to the desired testing temperature.

The heating chamber [71], shown in Figure 21, had a SiC susceptor insulated by alumina felt and an alumina tube. An Ameritherm Novastar 5 Induction Heater heated the SiC susceptor by creating a magnetic field around it that induces eddy currents on the surface of the SiC susceptor. The resistance of the SiC to these currents generates heat. A Barber Coleman 560 Controller with a K-type thermocouple placed in the heating chamber close to the specimen controlled the induction heater. A NESLAB HX-200 Recirculating Chiller cooled the induction heater and its coil.
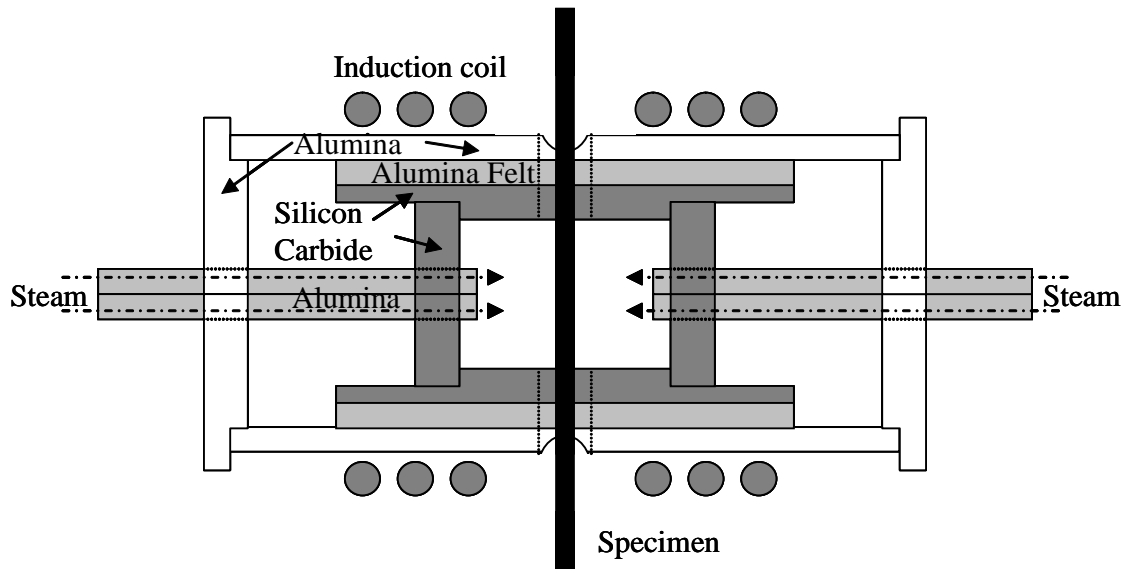
Figure 21: Schematic of the Heating Chamber

The mechanical tests were performed on an MTS 810 Material Test System with the

MTS TestStar IIs Controller and MTS TestStar IIs Software (Version 2.3B 289). The test

procedures were written in MTS MultiPurpose Testware (Version 2.3B 289). The specimens

were gripped using an MTS 647 Hydraulic Wedge Grip (25kN/5.5kip capacity) powered by an

MTS 685 Hydraulic Grip Supply. Stainless steel wire mesh was used as tabs in the gripped

region.

The grips were aligned using an MTS 609 Alignment Fixture, a 16 Gauge Flat Alignment

Specimen, and MTS Easy Alignment software (Version 2.01.001). Strain was measured using an

MTS High Temperature Extensometer (632-53E-14) with a Rockland Series 2000 Filter acting as

a low pass filter. A NESLAB HX-75 Recirculating Chiller cooled the extensometer and the grips

throughout the tests. The mechanical test set up was augmented by a custom made environmental apparatus.

Validation Experiments

Control of the heating chamber environment was important for the success of the experiments performed in this research. There were four control issues concerning the heating chamber environment. First, the heating chamber thermocouple must read accurately within the induction field generated by the induction heater. Second, the desired temperatures of 550°C and 750°C must be consistently reached and as quickly as possible to avoid specimen soaking, and then maintained throughout the entire test lasting between 3 minutes and 100 hours. Third, the temperature gradient along the specimen length must be known in order to show that the failures occurred in the hot zone, and that the hot zone was located along the gauge length of the dog bone specimen, and that the specimen gauge length and the environment were at the same temperature during the tests. Lastly, the moisture content level must be controlled, measured, and maintained throughout the experiments. The moisture content level was created by controlling the distilled water and filtered air flow rates and measuring their temperatures before entering the steam generator.

To test the accuracy of the thermocouple within the magnetic field of the induction heater, a FLIR System AB ThermaCAM PM695 optical/infrared camera was used to measure the temperature at the tip of the K-type thermocouple inside the heating chamber while the thermocouple temperature was recorded using the MTS TestStar II controller. These temperature readings were then compared. Initially, the temperature reading of the thermocouple increased by approximately 10-15°C when the induction heater was turned on and running at maximum power to heat the chamber from room temperature to the desired temperature. Since the optical/infrared camera did not record a corresponding temperature rise, this initial temperature jump must be attributed to an induced signal on the thermocouple from the induction heater, as opposed to an actual temperature increase.

When the heating chamber reached the test temperatures used in this study, 550°C and 750°C, the thermocouple recorded within +/-2°C of the optical/infrared camera. This is attributed

to the fact that once the induction heater heated the chamber to the desired temperature, it required less power, approximately 10%, to maintain the desired temperature inside the susceptor. Less power from the induction heater caused smaller eddy currents, which in turn induced a smaller signal on the thermocouple. Therefore, at the test temperatures used in this research, the thermocouple readings were within the accuracy required by these experiments.

To verify that the induction heater could achieve and maintain the desired temperature in the heating chamber a temperature stability specimen, Figure 22, was designed. It consisted of a Syl-iBN/BN/SiC testing specimen that had four K-type thermocouples attached using high temperature ceramic cement. The locations of the thermocouples were chosen to provide data to validate the temperature in the test set-up developed for this study.
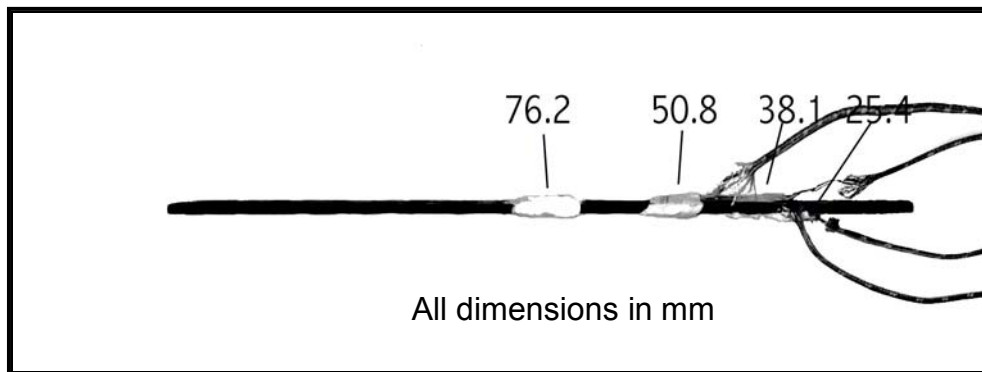
Figure 22: Temperature Stability Specimen

The temperature stability specimen was placed in the chamber at room temperature. It was heated in the different environments investigated in this research. The heating chamber temperature and the temperature stability specimen temperatures were recorded and compared. Figure 23 and Figure 24 are temperature versus time plots for the thermocouple located at the center of the temperature specimen, the 76.2 mm thermocouple in Figure 22. The data were recorded after the induction heater was turned on and set for the target of $550^{o}C$ and $750^{o}C$, respectively. The other three thermocouples displayed similar time responses.
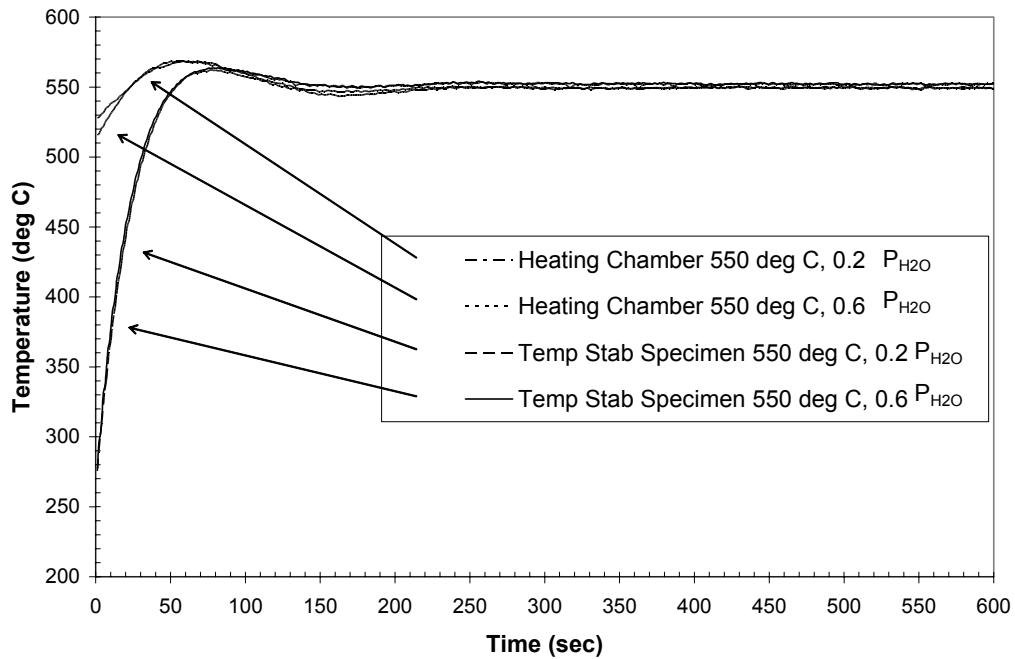
Figure 23: Temperature Stability Plots for 550°C
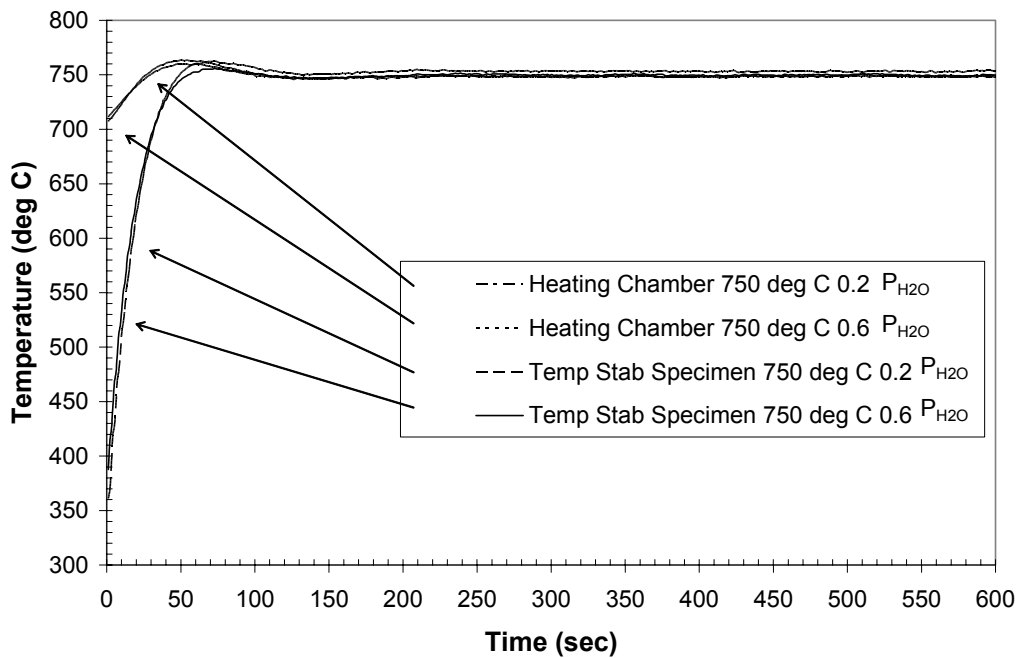
Figure 24: Temperature Stability Plots for 750°C

Initially, before the induction heater was turned on, the temperature of the heating chamber was considerably higher than that of the specimen. This was because the constantly supplied preheated moist air was in thermal equilibrium with both the insulated SiC susceptor and

50

the specimen that had the gripped regions cooled by a recirculating chiller. The recirculating

chiller removed heat from the specimen while the insulation around the susceptor caused the

susceptor to retain heat. However, after the induction heater was turned on, the heating chamber

temperature rose sharply. Since the induction heater heated the SiC susceptor very quickly, the

heat transfer by convection from the preheated moist air to the susceptor was quickly eliminated

causing the moist air to retain heat. This increased the heat transfer by convection from the moist

air to the specimen. The specimen temperature reaction was much slower because of the cooled

grip regions of the specimen.

There was a small initial overshoot in temperatures of both specimen and chamber. It

took approximately 3 minutes for the temperatures to reach steady-state. Although the specimen

temperature response was initially delayed, it reached state-state at approximately the same time

as the heating chamber. At this point the specimen and the heating chamber were in equilibrium.

Mechanical tests were initiated as soon as the heating chamber and specimen reached

equilibrium to minimize exposure to the environment.

The steady-state temperatures of the Temperature Specimen (Figure 22) were plotted as

a function of specimen length and symmetric about the center to generate temperature profiles

for all the 550°C and 750°C environments. The temperature profiles obtained ensured that the

hot section was within the specimen gauge length and were used to verify the failures occurred

within this hot gauge length. It also verified that the chamber design would not cause the portion

of the specimen nearest to the susceptor to be heated to a higher temperature than the gauge

length. Lastly, the temperature profile showed the specimen was not being inductively heated to

a higher temperature than the heating chamber environment.

Figure 25 is a plot of the temperature profiles for all the environments used in this study.

The plots show three important things concerning the specimen temperature. First, the specimen

did not experience higher temperatures in the portion of the specimen close to the SiC susceptor,

as shown by the thermocouple reading at 38.1 mm, the specimen location closest to the SiC

susceptor. Second, the hot zone was determined from the plots to be 19.25 mm across the

center of the specimen. After the experiments the failure location were measured and all failures

occurred within this gauge length. Third, the specimen temperature in the center of the gauge

length was the same as the heating chamber temperature. Hence, it was determined the Syl-

iBN/BN/SiC specimen was not being inductively heated to a higher temperature than the heating

chamber temperature.
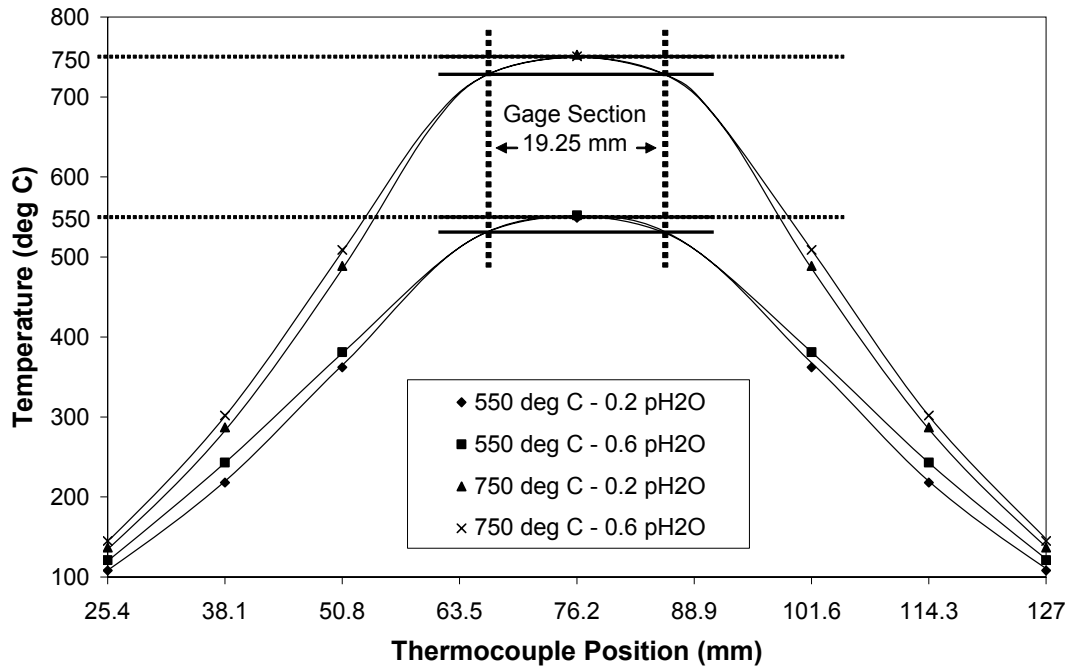
Figure 25: Temperature Profile Plots

To calculate the moisture content, the airflow rate, the air temperature, and the water flow

rate were needed. An Omega Engineering, Inc. Mass Flowmeter attached to the laboratory air

lines measured the airflow. The temperature of this air was recorded throughout the entire test.

After every test the water consumption was measured and divided by the test duration to verify

the water pump output.

Fluctuations in these measurements caused slight variations in the moisture content level

throughout the tests. Table 1 is a list of the data used in calculating the moisture content level for

all specimens tested in this research and the resulting moisture content level. The columns have

the water and airflow rates, as well as, the ambient air flow temperature, the test temperature,

and the moisture content level (as partial pressure). The flow rate was measured by weighing the

52

water before and after the test and dividing by the amount of time the pump was running. The

other data reported in the table are averages and standard deviations for measurements taken

every 20 seconds during the tests. The data show the environmental apparatus built in this

research was able to achieve and maintain the desired moisture content level.

Table 1: Test Data for Calculating Moisture Content Level

Specimen Number 1151-01-	Water Flow Rate (ml/min)	Ambient Air Flow Rate (l/min)	Ambient Air Temperature (^{o}C)	Heating Chamber Temperature (^{o}C)	Moisture Content Level (atm)
003-02-MT	1.060	5.367±0.011	28.6±0.3	553.3±0.6	0.21±0.0003
006-10-SR	1.088	5.351±0.017	26.8±0.4	550.8±1.0	0.22±0.0006
006-09-SR	1.016	5.324±0.019	28.5±0.9	550.2±0.6	0.21±0.0007
006-08-SR	1.015	5.316±0.018	28.9±0.8	550.2±0.6	0.21±0.0008
006-06-SR	1.012	5.317±0.024	28.4±0.8	550.2±0.6	0.21±0.0008
001-13-MT	4.016	3.510±0.006	25.8±0.3	552.8±0.6	0.61±0.0005
001-06-SR	3.973	3.522±0.020	28.6±0.5	550.2±0.8	0.61±0.0014
001-08-SR	3.992	3.485±0.030	29.7±0.7	550.3±0.7	0.61±0.0018
001-07-SR	3.967	3.520±0.027	29.5±0.6	550.1±0.6	0.61±0.0020
001-09-SR	3.987	3.512±0.037	30.0±0.7	550.1±0.6	0.61±0.0028
001-10-SR	4.080	3.522±0.035	25.2±2.5	550.3±0.6	0.61±0.0039
001-12-MT	1.027	5.333±0.009	27.3±0.4	747.2±0.8	0.21±0.0003
006-12-SR	1.003	5.316±0.011	28.9±0.4	750.3±0.6	0.21±0.0004
006-14-SR	0.979	5.327±0.022	25.1±0.5	750.4±0.6	0.20±0.0006
006-15-SR	0.971	5.284±0.074	24.2±0.7	747.8±11.9	0.20±0.0023
002-02-SR	0.975	5.299±0.092	21.9±2.6	749.8±2.3	0.20±0.0023
001-14-MT	4.010	3.520±0.006	25.3±0.2	747.5±0.8	0.61±0.0004
001-02-SR	4.001	3.498±0.007	28.5±0.4	749.3±0.6	0.61±0.0005
001-03-SR	4.057	3.505±0.009	27.5±0.3	749.0±1.0	0.61±0.0007
001-05-SR	3.969	3.514±0.012	29.0±0.5	750.1±0.5	0.61±0.0007
001-04-SR	3.937	3.467±0.052	27.2±0.9	750.3±0.5	0.61±0.0036

Specimen

There were three types of specimens used in this research: a test specimen, a fracture

surface specimen, and a crack density specimen. The failed test specimen created the fracture

surface specimen (i.e. it provided the fracture surface for examination) and the crack density

specimen (i.e. it provided the portion to be cut and polished to view the density of cracks). The

fracture surface specimen was analyzed to determine the phenomenological failure mechanisms

of CMC embrittlement. The crack density specimen was analyzed to determine the number of through-the-thickness cracks as a function of applied stress.

NASA Glenn Research Center provided the Syl-iBN fiber preforms to Honeywell Advanced Composites, Inc. to manufacture six composite panels containing 15 specimens each. These preforms were treated and processed in several steps. First the in-situ BN preforms had the BN interphase layer applied by CVI resulting in a 10.64 +/- 0.34% weight gain. Then a thin layer of SiC was applied by CVI to the BN coated woven preform resulting in a 53.40 +/-5.99% weight gain. SiC particle slurry was then infiltrated into the porous network resulting in a 30.10 +/-1.50% weight gain. This was followed by melt infiltration of molten Si that nearly filled the porous network resulting in a 13.92 +/- 0.80% weight gain. Therefore the matrix was predominantly SiC with some Si. Table 2 has several properties of the constituents for the Syl-iBN/BN/SiC CMC material. The material consisted of 8 plies of woven Syl-iBN tows each containing 800 fibers.

Table 2: Composite Constituent Properties

Constituent	Material	Volume Fraction (%)	Weight Gain (%)	Elastic Modulus (GPa)	Remarks
Fiber	Syl-iBN	37.10	N/A	380	5 Harness Satin 20 ends/inch
Interphase	BN	6.62	10.64	Unknown	~ 0.45 μm
Matrix	CVI SiC	19.33	53.40	425	~ 4 μm
	MI SiC	36.95	30.10	345	Process Temp ~ 1400°C
	Si		13.92		
	Porosity		0.00		

The test specimens were machined into a dog-bone shape to ensure the specimen failed in the hot zone. Figure 26 is a schematic drawing and a picture of the Syl-iBN/BN/SiC specimen. The specimen cross-section was 2.077 +/-0.029 mm thick and 10.176 +/- 0.032 mm wide. The specimens were approximately 152.4 mm long.
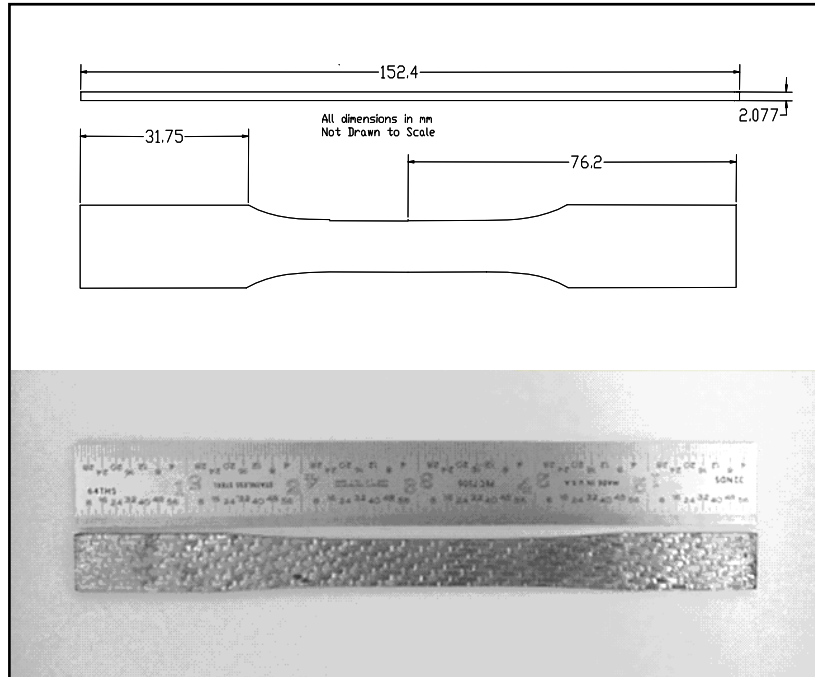
Figure 26: Specimen Dimensions

Figure 27 is an image of a failed specimen. The bottom portion of the failed Syl-iBN/BN/SiC specimen was used to get fracture surface data since it was removed from the heating chamber immediately following failure. This ensured the surface was not exposed to the hot humid environment after the failure. The fracture surfaces specimens, shown in Figure 28, were cut using either a Buehler Isomet 1000 or Buehler Isomet 2000 saw with Buehler Isocut Cutting Fluid approximately 12.5 mm away from the fracture surface and then mounted on silver SEM posts using various types of silver paste and paint.
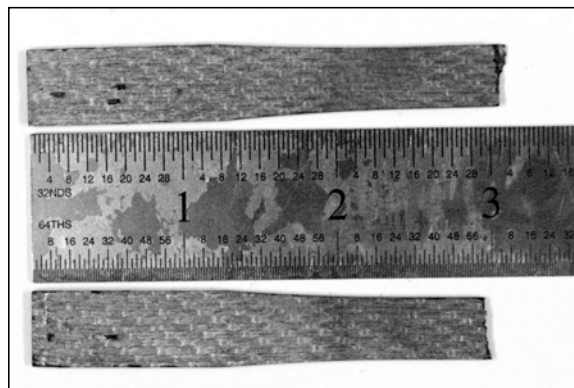
Figure 27: Failed Specimen

Figure 28: Fracture Surface Specimen

The top portion of the failed specimen had to stay in the heating chamber until the apparatus completely cooled. Although the water pump and induction heater were turned off at failure, the temperature of the heating chamber did not cool for several hours. Since the specimen was cut and an interior surface polished, any effects of the added exposure would not be seen. This interior surface provides information on the number of through-the-thickness cracks, which is important to modeling CMC failure.

The upper pieces of the failed Syl-iBN BN/SiC specimens were also cut using either a Buehler Isomet 1000 or Buehler Isomet 2000 saw with Buehler Isocut Cutting Fluid approximately 12.5 mm from the fracture surface. These pieces were mounted in Buehler Konductomet Conductive Filled Phenolic Mounting Compound using the Buehler Simplimet 2000 and then polished using Buehler Metadi Diamond Suspension water based solution (9, 6, 3, 1, 0.25 micron) and various Buehler polishing pads on either the Buehler Phoenix 4000 or the Buehler Vibromet 2, as shown in Figure 29.

Figure 29: Crack Density/Spacing Specimen

Crack density measurements were attempted in this research to see if the crack density was dependent on temperature and moisture content level. The measurements were made using both bright field and dark field lenses to accentuate the cracks. Interior and exterior plies were scanned, and cracks, which extended through the entire ply, were counted. The cracks per ply were averaged and divided by the specimen length to determine an overall specimen crack density measurement. Figure 30 has two examples of through-the-ply cracks seen in this research.
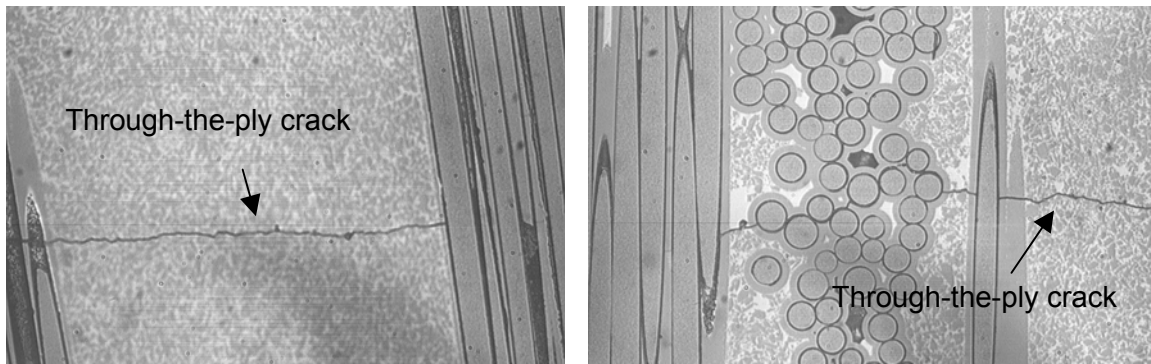
Figure 30: Through-The-Ply Cracks

Procedures

The same pre-test procedures were followed for the monotonic and the stress rupture tests. The first step was to set up and start the environment controllers. The water containers were filled with distilled water and weighed. The water pump and air regulator were calibrated for the desired flow rates. All temperature controllers were set to the desired temperature and the heating tapes were turned on.

The second step was to calibrate and align the extensometer. It was calibrated using an MTS Systems Corp. Calibrator (650.03) such that the extensometer read 2.5578 volts per 1.0% strain. The specimen was then vertically set into the grips. The extensometer was placed on the specimen and aligned perpendicular to the specimen. It was then moved away from the specimen and the upper grip released. The specimen was lowered and the heating chamber placed between the grips of the test machine directly above the specimen.

The third step consisted of putting the specimen into the heating chamber and setting up the extensometer. Once the steam generator was at the desired test temperature, the MTS

controller was used to raise the specimen into the chamber to its final position, where the upper grip was closed and the MTS system was set in the Load Controlled Mode with zero Newton load. This allowed for thermal expansion during the initial heating of the heating chamber. The extensometer was then placed on the specimen in the heating chamber and set to -0.4 volts.

The fourth step was reaching the desired environment in the heating chamber. First, the Ameritherm induction heater was turned on. As the temperature rose, the thermal expansion of the specimen brought the extensometer reading close to zero. The water was turned on when the heating chamber temperature reached 400°C. At the test temperature the extensometer was zeroed and the mechanical test started.

Post-test procedures were also the same for monotonic and stress rupture tests. The first step was to weigh the remaining water. This would give the volume of water used during the test, which in turn would give the number of moles of water used. The rate was calculated using the test duration. The second step was to remove the specimen. If the specimen failed, the MTS controller automatically removed the bottom portion from the heating chamber. If the specimen did not fail, it was carefully un-gripped and removed from the heating chamber. The last step consisted of downloading and saving the test data: load, extensometer voltage, the air flow rate and temperature, and the heating chamber temperature.

Field Emission Scanning Electron Microscopy (FESEM)

Each monotonic and stress rupture test generated a fracture surface specimen. FESEM of this specimen's surface provided qualitative data on the effects the various test environments had on the failure and damage mechanisms. Analysis of this microscopy showed physical changes in the constituents of the composite, if any. Conclusions drawn from the analysis aided in the development of the model. The microscopy was performed on a Leica Cambridge Stereoscan 360FE SEM using secondary electron imagery. The FESEM was set at 15 kV and 100 pA. The specimens were imaged at a 15-degree tilt to accentuate the fibers and surface topography

IV. Experimental Results

In this chapter, the experimental results of this research are presented. The results are from the following experiments: monotonic tests done at room temperature, monotonic tests done in different moisture and temperature environments, stress rupture tests done in different moisture and temperature environments, and crack density measurements on Syl-iBN/BN/SiC CMC material. The analysis of the FESEM images taken on the fracture surfaces of the failed specimen is also presented and an estimation of the total embrittlement times for the different environments is discussed.

Experiments

The stress rupture experiments conducted in this research were similar to experiments conducted by other researchers [10,17,54,]. However, a key distinction was that this research varies the moisture content level. Monotonic tension experiments were conducted at room temperature to establish a baseline for comparison of data collected in the different temperature and moisture conditions. Monotonic and stress rupture tests were conducted at $550^{o}C$ and $750^{o}C$ with moisture content levels of 0.0, 0.2, and 0.6 atm partial pressure of water vapor, pH_2O. The results of these experiments were presented on stress rupture curves, which provided insight into how environmental conditions affect the stress rupture strength and life of the Syl-iBN/BN/SiC CMC material. The experimental data was also used to further develop existing composite failure models.

Monotonic uniaxial tension tests consisted of subjecting specimens to a constantly increasing load over a short period of time until specimen failure. The load was applied in a uniaxial direction parallel to the longitudinal tows and perpendicular to the transverse tows. Stress-strain data was collected throughout the entire test. The room temperature stress-strain data provided baseline information on the consistency of material properties across different panels and ultimate failure stress and strain data. The baseline data was used to normalize test

data and removed any scatter associated with individual panel properties. The stress-strain curves also provided a graphical representation of how material properties change as the environment changes.

The monotonic test procedures consisted of loading the specimen to 10000 N over a three minute time period and recording the stress and strain until failure. A low pass filter set for 10 Hz was used throughout the entire test to remove as much of the noise as possible without inducing a time delay in the data. The individual panels display variations in mechanical properties because the current manufacturing process of SiC/SiC CMCs has many uncontrollable variables, such as fiber spacing. Therefore, one specimen from each of 6 different panels was tested in a room temperature monotonic tensile test to verify that variations were acceptable when compared to previously produced specimens. NASA Glenn Research Center conducted three of the tests while the other three tests were conducted at the Air Force Institute of Technology. Figure 31 is a plot of the six panel stress strain curves. It is clear that individual panels have variations in the material properties. However, five of the six panels have acceptable ultimate strengths and strains compared to the specifications of the manufacturer. The poor ultimate strength and strain properties of Panel 2 led to its rejection for future experiments.
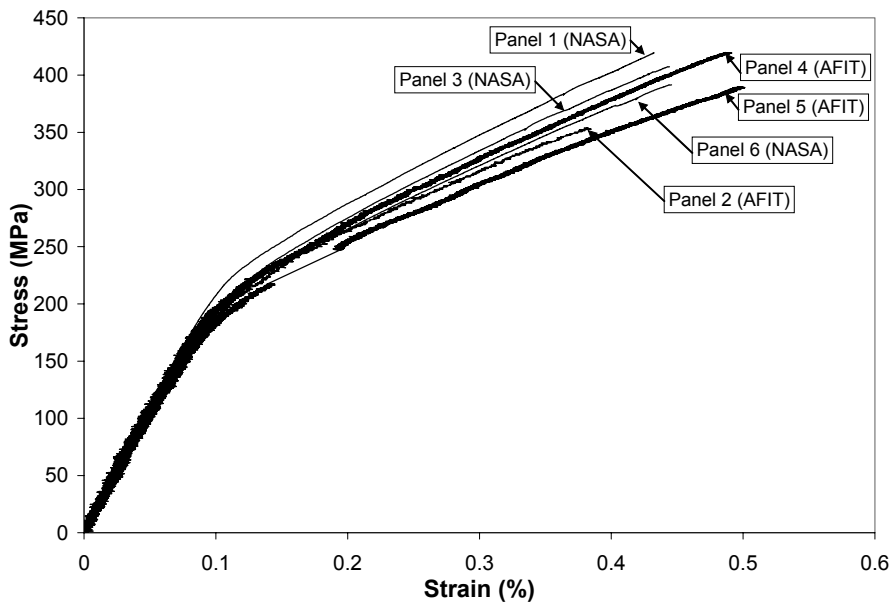
Figure 31: Stress Strain Curves for Six Panels

The modulus of elasticity for the composite, the matrix, and the fibers were calculated using the rule of mixtures and measurements from Figure 31. Table 3 is list of data for each panel, such as, the panel number, the volume fraction (f), the ultimate strength (σ_{ult}) and strain (ε_{ult}), and the modulus of elasticity for each constituent (E_c, E_f, and E_m). The average values, without incorporating Panel 2 data, were used in the model presented in Chapter V.

Table 3: Room Temperature Data – Monotonic Tests

Panel Number	f (%)	σ_{ult} (MPa)	ε_{ult} (%)	E_c (GPa)	E_f (GPa)	E_m (GPa)
1	36.7	419.44	0.432	233	383	199
2	36.4	353.68	0.381	212	381	174
3	38.1	407.27	0.443	216	374	179
4	37.6	419.51	0.486	218	368	183
5	36.9	389.05	0.506	213	372	177
6	36.2	391.48	0.446	220	366	188
Average	37.0	396.74	0.449	219	374	183
Average w/o Panel 2	37.1	405.35	0.463	220	373	185

Six monotonic tests were done under the following environmental conditions: 0.0, 0.2, and 0.6 atm pH$_2$O at both 550°C and 750°C. Figure 32 is a plot of three of the stress strain curves from three environmental monotonic tests done on specimens from Panel 1. Figure 33, Figure 34, and Figure 35 are similar plots for specimens from Panel 3, Panel 4, and Panel 5, respectively. Figure 36 is a plot of the ultimate strength versus failure strain data of all monotonic tests. Table 4 contains the same data.
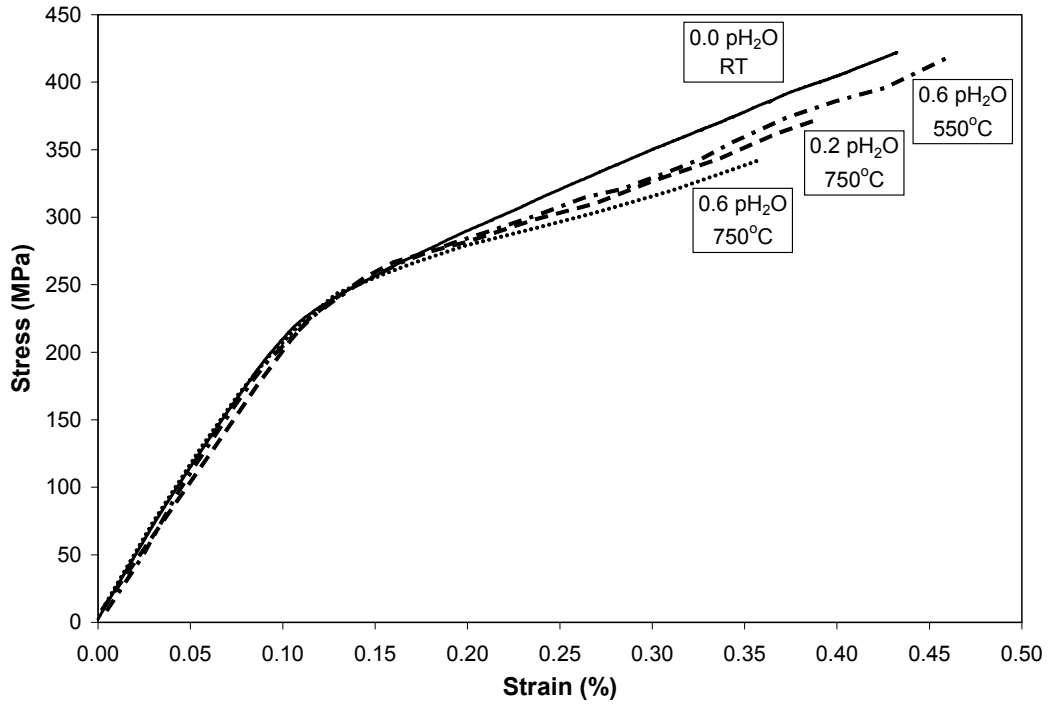
Figure 32: Environment Monotonic Stress Strain Curves – Panel 1
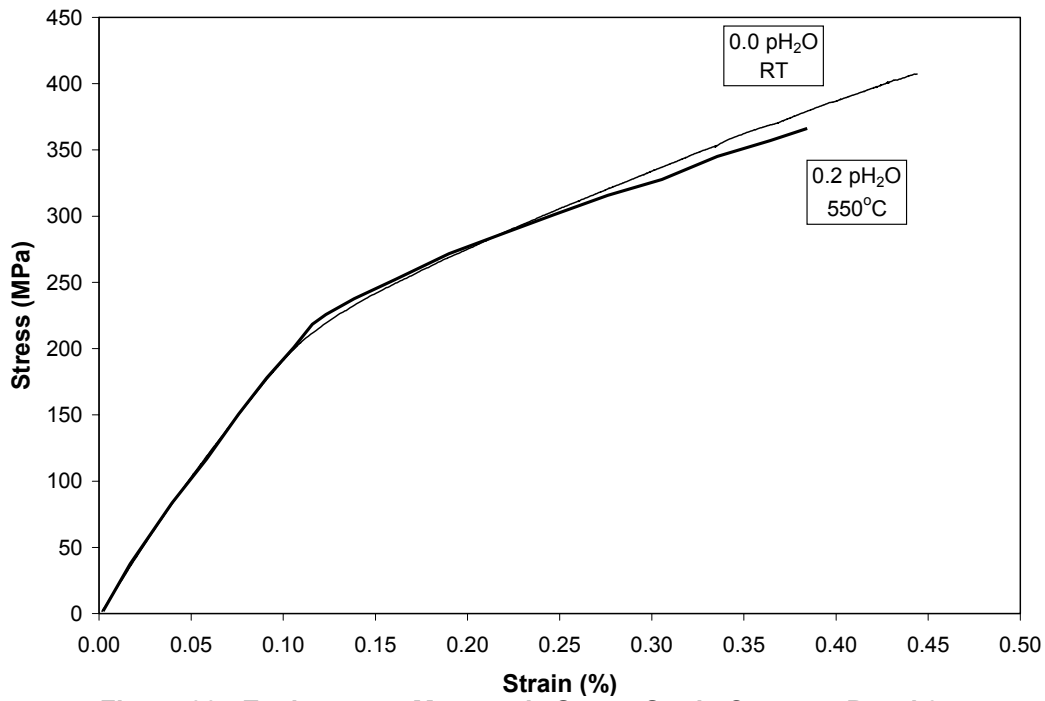
Figure 33: Environment Monotonic Stress Strain Curves – Panel 3
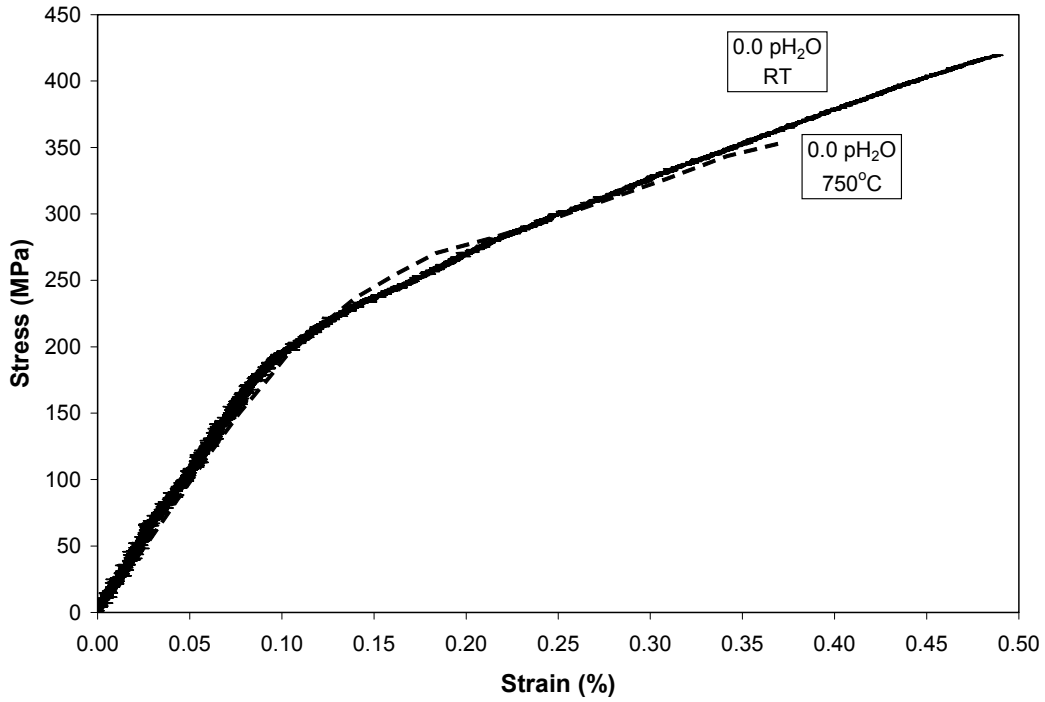
Figure 34: Environment Monotonic Stress Strain Curves – Panel 4
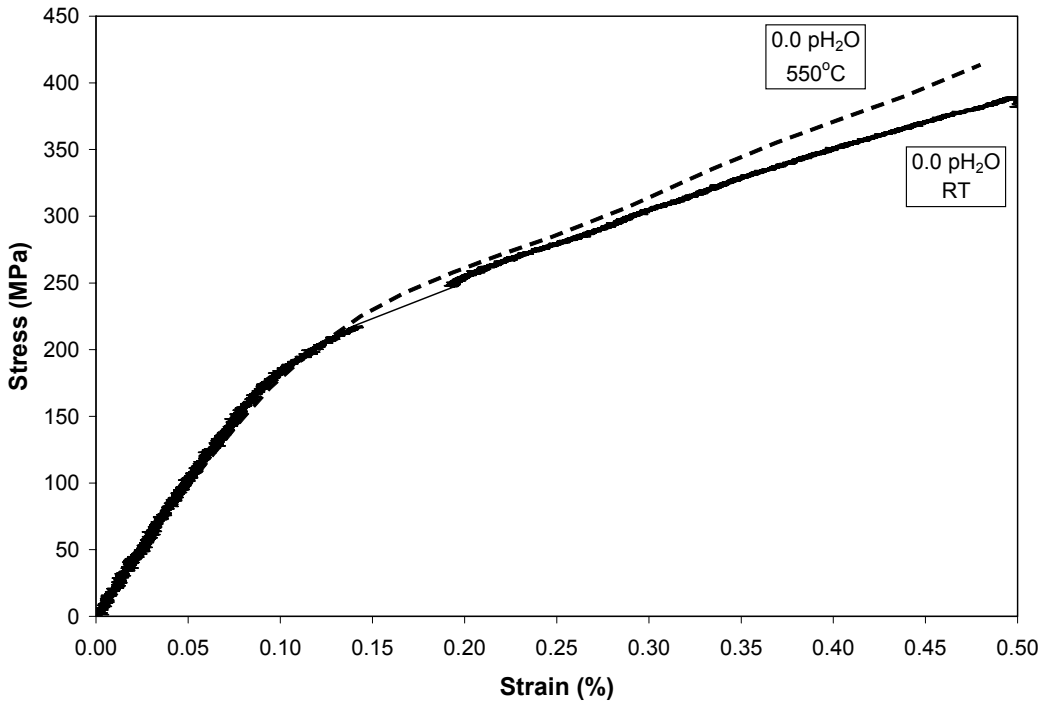
Figure 35: Environment Monotonic Stress Strain Curves – Panel 5
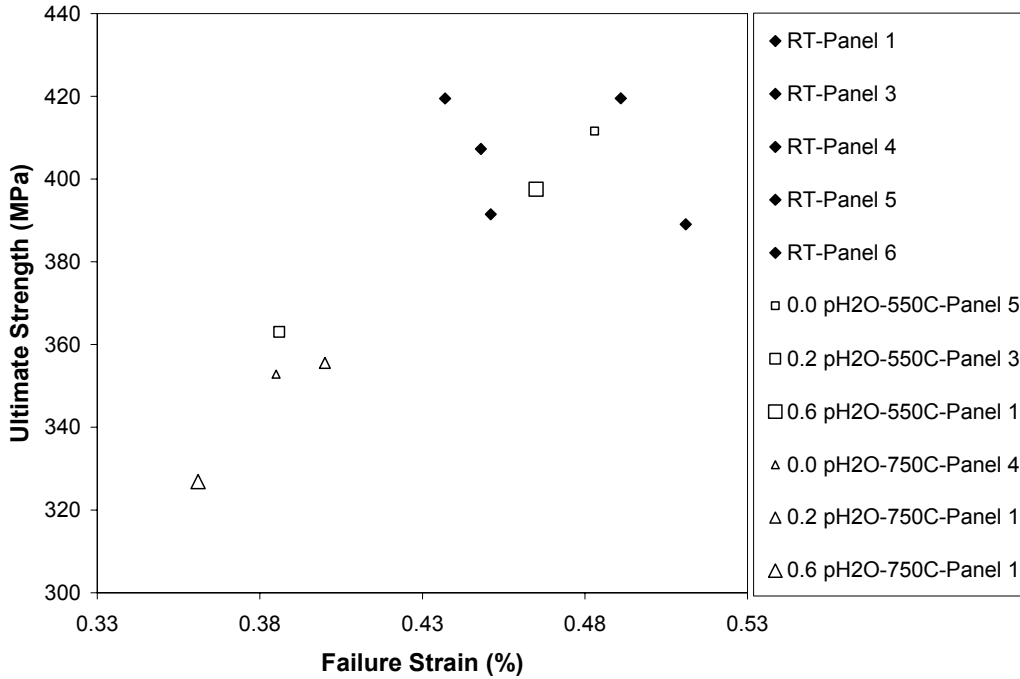
Figure 36: Stress Strain Data – Monotonic Tests – Various Test Conditions

Table 4: Stress Strain Data – Monotonic Tests

Test Conditions	σ_{ult} (MPa)	ε_{ult} (mm/mm)
Room Temperature - Panel 1	419.44	0.432
Room Temperature - Panel 3	407.27	0.443
Room Temperature - Panel 4	419.51	0.486
Room Temperature - Panel 5	389.05	0.506
Room Temperature - Panel 6	391.48	0.446
0.0 atm pH$_2$O - 550°C - Panel 5	411.59	0.478
0.2 atm pH$_2$O - 550°C - Panel 3	363.03	0.381
0.6 atm pH$_2$O - 550°C - Panel 1	397.55	0.460
0.0 atm pH$_2$O - 750°C - Panel 4	352.85	0.380
0.2 atm pH$_2$O - 750°C - Panel 1	355.55	0.395
0.6 atm pH$_2$O - 750°C - Panel 1	326.88	0.356

It is evident from Figure 32 through Figure 36 that temperature has either no effect, or a very small effect, on the monotonic stress strain behavior (i.e. the shape of the stress strain curve) and, therefore, has either no effect or very small effect on the modulii of elasticity for the CMC and constituents. However, temperature does affect the ultimate strength and ultimate strain of the material. At 550°C and 750°C there is approximately a 3.61% and 14.87% reduction in the average ultimate stress and 4.97% and 18.57% reduction in average failure strain,

respectively. Also from the data, the ultimate strength and failure strain reductions show no correlation with the moisture content level.

A stress rupture test consists of loading a specimen very quickly to a known load that results in a desired stress level based on the specimen's dimensions. The load is applied in a uniaxial direction parallel to the longitudinal tows and perpendicular to the transverse tows. The load is held constant until specimen failure or to a predetermined end time, which was 100 hours in this study. Similar to the monotonic test, each stress rupture test provided stress-strain data, a fracture surface specimen, and a crack density specimen. However, the stress rupture tests also provided applied stress versus failure time data. This data shows how the applied stress and the environment affect the life of the material.

The stress rupture test procedures consisted of loading the specimen to 75% of the desired load over a 2 second time span. Then the specimen was loaded to the desired load over another 2 second time span. This minimized the overshoot caused by the feedback control of the MTS controller. The load was maintained for the remainder of the test. During the initial 4 second loading, the low pass filter was set for 15 Hz. After initial loading, it was set for 3 Hz. This was done to remove the time lag in the data associated with using a low-pass filter during the initial ramped load and to remove a significant amount of noise in the latter part of the test.

This research collected data during twenty-nine stress rupture tests. Figure 37 is a plot of the stress rupture curves including the data from the monotonic tests from Table 4. Open and closed symbols denote experiments at 550°C and 750°C, respectively. The square, diamond, and triangle symbols represent the 0.0, 0.2, and 0.6 atm pH$_2$O conditions, respectively. The data points at 100 hours represent experiments where the specimen did not fail and the test was stopped. The data points at 0 hours are the monotonic test results. Figure 38 is a plot comparing the data collected in this research to the "as produced" fiber data collected from Yun and DiCarlo [27,28]. The degradation of strength due to increased temperature is seen clearly in this plot. However, the resolution of the data on this plot is such that it is difficult to see the effects of moisture. This plot shows similar behavior in the intermediate temperature range to the SiC/SiC

CMCs discussed in Chapter II with Nic (Figure 11) and HN fibers (Figure 13). Table 5 has a summary of the stress rupture test data only.
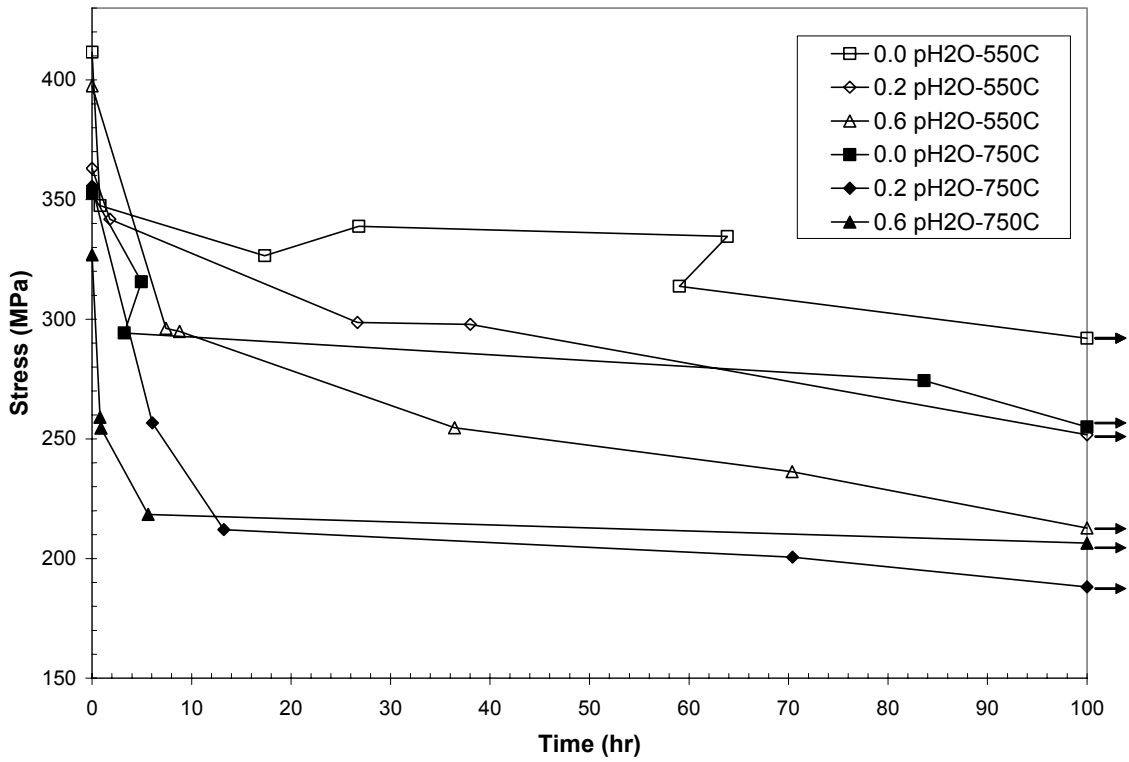
Figure 37: Stress Rupture Curves
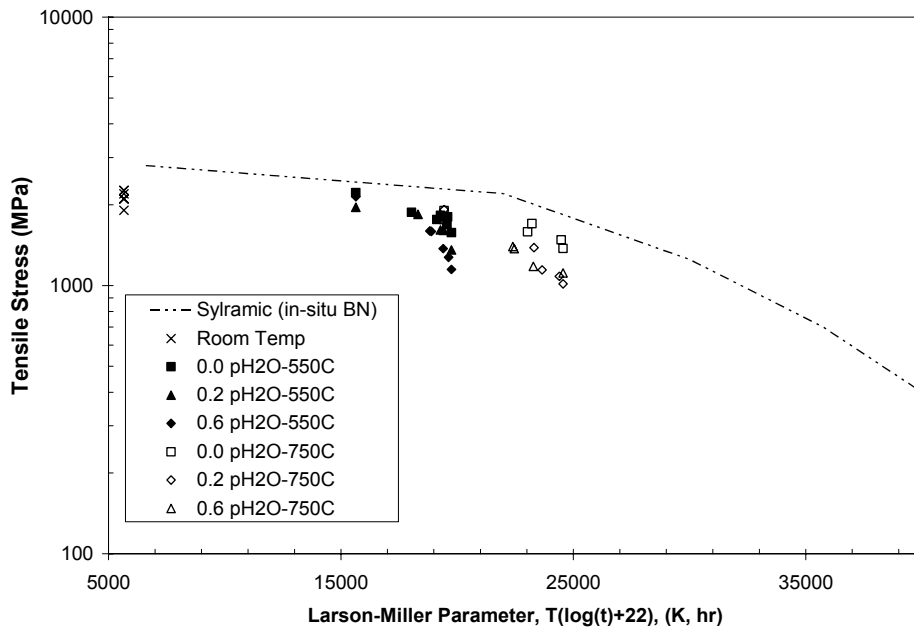
Figure 38: Larson-Miller Plot

Table 5: Stress Rupture Data

Panel	Specimen	Test Condition	Applied Stress (MPa)	Normalized Stress (MPa)	Failure Time (hr)
5	5	0.0 atm pH_2O - 550°C	347.44	0.893	0.81
5	4	0.0 atm pH_2O - 550°C	326.59	0.839	17.36
5	12	0.0 atm pH_2O - 550°C	338.83	0.871	26.82
5	3	0.0 atm pH_2O - 550°C	334.54	0.860	63.85
5	6	0.0 atm pH_2O - 550°C	313.79	0.807	59.03
5	2	0.0 atm pH_2O - 550°C	292.00	0.751	100.00+
6	10	0.2 atm pH_2O - 550°C	341.81	0.873	1.78
6	9	0.2 atm pH_2O - 550°C	298.66	0.763	26.66
6	8	0.2 atm pH_2O - 550°C	297.88	0.761	38.02
6	6	0.2 atm pH_2O - 550°C	251.64	0.643	100.00+
1	6	0.6 atm pH_2O - 550°C	296.16	0.706	7.43
1	8	0.6 atm pH_2O - 550°C	294.87	0.703	8.78
1	7	0.6 atm pH_2O - 550°C	254.65	0.607	36.44
1	9	0.6 atm pH_2O - 550°C	236.28	0.563	70.36
1	10	0.6 atm pH_2O - 550°C	212.76	0.507	100.00+
3	9	0.0 atm pH_2O - 750°C	315.605	0.775	4.97
3	11	0.0 atm pH_2O - 750°C	294.212	0.722	3.23
3	12	0.0 atm pH_2O - 750°C	274.331	0.674	83.63
3	10	0.0 atm pH_2O - 750°C	254.968	0.626	100.00+
6	12	0.2 atm pH_2O - 750°C	256.695	0.656	6.06
6	14	0.2 atm pH_2O - 750°C	212.088	0.542	13.24
6	15	0.2 atm pH_2O - 750°C	200.548	0.512	70.40
2	2	0.2 atm pH_2O - 750°C	188.111	0.532	100.00+
1	2	0.6 atm pH_2O - 750°C	259.035	0.618	0.78
1	3	0.6 atm pH_2O - 750°C	254.493	0.607	0.89
1	5	0.6 atm pH_2O - 750°C	218.424	0.521	5.64
1	4	0.6 atm pH_2O - 750°C	206.423	0.492	100.00+

Due to differences in panel properties, every attempt was made to use specimens from the same panel for the same environmental conditions (e.g. all tests conducted at 550°C with 0.6 atm pH_2O were done using specimens from Panel 1). This allowed the stress rupture curve to be normalized by the individual panel's room temperature ultimate strengths, thus removing scatter caused by variations between panels. The normalized stress is the applied stress divided by the room temperature monotonic tensile ultimate strength for that particular panel. Figure 39 and Figure 40 are the normalized stress rupture curves for the 550°C and the 750°C experiments, respectively. Normalizing by the room temperature ultimate strength shows how the test

temperature affects the CMC life. The lines on these plots have been placed there to show the general trend of the experimental data; they are not curve fits. Some observations from the 550°C cases in Figure 39 are as follows: there is more scatter in the 0.0 atm pH$_2$O data; there is a non-linear shift in the stress rupture curves with respect to moisture content; at times less than 2 hr, little distinction can be made in the data; as time increases, the curves become distinct and separate; and for both 0.2 and 0.6 atm pH$_2$O normalized stress rupture curves appear to converge to approximately to 70% and to 50% of the monotonic tensile strength as time approaches 100 hr. The 750°C curves in Figure 40 display some similarities to the 550°C cases and some unique features. The 0.0 atm pH$_2$O moisture content data has more scatter, similar to the 550°C data. The 0.2 and 0.6 atm pH$_2$O curves converge very quickly, in less than 20 hr, to approximately 50% of the monotonic tensile strength.
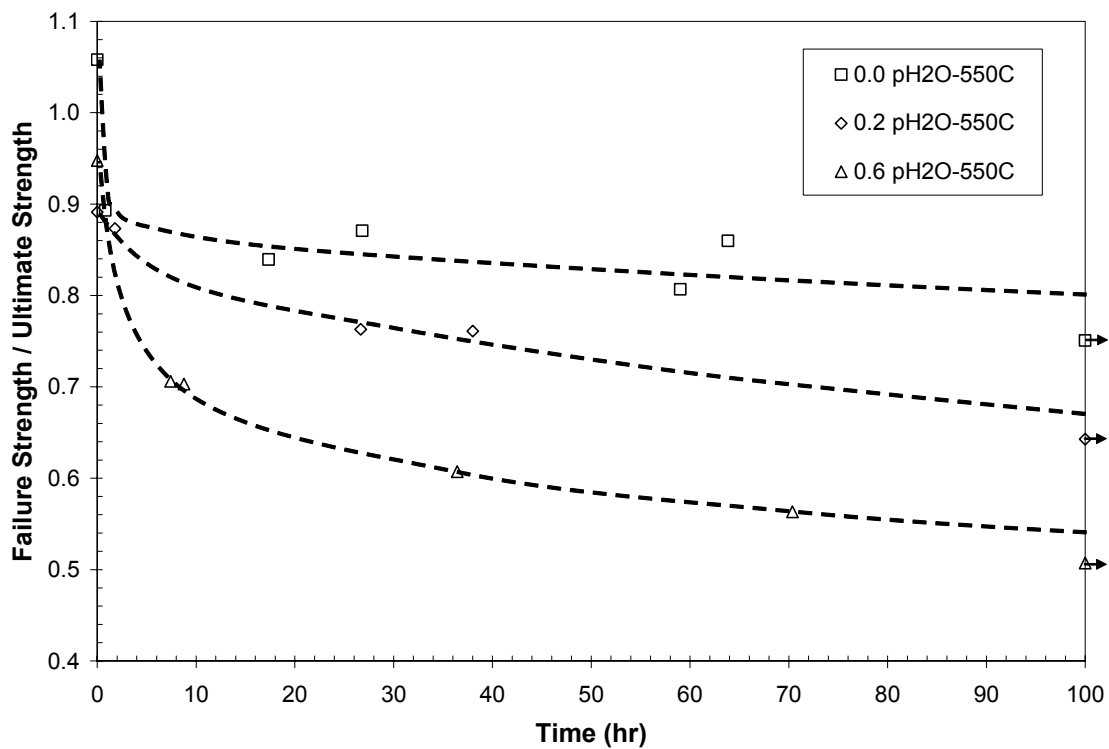
Figure 39: Normalized Stress Rupture Curve for 550°C
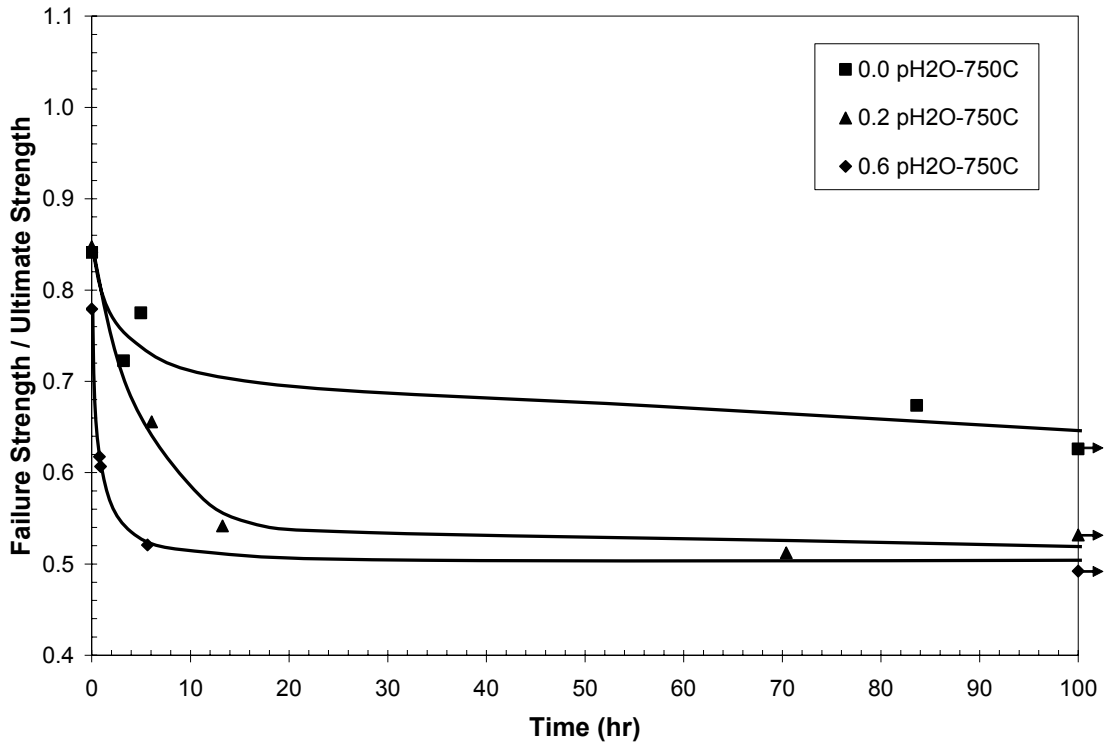
Figure 40: Normalized Stress Rupture Curve for 750°C

The 50% of the monotonic tensile strength equates to approximately 200 MPa. This point on the stress strain curve corresponds to 'the knee' in the response and is the point where through-the-thickness cracks have formed. Therefore, the number of through-the-thickness cracks as a function of applies stress is important. However, the results of the crack density measurements conducted in this research were inconclusive due to the compressive residue stresses in the material closing the cracks once the load was removed. Therefore, the specimens were given to Greg Morscher at NASA Glenn Research Center who used a plasma-etch technique that enhanced matrix cracks so that crack densities could be measured. Morscher validated this technique using Acoustic Emissions on Syl/BN/SiC and HN/BN/SiC specimens [72]. Figure 41 has a plot of the results. Based on these results, approximately 15-65 cracks are expected in the 19.25 mm gauge length of the specimens in this research depending on the applied stress level.
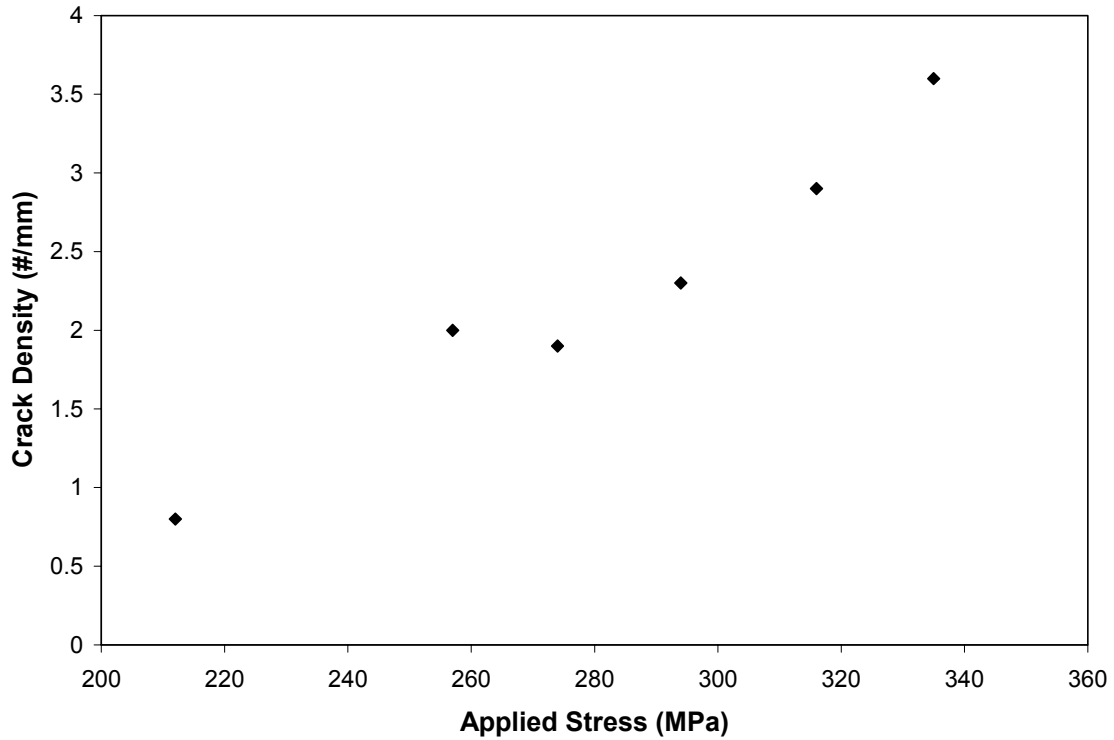
Figure 41: Crack Density Results

Field Emission Scanning Electron Microscopy (FESEM)

FESEM images show the physical characteristic of a fracture surface using very high magnification such that fracture patterns can be seen in the constituent materials of the failed CMC. A comprehensive and systematic approach to imaging specimens was used to compare physical traits of the fracture surface (i.e. the fracture patterns, featureless glass formation, and pesting) that resulted from exposure to different environments. Specimens that failed in a pristine environment (i.e. room temperature and ambient moisture content) were compared to those that failed in environments with intermediate temperature and humid conditions. Analysis of these images gives a better understanding of the effects of moisture and intermediate temperature on failure mechanisms of the CMC material. Furthermore, analysis of the images resulted in an estimation of the total embrittlement time for this material in the different environments by looking at images taken over random locations and comparing them to the images of specimens that

failed at a later time in the same environment. The fracture surface specimens mentioned in Chapter III were used in this FESEM analysis.

Each specimen had 27 FESEM images taken at the following magnifications: 3 at 30X, 6 at 100X, 6 at 1000X, 6 at 3000X, and 6 at 8000X. There are two exceptions. The first exception is specimen 6 from panel 5 tested at 550°C with 0.0 atm pH$_2$O. It has only 17 images at the following magnifications: 1 at 30X, 4 at 100X, 4 at 1000X, 4 at 3000X, and 4 at 8000X. The other exception is specimen number 14 from panel 6 tested at 750°C with 0.2 atm pH$_2$O. It has 26 images at the following magnifications: 3 at 30X, 6 at 100X, 6 at 1000X, 6 at 3000X, and 5 at 8000X. A computer malfunction corrupted the files resulting in poor or missing images.

The levels of magnification were chosen to gain specific information during the analysis. The 30X images give a good overall view of the fracture surface topology and its general appearance. The 100X images show individual tow topography and tow failure characteristics. The 1000X images show the interactions of large groups of fibers within a tow. The 3000X images show interactions between small groups of fibers. The 8000X images show fiber-to-fiber interactions. The micron bars in the lower right corner of the images are 800, 200, 20, 8 and 2 μm for the 30X, 100X, 1000X, 3000X, and the 8000X images, respectively.

Throughout the following analysis several terms will be used. The first set of terms concern the constituents, which are the fiber, the BN interphase, the CVI matrix, and the MI matrix. These regions are shown in Figure 42. The fracture surface of each constituent is unique: the CVI SiC has grain boundaries that radiate out away from the fibers; the MI SiC has grain boundaries that appear to be formed around particles in a random manner; and the fibers have fracture patterns that are relatively flat and smooth in appearance. The next term is fiber pullout and is shown in Figure 43. This is the length of fiber that is pulled out of the matrix material because the fiber failed somewhere in the stress transfer region of the fiber. The last set of terms concerns the pesting phenomenon of embrittlement. Puddles, droplets, and pesting are all results of the embrittlement process but represent different scales of the phenomenon. Puddles represent global or massive BN oxidation resulting in boria. Droplets represent smaller

volumes of boria. Pesting represents the effect embrittlement has on the fibers. These are

shown in Figure 44 and Figure 45.
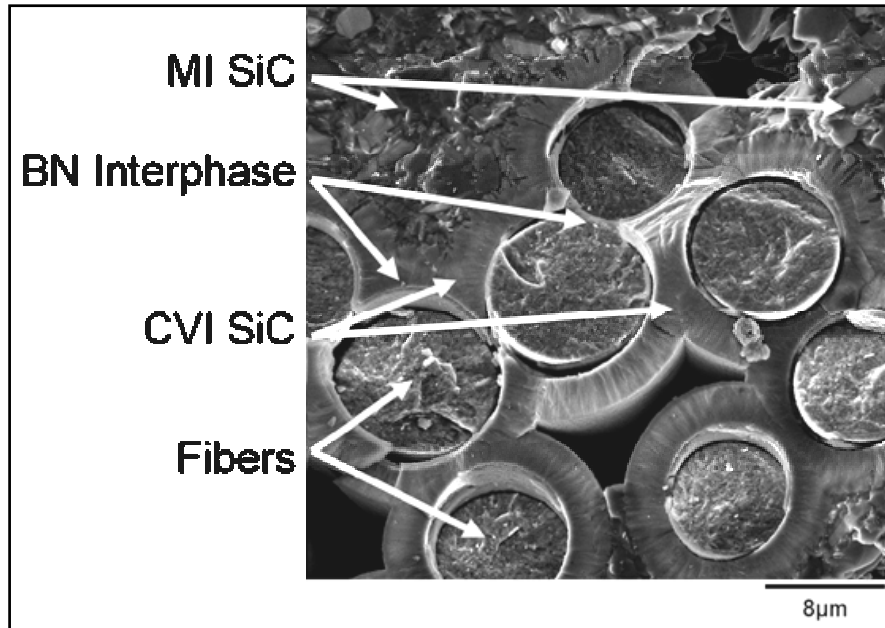
Figure 42: CMC Constituents
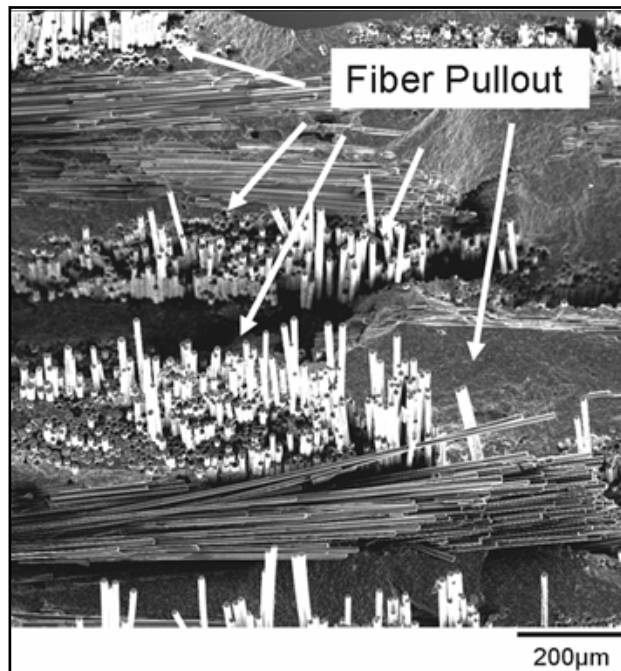
Figure 43: Fiber Pullout
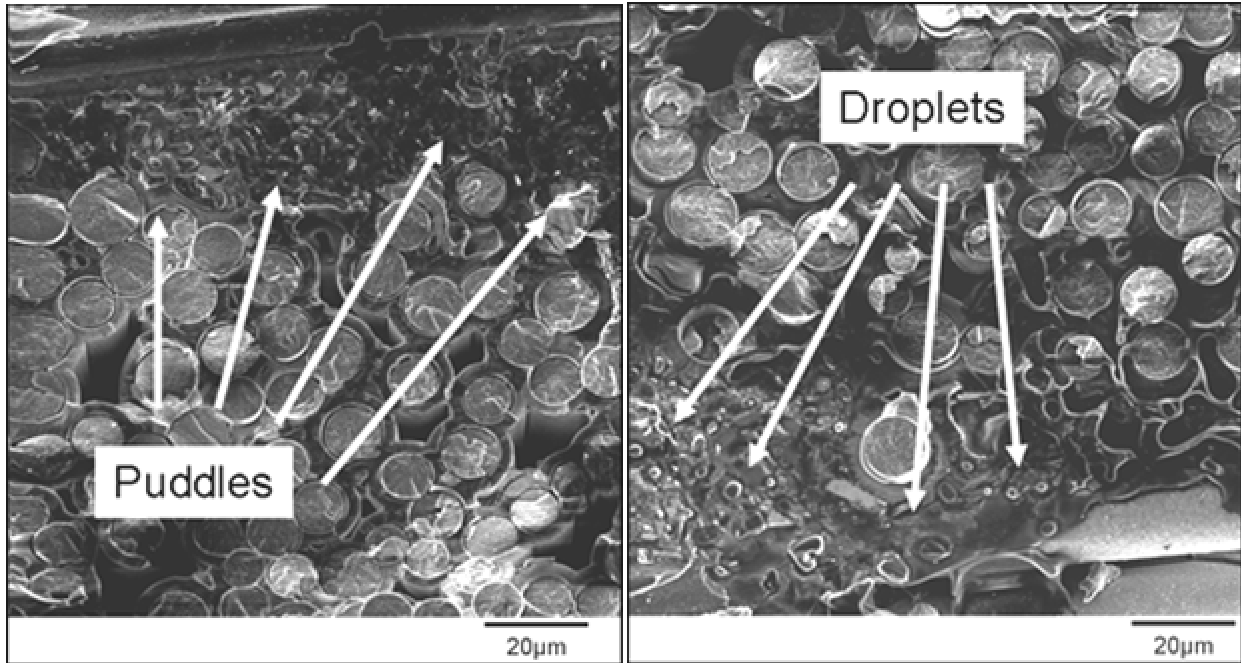
Figure 44: Embrittlement Features – Puddles and Droplets
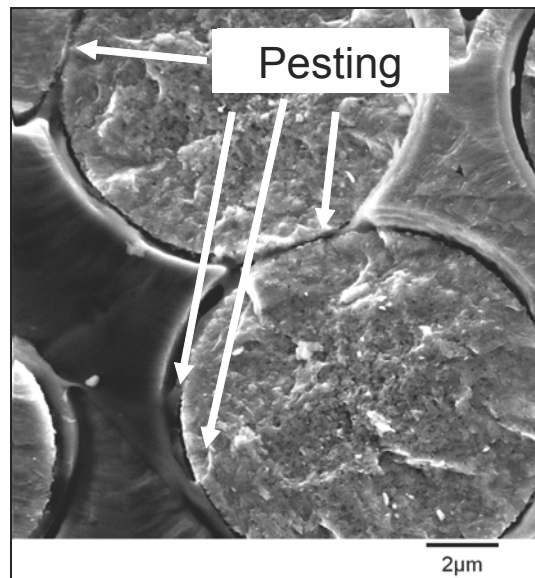
Figure 45: Embrittlement Features - Pesting

Analysis of the FESEM images from the three monotonic room temperature fracture surface specimens tested at AFIT gives a baseline of what the fracture surface should look like for this material after failure in ambient conditions. Although the images in Figure 46 through Figure 50 are only from one specimen, the analysis considered the images from all room temperature monotonic tensile test specimens. The 30X images in Figure 46 show that the entire

fracture surface appears consistently jagged and rough indicating a brittle fracture of the material and that the fracture plane is relatively flat and perpendicular to the loading direction.
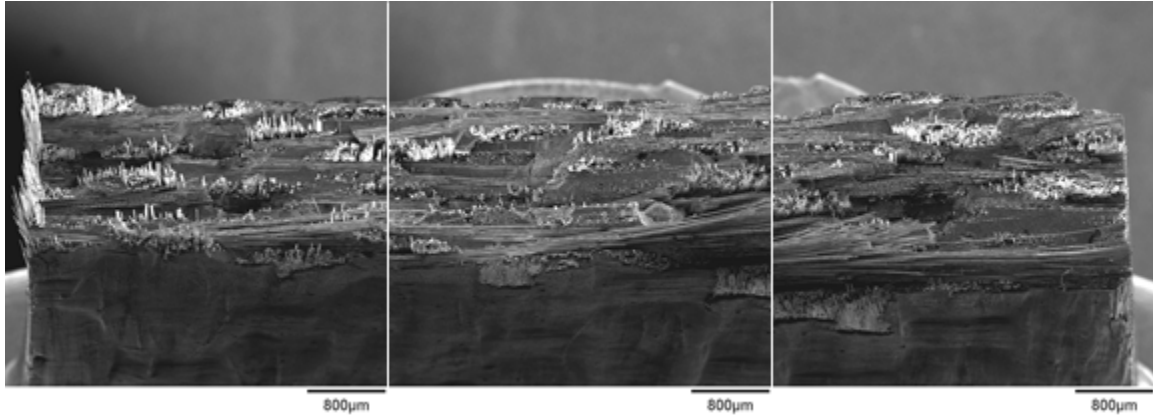
Figure 46: Fracture Surface at 30X - Room Temperature Monotonic

The 100X images in Figure 47 show that every tow has a wide range of fiber pullout lengths and that individual tows show similar fiber pullout characteristics to each other.
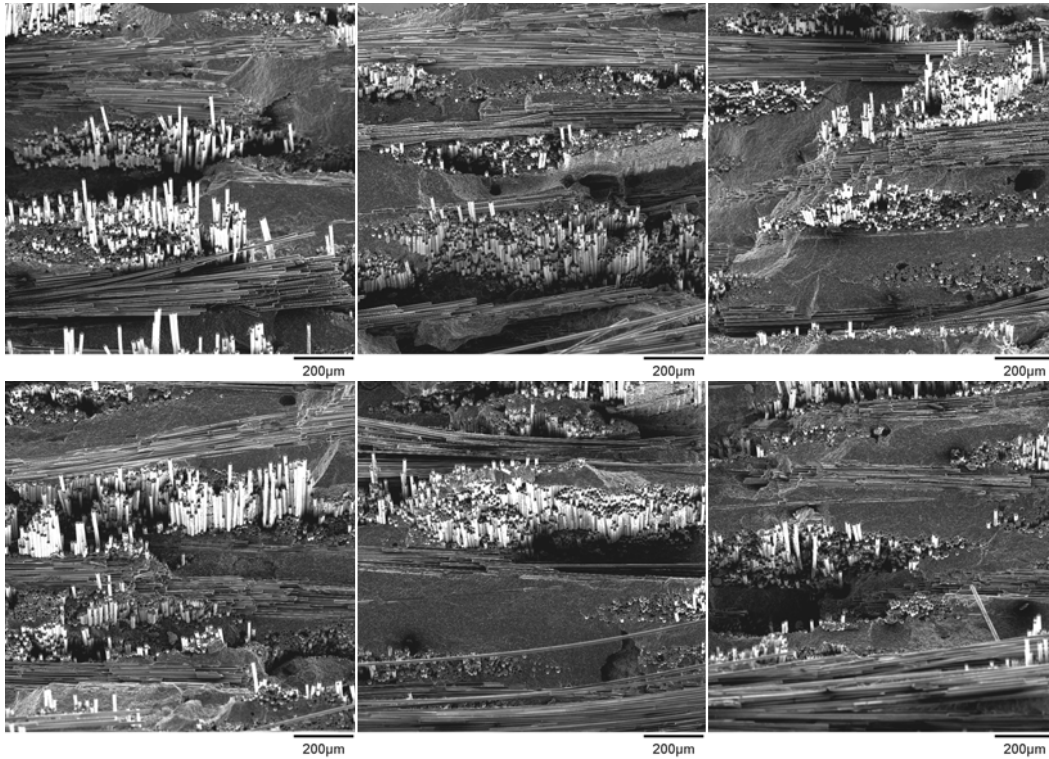
Figure 47: Fracture Surfaces at 100X - Room Temperature Monotonic

The 1000X images in Figure 48 show that the various fiber pullout lengths and depths are more visible and the fracture pattern on the CVI SiC layer is distinguishable from that of the MI SiC matrix. The 3000X images in Figure 49 show that the BN layer is distinguishable from the fiber and the CVI SiC images, that fiber debonding appears to be both interior (i.e. the interphase remains with the matrix) and exterior (i.e. the interphase remains on the fiber), and that failures of neighboring fibers occur at different fiber lengths. The 8000X images in Figure 50 show that most of the BN can be seen between the fiber and matrix, that the BN fracture pattern appears jagged and rough indicating a brittle fracture of the interphase, and that the fibers have individual fracture patterns separate from neighboring fibers and fail at different fracture planes.
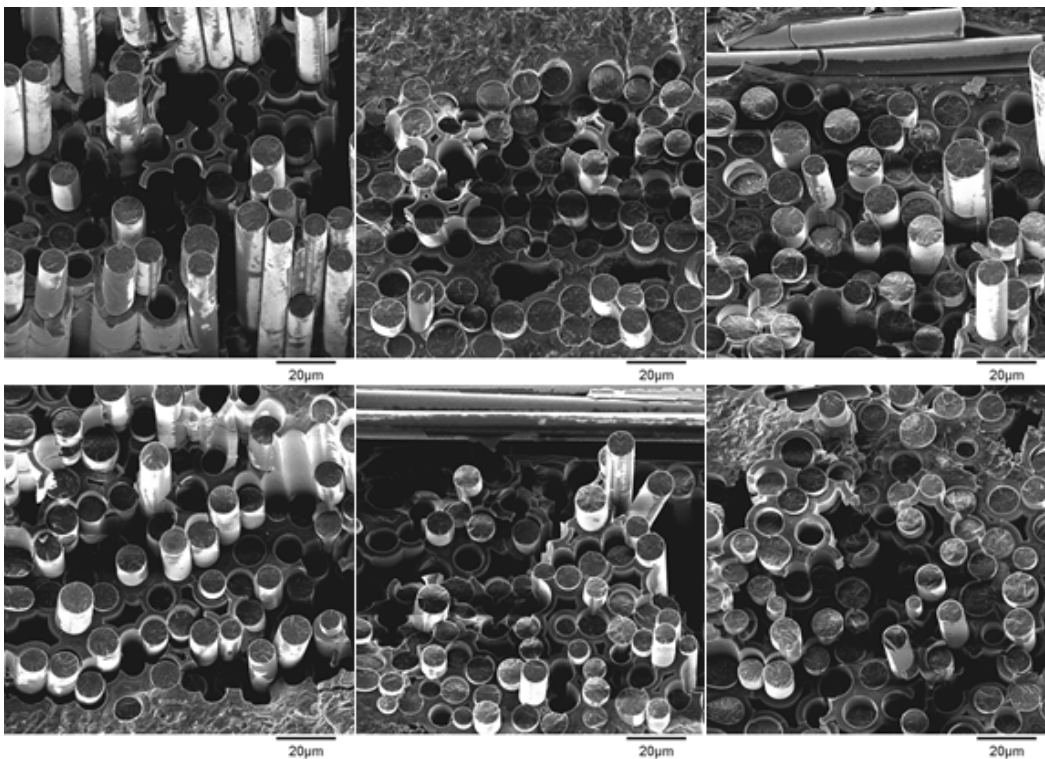
Figure 48: Fracture Surfaces at 1000X - Room Temperature Monotonic
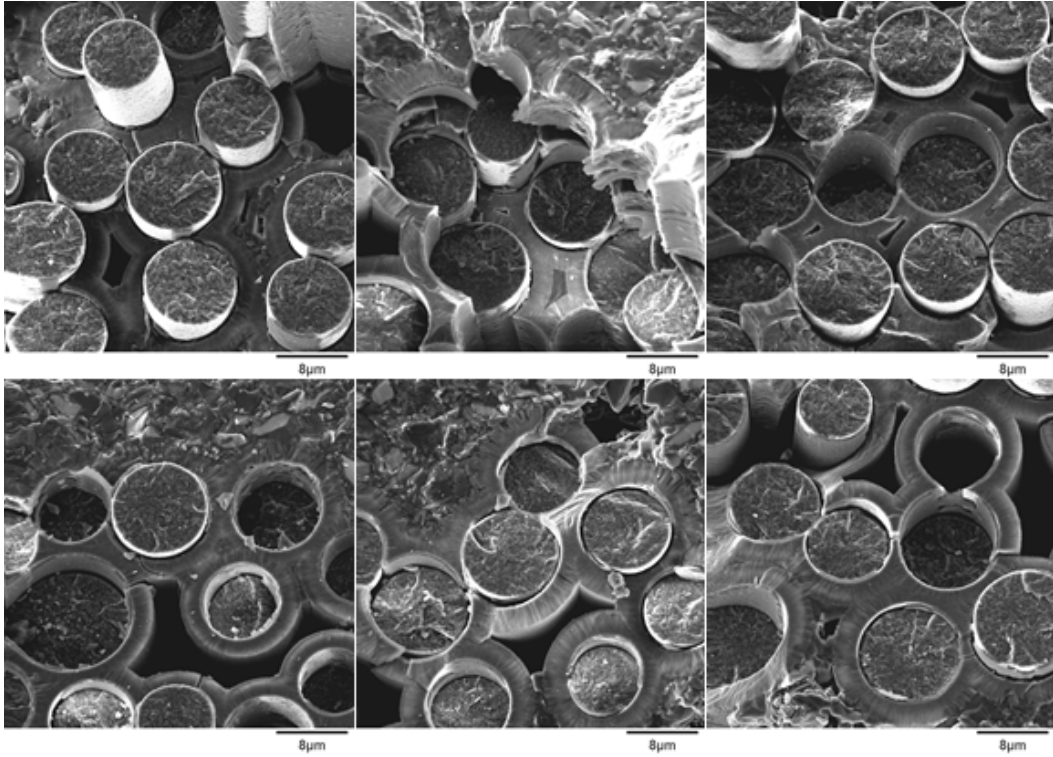
Figure 49: Fracture Surfaces at 3000X - Room Temperature Monotonic
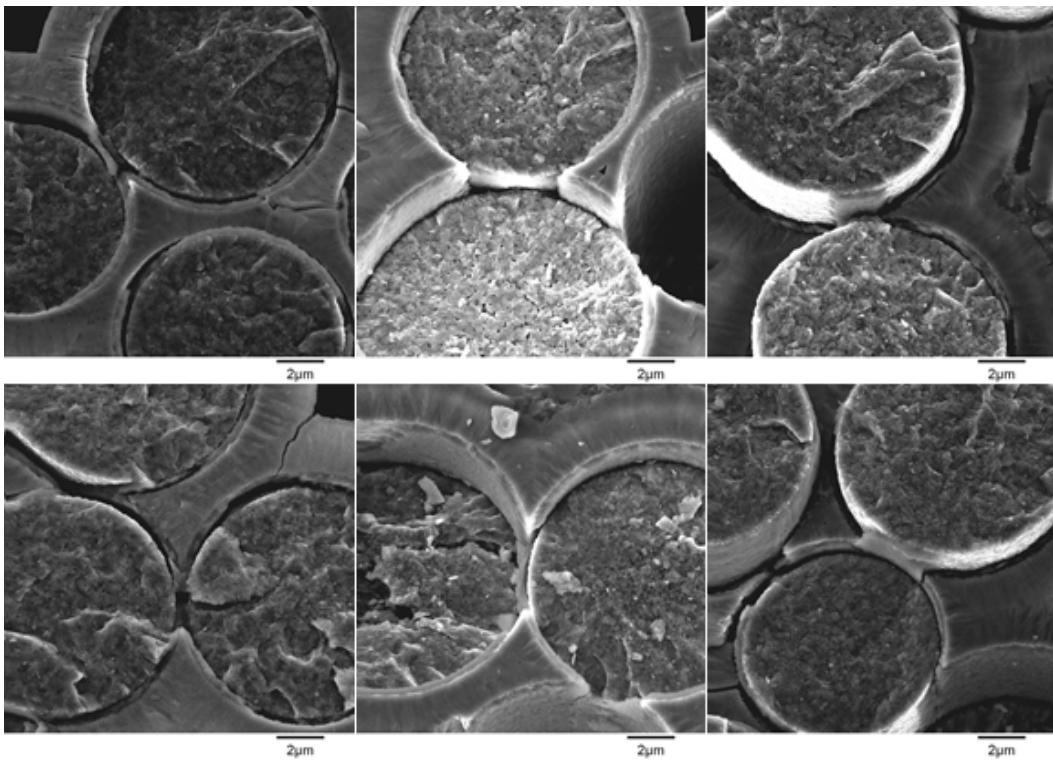
Figure 50: Fracture Surfaces at 8000X - Room Temperature Monotonic

Analysis of the FESEM images from the fracture surface specimens of the monotonic tests conducted in the various environments (Figure 51 through Figure 55) shows the effects of temperature and any effects due to the presence of moisture in the environment. Since these tests are so short, the effects of moisture on the constituents should not be evident. The figures are arranged such that moving from top to bottom shows specimens tested in increasing temperature and moving from left to right show specimens tested in increasing moisture content. The first image with the gray banner and black text, labeled -a-, is the representative image for the room temperature monotonic test conditions. The second row of images with the white banner and black text, labeled -b-, -c-, and -d-, are representative images of the $550^{o}C$ cases with 0.0, 0.2, and 0.6 atm pH_2O, respectively. The third row of images with the black banner and the white text, labeled -e-, -f-, and -g-, are representative images of the $750^{o}C$ cases with 0.0, 0.2, and 0.6 atm pH_2O, respectively.

Comparisons of the 30X images in Figure 51 show that there is a noticeable difference in the fiber pullout lengths. They are shorter in both the $550^{o}C$ and $750^{o}C$ images compared to room temperature image; however, there are no distinguishable differences between the lengths in the $550^{o}C$ and the $750^{o}C$ images. There also appears no effect on the fracture surface topography with respect to moisture content.
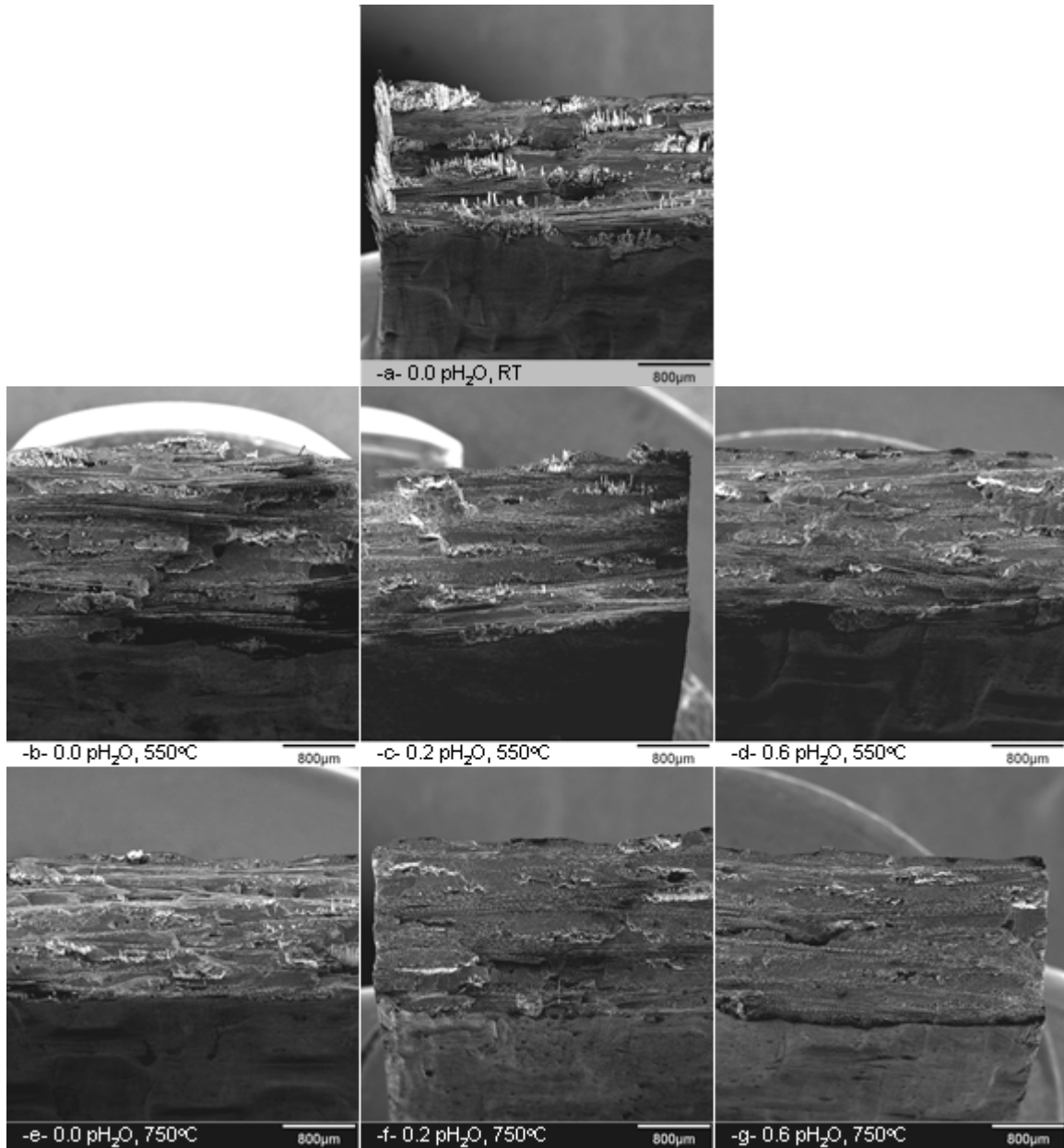
Figure 51: Environmental Monotonic Tests at 30X

Comparisons of the 100X images in Figure 52 again show the 550°C and 750°C images are similar. Every tow has a wide range of fiber pullout lengths; however, the 550°C and 750°C pullout lengths are shorter than the room temperature pullout lengths. Also, individual tows show similar fiber pullout characteristics with respect to moisture content.
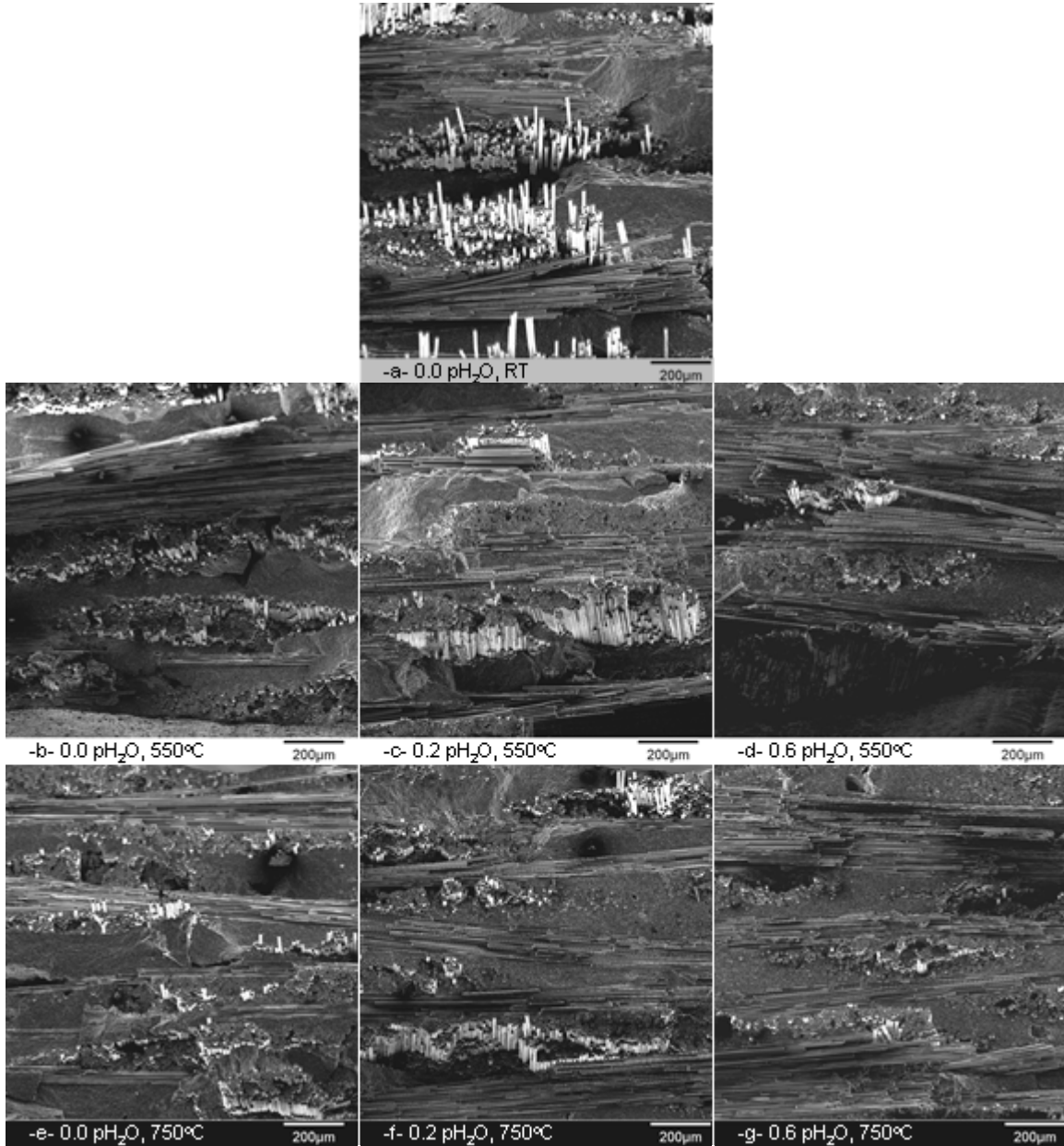
Figure 52: Environmental Monotonic Tests at 100X

Comparisons of the 1000X images in Figure 53 show that the variance in fiber pullout lengths and

depths is less at 550°C and 750°C than that of the room temperature results, that the distinctive

differences between the SiC matrix (CVI and MI portions) is similar to that of the room

temperature results, and that the moisture content had no affect on the 550°C or the 750°C

images (i.e. images -b-, -c-, and -d- are similar).
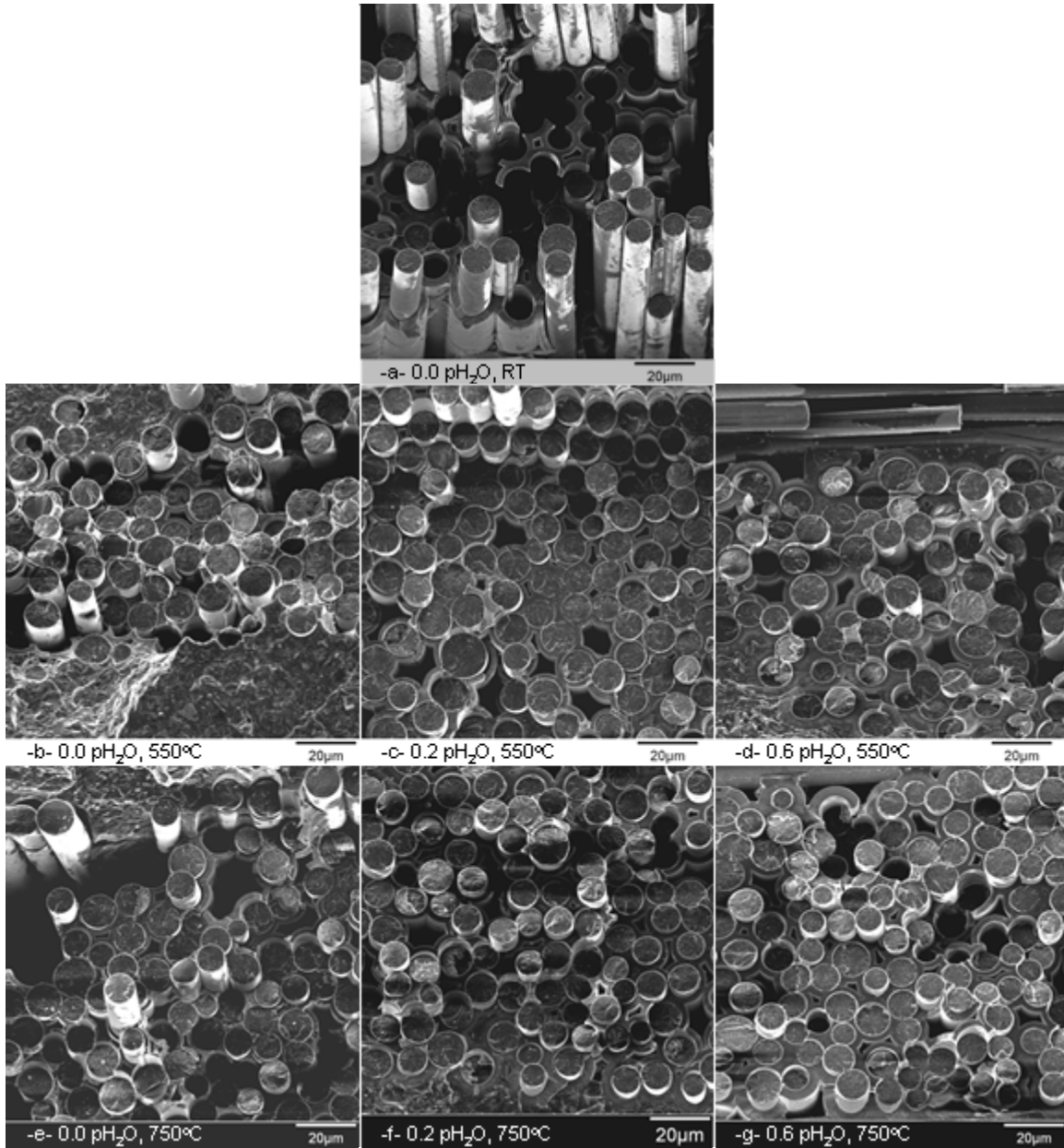
Figure 53: Environmental Monotonic Tests at 1000X

Comparisons of the 3000X images in Figure 54 show that at all conditions the BN layer is distinguishable from the fiber and the CVI SiC, that fibers experience both interior and exterior debonding, and that nearest neighbors fail at different fiber locations, however, they are generally shorter at 550°C and 750°C compared to room temperature.
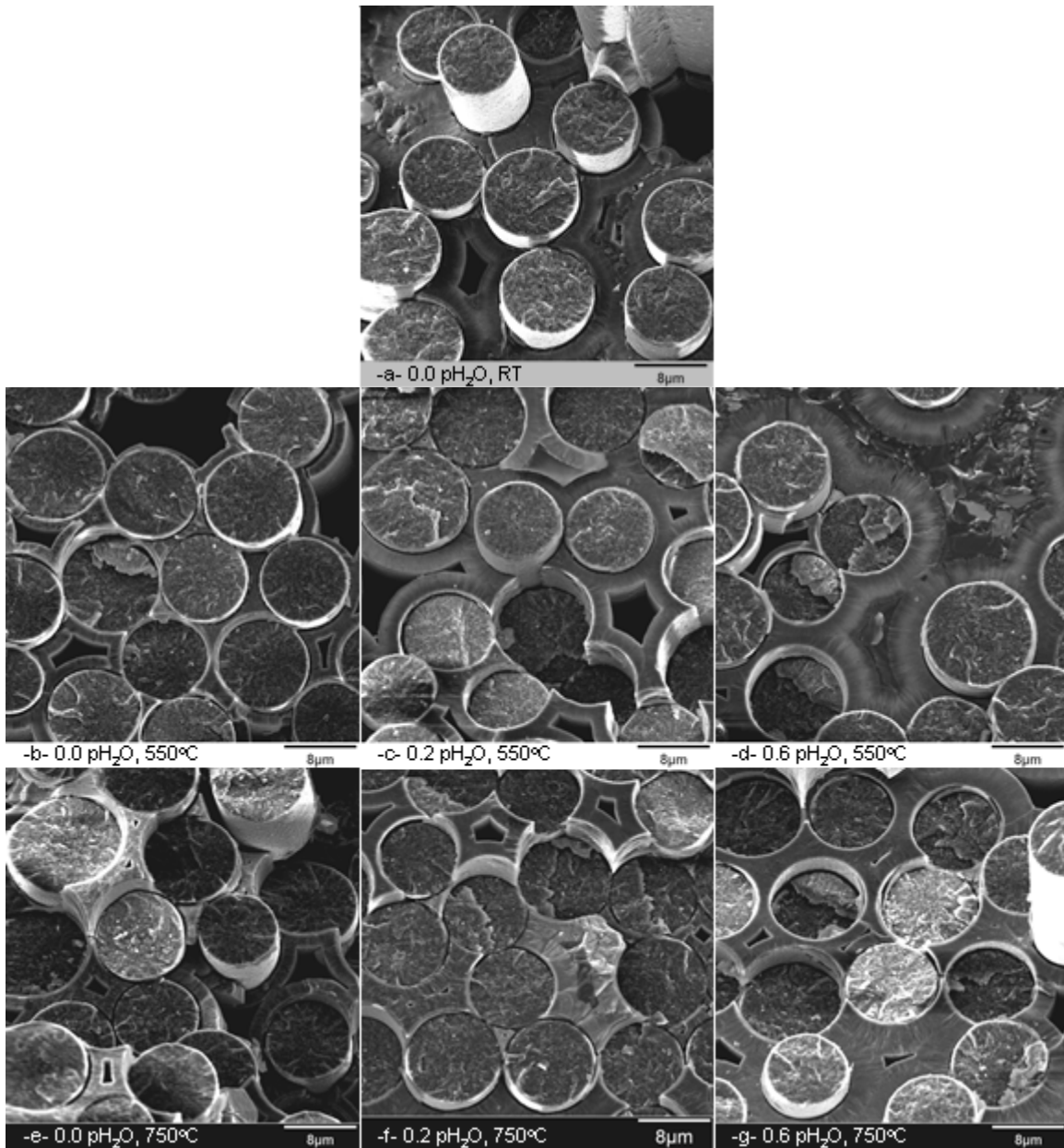
Figure 54: Environmental Monotonic Tests at 3000X

Comparisons of the 8000X images in Figure 55 show no distinguishable characteristics between the 550^oC, 750^oC, and room temperature results. At the magnification the brittle fracture of the matrix, fiber, and interphase material is obvious.
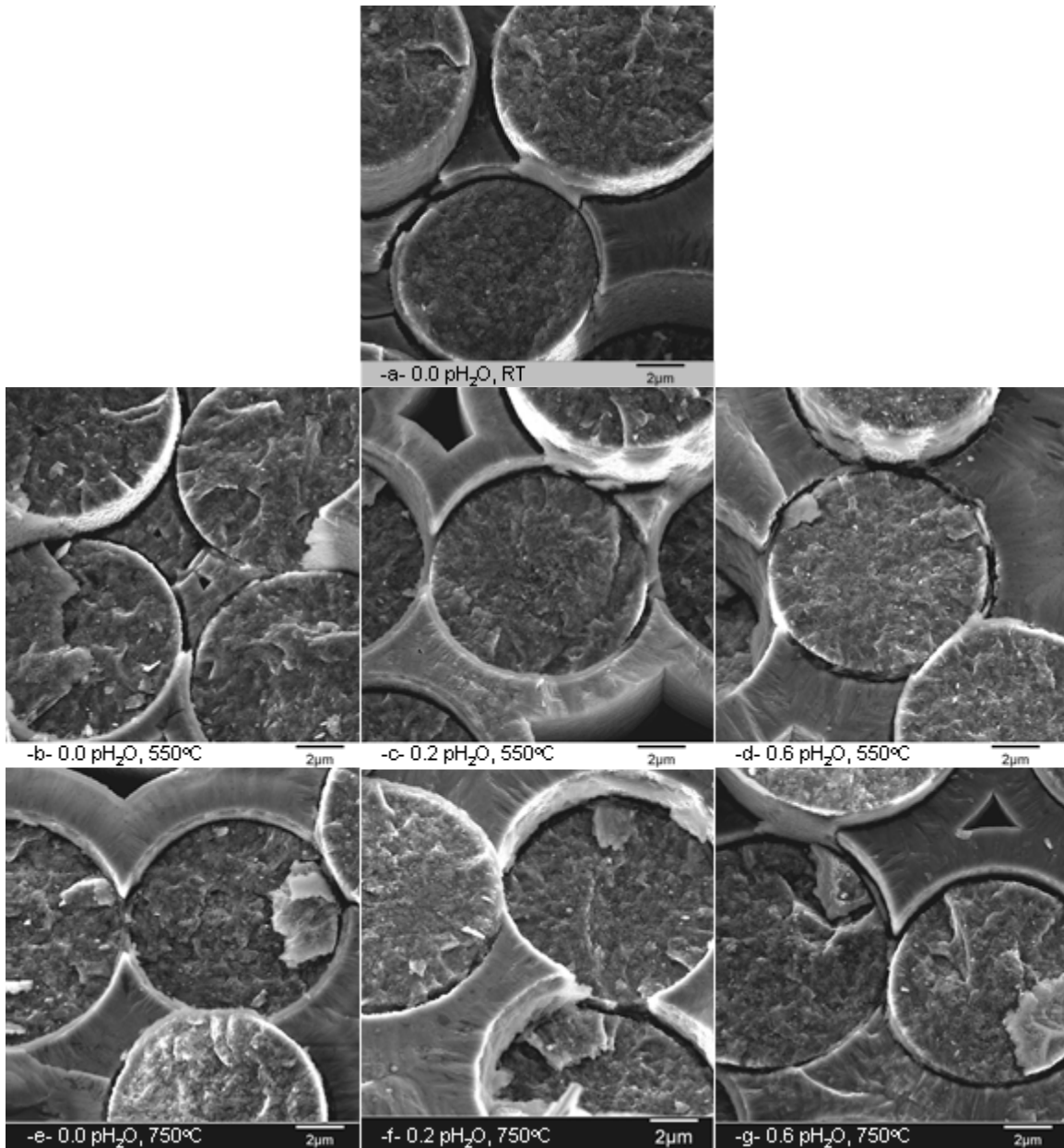
Figure 55: Environmental Monotonic Tests at 8000X

In summary of the monotonic tensile test fracture specimens, the only noticeable difference at 550°C, 750°C, and room temperature is the fiber pullout lengths. The pullout lengths are shorter for the 550°C and 750°C tests. There was no change in the failure mechanisms due to the variation of the moisture content level. The fracture surfaces of the CVI and MI SiC portions of the matrix and the BN interphase layer are similar at all three temperatures and are not affected by the moisture content.

The stress rupture tests in this research were conducted under the same environmental conditions as the environmental monotonic tests, 550°C and 750°C with 0.0, 0.2, and 0.6 atm pH$_2$O at each temperature. Analysis of the FESEM images from the fracture surface specimens of the stress rupture tests conducted in the various environments show the effects of temperature and moisture. These figures are arranged such that moving from top to bottom shows images specimens tested in increasing temperature and moving from left to right show specimens failed at later times. The first image with the gray banner and black text, labeled -a-, is the representative image for the room temperature monotonic test conditions. The images with the white banner and black text are representative images of the 550°C environment. The images with the black banner and the white text are representative images of the 750°C environment. The first image in each of the temperature series is the representative image for the respective environmental monotonic test specimen. The image at a particular time is a representative image for the specimen that failed at that time. The analysis considered all the images at all magnifications.

The first analysis is of the 0.0 atm pH$_2$O environments (Figure 56 through Figure 60). Comparisons of the 30X images in Figure 56 reinforce the earlier assessment that the 550°C and the 750°C specimens experienced shorter fiber pullout lengths compared to the room temperature specimen. Comparing image -f- to -b- and -k- to -h- in Figure 56 shows that as failure time increases the fiber pullout length appear to become less variable. Comparisons of the 100X images in Figure 57 provide more evidence that the fiber pullout length is dependent on temperature. Comparing image -f- to -b- and -k- to -h- in Figure 57 shows that the variability in the fiber pullout lengths decreases with failure time. Comparisons of the 1000X images in Figure 58 show that the oxidation of BN is starting to occur in both the 550°C and 750°C cases. This is seen in the form of puddles, indicated on the images with dotted lines, in -d-, -f-, and -g- in the 550°C case, and in -i-, -j-, and -k- in the 750°C.

The fibers within the puddles appear to be failing along the same fracture plane. The fibers outside of the puddles appear to be failing at various fiber lengths similar to pristine failures seen in monotonic specimen fracture planes. The 3000X images in Figure 59 start showing the

83

pesting evidence of embrittlement. At this magnification featureless glass can be seen on the CVI SiC as in images -d-, -e-, -f-, and -g- for the 550°C case, and images -j- and -k- for the 750°C case. This indicates the BN has oxidized to form B_2O_3, which is the first step of the embrittlement phenomenon. Pesting can be seen in the 550°C images after 17.36 hrs but none of the images are completely embrittled and some fibers demonstrate pristine failure mechanisms in all images.

The arrows show examples of embrittled fiber failures where neighboring fibers have fracture patterns that show they failed at the same time and along the same path. The 750°C images show similar results. At these locations the B_2O_3 has been volatized and the glass has solidified and embrittled the fiber. Not every fiber-to-fiber point inside a puddle is demonstrating an embrittle failure. In the 8000X images in Figure 60, the macro picture is lost and only fiber-to-fiber interactions can be seen. Arrows in these images indicate embrittled fiber failures. Here, the fracture patterns are more evident. Again, not every fiber-to-fiber point has become pested. The analysis of all images from these specimen concluded that the total time to embrittle all the fibers in the failure crack plane is much greater than 63.85 hrs for 550°C with 0.0 pH_2O and much greater than 83.86 hrs for 750°C with 0.0 pH_2O.

-a- RT, MT 800μm
-b- 550°C, MT 800μm
-c- 550°C, 0.81 hrs 800μm
-d- 550°C, 17.36 hrs 800μm
-e- 550°C, 26.82 hrs 800μm
-f- 550°C, 59.03 hrs 800μm
-g- 550°C, 63.85 hrs 800μm
-h- 750°C, MT 800μm
-i- 750°C, 3.23 hrs 800μm
-j- 750°C, 4.97 hrs 800μm
-k- 750°C , 83.63 hrs 800μm
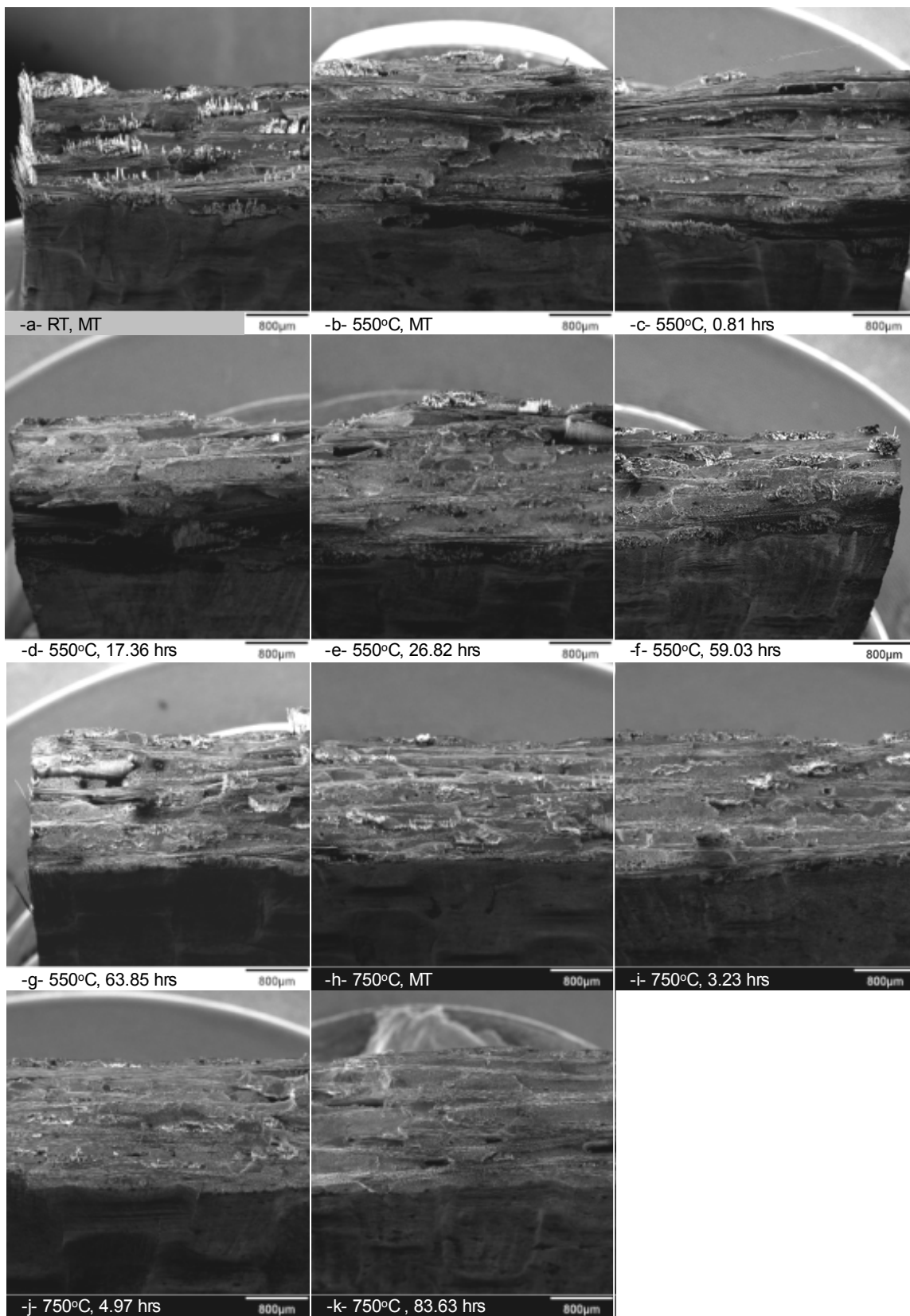
Figure 56: Stress Rupture Tests in 0.0 atm pH$_2$O at 30X

85

-a- RT, MT   200µm

-b- 550°C, MT   200µm

-c- 550°C, 0.81 hrs   200µm

-d- 550°C, 17.36 hrs   200µm

-e- 550°C, 26.82 hrs   200µm

-f- 550°C, 59.03 hrs   200µm

-g- 550°C, 63.85 hrs   200µm

-h- 750°C, MT   200µm

-i- 750°C, 3.23 hrs   200µm

-j- 750°C, 4.97 hrs   200µm

-k- 750°C , 83.63 hrs   200µm
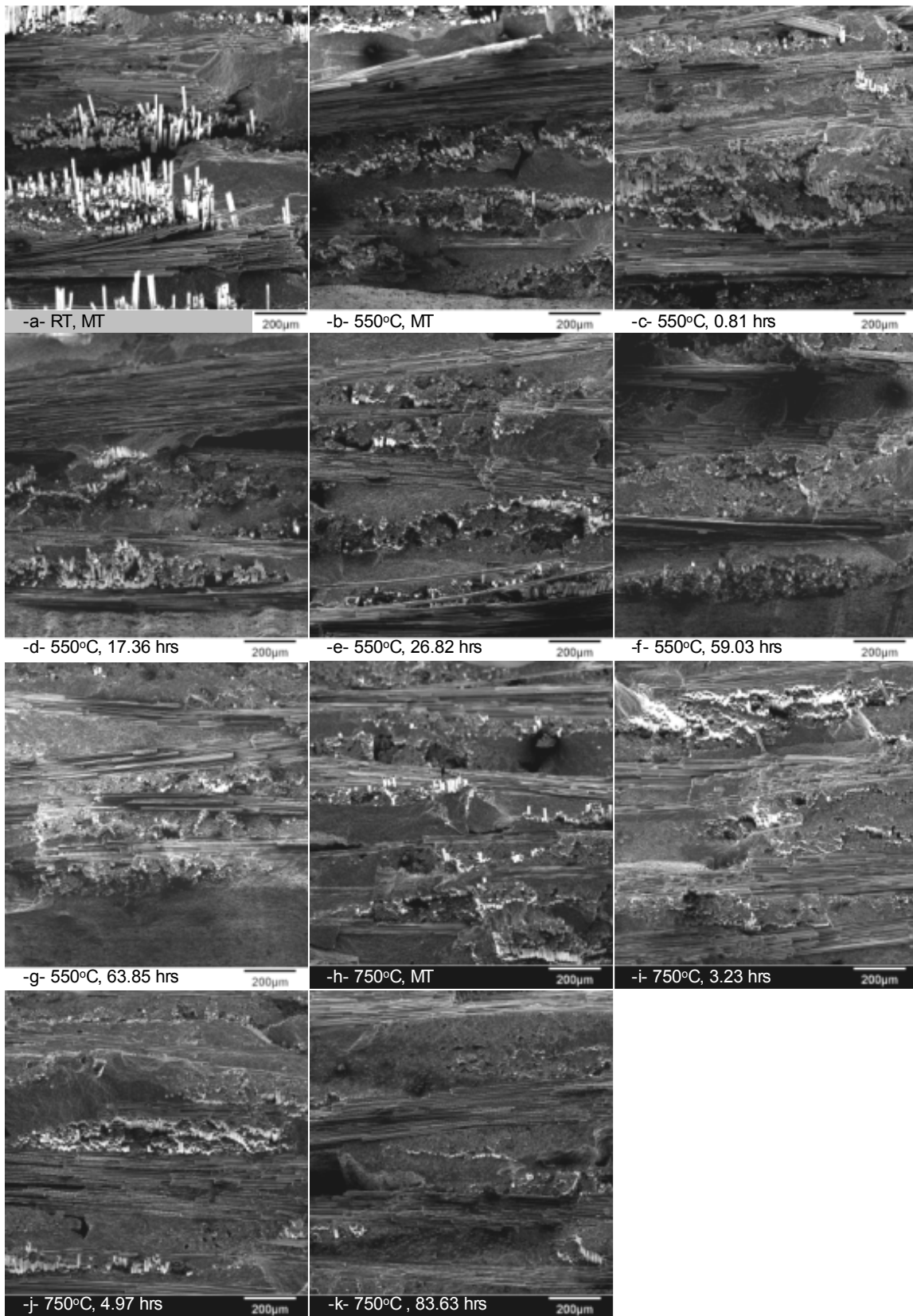
Figure 57: Stress Rupture Tests in 0.0 atm pH$_2$O at 100X

86

-a- RT, MT   20μm

-b- 550°C, MT   20μm

-c- 550°C, 0.81 hrs   20μm

-d- 550°C, 17.36 hrs   20μm

-e- 550°C, 26.82 hrs   20μm

-f- 550°C, 59.03 hrs   20μm

-g- 550°C, 63.85 hrs   20μm

-h- 750°C, MT   20μm

-i- 750°C, 3.23 hrs   20μm

-j- 750°C, 4.97 hrs   20μm

-k- 750°C , 83.63 hrs   20μm
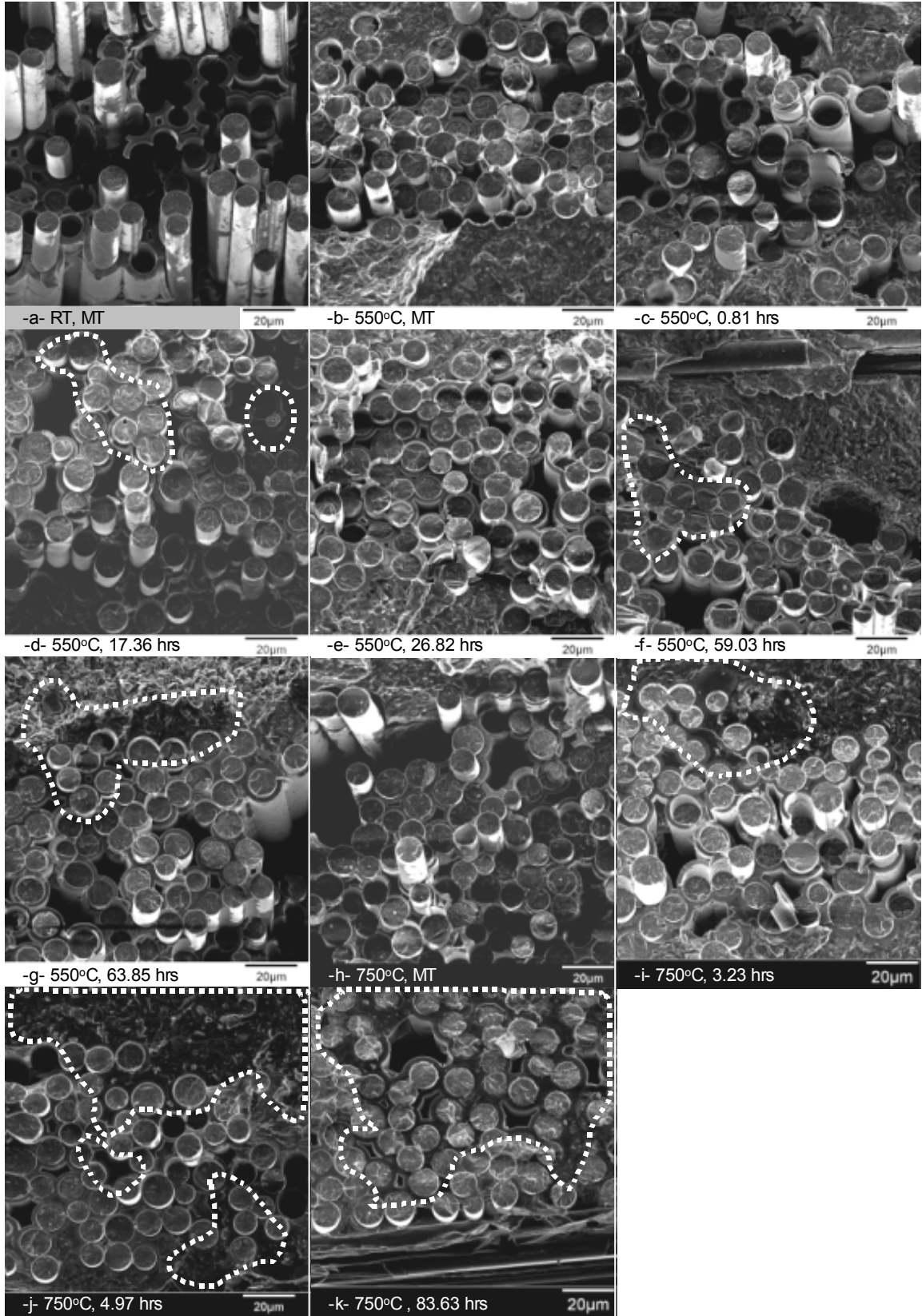
Figure 58: Stress Rupture Tests in 0.0 atm pH$_2$O at 1000X

-a- RT, MT

-b- 550°C, MT

-c- 550°C, 0.81 hrs

-d- 550°C, 17.36 hrs

-e- 550°C, 26.82 hrs

-f- 550°C, 59.03 hrs

-g- 550°C, 63.85 hrs

-h- 750°C, MT

-i- 750°C, 3.23 hrs

-j- 750°C, 4.97 hrs

-k- 750°C , 83.63 hrs
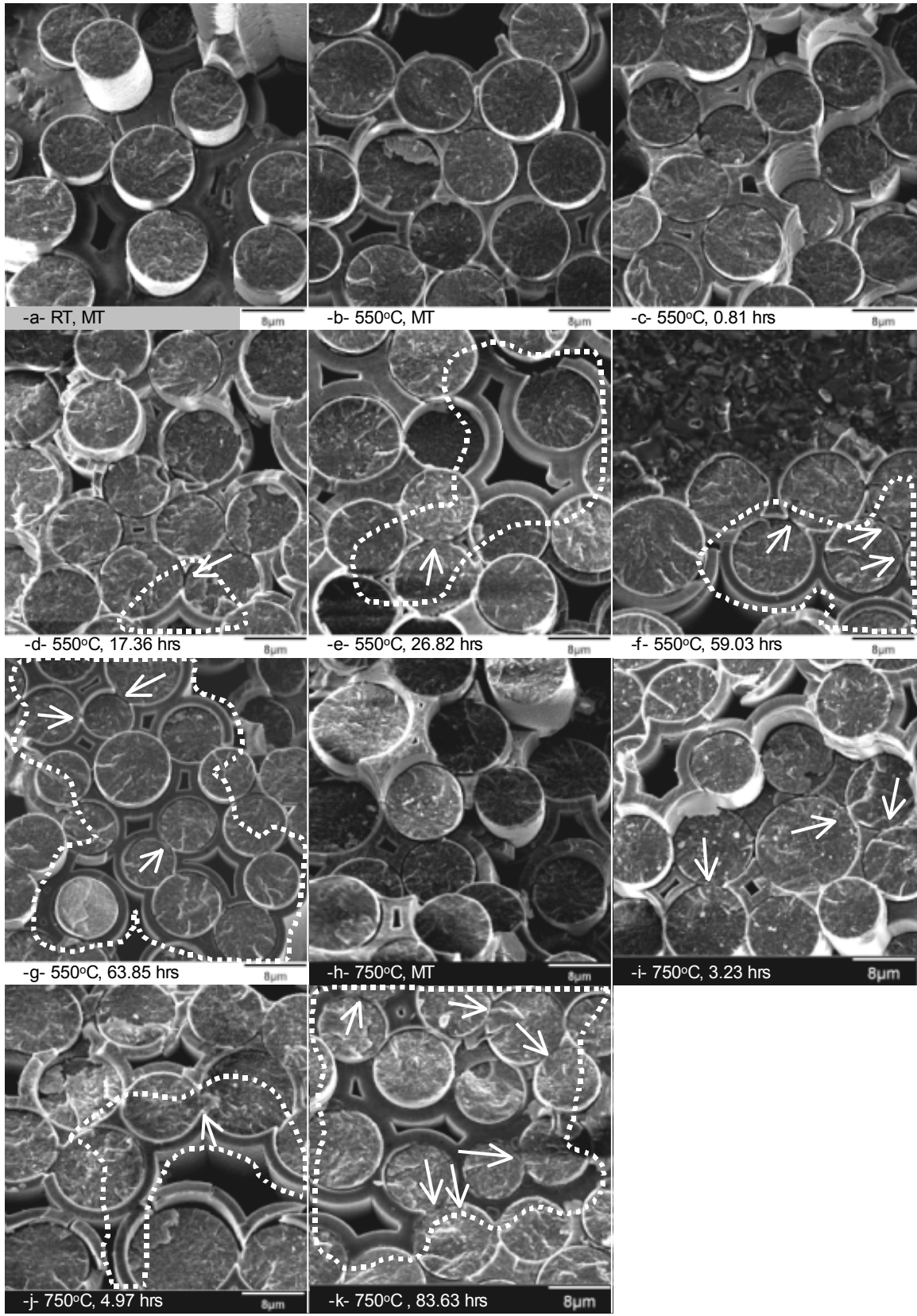
Figure 59: Stress Rupture Tests in 0.0 atm pH$_2$O at 3000X
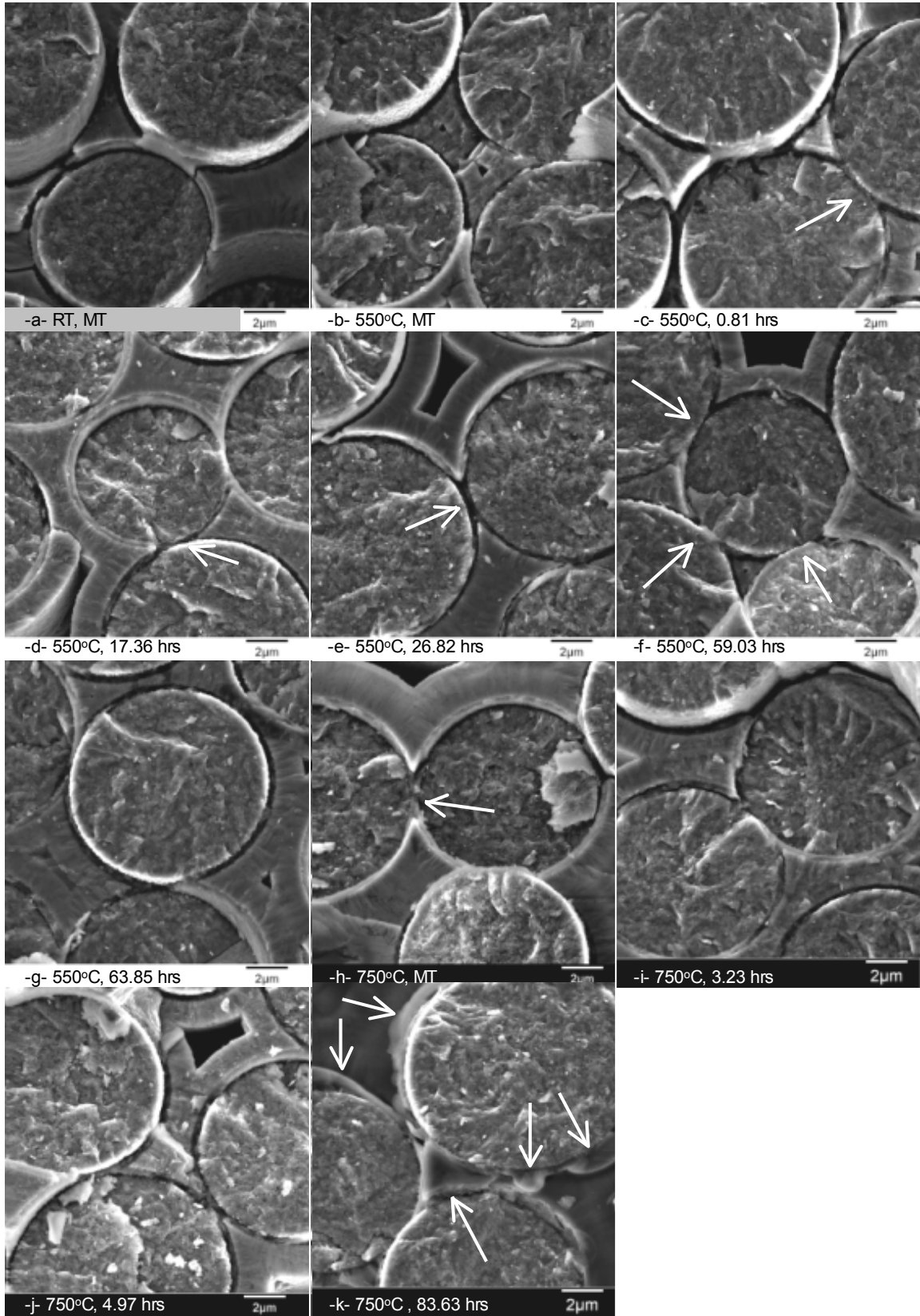
Figure 60: Stress Rupture Tests in 0.0 atm pH$_2$O at 8000X

The results from the 550°C with 0.0 atm pH$_2$O were as expected. Since most of the moisture had been removed from the test environment and the temperature is low, the final step in the embrittlement process should occur very slowly. It is obviously a slow process since glass, in the form of puddles and droplets did not start appearing until 36 hours into the test. Also, it took approximately 70 hours for the glass formations to start developing around groups of fibers and for the pesting to start forming.

The FESEM images for the 750°C with 0.0 atm pH$_2$O show slight evidence of embrittlement. The embrittlement becomes more evident as time increases. The shortest test (3.23 hrs) shows no evidence of embrittlement. The next test (4.97 hrs) shows slight BN recession and small puddles of glass in some locations on the 3000X and 8000X magnification images. The longer test (83.63 hrs) shows extensive embrittlement. These observations were not expected since most of the moisture had been removed from the test environment. The glass formations are most likely boria since boria formation does not require the presence of moisture. Also, some of the puddles appear to have originated from in-between the fiber and matrix and oozed out onto the fracture surface. This may have happened after failure of the stressed fibers when the mechanical strain was relieved causing the liquid boria to be forced out along the fiber.

The second analysis is of the 0.2 atm pH$_2$O environments (Figure 61 through Figure 65) and uses the same baseline as the 0.0 atm pH$_2$O images. The 30X images in Figure 61 show that, similar to the 0.0 atm pH$_2$O cases, the specimens experienced shorter fiber pullout lengths compared to the room temperature specimen in both the 550°C and 750°C cases. The 100X images in Figure 62 show that the variability in the fiber pullout lengths decreases with failure time. This is especially noticeable when comparing image -e- to -b- for the 550°C case and -i- to -g- for the 750°C case in Figure 62. The 1000X images in Figure 63 show that the oxidation of BN is starting to occur in both the 550°C and 750°C cases. The dotted lines indicate this in image -e- in the 550°C case, and in images -g-, -h-, and -i- in the 750°C case. The fibers within the puddles appear to be failing along the same fracture plane. The fibers outside of the puddles appear to fail at various fiber lengths similar to pristine failure seen in monotonic specimen fracture planes. The only exception to this is image -i- where the embrittlement cannot be seen in

the upper left and lower right corner because the fracture plane of the matrix is not flat due to the

presence of pores. However, on the flat portion of the fracture surface the puddle formation is

evident. The 3000X images in Figure 64 show the pesting evidence of embrittlement. The

featureless glass formation can be seen on the CVI SiC as in images -d- and -e- for the 550°C

case, and images -g-, -h-, and -i- for the 750°C case. In the 550°C and 750°C images, pesting

starts before 26.66 and 6.06 hrs, respectively. The arrows show examples of embrittled fiber

failures where neighboring fibers have fracture patterns along the same plane. The 8000X

images in Figure 65 show the fiber-to-fiber interactions. Arrows again indicate embrittled fiber

failures. The analysis of all images from these specimens concluded that the total time to

embrittle the entire failure crack plane is greater than 38.02 hrs for 550°C with 0.2 atm pH_2O and

between 13.24 hrs and 70.40 hrs for 750°C with 0.2 atm pH_2O.

-a- RT, MT   800μm   -b- 550°C, MT   800μm   -c- 550°C, 1.78 hrs   800μm

-d- 550°C, 26.66 hrs   800μm   -e- 550°C, 38.02 hrs   800μm

-f- 750°C, MT   800μm   -g- 750°C, 6.06 hrs   800μm   -h- 750°C, 13.24 hrs   800μm

-i- 750°C, 70.40 hrs   800μm
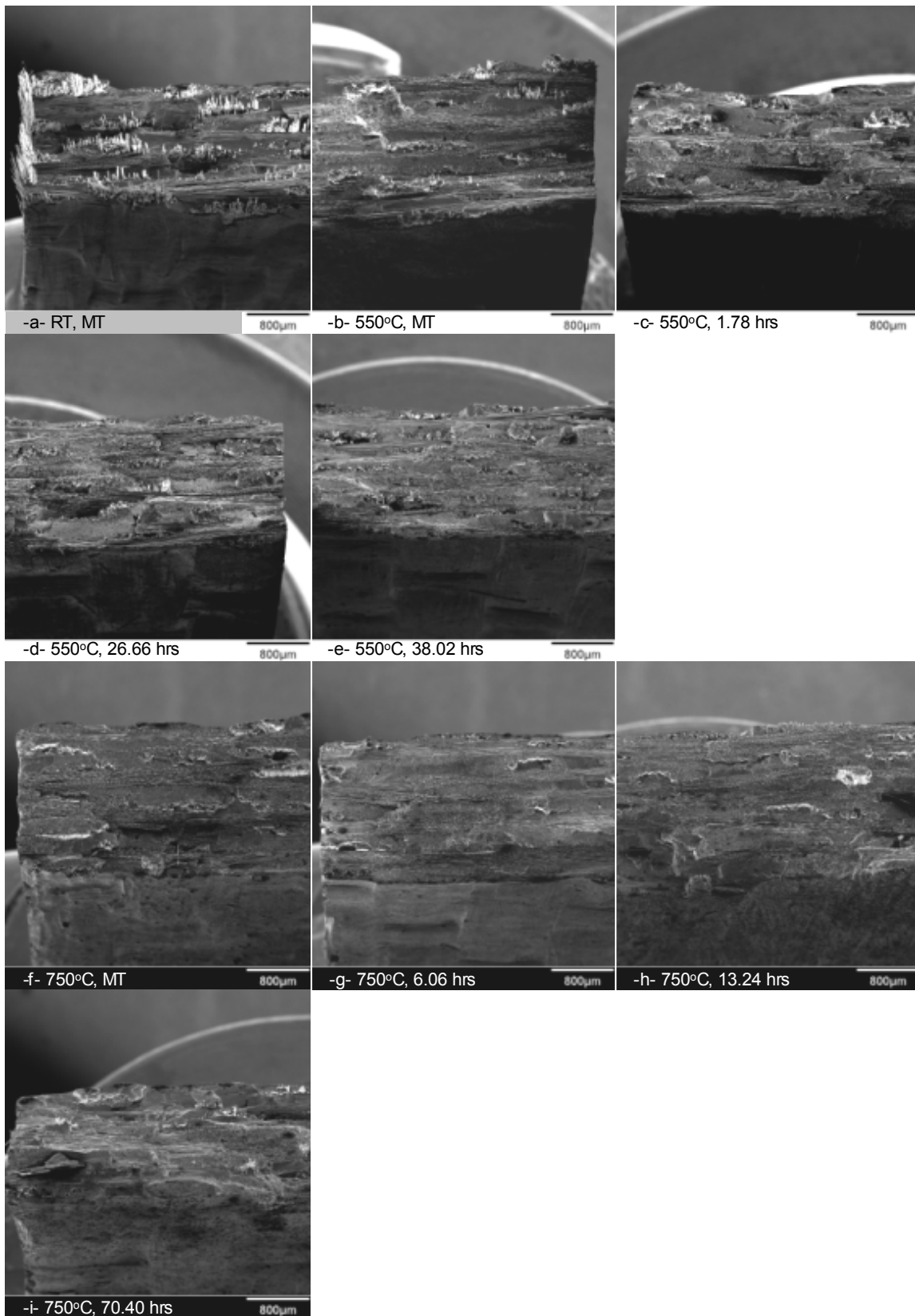
Figure 61: Stress Rupture Tests in 0.2 atm pH_2O at 30X

-a- RT, MT   200μm

-b- 550°C, MT   200μm

-c- 550°C, 1.78 hrs   200μm

-d- 550°C, 26.66 hrs   200μm

-e- 550°C, 38.02 hrs   200μm

-f- 750°C, MT   200μm

-g- 750°C, 6.06 hrs   200μm

-h- 750°C, 13.24 hrs   200 μm

-i- 750°C, 70.40 hrs   200μm
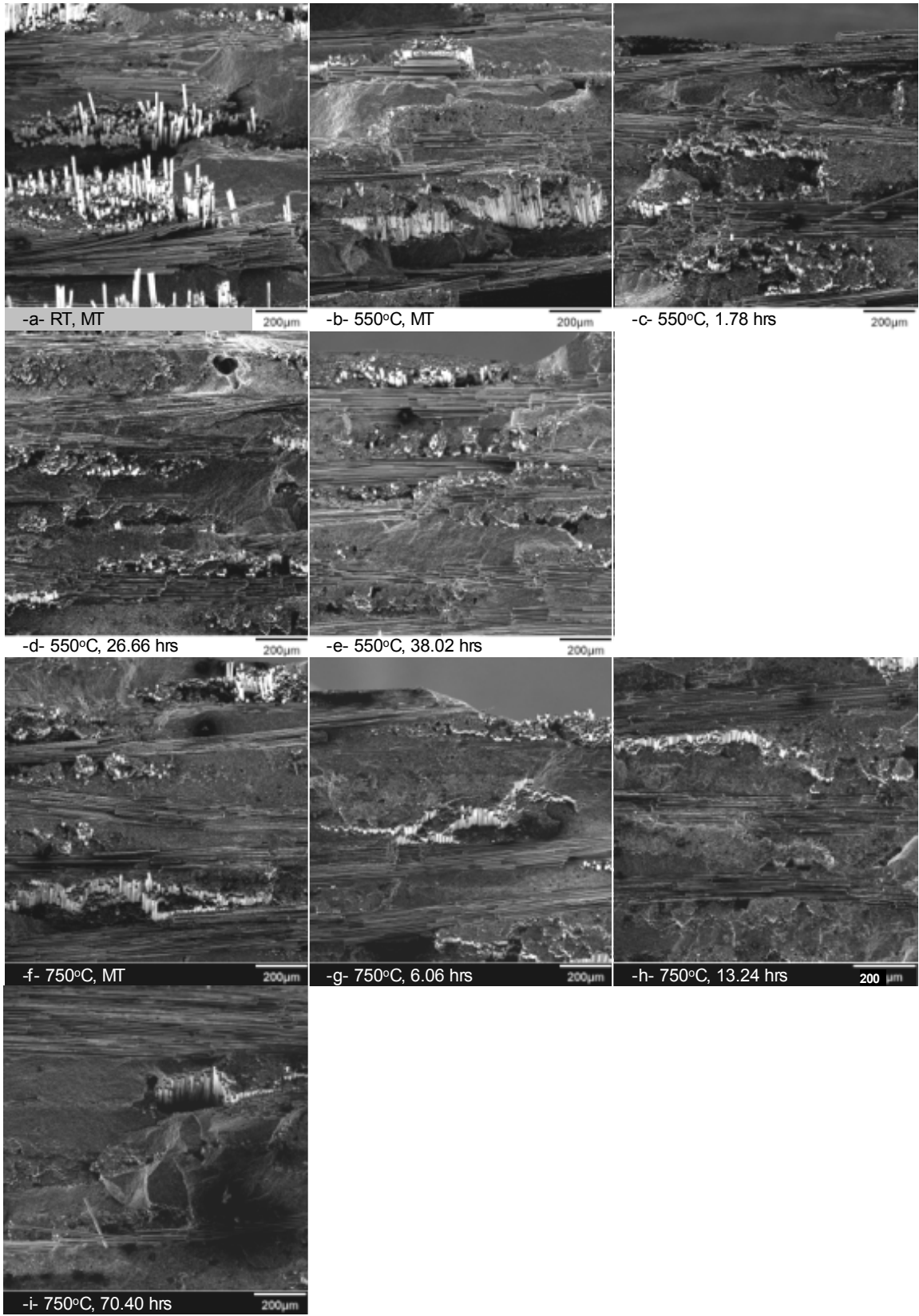
Figure 62: Stress Rupture Tests in 0.2 atm pH$_2$O at 100X

-a- RT, MT   20µm

-b- 550°C, MT   20µm

-c- 550°C, 1.78 hrs   20µm

-d- 550°C, 26.66 hrs   20µm

-e- 550°C, 38.02 hrs   20µm

-f- 750°C, MT   20µm

-g- 750°C, 6.06 hrs   20µm

-h- 750°C, 13.24 hrs   20µm

-i- 750°C, 70.40 hrs   20µm

Figure 63: Stress Rupture Tests in 0.2 atm pH$_2$O at 1000X

-a- RT, MT

-b- 550°C, MT

-c- 550°C, 1.78 hrs

-d- 550°C, 26.66 hrs

-e- 550°C, 38.02 hrs

-f- 750°C, MT

-g- 750°C, 6.06 hrs

-h- 750°C, 13.24 hrs

-i- 750°C, 70.40 hrs

Figure 64: Stress Rupture Tests in 0.2 atm pH$_2$O at 3000X

-a- RT, MT   2μm   -b- 550°C, MT   2μm   -c- 550°C, 1.78 hrs   2μm

-d- 550°C, 26.66 hrs   2μm   -e- 550°C, 38.02 hrs   2μm

-f- 750°C, MT   2μm   -g- 750°C, 6.06 hrs   2μm   -h- 750°C, 13.24 hrs   2μm

-i- 750°C, 70.40 hrs   2μm
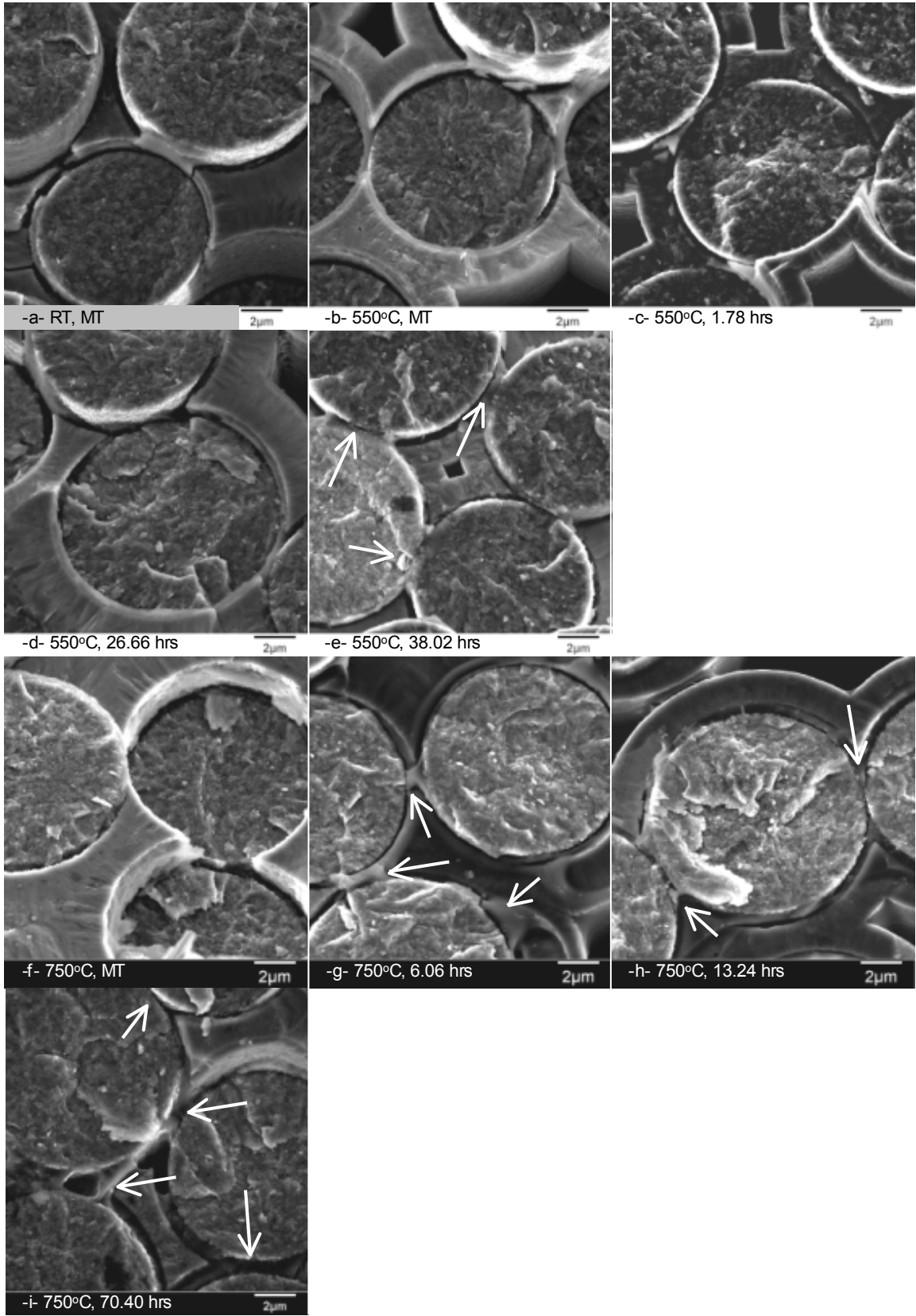
Figure 65: Stress Rupture Tests in 0.2 atm pH_2O at 8000X

Slight time dependent evidence of embrittlement can be seen in the 550°C with 0.2 atm pH$_2$O images. The two shorter tests (1.78 hrs and 26.66 hrs) show no evidence of embrittlement; however, the third test (38.02 hrs) shows slight evidence of embrittlement in the form of puddles of glass and BN recession. These puddles are most likely boria or borosilicate glass depending on the amount of SiO$_2$ and were distributed across the entire cross section. BN interphase recession can be seen at various locations, in particular, at near fiber-to-fiber contact points, on all the 8000X images. From these observations, it appears that the presence of moisture enhances the pesting characteristic of embrittlement over the longer test duration.

Evidence of embrittlement can be seen in the 750°C with 0.2 atm pH$_2$O images as a function of time. The shorter test (6.06 hrs) shows extensive evidence of embrittlement in the form of puddle formations, BN recession, and pesting. The second test (13.24 hrs) shows more evidence of embrittlement. Finally, the third test (70.40 hrs) shows an extensive display of pesting in the 8000X magnification images. Fewer puddles and droplets are seen in the images at 3000X and 1000X in the shorter tests. This is due to the fact that the environment has not had time to attack the boria and reduce it to borosilicate and silica glass, ultimately leading to pesting. Embrittlement in this environment was expected but not to the extent seen. In as little as 6 hours, extensive embrittlement was seen in the form of puddles, droplets, and BN recession.

The third analysis is of the 0.6 atm pH$_2$O environments (Figure 66 through Figure 70) and uses the same baseline as the 0.0 and 0.2 atm pH$_2$O images. The 30X images (Figure 66) and the 100X images (Figure 67) show that the variability of the fiber pullout lengths decreases as the failure time increases similar to the two previous environment cases. The 1000X images (Figure 68Figure 68) show that puddle formations have covered the entire fracture surface by 70.36 hrs for the 550°C case and by 5.64 hrs for the 750°C case. The 3000X images (Figure 69) show that pesting has occurred to all fibers by 36.44 hrs for the 550°C case and 5.64 hrs for the 750°C case. The 8000X images (Figure 70) show that the fracture patterns of fibers can be traced across neighbor fibers in both cases. The analysis of all images from these specimen concluded that the total time to embrittle the entire failure crack plane is between 8.78 hrs and 36.44 hrs for 550°C with 0.6 atm pH$_2$0 and between 0.89 hrs and 5.64 hrs for 750^{o}C with 0.6 atm pH$_2$0.

-a- RT, MT   800µm   -b- 550°C, MT   800µm   -c- 550°C, 7.43 hrs   800µm

-d- 550°C, 8.78 hrs   800µm   -e- 550°C, 36.44 hrs   800µm   -f- 550°C, 70.36 hrs   800µm

-g- 750°C, MT   800µm   -h- 750°C, 0.78 hrs   800µm   -i- 750°C, 0.89 hrs   800µm

-j- 750°C, 5.64 hrs   800µm
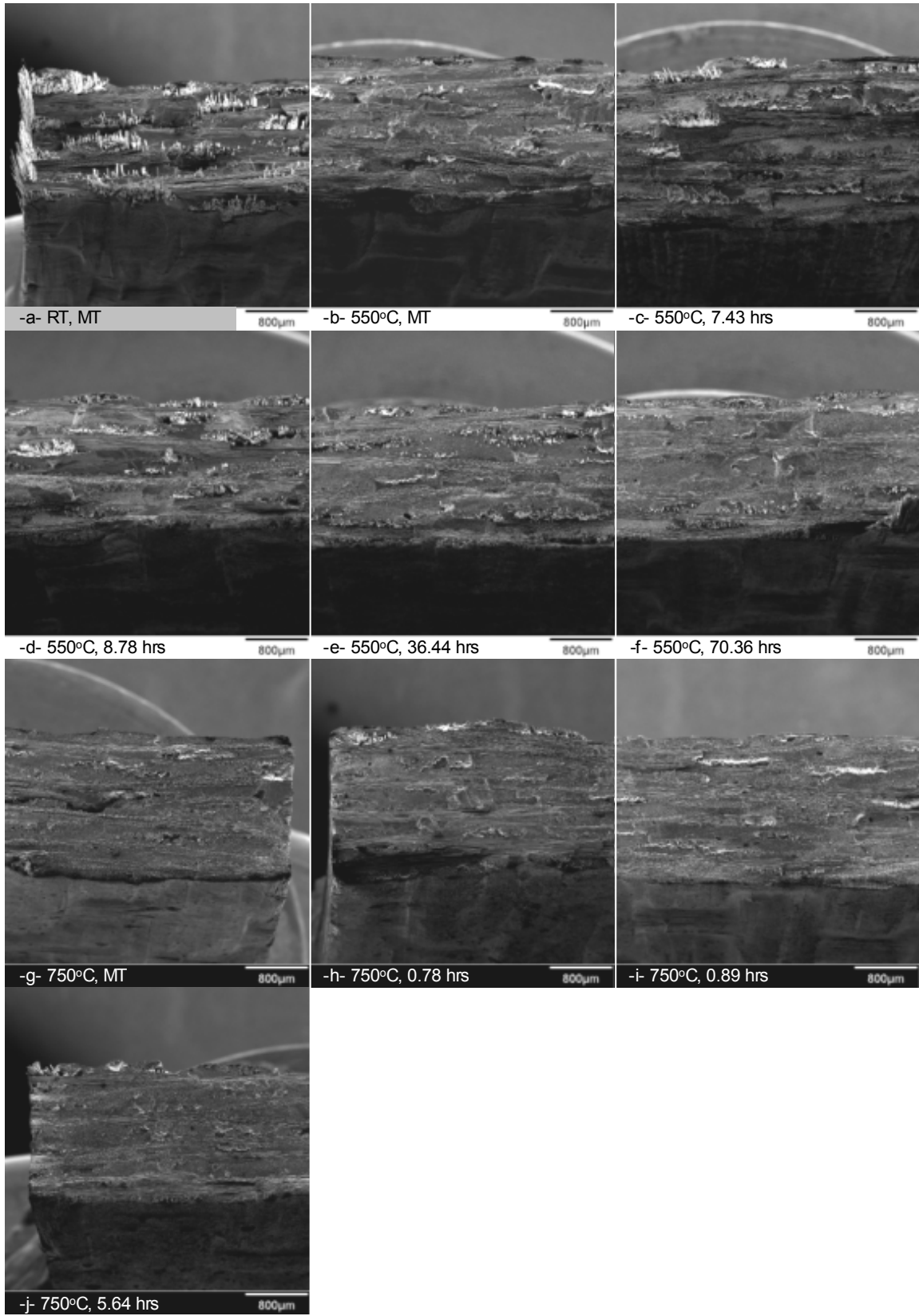
Figure 66: Stress Rupture Tests in 0.6 atm pH_2O at 30X

98

-a- RT, MT 200μm

-b- 550°C, MT 200μm

-c- 550°C, 7.43 hrs 200μm

-d- 550°C, 8.78 hrs 200μm

-e- 550°C, 36.44 hrs 200μm

-f- 550°C, 70.36 hrs 200μm

-g- 750°C, MT 200μm

-h- 750°C, 0.78 hrs 200μm

-i- 750°C, 0.89 hrs 200μm

-j- 750°C, 5.64 hrs 200μm
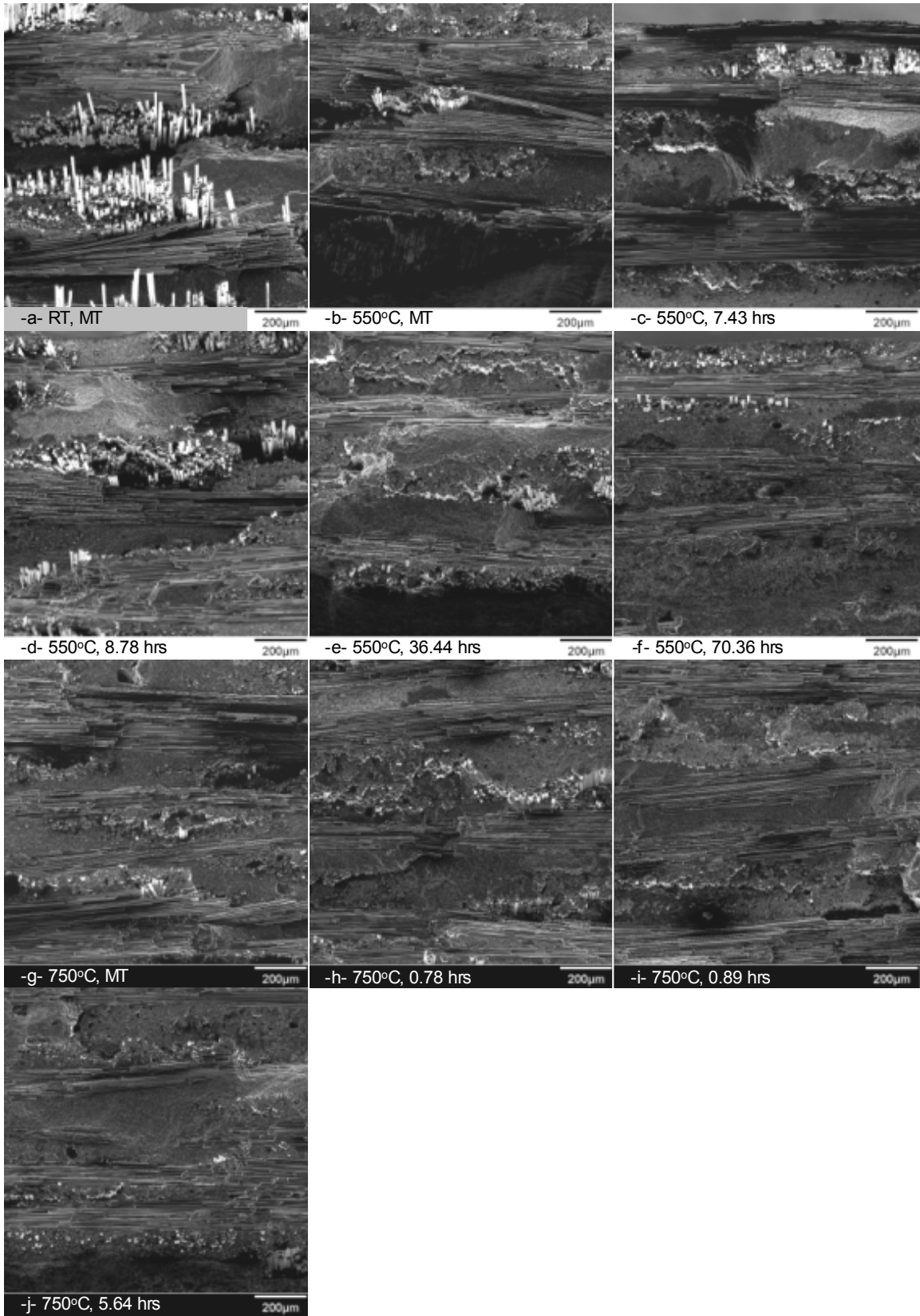
Figure 67: Stress Rupture Tests in 0.6 atm pH$_2$O at 100X
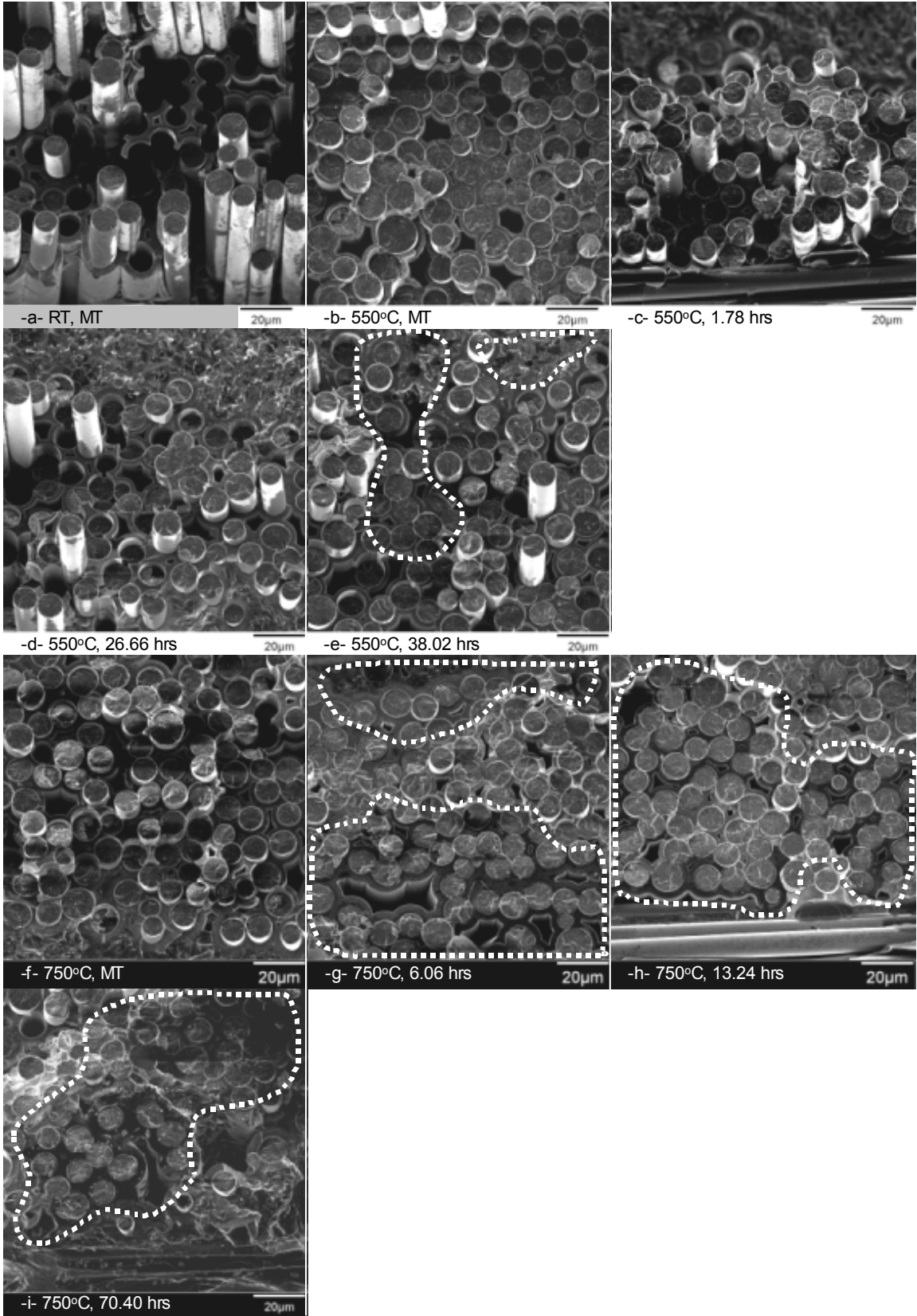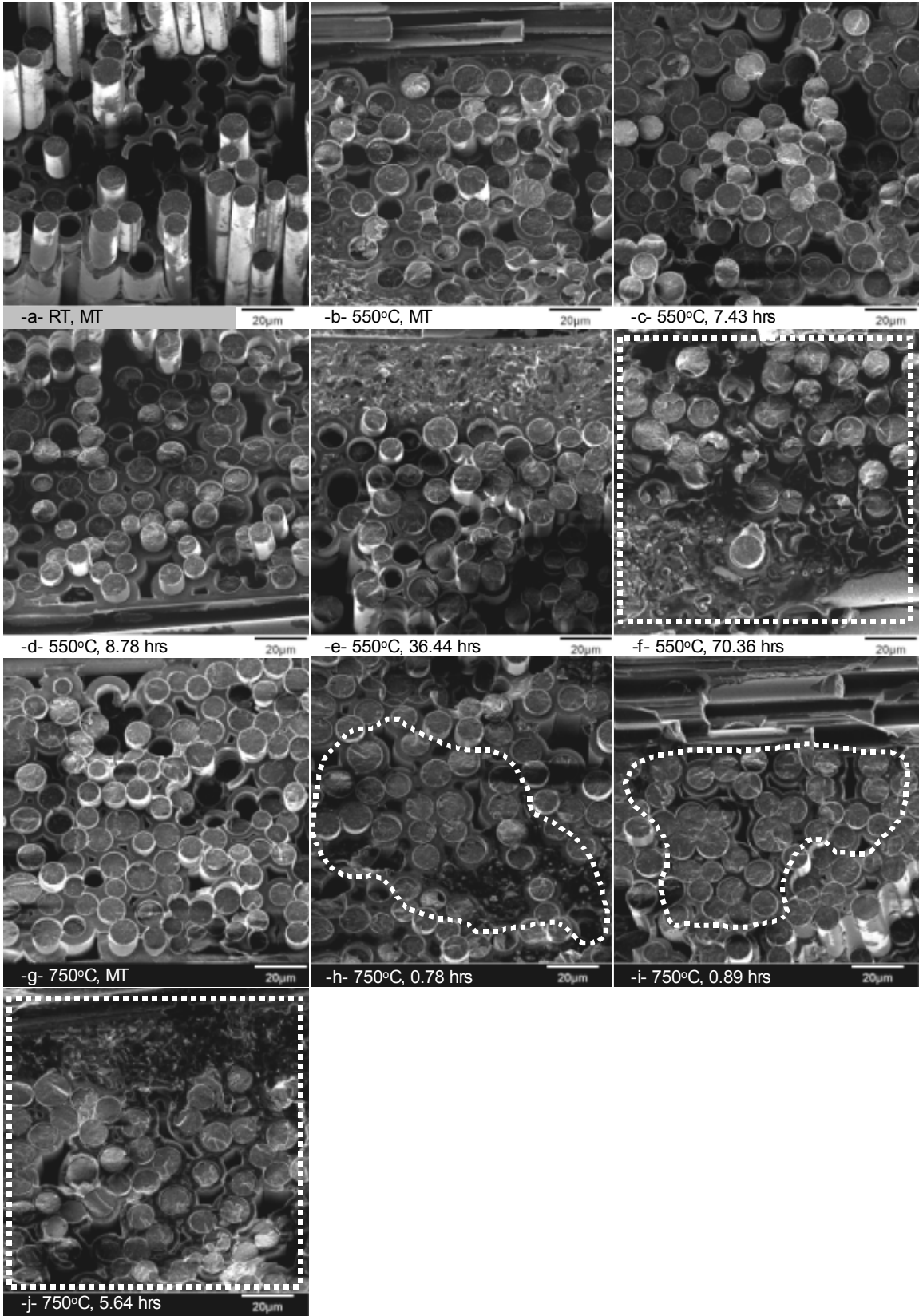
Figure 68: Stress Rupture Tests in 0.6 atm pH₂O at 1000X

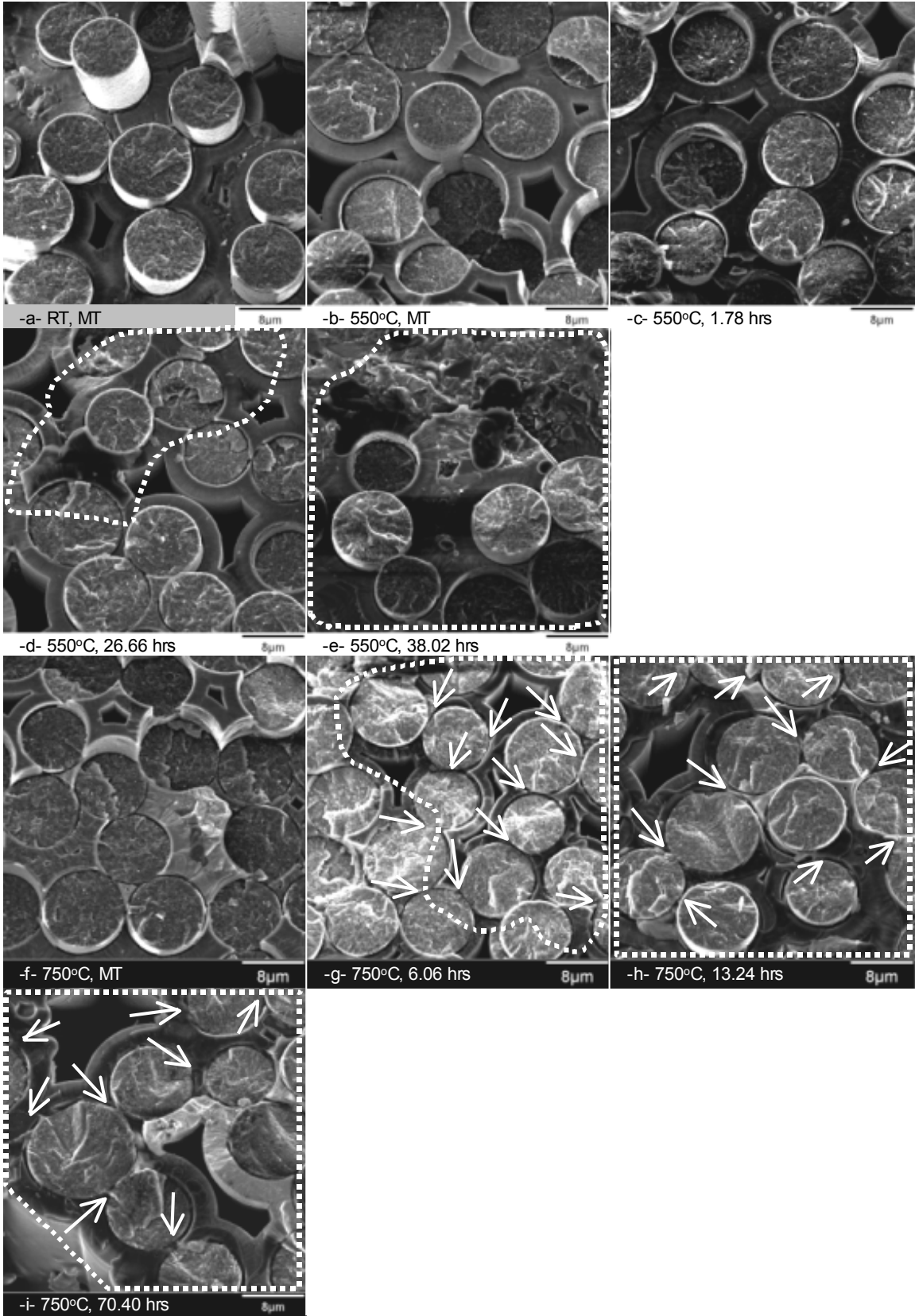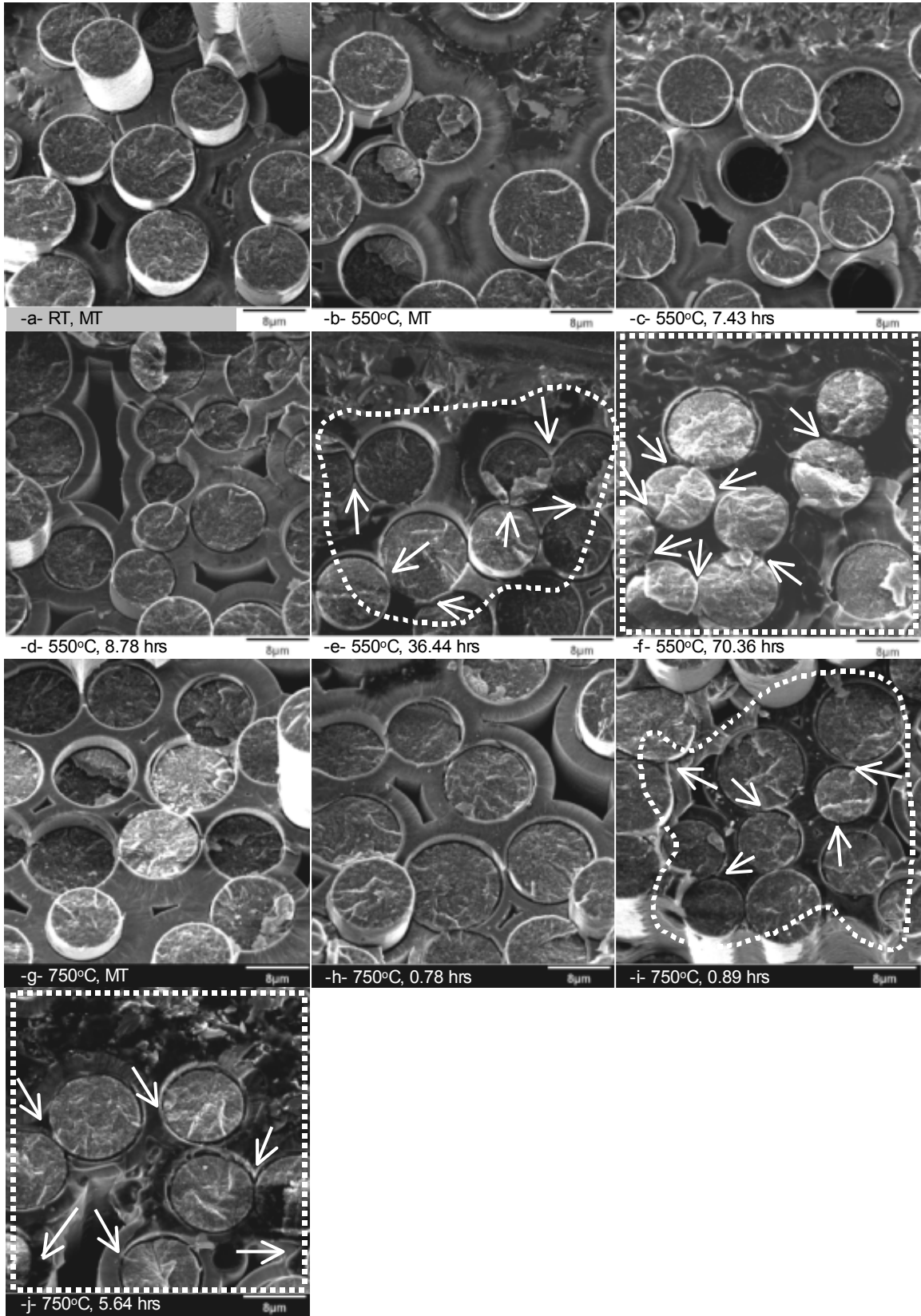**Figure 69: Stress Rupture Tests in 0.6 atm pH$_2$O at 3000X**
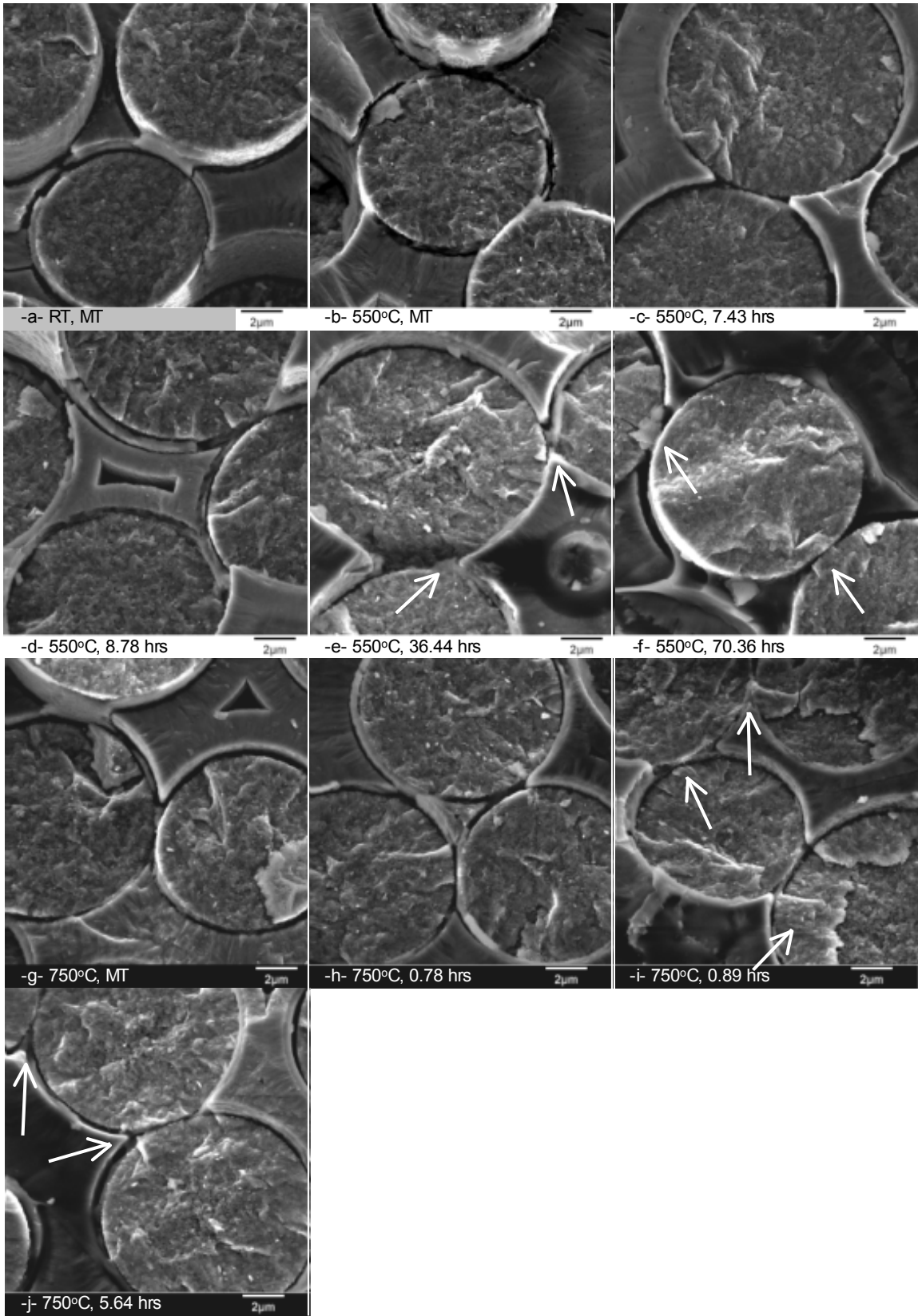
Figure 70: Stress Rupture Tests in 0.6 atm pH$_2$O at 8000X

Evidence of embrittlement can be seen in the 550°C with 0.6 atm pH_2O images as a function of time. The shorter tests (7.43 hrs and 8.78 hrs) show little evidence of embrittlement. Images from the intermediate time test (36.44 hrs) show more evidence of embrittlement. Again 3000X and 8000X magnification images show the best views of puddle formation and BN recession. The 550°C, 0.6 atm pH_2O case (36.44 hrs) has more evidence of embrittlement compared to the 550°C, 0.2 atm pH_2O case (38.02 hrs). Again, this shows the presence of moisture speeds up the embrittlement phenomenon.

The longest 550°C with 0.6 atm pH_2O test that failed (70.36 hrs) shows extensive embrittlement. The embrittlement is so extensive that puddles and droplets can even be seen the 1000X magnification images. The 3000X and 8000X magnification images again show the puddles, droplets, and BN recession. At 8000X magnification it can be seen that all the fibers failed along the same fracture plane as their neighboring fiber. This is occurring because the glass formation has pested these fibers together essentially forming one solid material instead of individual fibers. The pesting is also connecting these fibers to the matrix at locations where the fiber and matrix are close.

The FESEM images for the 750°C with 0.6 atm pH_2O show evidence of embrittlement. The evidence is more in the form of pesting than that of puddle formations and droplets. The shorter two tests (0.89 and 0.78 hrs) show extensive damage to the BN interphase. The environment has aggressively attacked the BN. In many of the images at 8000X magnification the BN recession is obvious, the pesting can be seen between fibers and between a fiber and the matrix, and the boria formations can be seen along the fiber and matrix. However, the large puddles cannot be seen like the ones seen in the previously two cases. The longer test (5.64 hrs) shows more extensive damages to the interphase material as well as puddle formations. The puddles in these images are less noticeable than the other examples but the pesting has already starting to form.

This research attempted to draw conclusions and correlations of the embrittlement phenomenon to the amount of moisture in the test environment. The goal was to find an empirical relationship in terms of moisture content for the coefficient and/or the exponent in the

area fraction of embrittlement equation developed by Morscher and Cawley [17]. As mentioned above, FESEM was used to locate the areas of embrittlement and to see if the amount of moisture affects this phenomenon. The embrittlement phenomenon did not occur in a similar fashion as that of Morscher and Cawley [17]. There was no clear embrittlement front to measure. Therefore, the total embrittlement time determined from the image analysis is only qualitative. From the analysis, estimated total embrittlement times were determined and are summarized in Table 6.

Table 6: Total Embrittlement Time for Various Environments

Environment Conditions	Estimated Total Embrittlement Time (hrs)
550°C, 0.0 atm pH_2O	> 63.85 hrs
550°C, 0.2 atm pH_2O	> 38.02
550°C, 0.6 atm pH_2O	8.78 - 36.44
750°C, 0.0 atm pH_2O	> 83.86
750°C, 0.2 atm pH_2O	13.24 - 70.40
750°C, 0.6 atm pH_2O	0.89 - 5.64

Summary

Experiments were conducted to generate the data to quantify the effects of temperature and moisture on the stress rupture life of the tested CMC. This section summarizes the experiment portion of the research. The conclusions based on monotonic tests done in this research are listed below.

- Modulii of elasticity of the tested CMC and hence its constituents (the fiber and matrix) does not change with temperature or moisture content.

- The average ultimate strengths for Syl-iBN/BN/SiC are 405 MPa for room temperature, 390 MPa for 550°C, and 345 MPa for 750°C.

- The ultimate strength at 550°C or 750°C showed no correlation to moisture content level.

- Prior to matrix cracking, the specimens from the various panels had identical stress strain behavior. After matrix cracking there was some variation in the stress strain behavior, however, the scatter was within range as seen in the CMC literature.

These conclusions were used in the modeling effort to define a starting point for the parameter sensitivity analysis. The conclusions based on stress rupture tests conducted in this research are listed below.

- Temperature and moisture content have detrimental effects on the stress rupture life.

- The 100-hour run-out stress is 80%, 70%, and 54% of the room temperature ultimate strength for 550^oC with 0.0, 0.2, and 0.6 atm pH_2O, respectively.

- The 100-hour run-out stress is 65%, 50%, and 50% of the room temperature ultimate strength for 750^oC with 0.0, 0.2, and 0.6 atm pH_2O, respectively.

- Crack density is not a function of the environment, only a function of applied stress. The stress rupture tests in this research cause between 15-65 through-the-thickness cracks in the 19.25 mm gauge length.

The data collected from these experiments were used to validate the modeling effort presented in Chapter V. The results of the model will be compared to the applied stress versus failure time data generated in these stress rupture tests. The conclusions based on the FESEM analysis and the crack density measurements taken in this research are provided below.

- Embrittlement consists of glass formations in the form of puddles, droplets, and pesting, where the pesting affects the toughness and life of the material by removing the individual fiber failure mechanisms.

- The embrittlement phenomenon is progressive with respect to time and moisture content level. More damage is done the longer the specimen is subjected to stress in the environment and the more moisture that is in the environment.

- The embrittlement time for the 550^oC with 0.0, 0.2, and 0.6 atm pH_2O are estimated to be >63.85 hrs, >38.02 hrs, between 8.78 and 36.44 hrs, respectively

- The embrittlement time for the 750^oC with 0.0, 0.2, and 0.6 atm pH_2O are estimated to be >83.86 hrs, between 13.24 and 70.40 hrs, and between 0.89 and 5.64 hrs, respectively.

Images were taken on both monotonic and stress rupture tests in all environments, including room temperature. These conclusions will be used in the development of the model as well as for the parameter sensitivity analysis.

V. Modeling

This research developed a time-based, phenomenological, Monte Carlo-type simulation of composite failure due to exposure to a hot humid environment. The simulation models the failure mechanisms of a Ceramic Matrix Composite (CMC) with ceramic fibers bridging a through-the-thickness crack. The model presented here is based on discussions with Curtin [73], has similarities to models developed by Morscher [10] and Morscher and Cawley [17], and relies on analytical results by Curtin [22], Curtin et al [21], Cao et al [23], Iyengar and Curtin [74], and Marshall et al [69].

This chapter presents the different aspects of the modeling effort of this research. The first section discusses the assumptions made in the model. The second section presents the details of the theory and equations of the model for the stress rupture behavior of a CMC with through-the-thickness cracks. It discusses the stress profile along the length of the fiber, the fiber strength, and the strength reduction of a pristine fiber due to the manufacturing process of the CMC. The third section addresses strength degradation of the fibers due to time and environmental effects. The fourth section covers the computer code. It presents the idealized specimen used in the computer model. The next section presents the modeling results. The last section covers the sensitivity analysis of the different parameters or variables used in the model.

Assumptions

In every modeling effort assumptions must be made. The following assumptions are based on previous work as well as on observations and data collected in this research. The model assumes the material properties of the interphase and the cross tow fibers are lumped into the matrix properties. It also assumes the through-the-thickness cracks are instantly formed and only through-the-thickness cracks are present. The third assumption is that the weave architecture of the material can be idealized to a unidirectional architecture allowing the use of equations derived by Curtin [22] and Curtin et al [21] for evaluating the probability of fiber failure

for unidirectional composites. The fourth assumption, based on observations from the FESEM analysis, is that embrittlement occurs over the entire fracture surface simultaneously, not in the 'picture frame' manner seen by previous researchers. Lastly, the model assumes that when an embrittled fiber fails, the neighboring embrittled fiber also fail, cascading throughout the tow failing all embrittled fibers in the tow.

Modeling Rupture with Through-The-Thickness Cracks

Composite behavior during a uniaxial tension test can be idealized by considering a large number (i.e. thousands) of individual uniaxial tensile loaded fibers at any cross section [22,73]. Stress rupture behavior can also be idealized in the same manner. Therefore, there must be an analysis of the stress profile along a fiber. Since there are cracks in the material, the fiber's proximity to a matrix crack and how the profile changes along the fiber length with respect to the environment and to time must be considered. It is also important to understand the fiber strength along its length and how it degrades with respect to both the environment and time.

There are four distinct stages of matrix cracking to consider when modeling the failure of the CMC specimen. The first stage consists of only one crack in the cross section. The second stage consists of multiple cracks at different planes, however, the stress transfer lengths do not overlap (i.e. the stress transfer length is less than the distance between different planes where cracks have developed). The third stage is where there are multiple cracks with the stress transfer lengths overlapping; however, the specimen has not reached the matrix crack saturation. The fourth and final stage is where the specimen has reached matrix crack saturation.

The single matrix-crack case and the matrix saturation case, although the easiest to model, are also the least realistic case for this research. The loads applied in the experiments were above the proportional limit to ensure matrix cracking throughout the gauge length but too low to cause matrix crack saturation. The most realistic case for this research is somewhere between the multiple matrix crack case with no overlap and the matrix crack saturation case. Therefore, since no previous work has been done on how overlapping stress transfer lengths can be modeled, the multiple crack case with no stress transfer length overlap was used.

Fiber failure is dependent on both the stress profile and the fiber strength along the fiber length and is affected by the presence of a crack. Chapter II presented the formulation of Morscher and Cawley [17] for the number of defects that could fail in each region as a result of the appropriate stress profile and region lengths (Equations 20 and 21). They are repeated below:

$$\Phi_u = \left(\frac{u}{L_o} \right) \left(\frac{\sigma_{f,c}}{\sigma_o} \right)^m \qquad\qquad \mathbf{24}$$

$$\Phi_z = \frac{\left(\dfrac{\sigma_{f,c}}{\sigma_c} \right)^{m+1}}{(m+1)} \qquad\qquad \mathbf{25}$$

From here, Morscher and Cawley [17] developed a probabilistic model based on groups of embrittled fibers and groups of pristine fibers (presented in Appendix A). The model presented here uses Equation 24 and 25 to develop individual fiber failure stresses, or strengths, in terms of $\sigma_{f,c}$.

Every fiber will have two strengths that could cause failure in each through-the-thickness crack. The first strength, S_u, is the value $\sigma_{f,c}$ that will cause failure in the crack opening region. The second strength, S_δ, is the value of $\sigma_{f,c}$ that will cause failure in the stress transfer region. The lower of these values will be the ultimate strength of the fiber in this particular through-the-thickness crack. The exact location of the fiber failure cannot be determined within a region using the techniques presented here. To determine this, the regions would have to be divided up into many smaller sub-regions and within each sub-region the stress profile would have to be determined using Equation 19. Determination of the location of the failure within a region was not considered necessary for this research.

The strengths for each region are determined by manipulating Equation 11 using Equation 24 and 25, respectively. This will give the strength for the two regions described above and displayed in Figure 17. The formulation for each region is as follows.

For the crack opening, Region 1, start with Equation 11:

$$P(\sigma, L) = 1 - e^{-\Phi(\sigma, L)} \qquad \textbf{26}$$

Substitute Equation 24 and simplify:

$$Rnd_u = 1 - e^{-\left(\frac{u}{L_o}\right)\left(\frac{S_u}{\sigma_{otT}}\right)^m} \qquad \textbf{27}$$

$$\ln(1 - Rnd_u) = -\left(\frac{u}{L_o}\right)\left(\frac{S_u}{\sigma_{otT}}\right)^m \qquad \textbf{28}$$

$$S_u = \sigma_{otT}\left[\frac{L_o}{u}\left(-\ln(1 - Rnd_u)\right)\right]^{\frac{1}{m}} \qquad \textbf{29}$$

where

$S_u \equiv$ strength in the crack opening region (MPa)
$\sigma_{otT} \equiv$ fiber reference stress as a function of time and temperature (MPa)
$L_o \equiv$ fiber reference length (mm)
$u \equiv$ crack opening length (mm)
$Rnd_u \equiv$ random number representing probability
$m \equiv$ Weibull parameter

For the stress transfer region, Region 2, start with Equation 11:

$$P(\sigma, L) = 1 - e^{-\Phi(\sigma, L)} \qquad \textbf{30}$$

Substitute Equation 25 and simplify with Equation 13:

$$Rnd_\delta = 1 - e^{-\frac{\left(\frac{S_\delta}{\sigma_c}\right)^{m+1}}{(m+1)}} \qquad \textbf{31}$$

$$\ln(1 - Rnd_\delta) = -\frac{(S_\delta)^{m+1}\left(\frac{R}{\sigma_{otT}^m \tau_T L_o}\right)}{(m+1)} \qquad \textbf{32}$$

$$S_\delta = \left[\sigma_{otT}^m \tau_T \frac{L_o}{R}(m+1)\left(-\ln(1 - Rnd_\delta)\right)\right]^{\frac{1}{m+1}} \qquad \textbf{33}$$

where

$S_\delta \equiv$ strength in the stress transfer region (MPa)

$\sigma_{otT} \equiv$ fiber reference stress as a function of time and
       temperature (MPa)

$m \equiv$ Weibull parameter

$\tau_T \equiv$ interfacial shear stress at temperature (MPa)

$R \equiv$ radius of the fiber (mm)

$Rnd_\delta \equiv$ random number representing probability

These regional fiber strengths, Equation 29 and 33, will degrade because of exposure to intermediate temperature and will be a function of time and therefore must be understood. The σ_{otT} in Equations 29 and 33 is the reference strength for a pristine fiber and is affected by the processing of the CMC material because it exposes pristine fibers to high temperature and pressures. The strength reduction factor presented in Chapter II to must be applied to σ_{otT} to account for the effect of the manufacturing process. For the strength in the crack opening region, multiply Equation 29 by Equation 22 and substitute Equation 16 for the crack opening, u:

$$S_u = \frac{\left[\dfrac{m(m+2)R}{2(m+1)\tau_{ult}L_o}\left(\dfrac{m+2}{m+1}\dfrac{\sigma_{ult}}{f_{init}}\right)^{m+1}\right]^{\frac{1}{m}}}{2800}\,\sigma_{otT}\left[\frac{L_o\,2\tau_T E_f\left(1+\dfrac{E_f f}{E_m(1-f)}\right)}{\sigma_{f,c}^2 R}\left(-\ln(1-Rnd_u)\right)\right]^{\frac{1}{m}} \qquad \textbf{34}$$

$$S_u = \left[\frac{m(m+2)E_f\left(1+\dfrac{E_f f}{E_m(1-f)}\right)\left(-\ln(1-Rnd_u)\right)}{(m+1)\sigma_{f,c}^2}\right]^{\frac{1}{m}}\left\{\frac{\tau_T}{\tau_{ult}}\right\}^{\frac{1}{m}}\left\{\frac{\sigma_{otT}}{2800}\right\}\left\{\frac{m+2}{m+1}\frac{\sigma_{ult}}{f_{init}}\right\}^{\frac{m+1}{m}} \qquad \textbf{35}$$

where

$S_u \equiv$ strength in the crack opening region (MPa)

$m \equiv$ Weibull parameter

$E_f \equiv$ modulus of elasticity of fiber (GPa)

$E_m \equiv$ modulus of elasticity of matrix (GPa)

$f \equiv$ volume fraction of fibers in loading direction

$Rnd_u \equiv$ random number representing probability

$\sigma_{f,c} \equiv$ stress on a fiber in the crack opening region

$\tau_T \equiv$ interfacial shear stress at test environment (MPa)

$\tau_{ult} \equiv$ interfacial shear stress during ultimate strength test (MPa)

$\sigma_{otT} \equiv$ fiber reference stress as a function of time and temp (MPa)

$\sigma_{ult} \equiv$ ultimate strength of composite (MPa)

$f_{init} \equiv$ initial volume fraction of fibers in loading direction

For the strength in the stress transfer length region, multiply Equation 33 by Equation 22:

$$S_\delta = \left[\left[\frac{\dfrac{m(m+2)R}{2(m+1)\tau_{ult}L_o}\left(\dfrac{m+2}{m+1}\dfrac{\sigma_{ult}}{f_{init}}\right)^{m+1}}{2800^m}\right]\sigma_{otT}^m \tau_T \frac{L_o}{R}(m+1)(-\ln(1-Rnd_\delta))\right]^{\frac{1}{m+1}}$$ **36**

$$S_\delta = \left[\frac{m(m+2)}{2}(-\ln(1-Rnd_\delta))\right]^{\frac{1}{m+1}}\left\{\frac{\tau_T}{\tau_{ult}}\right\}^{\frac{1}{m+1}}\left\{\frac{\sigma_{otT}}{2800}\right\}^{\frac{m}{m+1}}\left\{\frac{m+2}{m+1}\frac{\sigma_{ult}}{f_{init}}\right\}$$ **37**

where

$S_\delta \equiv$ strength in the stress transfer region (MPa)
$m \equiv$ Weibull parameter
$f \equiv$ volume fraction of fibers in loading direction
$Rnd_u \equiv$ random number representing probability
$\sigma_{f,c} \equiv$ stress on a fiber in the crack opening region
$\tau_T \equiv$ interfacial shear stress at test environment (MPa)
$\tau_{ult} \equiv$ interfacial shear stress during ultimate strength test (MPa)
$\sigma_{otT} \equiv$ fiber reference stress as a function of time and temp (MPa)
$\sigma_{ult} \equiv$ ultimate strength of composite (MPa)
$f_{init} \equiv$ initial volume fraction of fibers in loading direction

For these equations to be valid they must both converge to the same theoretical value, σ_{ult}/f_{init} for room temperature monotonic tests and some value less than σ_{ult}/f_{init} for environmental monotonic tests, when the distributive characteristic of the Weibull parameter, m, is removed. The limits of Equations 35 and 37 as m goes to infinity are both:

$$S_u = S_\delta = \left\{\frac{\sigma_{otT}}{2800}\right\}\left\{\frac{\sigma_{ult}}{f_{init}}\right\}$$ **38**

During a room temperature monotonic test, or fast fracture test, σ_{otT} is 2800 MPa making the first term in Equation 38 equal to 1, thus validating the strength equations for room temperature monotonic tests. For environmental monotonic tests, σ_{otT}, will be less than 2800 MPa making the first term in Equation 38 less than 1. This causes Equation 38 to converge to

111

some fraction of the theoretical value, σ_{ult}/f_{init}, thus allowing the strength equations to be used for all monotonic tests.

The experimental data collected can now be compared to the equation used in the model to see if the model is appropriate for the environments being investigated. As mentioned above, the strength equations must converge to the correct value, σ_{ult}/f_{init}, as m approaches infinity for room temperature tests. Also the equations should converge to some value less than σ_{ult}/f_{init} for the environmental tests because the coefficient, $\sigma_{otT}/2800$, is less than one as temperature increases.

The environmental monotonic test data show that this coefficient should be on average 0.9639 for 550°C and 0.8513 for 750°C. Using t = 0.03 hr (approximate exposure time for monotonic tests) and Equation 38, which is the strength equation with m equal to infinity, the coefficient is 0.8548 and 0.8029, respectively. This produces a percent error of -11.32% for the 550°C scenario and -5.69% for the 750°C scenario. These percent errors equate to 48.6 and 23.1 MPa, respectively. As shown in Figure 36, these magnitudes are within the scatter band of the data.

The above analysis provided the understanding of the stress profile and the strength along a fiber's length. Now an understanding on how time and the environment affect the stress and strength is needed. Both time and the environment will affect parameters differently.

Time and Environmental Effects on Fiber Stress Profiles

The stress on the fiber length in the crack opening region is only a function of time if fibers fail while under a constant load. That is, the stress on the fibers will remain constant if no fibers fail. However, as fibers fail, they no longer have any load bearing capability, so the fraction of fibers in the loading direction, f, decreases. This will cause an increase in stress on the remaining fibers because of load sharing.

A fiber that fails in the stress transfer region still retains some of its load carrying capacity due to interfacial shear properties. Since the exact location in the region is not known, the amount of the load the broken fiber carries is unknown. However, since failure locations are

uniformly distributed in the stress transfer region [73], one can assume that the load carrying capacity of the fibers that fail will also be uniformly distributed between 0.0 and 1.0, which represent no load carry capacity and full load carrying capacity, respectively. In effect, the load carrying capacity is the percentage of the load the fiber is experiencing. Any fiber that fails in the crack opening region, either due to stress or embrittlement, will have zero load carrying capacity (i.e. it no longer supports any load). Unbroken fiber will remain at a 1.0 load capacity (i.e. the can continue to support the full load). Fibers that fail in the stress transfer region will have a load carrying capacity between the two extremes.

Since this material was manufactured in an orthogonal weave, half of the total volume fraction, VF, is simply the volume fraction in the loading direction, f. As fibers fail the volume fraction in the loading direction decreases. However, if a fiber still supports some of the load, completely removing it from the population of fibers would be an underestimation of the remaining volume fraction in the loading direction. This would in turn cause the stress on the fibers to be too high. However, the individual fiber load carrying capacities can be summed over the entire crack plane giving a crack load carrying capacity, CAP. With this value, a new equivalent volume fraction in the loading direction can be calculated as:

$$f = \frac{VF}{2}\left(\frac{CAP}{N_f}\right)$$
39

where

$VF \equiv$ volume fraction of fibers
$CAP \equiv$ crack load carrying capacity
$N_f \equiv$ number of fibers

Fiber failure rate is also important. The change in individual fiber stress is small when there are individual fiber failures since there are tens of thousands of fibers in the specimen cross section. However, the change in individual fiber stress is dramatic when large numbers of fibers fail simultaneously. Figure 71 is a simplified case of how the stress on an individual fiber will change, in terms of an applied stress factor, if 10% of the remaining fibers simultaneously fail every hour. The applied stress factor is simply the number of times higher the stress on the fibers

is compared to the stress applied to the CMC specimen. In this example, the fibers in a

specimen with a volume fraction in the loading direction of 0.2 will experience 5 times the amount

of stress on the fibers as the specimen experienced. Therefore, if 200 MPa was applied on the

specimen the fibers in a through-the-thickness crack experience 1000 MPa. As fibers fail the

applied stress factor will increase.
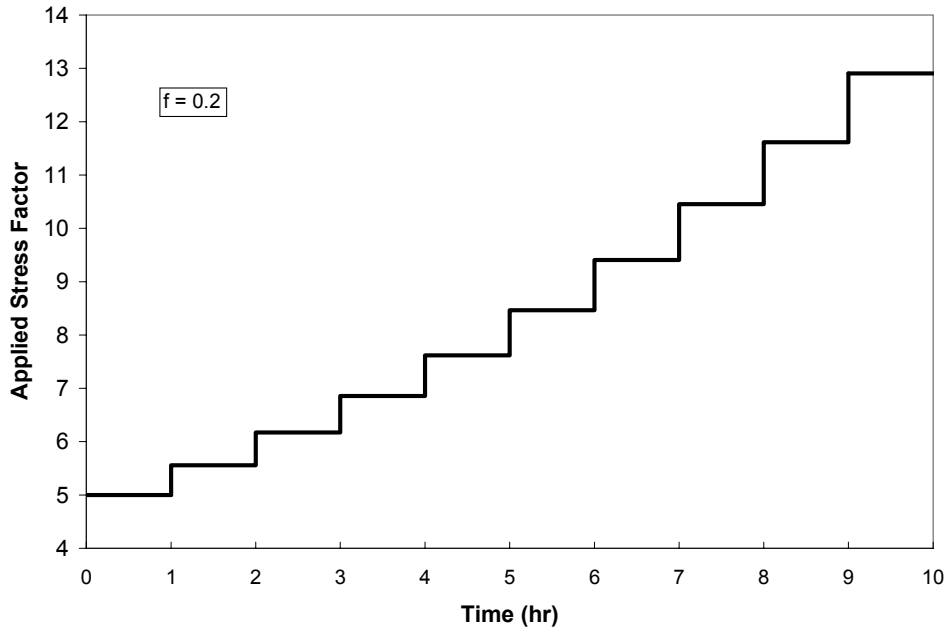
Figure 71: Applied Stress Factor versus Time

The stress in the stress transfer region will also change with respect to time if fibers fail

because it is also a function of $\sigma_{f,c}$. This stress is also a function of the interfacial shear stress, τ.

Therefore, the stress profile in the stress transfer region will have the same dependence on time

and environment as τ.

Time and Environmental Effects on Fiber Strength

The regional strengths, Equations 35 and 37, of a fiber can also be functions of time and

the environment. Strength degradation occurs because of creep and embrittlement. The regional

strength, Equations 35 and 37, can be broken up into terms that can be analyzed to understand

the time and environmental dependence as shown in Figure 72.

$$S_u = \left[\frac{m(m+2)E_f\left(1+\dfrac{E_f f}{E_m(1-f)}\right)\left(-\ln(1-Rnd_u)\right)}{(m+1)\sigma_{f,c}^2}\right]^{\frac{1}{m}}\left\{\frac{\tau_T}{\tau_{ult}}\right\}^{\frac{1}{m}}\left\{\frac{\sigma_{otT}}{2800}\right\}\left\{\frac{m+2}{m+1}\frac{\sigma_{ult}}{f_{init}}\right\}^{\frac{m+1}{m}}$$

$$S_\delta = \left[\frac{m(m+2)}{2}\left(-\ln(1-Rnd_\delta)\right)\right]^{\frac{1}{m+1}}\left\{\frac{\tau_T}{\tau_{ult}}\right\}^{\frac{1}{m+1}}\left\{\frac{\sigma_{otT}}{2800}\right\}^{\frac{m}{m+1}}\left\{\frac{m+2}{m+1}\frac{\sigma_{ult}}{f_{init}}\right\}$$

Random Terms

Interfacial Shear Stress Terms

Reference Stress Terms

Ultimate Strength Terms
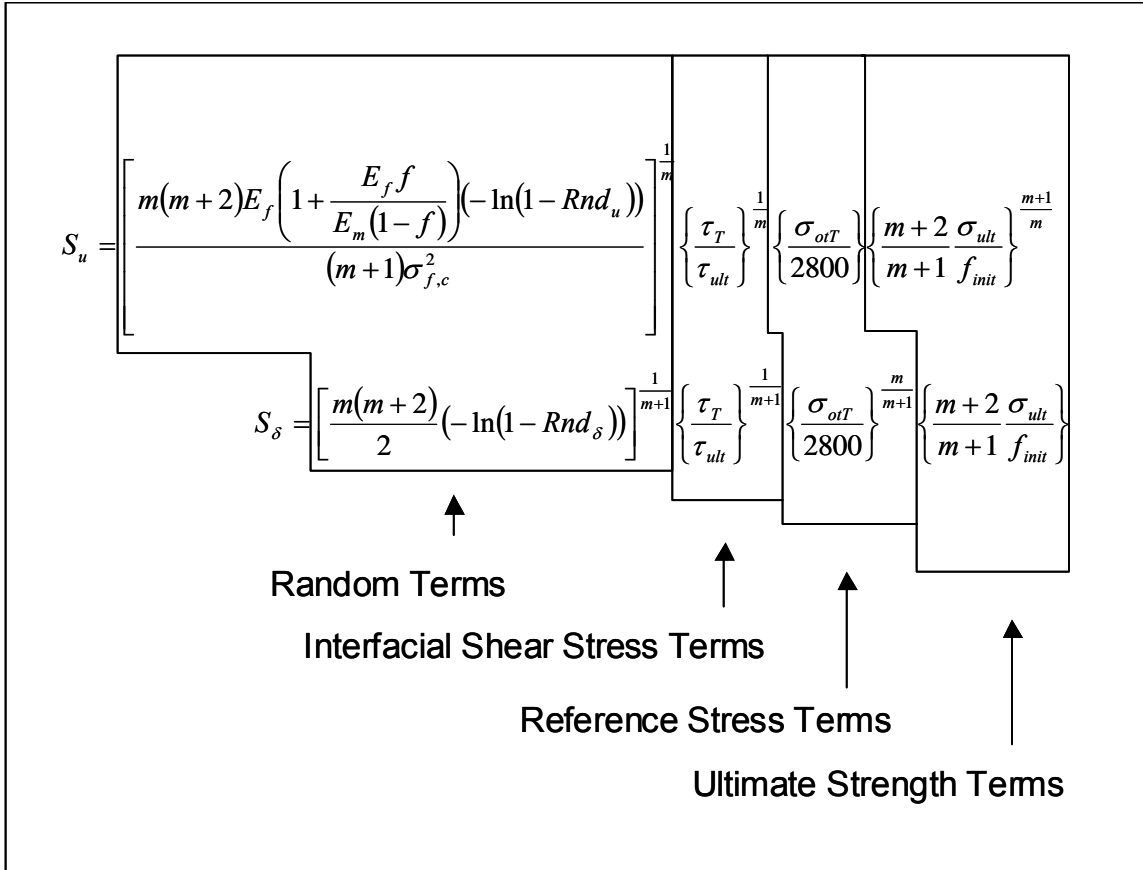
Figure 72: Terms Within the Strength Equations

The Weibull parameter, m, appears in almost all of the terms of Equations 35 and 37 either as a coefficient, an exponent, or both. This variable is a fitting parameter that defines the variability of the strengths among different fibers throughout the cross section. It is assumed to be time independent, but could also have environment dependence. Both regional strengths would be affected by any m dependence on temperature, whereas, only the crack opening regional strength would be affected by the dependence of m on moisture content.

The term in square brackets in Equation 35 is indirectly a function of time if fibers fail at different times. As fibers fail, CAP decreases, causing the volume fraction to decrease according to Equation 39 and the stress on the fiber, $\sigma_{f,c}$, to increase according to Equation 18. All other variables in this term are time independent. The term in square brackets in Equation 37 is time independent.

Furthermore, the terms in square brackets of both Equations 35 and 37 have a random number, which produces the variability in strengths across the cross section of the crack as well as between the regions. Most fiber strengths are determined by the strength of the fiber in the stress transfer region because it is a larger region and will have more defects causing a lower strength. However, some fibers will be stronger in the stress transfer region than in the crack opening region because of this randomness and variability in the equations. There may be a defect in the crack opening region that will cause failure at a lower stress than what is needed for failure in the stress transfer region.

The first terms in braces of both Equations 35 and 37 represent the interfacial shear stress dependence of fiber strength (see Figure 72). Both equations have the same term with slightly different exponents. The term τ_{ult}, which is time independent, corresponds to the τ of the specimen used in the ultimate tensile test. However, τ_{ult} could be environment dependent. The term τ_T corresponds to the interfacial shear stress of the specimen for the test environment and conditions to be modeled. This could be both time and environment dependent.

If modeling a specimen at room temperature and the room temperature ultimate strength is used, the terms reduce to 1. Similarly, if modeling a specimen in a particular environment and the ultimate strength for that environment is known and used, this term again reduces to 1. For these cases, knowledge of the dependence of the interfacial shear stress with respect to time and environment is not needed. However, if the room temperature strengths are used to model a specimen in other environments, this term is less than 1 and represents the reduction of strength from the room temperature ultimate strength because of the environment. Here, the knowledge of dependence of the interfacial shear stress with respect to time and environment is needed.

The second terms in braces in Equations 35 and 37 are the reference stress terms (see Figure 72). Since fiber strength in a composite with through-the-thickness cracks is assumed to degrade similar to as-produced fibers [10], the fiber strength found by Yun and DiCarlo [27,28] can be used as the reference stress. This reference stress is a function of both time and temperature. Figure 73 is a plot of the Syl-iBN/BN/SiC fiber data collected by Yun and DiCarlo.

116

The following derivation uses the formulation of Morscher and Cawley [17] but incorporates the test temperature and material data used in this research.
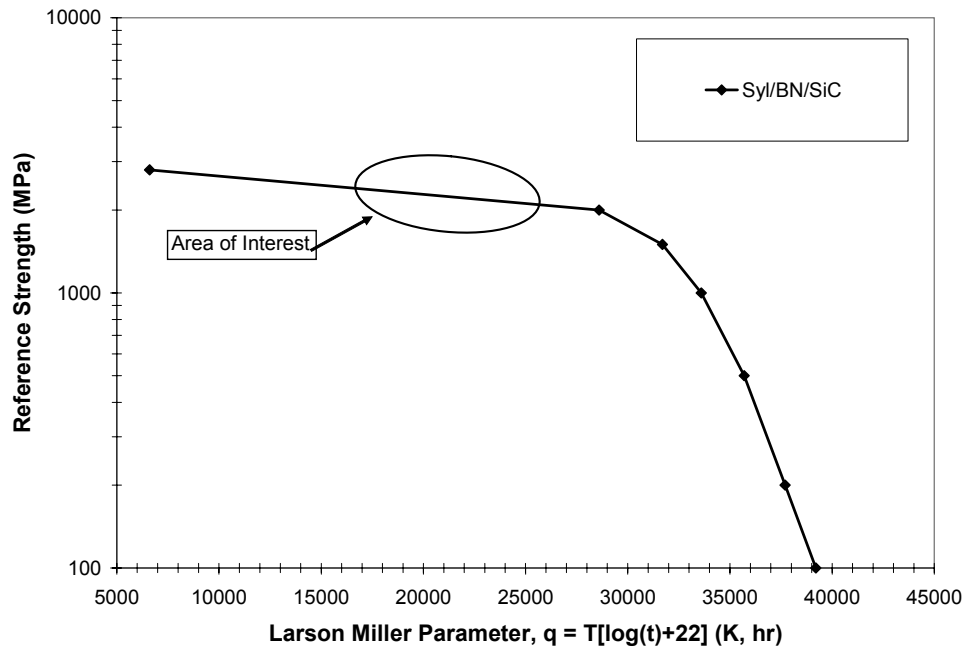
Figure 73: Larson-Miller Plot for Syl-iBN/BN/SiC Fibers [28]

The steps are as follows:

Use the following (σ_{otT}, q) data points from Figure 73:

<div align="right">**40**</div>

$$(\ 2800 \ , \ 6600 \ )$$
$$(\ 2000 \ , \ 28600 \ )$$

The equation of the straight line on this semi-log plot is:

$$\log(\sigma_{otT}) = sq + b \qquad \textbf{41}$$

Solve for the slope, s, of the line in Figure 73 using the two points in Equation 40:

$$s = \frac{\log(2800) - \log(2000)}{6600 - 28600} \qquad \textbf{42}$$

$$s = -0.0000066421 \qquad \textbf{43}$$

117

Use Equation 41, and solve for the y-intercept of the line, b:

$$\log(2800) = -0.0000066421(6600) + b$$
$$\log(2000) = -0.0000066421(28600) + b$$

44

$$b = 3.49099644$$

45

Substitute s and b and solve Equation 41 for σ_{otT}:

$$\sigma_{otT} = 10^{-0.0000066421q + 3.49099644}$$

46

The plot in Figure 74 shows equivalence of Equation 46 and its counterpart based on the data from Yun and DiCarlo [27] for the area of interest in this research. Therefore, the reference stress in terms of time and temperature is:

$$\sigma_{otT} = 10^{-0.0000066421T[\log(t)+22]+3.49099644}$$

47
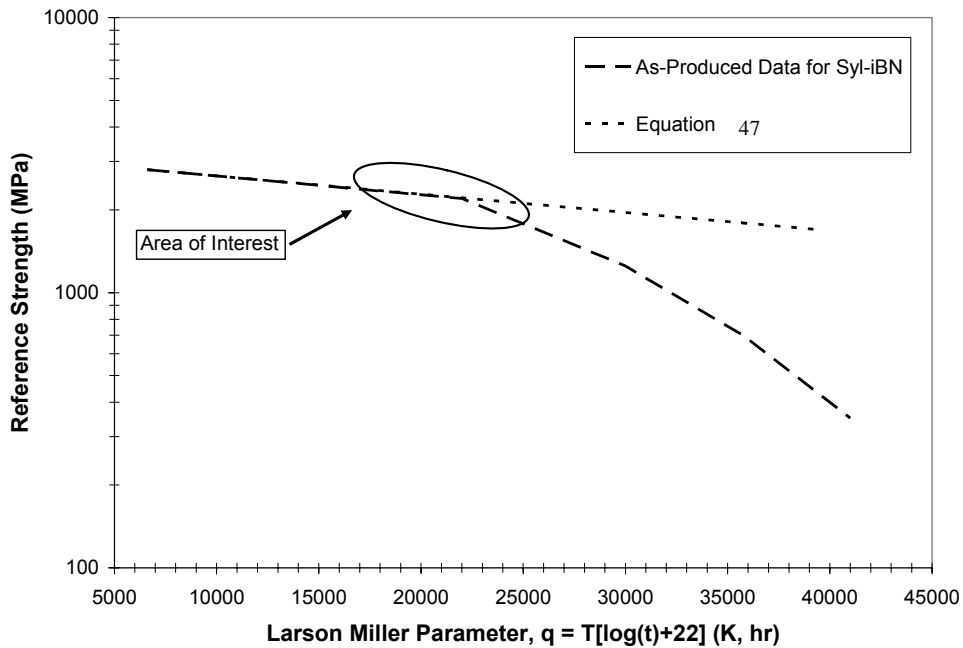
Figure 74: Reference Stress Larson-Miller Plot

Figure 75 has 5 curves generated by using temperatures of 550, 650, 700, 750, and 850°C in Equation 47. The equations for these curves have coefficients and exponents that are temperature dependent and are of the form:

$$\sigma_{otT} = C_{ref} t^{E_{ref}}$$ **48**

$$C_{ref} = C_{refa} T + C_{refb}$$ **49**

$$E_{ref} = E_{refa} T + E_{refb}$$ **50**

where

$C_{ref} \equiv$ coefficient of reference strength
$E_{ref} \equiv$ exponent of reference strength
$C_{refa} \equiv$ linear term for coefficient of reference strength
$C_{refb} \equiv$ constant term for coefficient of reference strength
$E_{refa} \equiv$ linear term for exponent of reference strength
$E_{refb} \equiv$ constant term for exponent of reference strength
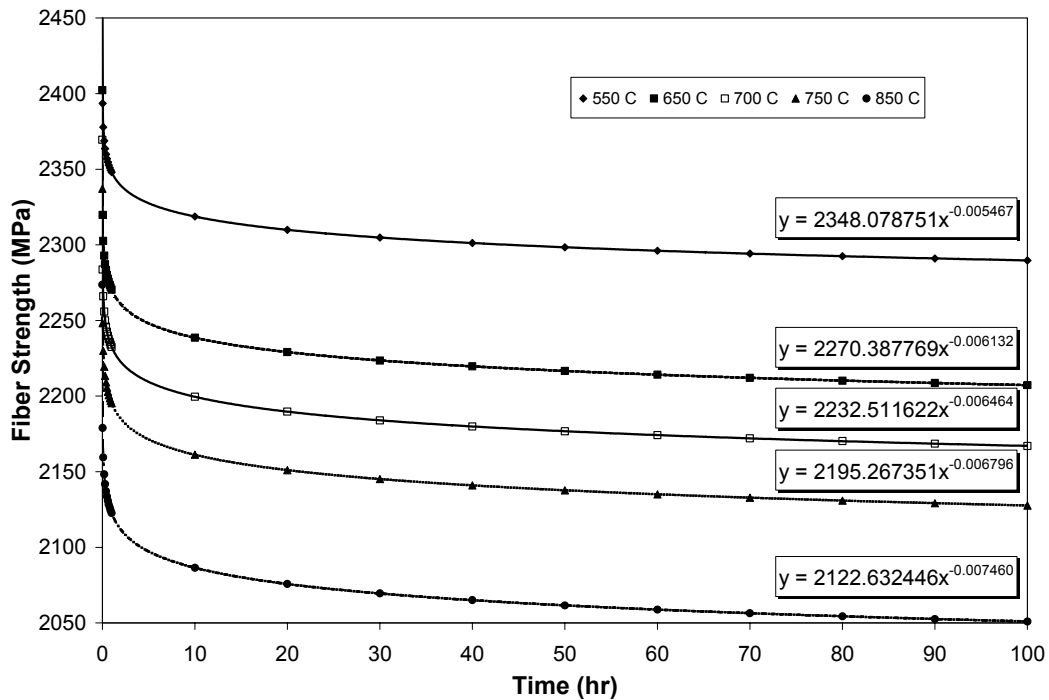
Figure 75: Reference Stress versus Time at Different Temperatures

The curves in Figure 76 show the relationship between the coefficients of the power law and temperature. It also has the equation of the line that fits these coefficients. Figure 77 has a similar plot and equation for the exponents of the power law relationships.
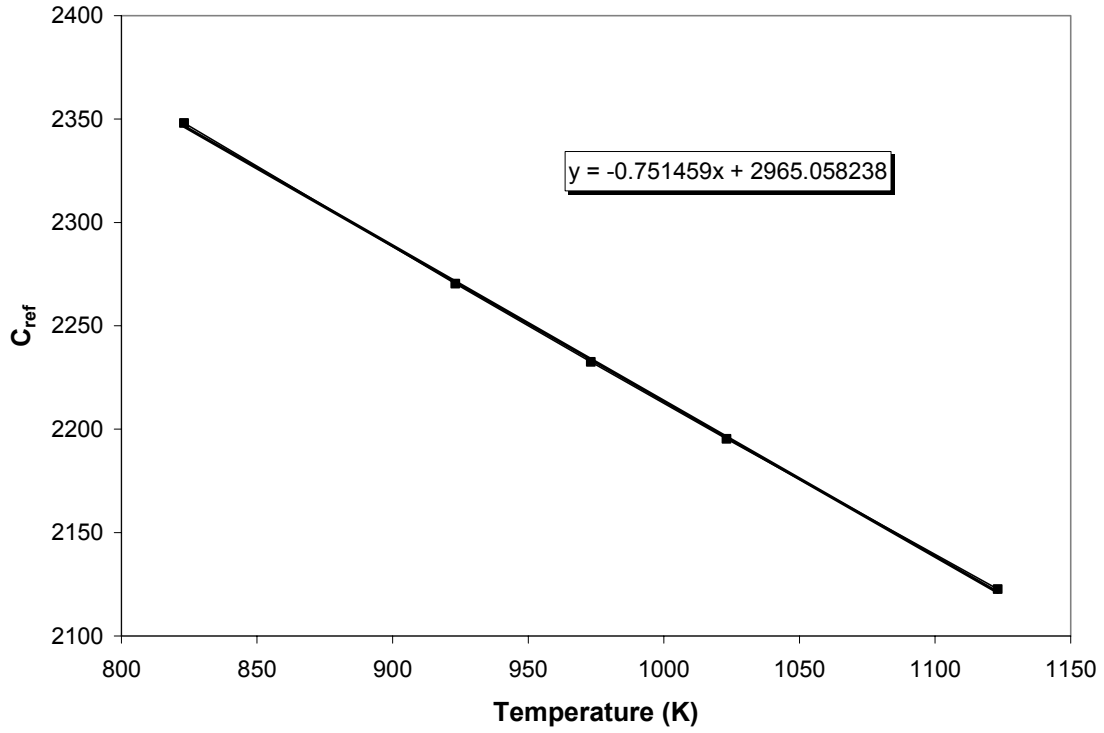
Figure 76: Coefficient of Reference Strength as a Function of Temperature
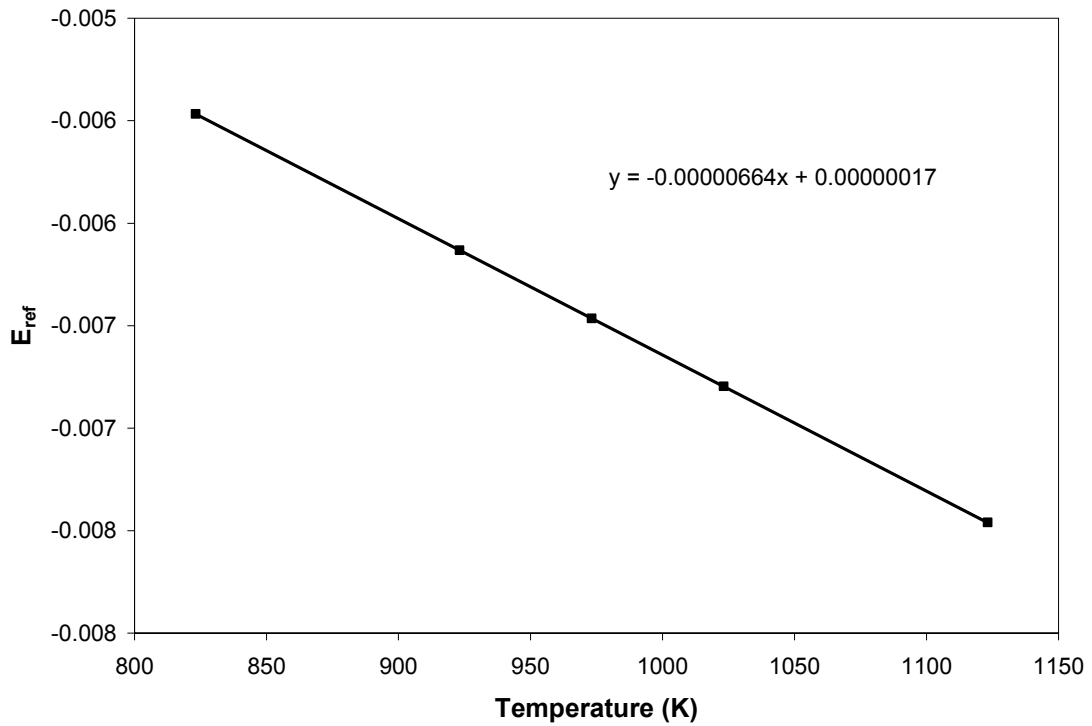
Figure 77: Exponent of Reference Strength as a Function of Temperature

Therefore, the power law relationship for σ_{otT} is:

$$\sigma_{otT} = C_{ref} t^{E_{ref}}$$
51

$$C_{ref} = -0.751459T + 2965.058238$$
52

$$E_{ref} = -0.00000664T + 0.00000017$$
53

Equation 51 is within ±0.07% of Equation 47 over the temperature range 550-750°C in the time range 0.0001-100 hr; however, it is more computationally friendly for modeling purposes.

The third terms in braces in Equations 35 and 37 are the ultimate tensile strength term (see Figure 72). This term corresponds to the ultimate tensile strength of a specimen tested at room temperature or in a particular environment. Either data point can be used as long as the appropriate interfacial shear stress, τ_T, which was discussed earlier, is used. This term is time independent and environment dependent. The ultimate strength decreases with an increase in temperature as shown by the experiments in Chapter IV.

The Effect of Embrittlement and Matrix Cracking on Fiber Strength

The regional strengths in Equations 35 and 37 do not have terms that can capture the effects of embrittlement of matrix cracking. The microscopy in this research showed the embrittlement occurred much faster and occurred simultaneously across the crack plane. Therefore, the embrittlement was assumed to occur across each tow simultaneously. Since there was no way to measure an amount of embrittled area as suggested by Morscher and Cawley [17] (i.e. measure a front between the embrittled area and the pristine area as a function of time), the embrittlement was assumed to be linear across each tow over the total embrittlement time. The embrittled fibers in a tow were linked together through computer code such that when one failed they all failed. This captures the failure mechanism associated with embrittlement.

The single matrix crack case is the simplest case to model since there are no other cracks that can affect each other and there is only one crack where the failure could occur. It

requires only one initialization of fiber strengths. Once catastrophic failure occurs, the

computation is done for that stress level. The same initial strengths are used for every stress level

for consistency. In this case there are no other cracks that could affect each other because of

overlapping stress transfer lengths. It is also the computationally fastest model since there is only

one crack to check for catastrophic failure.

The derivation for the regional strengths for a single matrix crack is identical to that for

the multiple crack scenario presented earlier up to before the strength reduction factor is applied.

The strength reduction factor is different for the single crack scenario because Curtin [22] derived

a different ultimate tensile strength for the single crack case. The derivation for the strength

reduction factor for the single crack case is given next.

Curtin et at [21] found the ultimate strength of a CMC with one matrix crack to be:

$$\sigma_{ult} = f\sigma_c e^{\frac{1}{m+1}} \qquad\qquad \textbf{54}$$

$$\sigma_c = \left(\sigma_o^m \cdot \tau \cdot \frac{L_o}{R} \right)^{\frac{1}{(m+1)}} \qquad\qquad \textbf{55}$$

Substitute Equation 55 into Equation 54 and solve for σ_o for a composite fiber:

$$\sigma_{o\,composite} = \left[\frac{R}{L_o e \tau} \left(\frac{\sigma_{ult}}{f_{init}} \right)^{m+1} \right]^{\frac{1}{m}} \qquad\qquad \textbf{56}$$

Yun and DiCarlo [27,28] found that the σ_o for the as-produced SiC fibers used in this research is

2800 MPa. Therefore the strength reduction factor becomes:

$$SR = \frac{\left[\frac{R}{L_o e \tau} \left(\frac{\sigma_{ult}}{f_{init}} \right)^{m+1} \right]^{\frac{1}{m}}}{2800} \qquad\qquad \textbf{57}$$

For the crack opening region strength, multiply Equation 29 by Equation 57 and substitute

Equation 16:

$$S_u = \frac{\left[\frac{R}{L_o e \tau_{ult}}\left(\frac{\sigma_{ult}}{f_{init}}\right)^{m+1}\right]^{\frac{1}{m}}}{2800}\sigma_{otT}\left[\frac{L_o 2\tau_T E_f\left(1+\frac{E_f f}{E_m(1-f)}\right)}{\sigma_{f,c}^2 R}\left(-\ln(1-Rnd_u)\right)\right]^{\frac{1}{m}} \qquad \textbf{58}$$

$$S_u = \left[\frac{2E_f\left(1+\frac{E_f f}{E_m(1-f)}\right)}{e\sigma_{f,c}^2}\left(-\ln(1-Rnd_u)\right)\right]^{\frac{1}{m}}\left\{\frac{\tau_T}{\tau_{ult}}\right\}^{\frac{1}{m}}\left\{\frac{\sigma_{otT}}{2800}\right\}\left\{\frac{\sigma_{ult}}{f_{init}}\right\}^{\frac{m+1}{m}} \qquad \textbf{59}$$

For the stress transfer length regional strength, multiply Equation 33 by Equation 57:

$$S_\delta = \left[\left[\frac{\frac{R}{L_o e \tau_{ult}}\left(\frac{\sigma_{ult}}{f_{init}}\right)^{m+1}}{2800^m}\right]\sigma_{otT}^m \tau_T \frac{L_o}{R}(m+1)\left(-\ln(1-Rnd_\delta)\right)\right]^{\frac{1}{m+1}} \qquad \textbf{60}$$

$$S_\delta = \left[\frac{(m+1)}{e}\left(-\ln(1-Rnd_\delta)\right)\right]^{\frac{1}{m+1}}\left\{\frac{\tau_T}{\tau_{ult}}\right\}^{\frac{1}{m+1}}\left\{\frac{\sigma_{otT}}{2800}\right\}^{\frac{m}{m+1}}\left\{\frac{\sigma_{ult}}{f_{init}}\right\} \qquad \textbf{61}$$

For the multiple cracks with no stress transfer length overlap things are different. Here the cracks do not affect each other but there are multiple cracks where the catastrophic failure could occur. Morscher [10] found in his modeling effort that the crack that caused the first embrittled fiber failure was not necessarily the one that would cause ultimate failure of the composite. This assumption is also valid here. Since each crack has its own initialization, each will have a different distribution of strengths across the crack plane. Therefore, a crack may have an embrittled fiber fail early enough in the test such that the failure of the neighboring embrittled fibers does not result in catastrophic failure near that crack. A different crack could have its first failure later in the test where the embrittlement results in enough fiber failures to cause the failure of the composite. The multi-crack case is essentially running the single crack case multiple times.

This phenomenon is directly related to the total embrittlement time (i.e. the time it takes for all fibers to be strongly bonded to the neighboring fibers). The longer it takes for all the fibers surrounding a crack to embrittle the more likely this could happen. With a long total embrittlement time, or low embrittlement rate, there will be fewer fibers that will fail because they are embrittled early in the test. As time progresses and more fibers in a tow are embrittled, the number of embrittled failure increases when a fiber fails. When the larger numbers of fibers are removed and the stress increases dramatically, more individual fibers will fail in other tows, which in turn results in their neighboring embrittled fibers to fail. This cascades throughout the specimen resulting in the catastrophic failure.

Multiple matrix cracks with stress transfer overlap is the most complicated case because the cracks affect each other and there are multiple locations where the catastrophic failure could occur. The present formulation does not consider this situation.

The matrix crack saturation case is fairly easy to model because the fibers experience the same stress along the entire length of the fiber. Here, the specimen is damaged in such a way that only the fibers are supporting the load. The stress transfer regions overlap such that no stress is transferred to the matrix. The only difficult part in modeling this case is relating a fiber failure due to one crack to all the other cracks. Ideally, a fiber failure due to any crack will fail the fiber at all locations of other cracks since no load is shed between the matrix and the fiber in this case. This would lead to very large fiber pullout length. The monotonic tests were most likely to result in matrix crack saturation and the modeling effort was not designed to analyze the monotonic loading conditions. Therefore, matrix crack saturation was not considered in this research.

Computer Model

To use the equations formulated previously, a computer model was written in FORTRAN 90/95 programming language using Compaq Visual Fortran (Version 6.6). The algorithm incorporated the multiple matrix crack case where there is no overlap of the stress transfer regions. This section covers the computer portion of the modeling effort. This section includes the basic framework that the computer code follows. It explains the idealized specimen that was

created to use with the modeling equations. The model validation is discussed and the results are presented.

The basic framework of the computer model is as follows:

- Calculate the applied stress, $\sigma_{f,c}$, using Equation 18.

- Calculate the initial fiber strengths, S_u and S_δ, using Equation 35 and 37.

- Sort fibers by strength and check for fiber failures starting with the weakest fiber. Update the applied stress and volume fraction of load bearing fibers, $\sigma_{f,c}$ and f, (Equations 18 and 39) after each failure. Continue until the weakest fiber survives or the specimen fails.

- If specimen survives, increment one time step.

- Embrittle appropriate number of fibers across crack plane.

- Degrade strength by calculating individual strength, S_u and S_δ, using Equation 35 and 37.

- Sort fibers by strength and check for fiber failures starting with the weakest fiber. If the fiber fails and is embrittled, fail all embrittled fibers in the tow. Update the applied stress (Equations 18 and 39) after each failure. Continue until weakest fiber survives or the specimen fails.

- Repeat Step 4-7 until specimen failure.

Figure 78 is a flow chart of the computer code that includes the basic framework presented above.
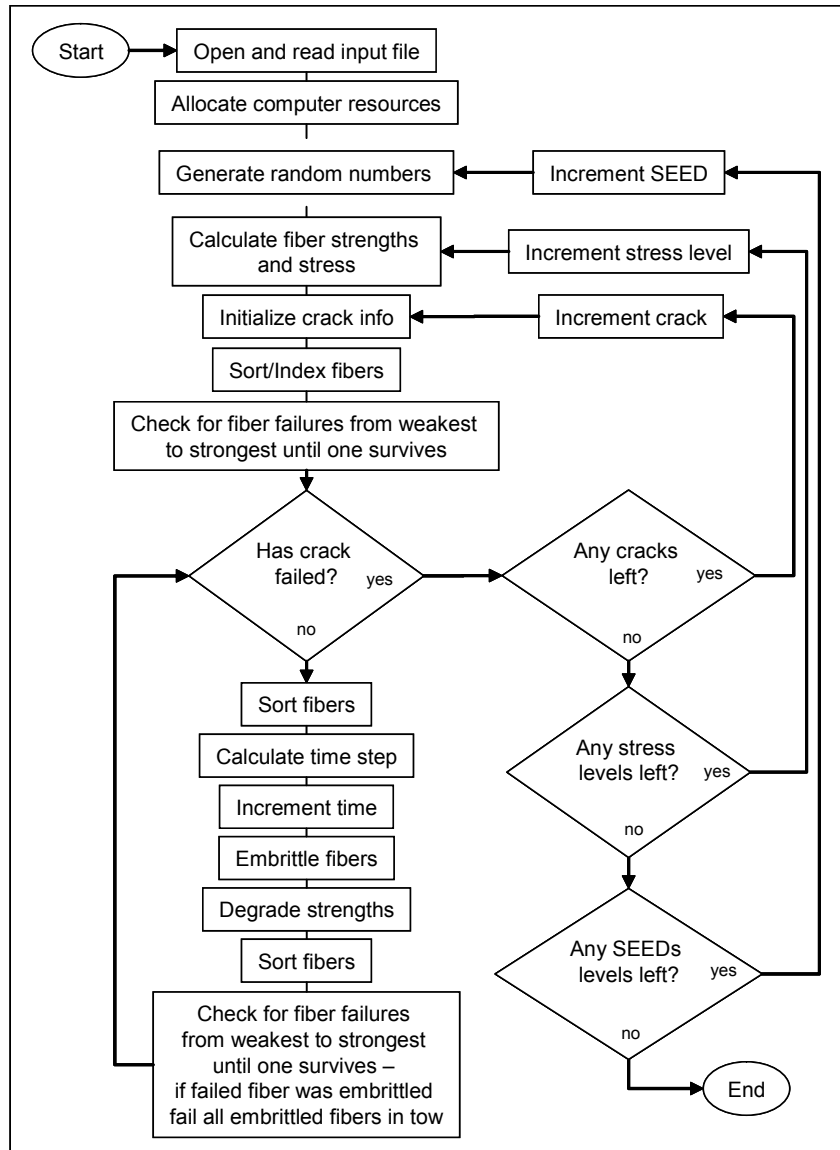
Figure 78: Flow Chart of Computer Logic

The modeling effort in this research looked at individual fibers and how the environment and the applied stress caused them to fail and how these individual failures contributed to the overall specimen failure. To do this, an idealized geometry of the constituents and cross-section of the specimen was created. The specimen was idealized as a unidirectional composite where the zero degree tow/fiber properties were combined with the matrix interphase properties. Therefore, the modulus of elasticity for the matrix in the model is really the modulii of elasticity for the matrix material, the cross tows fibers/tows, and the interphase. The manufacturer provided the preform dimensions and volume fractions that allowed the number of fibers to be calculated.

126

A unit cell was created that consisted of one fiber, with a radius of 0.005 mm, and the appropriate amount of matrix material to maintain the volume fraction in the loading direction of 0.1855. For these conditions, the unit cell dimension is 0.020577 mm. Figure 79 is a microscopic image of fibers and how it compares to the unit cell of the model. The figure has an example, the image on the left, of what a tow looks like and where the fibers are typically located in relation to one another. The center image is magnified for clarity. The dimension of the fiber in the center photo is the same as the dimension of the fiber in the unit cell shown in the image on the right. With the unit cell dimension and the overall dimensions of the specimen cross-section, the number of fibers in the x and y direction in the plane of the cross-section were calculated to be 104 and 512, respectively. Here, x is the thickness direction and y is the width direction. Therefore, 53248 total fibers were in the load bearing direction across specimen cross-section of 21.136 mm^2.

These fibers were not given any specific locations in the crack plane but were assigned to specific tows. Although a unit cell has the correct volume fraction associated with it, the fiber is still assumed to be adjacent to other fibers. When a unit cell becomes embrittled, its fiber is still connected to its nearest neighbors, as shown in the left and center images of Figure 79. The unit cell dimensions were only used for determining the number of fibers in the cross-section, the number of fibers in a tow, and the dimensions of the tow.
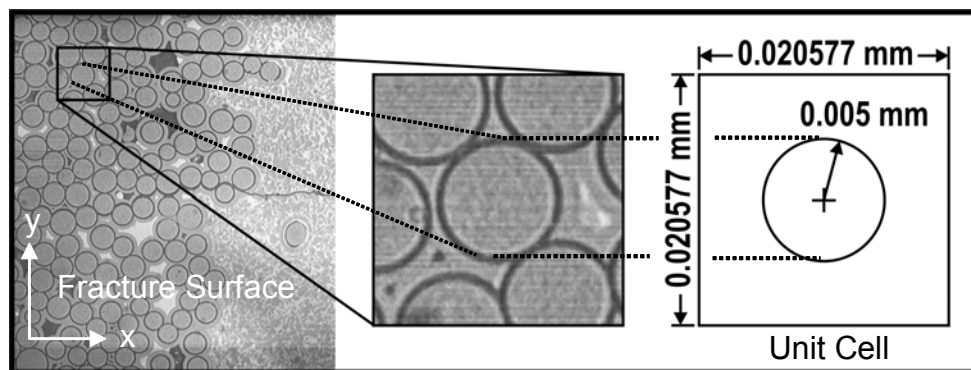
Figure 79: Unit Cell

Each tow was manufactured with 800 fibers per tow. A portion of the cross-section of a typical specimen can be seen in Figure 80. This image shows that some tows merged together

during the manufacturing process. Also from the image you can see that no matter where the specimen is cut some of the tows will have fiber removed from the cross-section. Based on the manufacturing process there were 8 plys along the specimen thickness and based on observations, approximately 7-9 tows through the specimen width depending on where the cut was made.

Earlier, 104 fibers in the thickness direction were calculated. This leads to an individual tow having 13 fibers in the thickness direction. Also earlier, 512 fibers in the width direction were calculated. With 7, 8, and 9 tows (based on observations) this would lead to 57, 64, and 73 fibers in the width direction, respectively, and to 741, 832, and 949 fibers per tow, respectively. The most realistic idealized tow is 832 fibers. Therefore it is assumed there are 8 tows in the width direction. An individual tow can be seen in the center image of Figure 80 and the idealized tow can be seen in the right image. The tiny squares in the right image of the figure are unit cells from Figure 79.
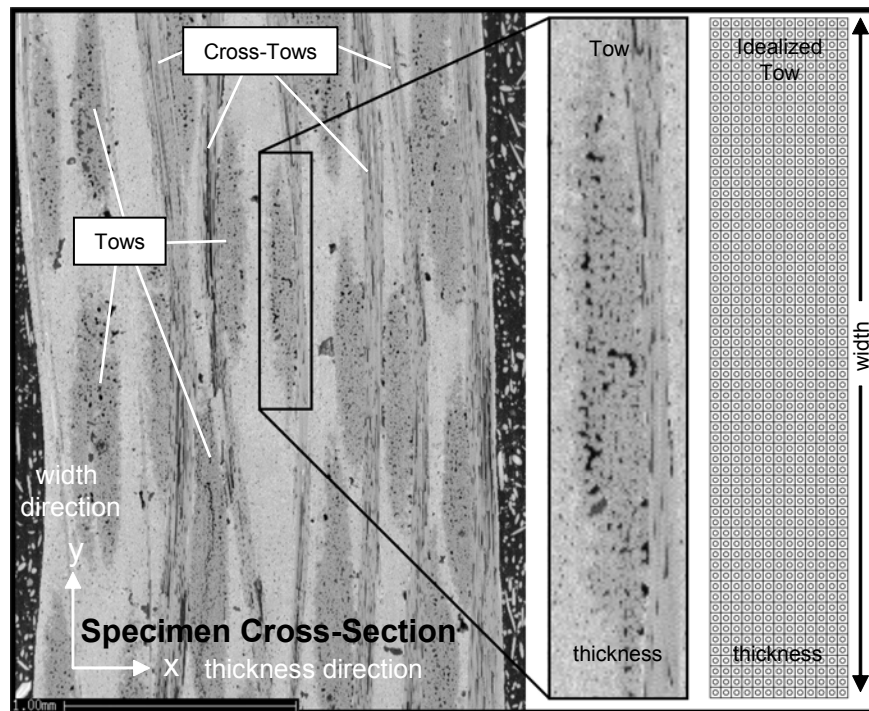
Figure 80: Idealization of the Tows across the Specimen Cross-Section

Since there are 8 tows in both the thickness and the width direction, the specimen has 64 tows as the total number of tows in the cross-section. Figure 81 has graphical representation of

128

how the specimen (shown in the left of the figure) became idealized for the model (shown in the right of the figure). The tows in the loading direction (i.e. load applied perpendicular to the plane of the page) are represented as ovals in the real cross-section and as rectangles in the idealized cross-section. The cross tows are represented as lines in the real cross-section. Since the cross tows have been combined with the matrix and interphase in the idealized cross-section they are not represented in the idealized cross-section. The rectangles in Figure 81 are the same rectangles in Figure 80.
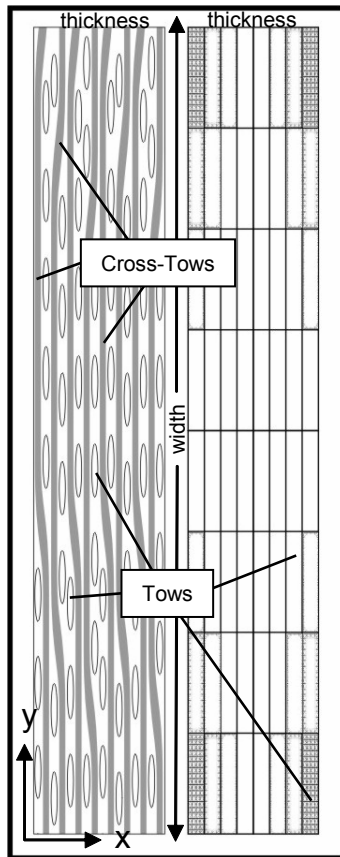
Figure 81: Idealization of the Specimen Cross-Section

Table 7 is a summary of all the dimensions of the idealized specimen. Using these values keeps the volume fraction of fibers in the loading direction, number of tows in x and y direction, and specimen width and thickness consistent with reality.

Table 7: Model Parameters

Variable		Value Used in Model	Estimated Value in actual Specimen Cross-Section
Number of Fibers in x-direction	NFx	104	N/A
Number of Fibers in y-direction	NFy	512	N/A
Total Number of Fibers	NF	53248	51200
Number of Tows in x-direction	NTx	8	8
Number of Tows in y-direction	NTy	8	7-9
Total Number of Tows	NT	64	64
Fibers per Tow in x-direction	NFPTx	13	N/A
Fibers per Tow in y-direction	NFPTy	64	N/A
Number of Fibers per Tow	NFPT	832	800

Once the computer code was developed it was validated. Micro-models were built in order to follow the calculations step by step through the model run. Micro-models are simply smaller specimens with smaller numbers of fibers, tows, fibers per tow, width, and thickness. The smaller micro-models made it possible to follow every calculation and compare it to hand calculations. The micro-models were not used in a convergence analysis. They were only used to verify the code was performing as intended. Once the code was verified to work as intended, the real dimensions were used in the analysis.

The code must define the individual fibers and tows and how they are related to each other. The individual fiber regional strengths must be calculated and degraded according to the time-based equations above. The specimen fibers must be embrittled with time and the appropriate fibers must fail according to the failure criteria used.

Six micro-models were designed to maintain the correct volume fraction in the loading direction. Table 8 is a list of the dimensions used for each micro-model configuration and the configuration used to represent the actual experimental specimen.

Table 8: Micro-Model Configurations

	MM 1	MM 2	MM 3	MM 4	MM 5	MM 6	Real
Thickness (mm)	0.0823	0.1235	0.1235	0.2469	0.2469	0.6585	2.1400
Width (mm)	0.1235	0.1646	0.2469	0.4938	0.9877	0.9877	10.5352
NFx	4	6	6	12	12	32	104
NFy	6	8	12	24	48	48	512
NF	24	48	72	288	576	1536	53248
NTx	2	2	2	3	3	8	8
NTy	2	2	3	4	8	8	8
NT	4	4	6	12	24	64	64
NFPTx	2	3	3	4	4	4	13
NFPTy	3	4	4	6	6	6	64
NFPT	6	12	12	24	24	24	832

The first micro-model has a small number of fibers, fibers per tow, and tows. This allowed each fiber to be monitored as the code executed line by line. This was done to verify the equations were implemented correctly. Each micro-model grows in specimen size, number of tows and fibers per tow, each maintaining the appropriate volume fraction. This allowed the code to be thoroughly investigated to see if the changes in dimensions affected the results or caused any instability in the code. The code functioned properly for all micro-models.

For validation purposes experimental values were used as variables if they were known either through experimentation done here or from previous work. Variables that were not known were estimated. Here, the code was being validated to work properly so correct variables were not necessary. As long as reasonable values were used and they were used in both the hand calculations and the code calculations, the validation could be accomplished. For example, Total Embrittlement Time was specifically chosen to embrittle two fibers per time step to validate the embrittlement and strength reduction processes. Using this type of embrittlement step allowed the code to quickly embrittle the entire specimen so that the validation comparison of hand calculations and code calculations could be done efficiently and effectively.

Comparing computer results step by step to hand calculations at specific times, the code was validated to verify that it worked properly through all six micro-models. The fiber strengths reduced according to Equation 35 and 37 above. The embrittlement process occurred throughout the entire specimen simultaneously. When a pristine fiber failed in stress transfer length, the fiber

retained a percentage of its load carrying capacity, and if it failed in the crack opening, it retained

no load carrying capacity. When an embrittled fiber failed, the embrittled sibling fibers in that tow

also failed and none of them retained any of their load carrying capacity.

Model Behavior

The model presented above has several variables that were needed or had to be

determined. These variables were determined using known material properties, manufacturing

specifications, experimental results presented in Chapter IV, or results presented in previous

work. E_c and E_f are material properties for the Syl-iBN/BN/SiC CMC (Tabl2). C_{refa}, C_{refb}, E_{refa},

E_{refb}, σ_{refo}, and σ_{refEo} were calculated from the data obtained by Yun and DiCarlo [27,28] and

presented in Equations 48 through 50. The initial volume fraction in the loading direction, f_{init}, was

calculated from the manufacture's reported material volume fraction. The manufacturer also

reported the fiber radius. σ_{ult} was determined using experimental work done here, while τ_T and

τ_{ult} were estimated using work by Morscher [10]. This initial analysis looked at how changes in m,

NC_o, or total embrittlement time (TET) affected the stress rupture curve. Table 9 is a list of values

used for these variables.

Table 9: Variable Values Used in Model Initially

E_c = 220 GPa	NF = 53248
E_f = 373 GPa	NFx = 104
σ_{ult} = 405 MPa	NFy = 512
τ_{ult} = 45 MPa	NT = 64
τ_T = 45 MPa	NTx = 8
Temp = 1023.15 K	NTy = 8
f_{init} = 0.1855	NFPT = 832
C_{refa} = -0.751459	NFTx = 13
C_{refb} = 2965.058238	NFTy = 64
E_{refa} = -0.00000664	R = 0.005 mm
E_{refb} = 0.00000017	m = 5-10
σ_{refo} = 2800 MPa	NC_o = 2-30
σ_{refEo} = 2800 MPa	TET = 2-100 hrs

The Weibull parameter, m, is a fitting parameter. The final value was determined after all

the variables were determined. However, an initial understanding of the effects that m would

have on the stress rupture curve was needed before determining the other variables. Therefore,

values were chosen for the other variables in the model and held constant while m was varied. Total embrittlement time of 2 hrs and the number of crack, NC_o, of 10 were used with m varying between 6 and 10. Figure 82 is a plot of the modeling results with variation in m. The plot is the Normalized Failure Stress (i.e. stress rupture failure stress divided by the room temperature ultimate strength) versus Failure Time. The variation has very little effect on the initial portion of the curves and a large effect on the latter portion or bottom part of the curve. The selection of m will be governed more by the flat part of the stress-rupture curve than by the initial portion.
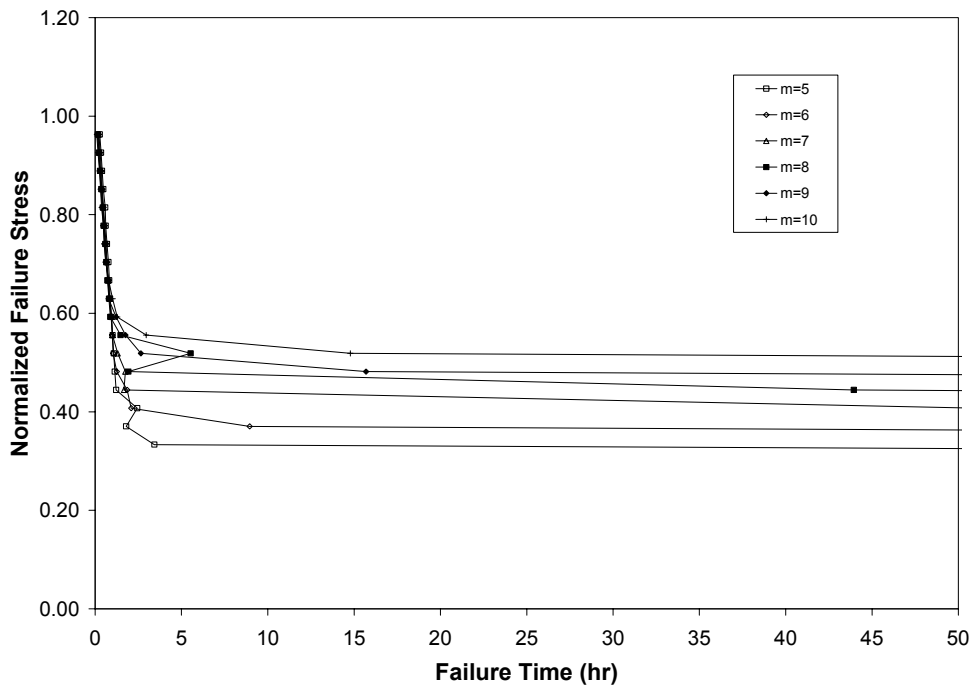
Figure 82: Variation in m

As mentioned earlier, the model was designed to incorporate the multiple crack case where there is no stress transfer length overlap. The code essentially initializes every crack independently and then runs the equations for one crack at a time. The specimen failure time is the shortest crack failure time. This suggests that the number of cracks is important for the model to be successful. However, multiple cracks take an enormous amount of computational time. A specimen with 2 cracks takes approximately 15 minutes to complete. A specimen with 8 cracks takes approximately 2 hours. Observations during the crack density measurement experiments

presented in Chapter IV support as many as 65 cracks for some of the tests depending on the loading conditions.

If the stress rupture curves converge as NC_o increases, using this minimum value for the rest of the parameter sensitivity analysis can save a significant amount of time. Therefore, the initial model analysis looked at the number of cracks equal to 2, 5, 10, 15, 20, and 30 cracks. The goal was to see not only how the stress rupture curve varied with respect to NC_o but also to see what minimum value of NC_o could be used and still maintain accuracy. Table 10 is a list of the variables used in this analysis. Figure 83 is a plot that shows that stress rupture curves converge as NC_o is increased. Based on this, a value of 10 was used for the remainder of the preliminary analysis.

Table 10: Variable Values Used in Model for NC_o Variations

E_c = 220 GPa	NF = 53248
E_f = 373 GPa	NFx = 104
σ_{ult} = 405 MPa	NFy = 512
τ_{ult} = 45 MPa	NT = 64
τ_T = 45 MPa	NTx = 8
Temp = 1023.15 K	NTy = 8
f_{init} = 0.1855	NFPT = 832
C_{refa} = -0.751459	NFTx = 13
C_{refb} = 2965.058238	NFTy = 64
E_{refa} = -0.00000664	R = 0.005 mm
E_{refb} = 0.00000017	m = 6
σ_{refo} = 2800 MPa	NC_o = 2-30
σ_{refEo} = 2800 MPa	TET = 3 hr

Figure 83: Variation in NC$_o$

Modeling Results

Using the experimental results reported in Chapter IV, results reported from previous work, material properties, and panel specifications reported by the manufacturer, the model was used to match the trends in the experimental data. Table 11 is a list of the final values used in the model to achieve these results. Figure 84 is a plot of both the experimental and modeling results for the 550°C environments.

Table 11: Final Variable Values Used in Model for 550°C

E_c = 220 GPa	NF = 53248
E_f = 373 GPa	NFx = 104
τ_{ult} = 45 MPa	NFy = 512
τ_T = 45 MPa	NT = 64
f_{init} = 0.1855	NTx = 8
C_{refa} = -0.751459	NTy = 8
C_{refb} = 2965.058238	NFPT = 832
E_{refa} = -0.00000664	NFTx = 13
E_{refb} = 0.00000017	NFTy = 64
σ_{refo} = 2800 MPa	R = 0.005 mm
σ_{refEo} = 2800 MPa	m = 13
σ_{ult} = 390 MPa	NC$_o$ = 10
Temp = 823.15 K	TET = 25, 100, 300 hr
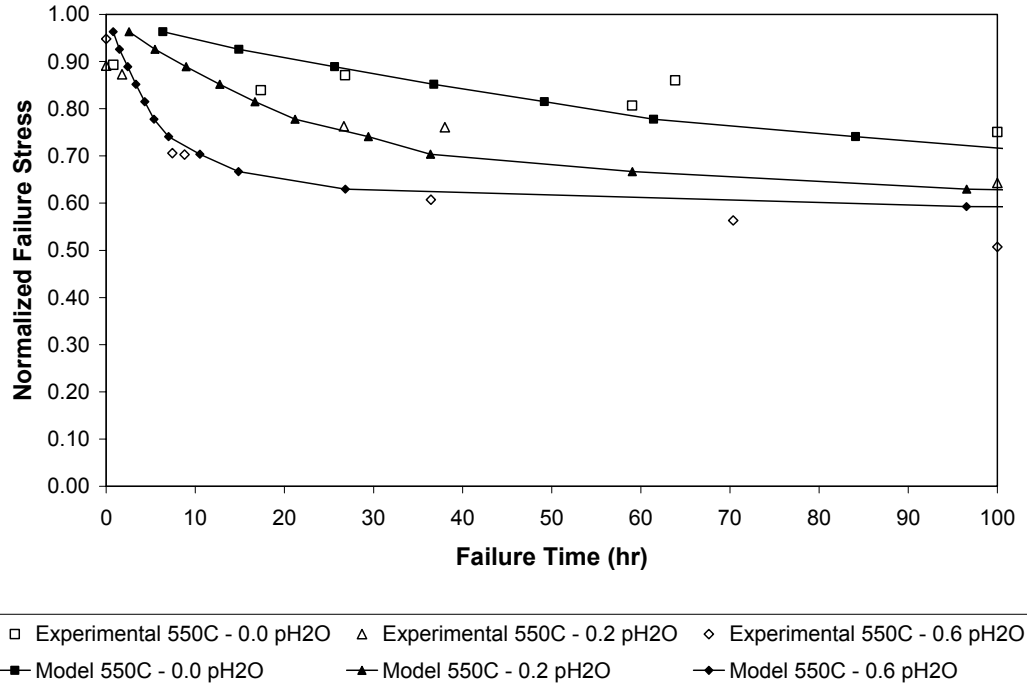
Figure 84: Normalized Experimental and Modeling Results – 550$^{\mathrm{o}}$C

The Weibull parameter, m, is a fitting parameter and was chosen to match the model to the experimental results. The parameter sensitivity analysis presented in the next section explains this. The number of cracks, NC_o, was also chosen based on other results that will be presented in the parameter sensitivity analysis. There are three values for TET. These values represent the time it takes to embrittle all the fibers in a crack and was estimated based on the observations seen in the microscopy analysis in Chapter IV for 0.0, 0.2, and 0.6 atm pH_2O environments.

Looking at all the curves in Figure 84, there is a non-linear shift in the stress rupture curves with respect to pH_2O. At times less than 2 hr, little distinction can be made in the data. As time increases, the curves become distinct and separate. The 550$^{\mathrm{o}}$C with 0.0 atm pH_2O curve approaches a 0.75 normalized stress value at 100 hours and appears to be approaching a normalized stress value of approximately 0.6 some time after the 100-hour test limit. Both the 550$^{\mathrm{o}}$C with 0.2 and 0.6 atm pH_2O normalized stress rupture curves converge to approximately 0.6 of monotonic tensile strength within 100 hours.

136

Figure 85 is a plot of the experimental data and modeling results for the 750°C environments. Table 12 is a list of the final values used in the model to achieve these results. Again there is a non-linear shift in the stress rupture curves with respect to pH$_2$O. The 750°C with 0.0 atm pH$_2$O curve is approaching the 0.5 normalized stress rupture strength, but will not reach it until after 100 hours. The 750°C with 0.2 and 0.6 atm pH$_2$O curves converge very quickly, in less than 20 hr, to 0.5 normalized stress rupture strength. Similar to the 550°C cases, the variations in the curves were the result of changing Total Embrittlement Time. From Figures 84 and 85 the modeling curves show good agreement with the experimental data. Although the model does not capture the scatter of the experimental data, the trends in the data are represented well.

Table 12: Final Variable Values Used in Model for 750°C

E_c = 220 GPa	NF = 53248
E_f = 373 GPa	NFx = 104
τ_{ult} = 45 MPa	NFy = 512
τ_T = 45 MPa	NT = 64
f_{init} = 0.1855	NTx = 8
C_{refa} = -0.751459	NTy = 8
C_{refb} = 2965.058238	NFPT = 832
E_{refa} = -0.00000664	NFTx = 13
E_{refb} = 0.00000017	NFTy = 64
σ_{refo} = 2800 MPa	R = 0.005 mm
σ_{refEo} = 2800 MPa	m = 13
σ_{ult} = 345 MPa	NC$_o$ = 10
Temp = 1023.15 K	TET = 3, 20, 300 hr
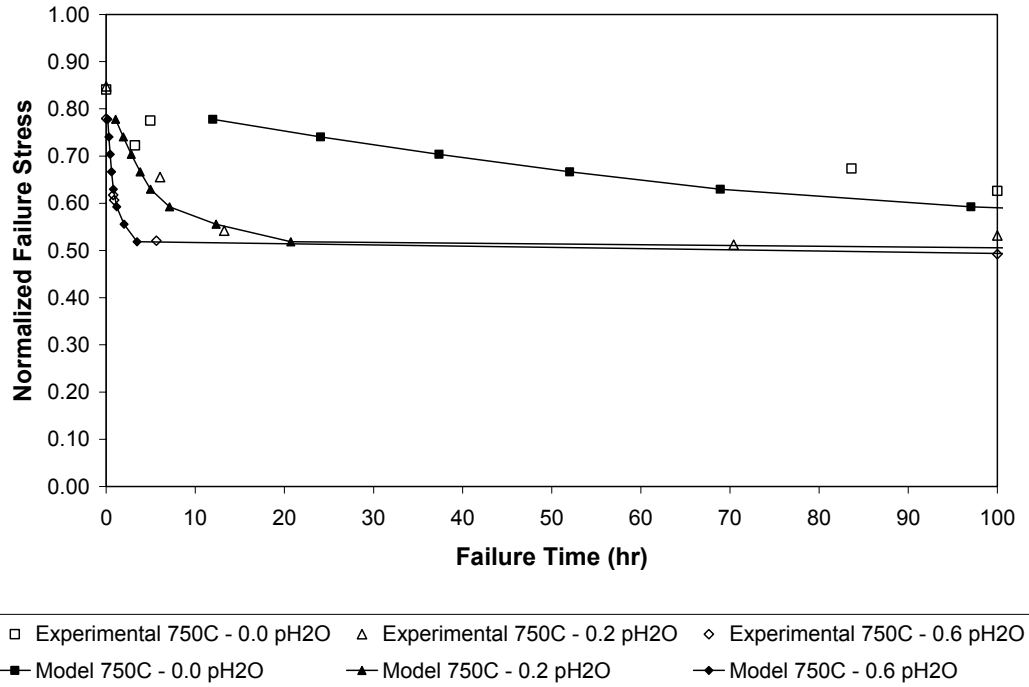
Figure 85: Normalized Experimental and Modeling Results – 750°C

Parameter Sensitivity Analysis

A parameter sensitivity analysis looks at how the different variables in the model affect the failure stress versus failure time plot for the specimen. The 550°C and the 750°C with 0.2 atm pH$_2$O cases were used as the baselines for the parameter sensitivity analysis. Table 13 is a list of the baseline variables used for all the following parameter sensitivity analyses. Parameters were varied by specific amounts to see the sensitivity of the stress rupture curve to variations.

Table 13: Parameter Sensitivity Analysis Baseline Variables

	550°C	750°C
NC_o	10	10
E_c	220 GPa	220 GPa
E_f	373 GPa	373 GPa
m	13	13
σ_{ult}	390 MPa	345 MPa
τ_{ult}	45 MPa	45 MPa
τ_T	45 MPa	45 MPa
C_{refa}	-0.751459	-0.751459
C_{refb}	2965.058238	2965.058238
E_{refa}	-0.00000664	-0.00000664
E_{refb}	0.00000017	0.00000017
σ_{refo}	2800 MPa	2800 MPa
σ_{refEo}	2800 MPa	2800 MPa
f_{init}	0.1855	0.1855
R	0.005 mm	0.005 mm
TET	100 hr	20 hr

Before continuing with the parameter sensitivity analysis, the Monte Carlo-type simulation must be explained. There are two reasons why the model presented here is considered a Monte Carlo-type simulation. The first concerns the equations in the model. The strength equations have random numbers that are generated for each region for every fiber in every crack of the specimen being modeled. Also, every fiber that fails in the stress transfer region has its load carrying capacity randomly reduced to between 0.0 and 1.0 such that the results are uniformly distributed for the entire crack. Looking at individual fibers and their individual performance is similar to the Monte Carlo simulations by Zhou and Curtin [75] and Ibnabdeljalil and Curtin [76] that used lattice Green functions to calculate the stress field and compared that to the individual fibers.

The second reason why the model presented here is considered a Monte Carlo-type simulation concerns the number of model runs performed to generate the final curves. Throughout the parameter sensitivity analysis the curves will be presented with a number in parentheses. That number is the number of model runs that that were averaged to create the final curve. For example, a curve identified as NC_o = 10 (29) means 29 model runs with 10 cracks each were averaged to create the curve in the plot. By averaging several model runs, the amount of scatter was reduced. For every parameter analysis, 32 models were started. Some

model runs did not finish because the failure time for the low stress levels were greater than the maximum computer capacity, or because of a computer zero during logical comparisons. These situations would cause a model run to continue using small time steps after total embrittlement, thus never reaching the failure time in a reasonable amount of computing time. These runs were ended so another batch of models could be started. The percent difference between averaging 20 runs compared to 21 runs resulted in less then 1.5% for all points along the stress rupture curve. Therefore, batches of model runs were continued until at least 20 runs were successfully completed in a reasonable amount of time.

The first parameter of interest is the number of through-the-thickness cracks, NC_o. The initial model analysis with estimated values for some of the variables showed the stress rupture curve converged as the number of cracks increased. Once the variables were determined for this research, the convergence was checked again. Figures 86 and 87 are plots of the results of running the model with the 550°C and 750°C baseline variables given in Table 13 and varying NC_o as 2, 5, 10, 15, 20, and 30. Both plots show similar results.
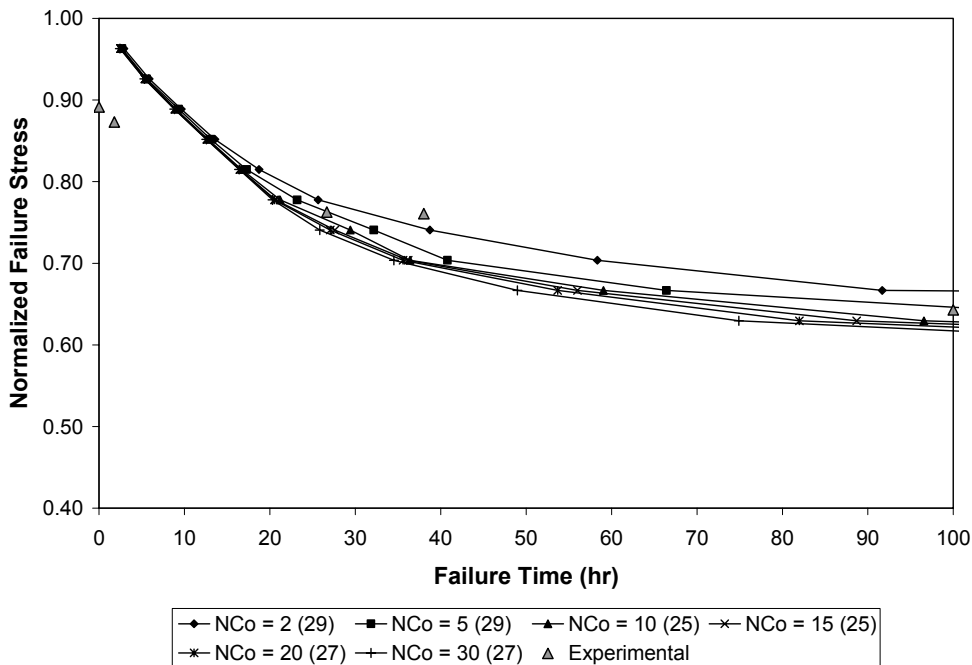
Figure 86: Variation in NC_o at 550°C with 0.2 atm pH_2O
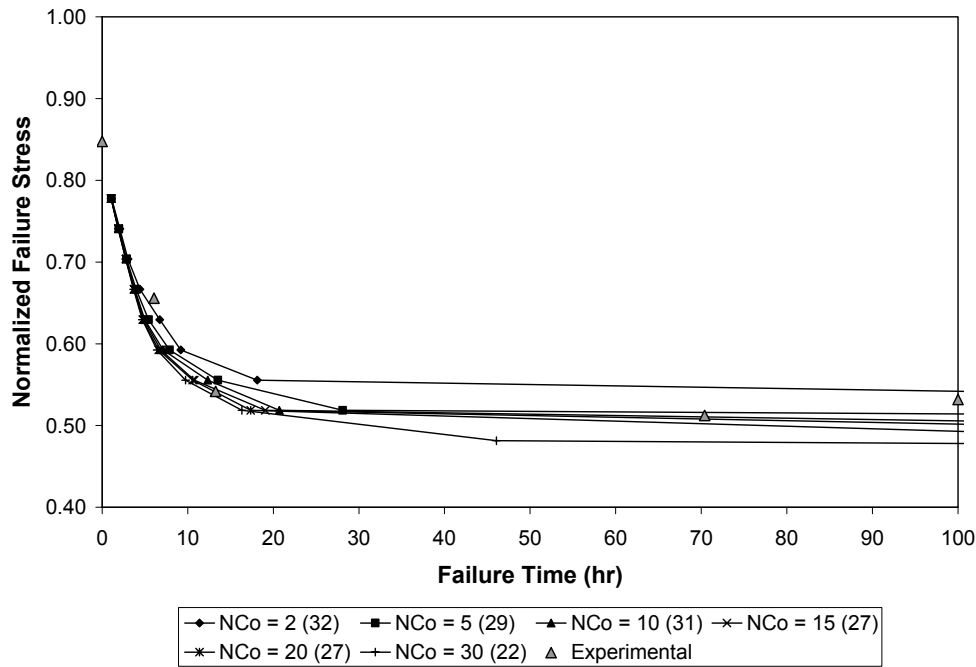
Figure 87: Variation in NC_o at 750^oC with 0.2 atm pH_2O

In the initial portion of the plots, the curves are not affected by the NC_o variation. This is the part of the plots where the specimen will experience a higher number of cracks because the applied stress is large. In the bottom portion of the plots, the stress rupture curves are converging toward the same curve with increasing NC_o. However, this is the part of the curve where there will be fewer cracks. Since the model is not designed to incorporate matrix crack propagation or matrix crack dependence on applied stress, a realistic value for NC_o must be chosen for the entire curve. Since the initial portion is not dependent on the number of cracks, NC_o can be based on the lower portion of the curve.

It is very difficult to distinguish between the various stress rupture curves in the 750^oC with 0.2 atm pH_2O plot, Figure 87, with NC_o between 5 and 20. The stress rupture curve in the plot corresponding to an NC_o of 30 stands out but 30 cracks is not realistic in this portion of the curve because the applied stress is slightly above the proportional limit. A limited number of cracks should be expected at these applied stresses. The 550^oC with 0.2 atm pH_2O plot shows that at 60 hrs the variation of the failure stresses is approximately ±0.02 of the normalized failure stress with the NC_o of 10 curve being in the middle. Therefore, 10 cracks appear to be a valid

141

number of cracks to use in the model for future sensitivity analysis. This supports the initial

suggestion presented earlier that 10 cracks would provide valid modeling results.

The next set of parameters includes those associated with material properties. Effects

due to variations in these are important to understand because of the inherent variability of CMC

material properties. The first parameter is the modulus of elasticity of the composite, E_c. A ±20%

variation in E_c was initially investigated. This variation resulted in an E_c of 264 and 176 GPa.

These values of E_c resulted in an E_m of 239 and 131 GPa, respectively, based on the rules of

mixtures. Figures 88 and 89 are plots of the parameter sensitivity results for 550^oC and 750^oC

with 0.2 atm pH_2O, respectively. The plots show this model is not sensitive to a variation in E_c.

The modulus of elasticity of the fibers, E_f, is the next parameter of interest. A ±20% variation in E_f

was initially investigated. This variation resulted in an E_f of 298 and 448 GPa. These values of E_f

resulted in an E_m of 202 and 168 GPa based on the rules of mixtures. Figures 90 and 91 are

plots of the results based on this variation for 550^oC, and 750^oC with 0.2 atm pH_2O cases,

respectively. The plots show this model is not sensitive to a variation in E_f.
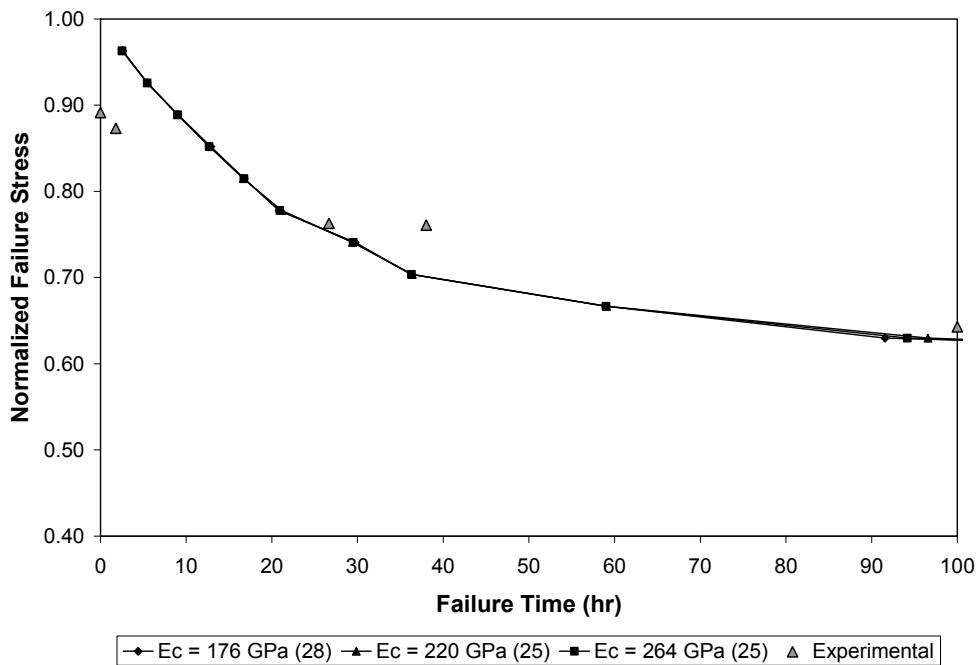
Figure 88: Variation in E_c at 550^oC with 0.2 atm pH_2O
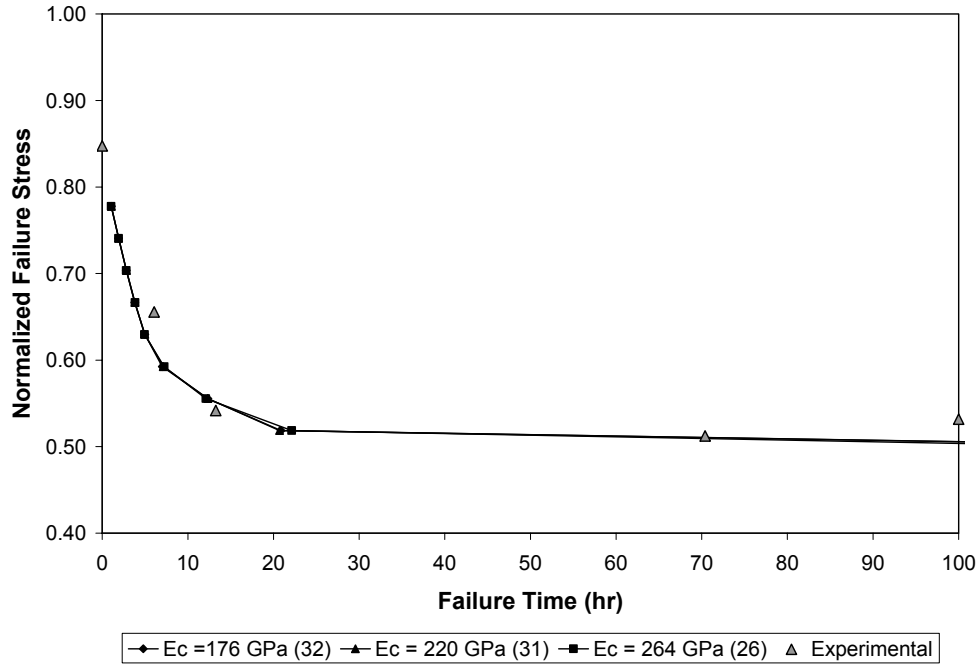
Figure 89: Variation in E_c at 750°C with 0.2 atm pH_2O
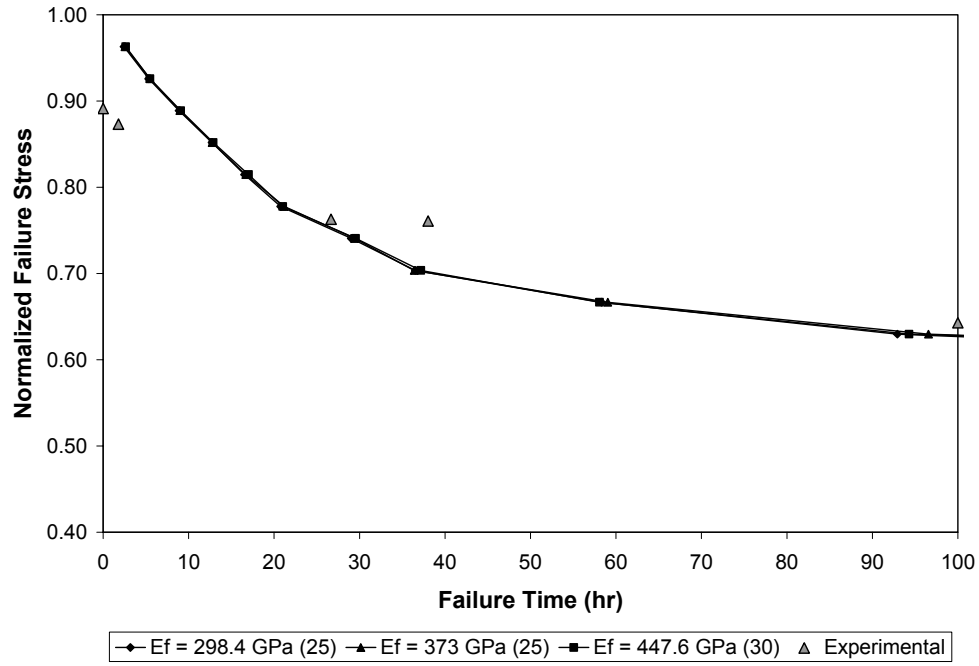
Figure 90: Variation in E_f at 550°C with 0.2 atm pH_2O

143
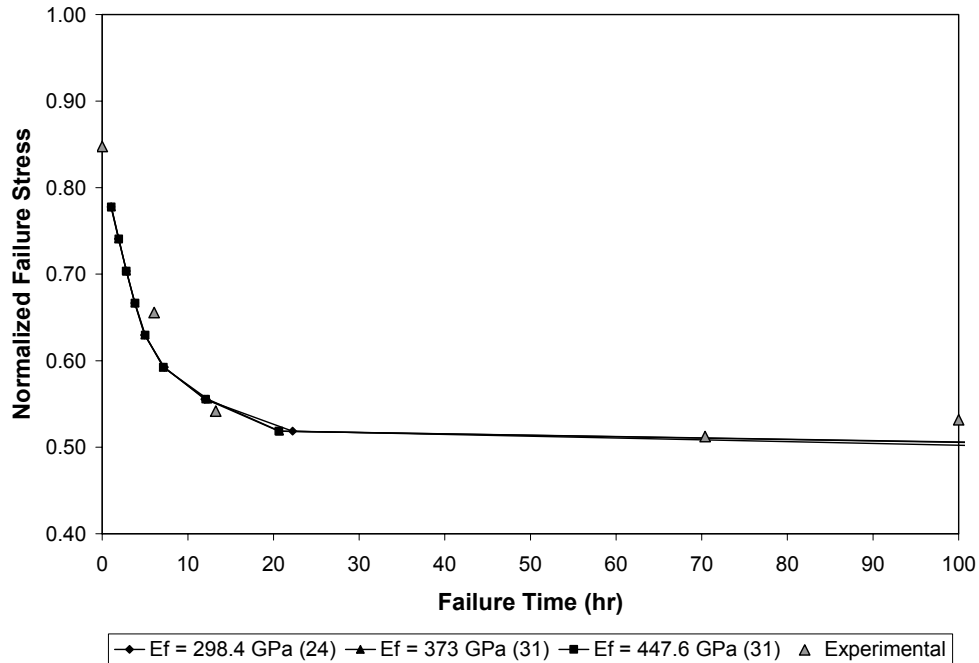
Figure 91: Variation in E_f at 750°C with 0.2 atm pH$_2$O

The next parameter of interest is the room temperature ultimate strength, σ_{ultRT}. The room temperature monotonic tests presented in Chapter IV had a +14.16/-16.30 MPa variation with an average of 405.35 MPa. Therefore, a ±5% variation in the room temperature ultimate strength that represents approximately ±20 MPa was investigated in this analysis. Figures 92 and 93 are plots of the parameter sensitivity results for the 550°C and 750°C with 0.2 atm pH$_2$O cases, respectively. These plots show that the 550°C with 0.2 atm pH$_2$O model is more sensitive to variations in the room temperature ultimate strength than the 750°C with 0.2 atm pH$_2$O model.
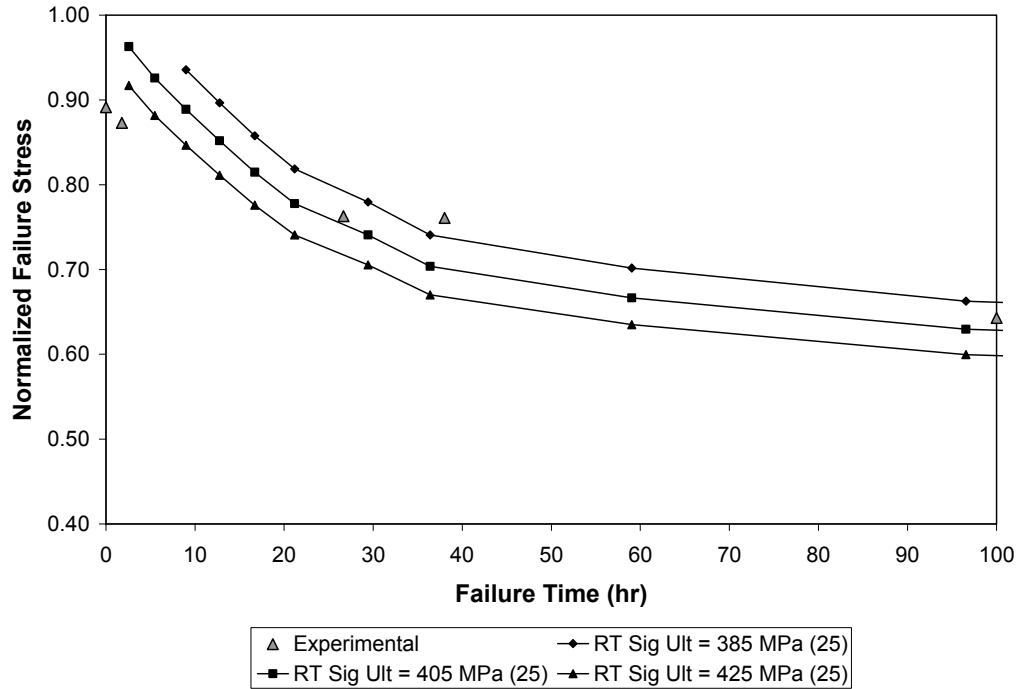
Figure 92: Variation in σ_{ultRT} for 550°C with 0.2 atm pH$_2$O
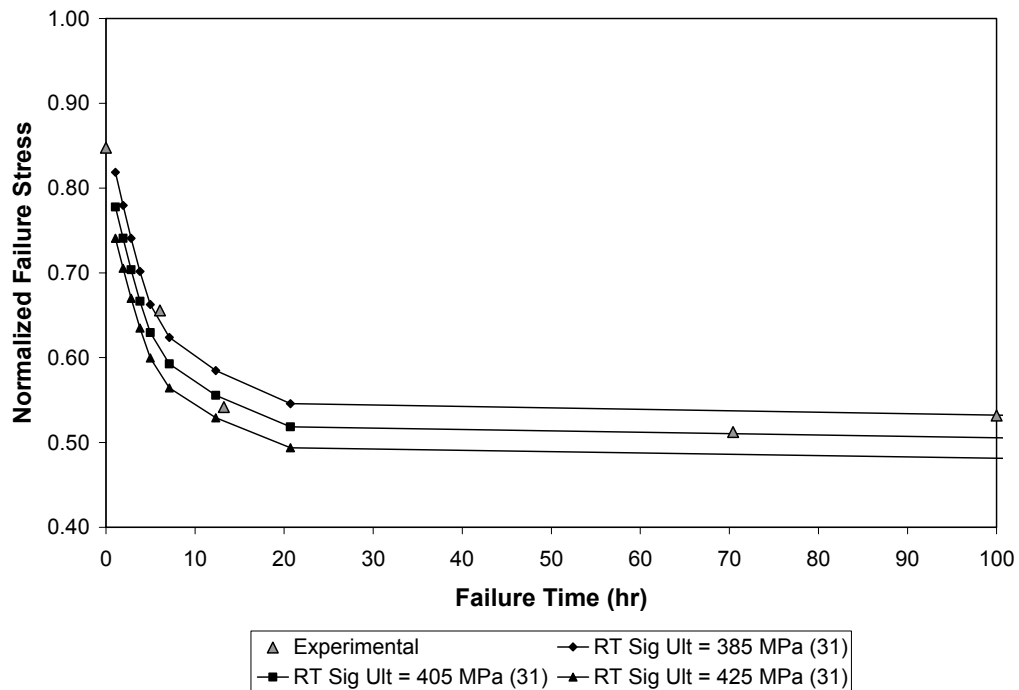
Figure 93: Variation in σ_{ultRT} for 750°C with 0.2 atm pH$_2$O

A ±10% variation in the test temperature ultimate strength, which represents

approximately ±38 MPa for 550°C with 0.2 atm pH$_2$O case and approximately ±35 MPa for the

750°C with 0.2 atm pH_2O case, was considered in this analysis. However, a +10% variation for

the 550°C with 0.2 atm pH_2O case would cause the environmental ultimate strength to be 429

MPa. This would be greater than the room temperature monotonic ultimate strength of 405 MPa.

It is unrealistic to allow the variation of the testing temperature ultimate strength to be greater

than the room temperature ultimate strength. Therefore, 405 MPa was used instead of 429 MPa.

Therefore, the variation is a +4/-10% variation in environmental ultimate strength. Figures 94 and

95 are plots of the parameter sensitivity results for the 550°C and 750°C with 0.2 atm pH_2O

cases.
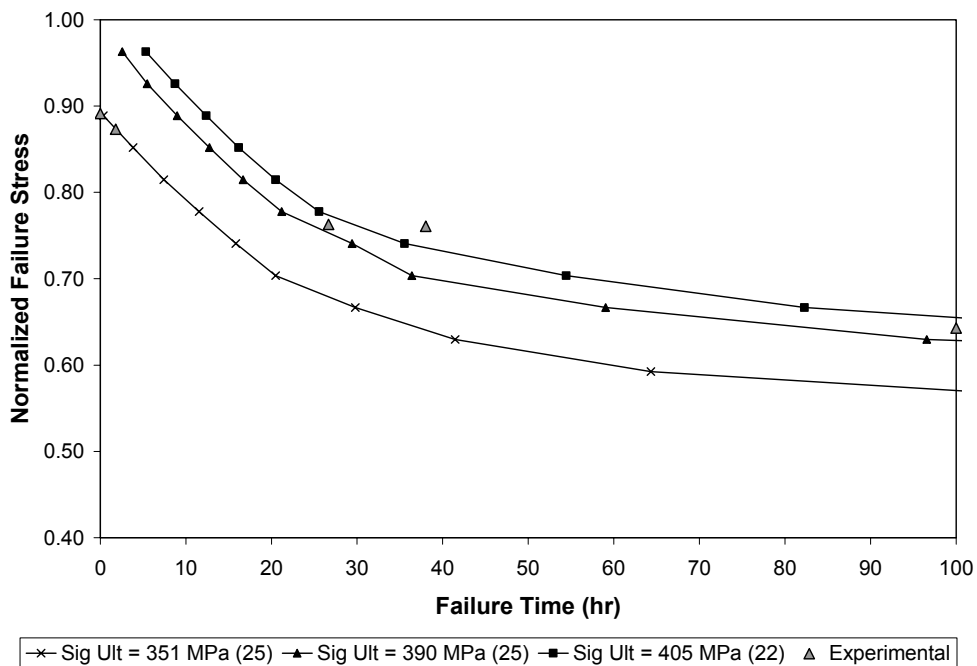
Figure 94: Variation in Environment σ_{ult} at 550°C with 0.2 atm pH_2O
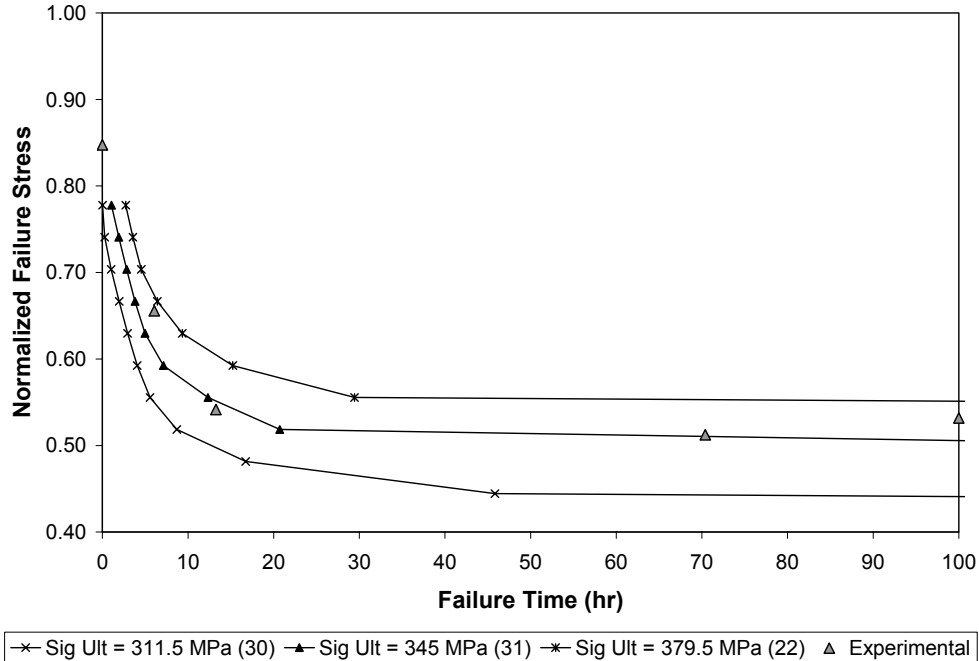
Figure 95: Variation in Environment σ$_{ult}$ at 750°C with 0.2 atm pH$_2$O

These plots show that the 550°C with 0.2 atm pH$_2$O case is more sensitive than the

750°C with 0.2 atm pH$_2$O case to variation in the environmental ultimate strength. All the

experimental data for the 750°C with 0.2 atm pH$_2$O case and all but one of the experimental data

for the 550°C with 0.2 atm pH$_2$O case fall within the band generated by this variation.

The parameter sensitivity analysis did not look directly at the variation in interfacial shear

stress. It looked indirectly by investigating the effects of variation in the ratio of the interfacial

shear stress in the stress-rupture environment to the interfacial shear stress of the monotonic test

environment. As mentioned earlier, the strength equations for both regions have this τ ratio. The

magnitudes of the interfacial shear stresses were not as important as the relationship between

the two.

The τ ratio should be 1 because the model uses the ultimate strength corresponding to

the test environment. This assumes the interfacial shear stress is only temperature dependent

and not moisture content dependent. Another assumption made is that the interfacial shear

stress is not time dependent. It is feasible that the interfacial shear stress changes as the fibers

become embrittled. However, there is no evidence to support or refute this possibility. Therefore,

the parameter sensitivity analysis looked at a ±20% variation in the τ ratio. The baseline values

147

in Table 13 were used along with τ ratio of 0.8 and 1.2. Figures 96 and 97are plots of the results for the 550°C and 750°C with 0.2 atm pH$_2$O cases, respectively.
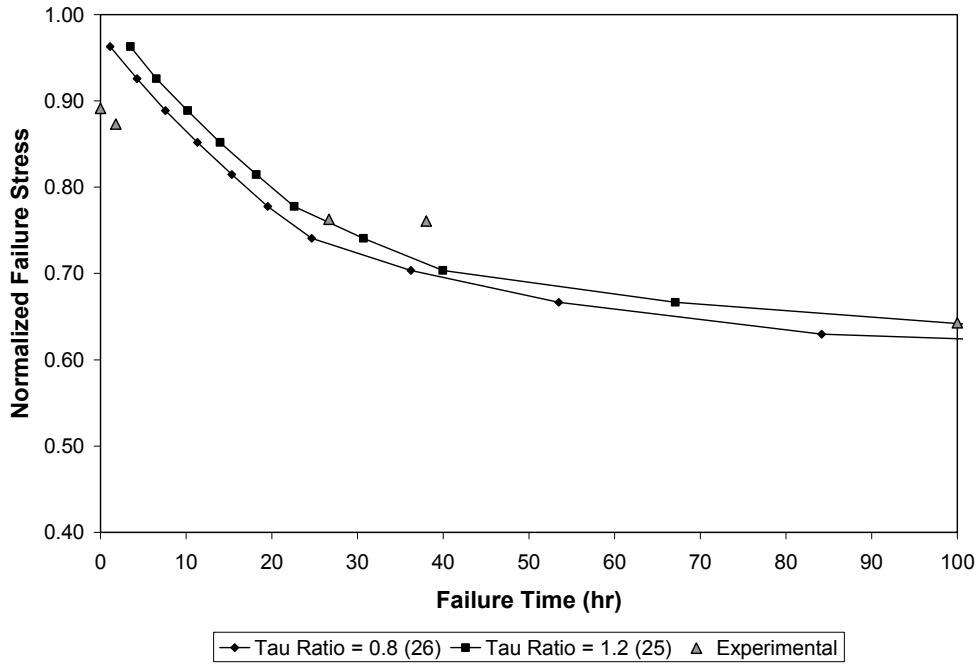
Figure 96: Variation in τ Ratio at 550°C with 0.2 atm pH$_2$O
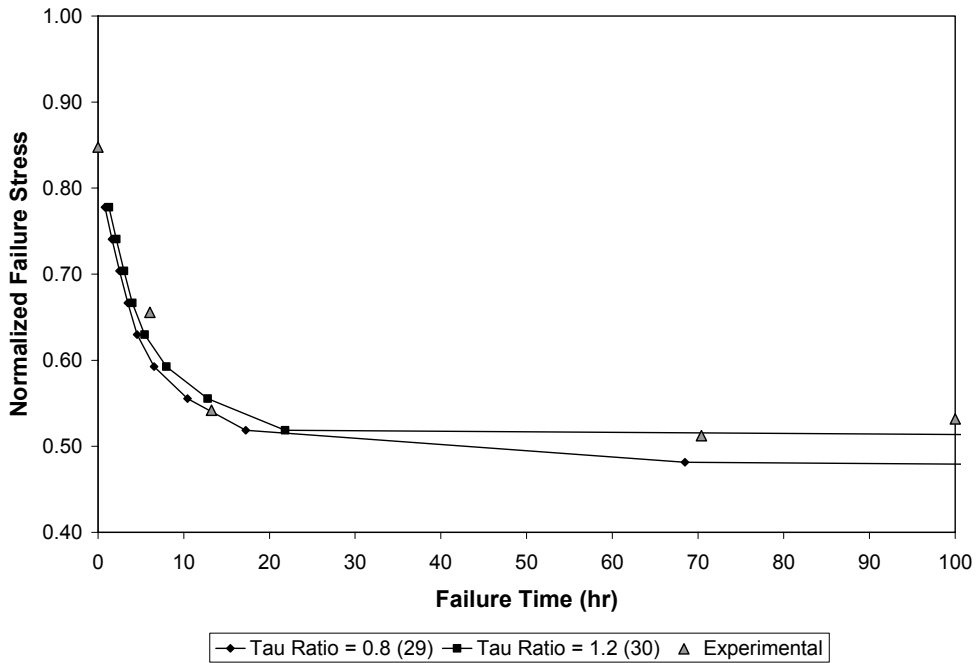
Figure 97: Variation in τ Ratio at 750°C with 0.2 atm pH$_2$O

The curves in these figures form a normalized failure stress band where the stress rupture curve should fall for many different scenarios for the τ ratio. The upper and lower part of the band is formed by assuming the τ ratio is 1.2 and 0.8, respectively, and the τ ratio is constant with respect to time. Therefore, the band will contain the stress rupture curves for all constant τ ratios between 0.8 and 1.2. It will also include stress rupture curves for τ ratios that change with respect to time (over the first 100 hours) from 0.8 to 1.2 or vice versa.

The model appears to be slightly sensitive to τ ratio variation. A ±20% change in the τ ratio for the 550°C with 0.2 atm pH_2O case resulted in a 2.37 hr bandwidth in failure time in the high stress, short failure time portion of the plot and a 0.025 normalized failure stress bandwidth ($\approx$ 10 MPa) in the low stress, 100 hr failure time portion of the plot. A ±20% change in the τ ratio for the 750°C with 0.2 atm pH_2O case resulted in a 0.46 hr bandwidth in failure time in the high stress, short failure time portion of the plot and a 0.05 normalized failure stress bandwidth ($\approx$ 20 MPa) in the low stress, 100 hr failure time portion of the plot. Therefore, the model is more sensitive to variations in the τ ratio at 550°C with 0.2 atm pH_2O than at 750°C with 0.2 atm pH_2O in the high stress, short failure time region. The model is more sensitive to variations in the τ ratio at 750°C with 0.2 atm pH_2O than at 550°C with 0.2 atm pH_2O in the low stress long failure time region at either temperature, although, a 10-20 MPa variation at 100 hours is not considered very significant considering the scatter in data for this material.

The parameter sensitivity analysis looked into two variations, one linear and one exponential, in the reference strength of pristine fibers, σ_{otT}. A linear variation creates parallel shifts in the line in Figure 74 and represents same degradation rate but starting at different magnitudes. The +10%, +5%, -5%, and -10% are shown in Figure 98 and were generated by multiplying Equation 46 by a variation of 0.9, 0.95, 1.05, and 1.1, denoted as var in the following equation:

$$\sigma_{otT} = \text{var} \cdot 10^{-0.0000066421q+3.49099644} \qquad \textbf{62}$$
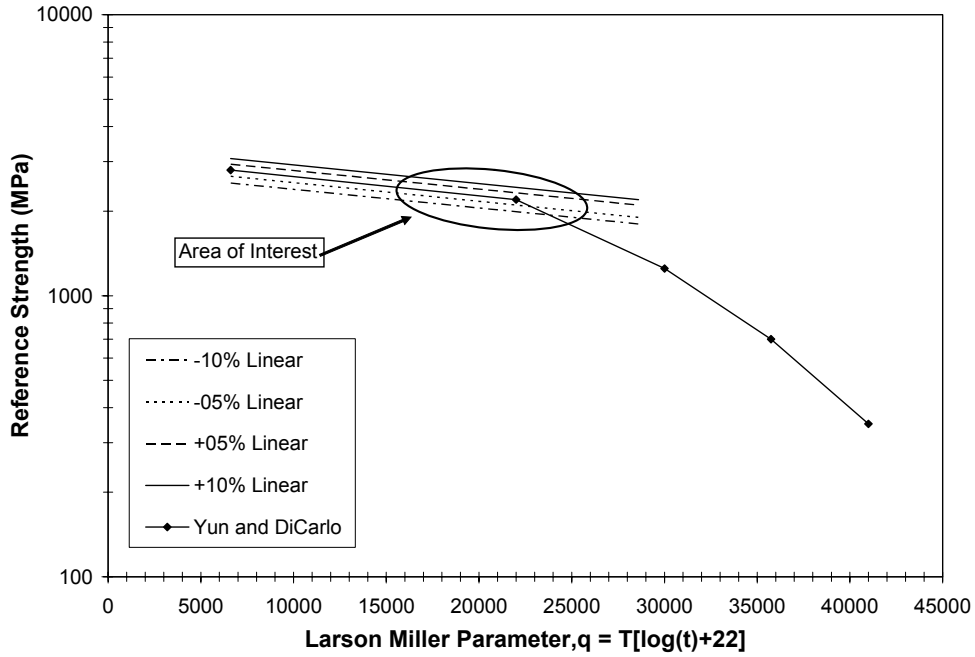
Figure 98: Linear Variation in σ_{otT} for Pristine Fiber

The process described earlier from Equation 40 to 53 was used with Equation 39 to generate new values for C_{refa}, C_{refb}, E_{refa}, and E_{refb} (summarized in Table 14). The modeling results from this analysis using these coefficients are shown in Figures 99 and 100 for the $550^{o}C$ and $750^{o}C$ with 0.2 atm pH_2O models, respectively.

Table 14: Coefficients for Linear Variation in σ_{otT}

	C_{refa}	C_{refb}	E_{refa}	E_{refb}
-10%	-0.676313	2668.552415	-0.00000664	0.00000017
-5%	-0.713886	2816.805326	-0.00000664	0.00000017
0%	-0.751459	2965.058238	-0.00000664	0.00000017
+5%	-0.789032	3113.311150	-0.00000664	0.00000017
+10%	-0.826605	3261.564062	-0.00000664	0.00000017
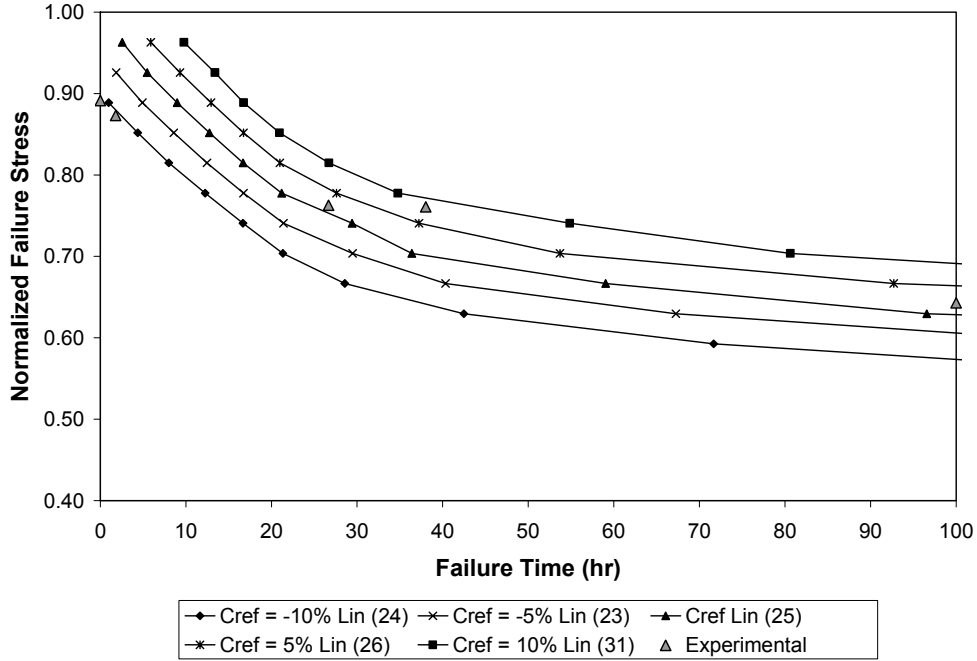
Figure 99: Linear Variation in σ_{otT} at 550°C with 0.2 atm pH$_2$O
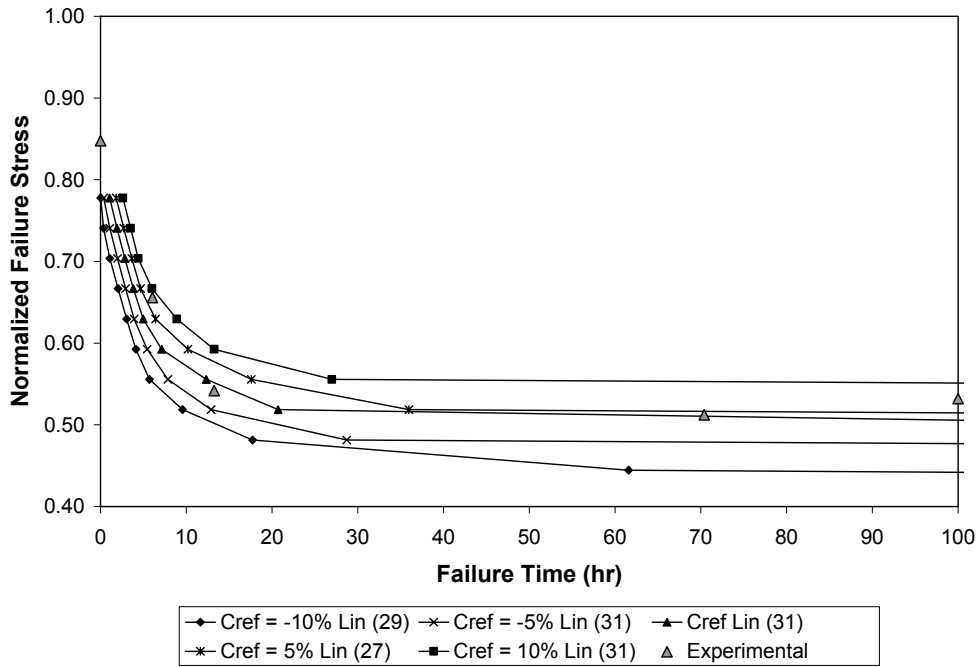
Figure 100: Linear Variation in σ_{otT} at 750°C with 0.2 atm pH$_2$O

Similar to all other variation analysis, the 550°C with 0.2 atm pH$_2$O model is more sensitive to linear variation in σ_{otT} than the 750°C with 0.2 atm pH$_2$O model. Also, a small ±10% shift in the original reference strength captures all the experimental data points for both cases. Both models are very sensitive to variation in σ_{otT}.

An exponential variation creates at non-parallel shifts in the line in Figure 74 and represents different rates of degradation of σ_{otT} starting at the same initial magnitude. The +20%, +10%, -10%, and -20% variation are shown in Figure 101 and were generated by multiplying Equation 51 by a variation of 0.8, 0.9, 1.1, and 1.2, denoted as var in the following equation:

$$\sigma_{otT} = 10^{-0.0000066421 \cdot var \cdot q + 3.49099644}$$

63
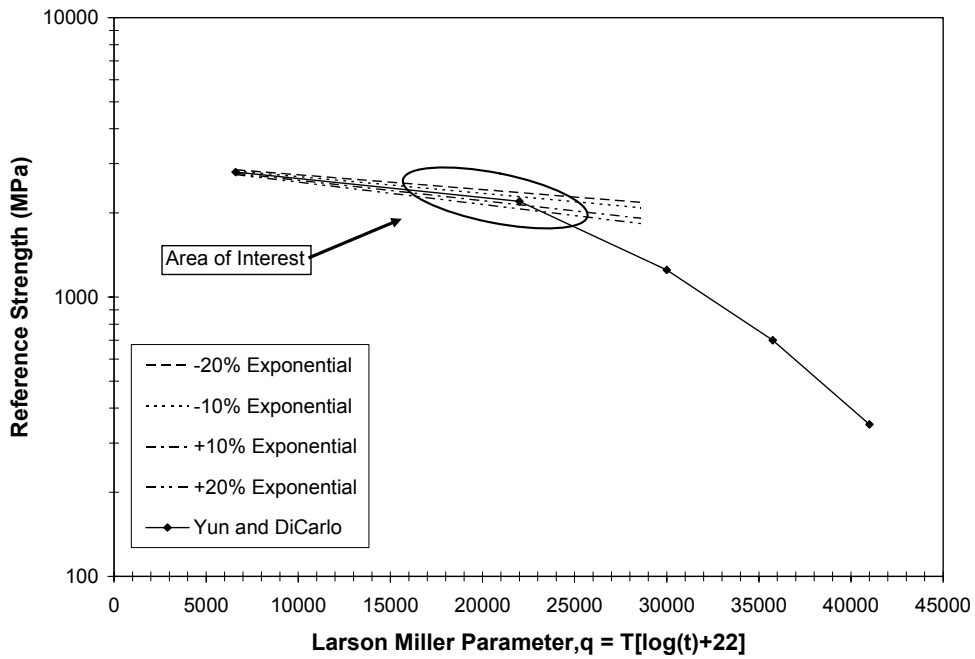
Figure 101: Exponential Variation in σ_{otT} for Pristine Fiber

The process described earlier from Equation 40 to 53 was used with Equation 39 to generate new values for C_{refa}, C_{refb}, E_{refa}, and E_{refb} (summarized in Table 15). The results of the model runs using these coefficients are shown in Figures 102 and 103 for the 550°C and 750°C with 0.2 atm pH_2O models, respectively.

Table 15: Coefficients for Exponential Variation in σ_{otT}

	C_{refa}	C_{refb}	E_{refa}	E_{refb}
-20%	-0.641764	3009.001446	-0.00000531	0.00000001
-10%	-0.698773	2987.890712	-0.00000598	0.00000009
0%	-0.751459	2965.058238	-0.00000664	0.00000017
+10%	-0.800043	2940.637200	-0.00000731	0.00000008
+20%	-0.844734	2914.753913	-0.00000797	0.00000009
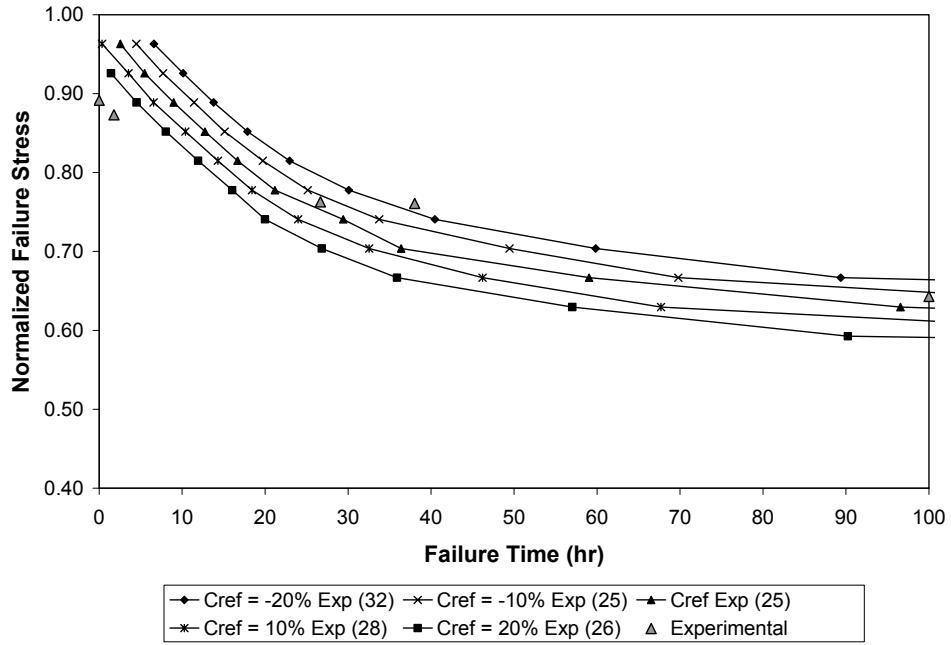
Figure 102: Exponential Variation in σ_{otT} at 550°C with 0.2 atm pH$_2$O
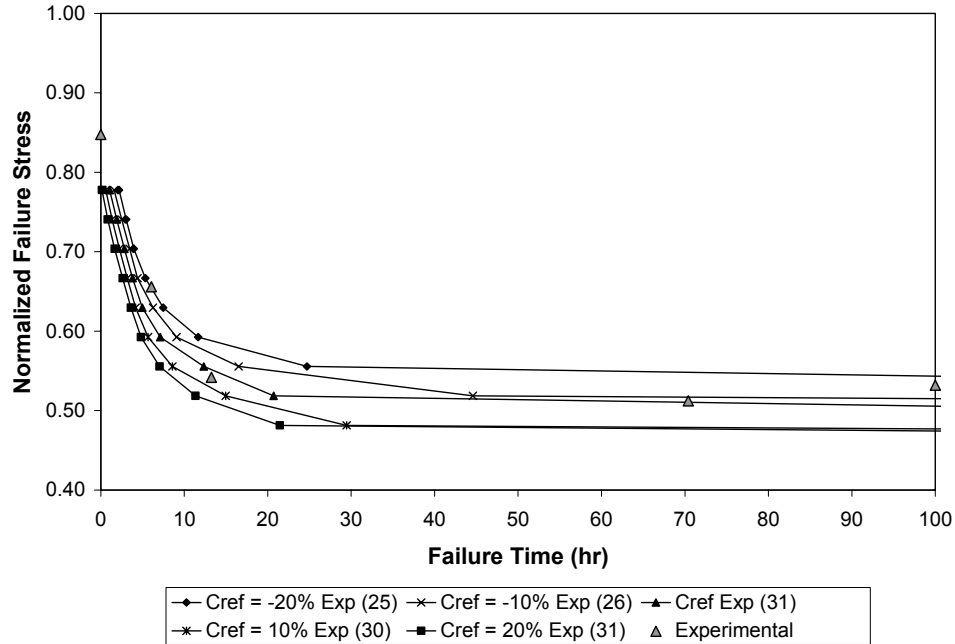
Figure 103: Exponential Variation in σ_{otT} at 750°C with 0.2 atm pH$_2$O

Again, the 550°C with 0.2 atm pH$_2$O model is more sensitive to exponential variation in σ_o than the 750°C with 0.2 atm pH$_2$O model. However, both models are less sensitive to exponential variation than linear variation. A ±20% shift in the original reference strength captures all the experimental data for the 750°C with 0.2 atm pH$_2$O case. However, a 20% shift in the original reference strength does not capture all the experimental data for the 550°C with 0.2 atm pH$_2$O case.

The Weibull Parameter, m, is a fitting parameter that is used in the Curtin [22] and Curtin et al [21] derivations of fiber strength. It is used here in the derivation of both the fiber strengths in the crack opening region and the stress transfer region. It also establishes the distribution of fiber strengths over a through-the-thickness crack region and in the stress transfer region.

Figure 104 is a plot of the distribution of initial fiber strength with different m values for the 550°C with 0.2 atm pH$_2$O case. The plot has the Fiber Strength Index along the x-axis which is a number assigned to the fibers to rank order them from weakest to strongest fiber. As m increases the curves become more flat. As m approaches infinity the curve converges to a flat line thus removing the distribution of strengths. The fiber strengths for m = 5000 range between 2104.4 and 2109.7 MPa. The theoretical value for the fiber strength when m = ∞ is the ultimate

composite strength at 550°C divided by the volume fraction in the loading direction which is equal to 2102.4 MPa. This is in agreement with the computed value from the analysis.
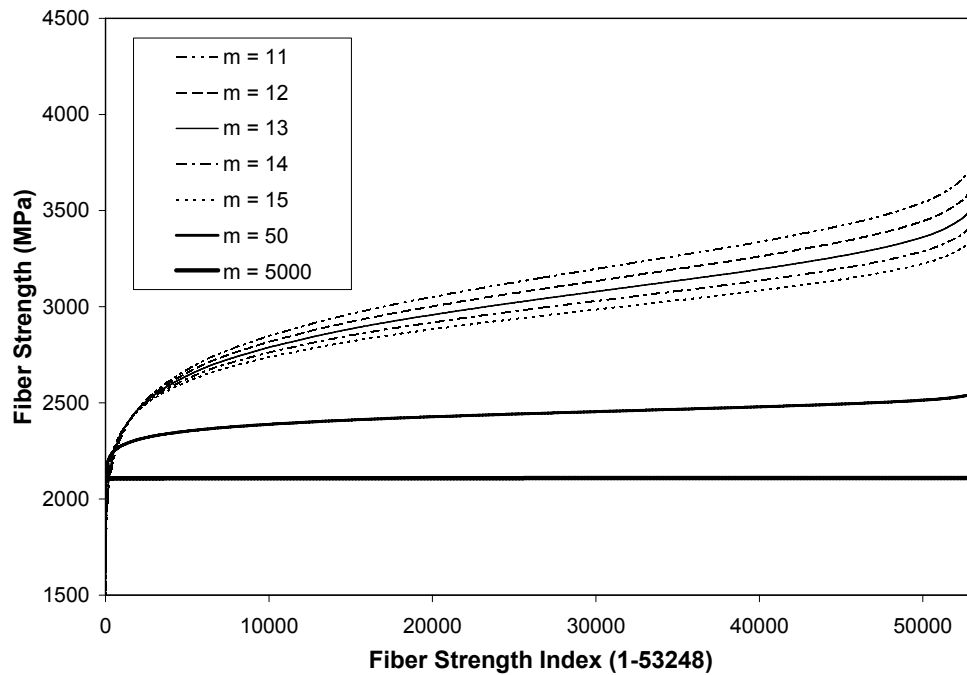
Figure 104: Initial Fiber Strengths for Various m Values

In the parameter sensitivity analysis, m values of 11, 13, and 15 are used in the model. This represents a ±15% variation from the empirically obtained value of 13. Figure 105 is a plot of the results of the model runs for the 550°C with 0.2 atm pH_2O case. The curves are affected in an interesting manner. Before 23 hours the specimen life is reduced as a result of increasing m. However, after 23 hours the specimen life increases with an increase in m. At 23 hours there is no change in the failure with respect to m.
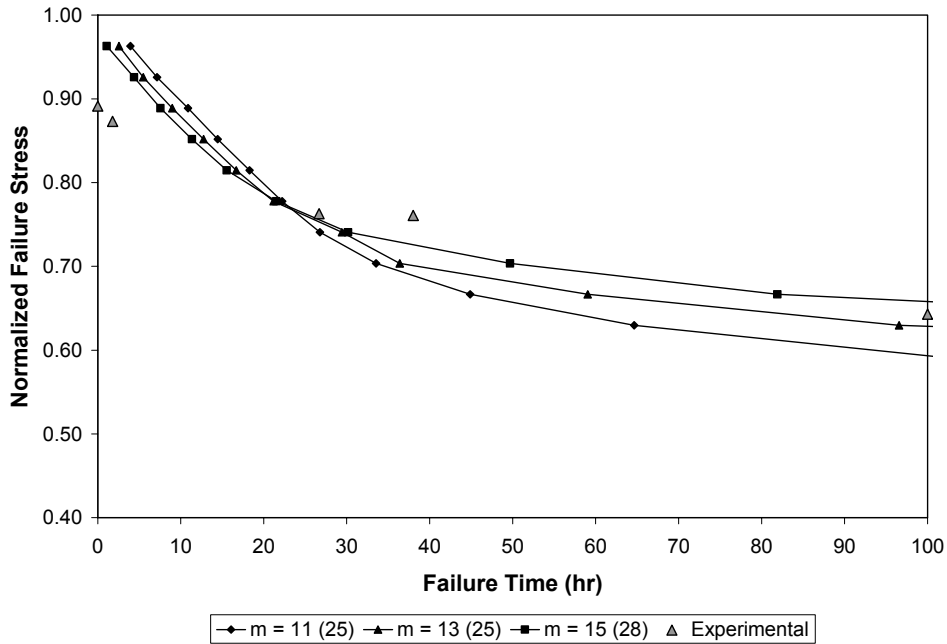
Figure 105: Variation in m at 550°C - with 0.2 atm pH_2O

Figure 106 is a plot of the results of the model runs for the 750°C with 0.2 atm pH_2O case. The curves are affected in a similar manner as the case above. Before 4.5 hours the specimen life is reduced as a result of increasing m. Again, this was expected since the fiber strength reduces as m increases. The change in failure time here is smaller than the 550°C with 0.2 atm pH_2O case. However, after 4.5 hours the specimen life increases with an increase in m. Similar to the sensitivity analysis for the 550°C with 0.2 atm pH_2O case above, this was not expected. At 4.5 hours there is no change in the failure with respect to m.
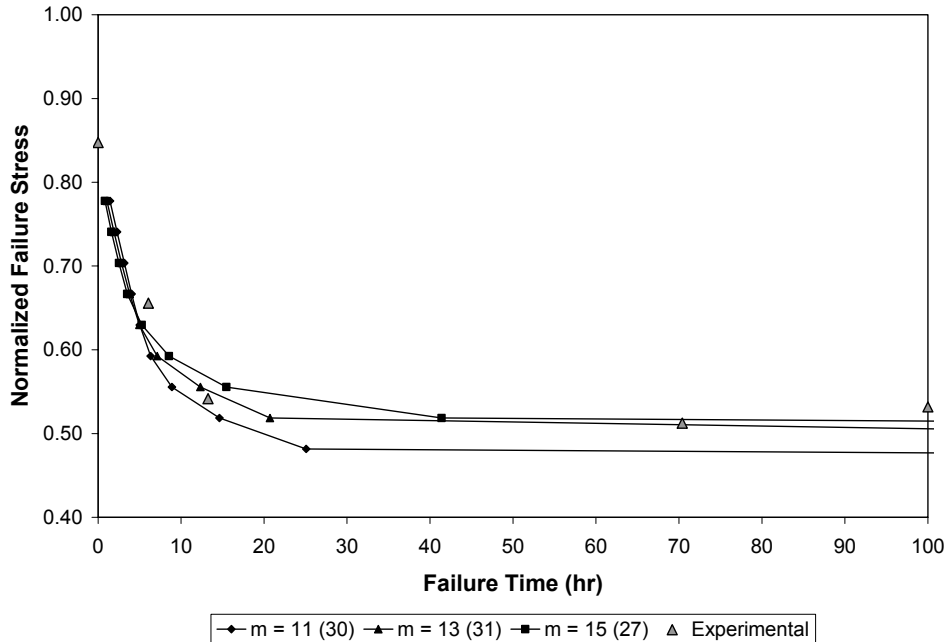
Figure 106: Variation in m at 750°C - with 0.2 atm pH$_2$O

This clearly shows that the present formulation is sensitive to the parameter m, which is an empirically determined parameter. So its determination is probably the most important part of the analysis. A ±15% change in m resulted in a +53/-58% change in failure time in the high stress, short failure time portion of the 550°C with 0.2 pH$_2$O moisture content plot. A ±15% change in m resulted in a 0.065 normalized failure stress variation in the low stress, 100 hr failure time portion of the plot. This corresponds to approximately 26 MPa. A ±15% change in m resulted in a +35/-21% change in failure time in the high stress, short failure time portion of the 750°C with 0.2 atm pH$_2$O plot. A ±15% change in m resulted in a 0.037 normalized failure stress variation in the low stress, 100 hr failure time portion of the plot. This corresponds to approximately 15 MPa. Therefore, the 550°C with 0.2 atm pH$_2$O model is more sensitive than the 750°C with 0.2 atm pH$_2$O model to the variation of m.

Summary

The model presented in this chapter successfully simulated the failure of the Syl-iBN/BN/SiC CMC in an intermediate temperature humid environment. The model was shown to be applicable in the 550-750°C temperature range with 0.0-0.6 atm pH$_2$O. The temperature of

the test environment affected the degradation of the composite strength and the moisture content level affected the time it took for total embrittlement to occur. The total embrittlement time is the most important variable to quantify stress rupture behavior in a humid environment at intermediate temperatures.

A parameter sensitivity analysis looked at the variation in the key parameters used in the model. These parameters were varied by specific amounts to reveal the sensitivity of the model. Variation in the number of cracks, NC_o, shows that the stress rupture curve converges as the NC_o increases. However, little fidelity in the curve is gained beyond 10 cracks. Variation in m controls the overall shape of the curve. As m increases the intercept of the initial portion of the stress rupture curve is decreased and the flat portion of the curve is increased. Variation in E_c and E_f had little effect on the stress rupture curve. Variation in the τ ratio had slight effects on the stress rupture curve. The variation analyzed in this parameter sensitivity analysis generated a bandwidth for various scenarios (i.e. if the interfacial shear stress is a function of time and the τ ratio varies between 0.8 and 1.2) for the effect the environment could have on the interfacial shear stress. Variation in the room temperature ultimate strength (σ_{ultRT}), the environmental ultimate strength (σ_{ult}), and the fiber reference strength (σ_o) had significant effects on the stress rupture curve. Small variations of ±5% in σ_{ultRT} and ±10% in σ_{ult} and a ±10% linear variation in σ_{otT} captured nearly all the experimental data points in both cases. In all parameters, the 550°C model was more sensitive than the 750°C as summarized in Table 16.

Table 16: Parameter Sensitivity Analysis Results

Parameter	Variation	Variables Used in Model	Results/Comment
Number of Cracks NC_o	2-30	NC_o = 2, 5, 10, 15, 20, and 30	Initial portion of curves not affected. Bottom portion of curve affected but converges as NCo increases. NCo = 10 chosen for analysis.
Modulus of Elasticity for composite E_c	+20% -20%	E_c = 264 GPa, E_m = 239 GPa E_c = 176 GPa, E_m = 131 GPa	Variation had little to no effect on stress rupture curves.
Modulus of Elasticity for fiber E_f	+20% -20%	E_f = 298 GPa, E_m = 202 GPa E_f = 448 GPa, E_m = 168 GPa	Variation had little to no effect on stress rupture curves.
Weibull Parameter m	+15% -15%	m = 15 m = 11	Initial portion slightly affected – as m increases stress rupture life decreases. Bottom portion sensitive – as m increases the stress rupture failure stress increases.
Ultimate Strength at Room Temperature σ_{ultRT}	+5% -5%	σ_{ultRT} = 425 MPa σ_{ultRT} = 385 MPa	Entire curve is very sensitive to variation. See Figures 92 and 93.
Ultimate Strength at Environment σ_{ult}	+4% -10%	σ_{ult} = 405 MPa σ_{ult} = 351 MPa	Entire curve is very sensitive to variation. See Figures 94 and 95.
Interfacial Shear Stress Ratio τ_T/τ_{ult}	+20% -20%	τ ratio = 0.8 τ ratio = 1.2	Slightly sensitive - 2.37 and 0.46 hr band in failure time in initial portion of the plots and a 0.025 and 0.05 ($\approx$ 10 and 20 MPa) normalized failure stress band in the bottom portion of the plot for 550°C and 750°C, 20% moisture content cases, respectively.
Reference Strength σ_{otT}	Linear +10%,+5% -5%,-10%	See Table 14 for changes to C_{refa}, C_{refb}, E_{refa}, and E_{refb}	Entire curve is very sensitive to variation. See Figures 99 and 100.
	Exponential +20%,+10% -10%,-20%	See Table 15 for changes to C_{refa}, C_{refb}, E_{refa}, and E_{refb}	Entire curve is very sensitive to variation. See Figures 102 and 103.

VI. Discussion

This research set out to answer three important questions regarding the performance of the Syl-iBN/BN/SiC CMC in an intermediate temperature and humid environment. The first question is how does the environment affect the principal CMC constituents: the fiber, the matrix, and the interphase. The second question is how does the environment affect the stress rupture life of the CMC. The third question is can CMC failure mechanisms be accurately modeled to predict fiber and subsequent CMC failure. The approach to answering these questions was to gather experimental data to understand the failure mechanisms and CMC strength degradation as temperature and moisture were varied. This information was then coupled with the previous CMC models to expand them to include environmental effects. This chapter discusses how the experimental and modeling results of Chapter IV and V provide new insight on the effects of temperature and moisture.

Environmental Effects on the Principal Constituents of the CMC

The FESEM data collected in this research shows that the environment had little effect on the matrix and fiber material but dramatic effects on the interphase material. This was expected since there was no previous literature that suggested the material properties of the matrix or fiber would change with respect to pH_2O. Previous research presented in Chapter II shows that BN is susceptible to oxidation and this leads to pesting at the temperature used in this research. This research shows that the temperature and pH_2O have independent effects on the pesting phenomenon that is associated with embrittlement. Heredia et al [13] suggested that there is one temperature, referred to as the pesting temperature, where embrittlement occurs for a particular material, environment, and loading condition and that pesting temperatures for CMCs occur in the 600-900°C range. This research shows that for the Syl-iBN/BN/SiC CMC, the pesting phenomenon occurs over the range of temperatures, not at one temperature. Further, the pesting phenomenon is dependent on the pH_2O.

Temperature and pH_2O affect the amount of time it takes to replace the BN interphase with SiO_2 through the chemical reactions (Equation 2 through 6 in Chapter II). Morscher and Cawley [17] found that a similar SiC/SiC CMC material experienced total embrittlement in approximately 21 hours at 815^oC with ambient pH_2O. They observed and postulated that the small amount of moisture in the test environment caused the embrittlement phenomena to occur very slowly starting at the outside edge of the specimen moving towards the center of the specimen along the fracture plane. This research, however, shows that more moisture in the testing environment results in accelerated total embrittlement time for the Syl-iBN/BN/SiC CMC. At 750^oC with 0.0, 0.2, and 0.6 atm pH_2O, according to FESEM observations and modeling calculations, total embrittlement occurs at approximately 300, 20, and 3 hr, respectively. At 550^oC with 0.0, 0.2, and 0.6 atm pH_2O, total embrittlement occurs at approximately 300, 100 and 20 hrs, respectively. These results clearly show that the amount of moisture and temperature play important roles in determining the total embrittlement time for SiC/SiC CMCs.

The kinetics of the embrittlement were also different from that seen by others [10,13] and quantified by Morscher and Cawley [17]. The embrittlement in this research occurred simultaneously over the entire cross section of the crack plane as opposed to staring at the outside edge and moving toward the center of the specimen. This difference was originally attributed to two possible reasons, the first being gas flow velocity and the second being a change from gaseous diffusion controlled to surface chemistry kinetics controlled embrittlement.

The gas flow velocity in this research is higher than previous research. Since previous researcher typically used resistance heaters, there was little to no flow around the test specimen. The gas stream flow will cause areas of higher pressure caused by impingement points and areas of lower pressure caused by separated flow on the surface of the specimen. The magnitude of pressure change and location of these points will depend on the velocity of gas stream and the surface of the specimen. Ogbuji's data [41] showed that, in unloaded specimens, the velocity of the test vapor stream caused accelerated recession rates on the exposed ends of the fiber/interphase at cut surfaces. He also showed that the angle of the vapor stream did not affect the embrittlement. The retained strengths of his specimens were reduced when moisture

was present in the gas stream and as the velocity of the gas stream was increased. The

pressure differences could result in flow into the crack via mass transport if the cracks are large

enough.

Using a Knudson analysis, the likelihood of flow through a crack can be determined. The

Knudson Number, K_n, is the ratio of the mean free path of the gas (i.e. the distance a molecule of

gas will travel before colliding with another molecule) to the dimension of the crack that the gas is

diffusing or flowing through. The value of K_n tells us if the gas flow or gaseous diffusion will

dominate in the crack [77]. For the analysis, it is reasonable to model the crack as several pores

with radius equal to the crack opening. This model gives a worst case scenario since the cracks

are continuous and interconnected. The mean free path as a function of temperature is

calculated using the following:

$$\lambda = \frac{kT}{\sqrt{2}\pi\sigma^2 p}$$

64

where

$\lambda \equiv$ mean free path (m)
$k \equiv$ Boltzmann's constant (1.38E-23 J/K)
$T \equiv$ temperature (K)
$P \equiv$ pressure (Pa)
$\sigma \equiv$ molecular diameter (m)

Using Equation 64, the mean free path of air, O_2, and H_2O at 550°C are approximately

1750 Å, 2470 Å, and 3220 Å, respectively; and at 750°C they are 2170 Å, 3070 Å, and 4000 Å,

respectively. With crack sizes between 2000-5000 Å, K_n is between approximately 0.35 and 2.0

for these molecules and temperatures. For viscous flow $K_n \ll 1$. Therefore, it is unlikely these

cracks are large enough to support viscous or continuous flow. Since there is no viscous flow

through the crack, the molecules will collide with the crack surfaces as they diffuse towards the

center of the crack. The collisions will result in consumption as mentioned earlier. The

consumption slows the gaseous diffusion rate of the molecules towards the center of the

specimen such that the embrittlement front will move from the outer edge of the specimen towards the center.

The second potential explanation for the difference in embrittled regions was that there is a transition from gaseous diffusion controlled embrittlement seen at high temperature to surface chemistry kinetics controlled embrittlement seen at low temperatures. As mentioned earlier, Morscher [66] saw gaseous diffusion controlled embrittlement in a similar material tested at 815°C. The 65-265°C difference in the test temperature used in this research will decrease both the chemical reaction rate and the gaseous diffusion rate; however, as presented in Chapter II, the surface chemistry kinetics rate will be affected more significantly than the gaseous diffusion rate.

This research shows that embrittlement at intermediate temperatures with moisture is not controlled by gaseous diffusion of reactants through the crack opening like previous researchers have seen at higher temperatures for similar SiC/SiC materials. The molecules still diffuse through the cracks and pores but the reactions are so slow that the cracks become saturated with reactants before the reactions occur. Therefore, the reactions occur across the entire cross sectional area. The surface chemistry kinetics of these reactions are functions of the concentrations of the reactants and the products. Therefore, the amount of embrittlement seen is dependent on the pH$_2$O. The stress rupture plots generated in this research show that there is a direct correlation of the stress rupture strength with the concentration of moisture at 550°C and 750°C. Therefore, it is clear that the embrittlement phenomenon is surface chemistry kinetics controlled at 550°C and 750°C. Halbig et al [65] observed the same results for the C/SiC CMCs they tested at 700°C.

Moisture Effects on the Life of the Syl-iBN/BN/SiC CMC

Embrittlement has detrimental effects on the Syl-iBN/BN/SiC CMC. The pesting of fibers together is the primary explanation for the decrease in strength shown in the stress rupture plot, Figure 39. Because of the pesting, a crack has a path to propagate across and fail neighboring fibers that would have otherwise not failed. A group of pested fibers will essentially take on the strength characteristics of the weakest fiber. When the weakest fiber fails, the remaining fibers

will fail, thus removing a large number of fibers. This dramatically increases the stress on other fibers and increases the possibility that another fiber in another tow will now fail. This creates a cascading effect across the entire crack plane.

Another explanation for the strength reduction may be that the moisture is attacking the BN interphase on exterior debonded fibers and causing surface flaws in the BN interphase. Over time these flaws reach the critical flaw length and failure results. This would explain why there is a decrease in strength during stress rupture tests but not during the monotonic tests. In the monotonic tests, there is not enough time for the flaws to grow before the increasing applied stress surpasses the fiber failure stress at a location with a preexisting critical flaw.

The results in this research showed that the moisture level had clear detrimental effects on the isothermal stress rupture strength at 550°C and 750°C. At 750°C with 0.0, 0.2, and 0.6 atm pH_2O, the normalized 100-hour stress rupture strength was 0.65, 0.5, and 0.5, respectively. At 550°C with 0.0, 0.2, and 0.6 atm pH_2O, the normalized 100-hour stress rupture strength was 0.8, 0.7, and 0.54, respectively. The strength dependence on temperature is similar to previous results, that is, higher temperatures lead to increased strength degradation. Prior to this research, the effect of moisture level was not known and cannot be compared to the results presented here. However, the results were expected since more moisture would lead to more boria being leached out of the borosilicate glass formations, thus solidifying the glass faster and changing the failure mechanism.

It appears from the data collected here that the normalized stress rupture curves approach the 50% value for the 750°C cases.   This is the point in the monotonic test where through-the-thickness cracks have started forming. The data suggest that prior to through-the-thickness crack formation the material demonstrates long life, and that once a through-the-thickness crack is formed the material experiences significant damage. Once these cracks are formed, the environment has complete access to the crack surface via the cracks and the pores in the matrix. Morscher [10] saw similar results in his work. Figure 38 is a plot of the data collected here showing a similar degradation in the Larson-Miller curve as that shown in Figure

10, Figure 11, and Figure 12. These dips indicate that embrittled fiber failure is taking over as the primary failure mechanism.

Although the area of embrittlement differed in this research from previous research, the failure mechanisms of the fibers were similar. In the unembrittled regions, fibers failed when the applied stress on the fibers exceeded their strengths. Given the variations in fiber strength along a fiber length, individual fibers failed at various locations uniformly distributed along the loading axis of the fibers, thus, creating fiber pullout as seen in the FESEM images. In the embrittled regions, fibers failed because of fibers pesting to neighboring fibers that were weaker. The failure crack propagated across the pested fibers along the same plane, thus failing large groups of fibers. The FESEM images confirm fracture patterns emanating from the pested locations as presented in Chapter IV. This essentially reduces the strength of stronger fibers to the equivalent strength of the weakest fiber in the embrittled group.

As mentioned earlier, the pH_2O accelerates the embrittlement process. The acceleration of the embrittlement phenomenon increases the number of fibers that became pested to other fibers at a given point in time. The embrittlement essentially reduced the strength of all the embrittled fibers in a group to the strength of the weakest fiber in the group. Therefore, the failure of the weakest fiber results in the failure of all the embrittled fibers in the group. This shortened the life of the CMC as shown clearly in experimental results portion of Chapter IV.

Modeling Environmental Effects

The modeling portion of this research consisted of combining previous efforts done by Curtin [22], Curtin et al [21], and Morscher and Cawley [17] with experimental data and observations from this research and applying them in a unique Monte Carlo-type fiber simulation to estimate the stress rupture life of the Syl-iBN/BN/SiC CMC system. Once the model was successful at modeling the failure of the Syl-iBN/BN/SiC CMC in an intermediate temperature and humid environment, a parameter sensitivity analysis looked at the variation in the key parameters used in the analysis.

There were five assumptions in the modeling portion of this research. The first assumption was that the material properties of the interphase, cross tow fibers, and the matrix

could be combined together, which was developed and used by Morscher and Cawley [17]. This assumption was made since this makes analysis reasonable and models the main damage mechanism, i.e. fiber breakage in the applied load direction. This assumption means that the reported modulus of elasticity for the matrix material includes the modulus of elasticity for the matrix material, the interphase material, and the cross fibers (i.e. 90° tows).

The second assumption was that through-the-thickness cracks formed instantaneously and partial cracks did not exist. This assumption is based on the fact that the applied stresses in all tests were above the proportional limit guaranteeing through-the-thickness cracks. The number of cracks used in the model is based on crack density measurements on the failed specimen and is a function of applied stress. It is unknown at what particular time during the test the crack formed and how fast it propagated. Use of post-test crack density measurements provides worst case results (i.e. conservative estimate) since the cracks are assumed to form instantly at the beginning of the test, however, it may take some time to grow.

The third assumption was that the weave architecture of the material could be idealized to a unidirectional architecture allowing the use of equations derived by Curtin [22] and Curtin et al [21] for evaluating the probability of fiber failure for unidirectional composites. This assumption is necessary because there is no published theory or analysis for fiber strength based on weave architectures for composite materials. It is reasonable for this model since the analysis is only concerned with the effective fiber lengths in the loading direction (i.e. 0° tows) in the presence of through-the-thickness cracks, and at such a microscopic level the weave architecture does not play a role in the fiber strength characteristics.

The fourth assumption dealt with the embrittlement phenomenon. It was expected to occur similar to what Morscher and Cawley [17] saw in their experiments except at a faster rate. They found that the environment attacked the specimens, via cracks in the matrix, from the outside edge towards the center of the specimen. They used a power law relationship to model the embrittled area because the embrittlement front followed a gaseous diffusion pattern through the crack. Observations from the FESEM analysis in this research showed that the embrittlement occurred over the entire fracture surface simultaneously, not in the 'picture frame' manner where

outside tows completely embrittle before the interior tows started to embrittle. This new type of failure mechanism led to the assumption that each tow embrittled at the same rate simultaneously. This meant that at a particular time all tows had the same number of pristine and embrittled fibers.

The last assumption dealt with embrittled fiber failure. The model assumes that when an embrittled fiber fails the neighboring embrittled fibers also fail cascading throughout the tow failing all embrittled fibers in the tow. This differs from the assumption of Morscher and Cawley [17] that all embrittled fibers in the cross section fail. Although the assumptions were different, the outcome was very similar. Since failing groups of fibers simultaneously caused a step increase in the applied stress, several more fibers (some embrittled) in other tows failed, thus creating a cascading effect across all the embrittled fibers.

Using these assumptions, new strength equations were developed. They were based on the formulation by Curtin [22] and incorporated some features of Morscher and Cawley [17]. However, this research applied the strength equations in a Monte Carlo-type fashion to each individual fiber. The model captures the following physical characteristics of CMC failure in intermediate temperature, humid, stress rupture conditions: strength degradation caused by creep, Weibull distribution of individual fiber strengths, strength reduction due to the manufacturing process, the time it takes to embrittle the fibers in a crack, and the effect pesting has on neighboring fibers.

Since creep is a thermally activated mechanism, the test temperature and its effects must be included in the model. The initial strengths of the individual fibers are reduced because of the manufacturing process (high temperatures and pressures). This reduction is captured through the application of the strength reduction factor, a constant reduction applied from the on set of testing. The temperature dependent time-based degradation of the fiber reference strength is captured in the reference stress equation that has the coefficient and the exponent as a function of temperature.

Moisture effects are incorporated in the model through the total embrittlement time. The model captures the embrittled fiber failure mechanism by failing all embrittled fibers in a tow when

one fails. Figures 106 and 107 are plots of the modeling results using different total

embrittlement times for the 550°C and 750°C environments, respectively. The total embrittlement

time decreases as temperature and moisture increase. The trends in the modeling results as the

total embrittlement time changes match the trends in the experimental data as the moisture

content changes. It is clear from these plots that the total embrittlement time is very important to

modeling the behavior of the stress rupture strength degradation of the CMC as moisture content

changes.
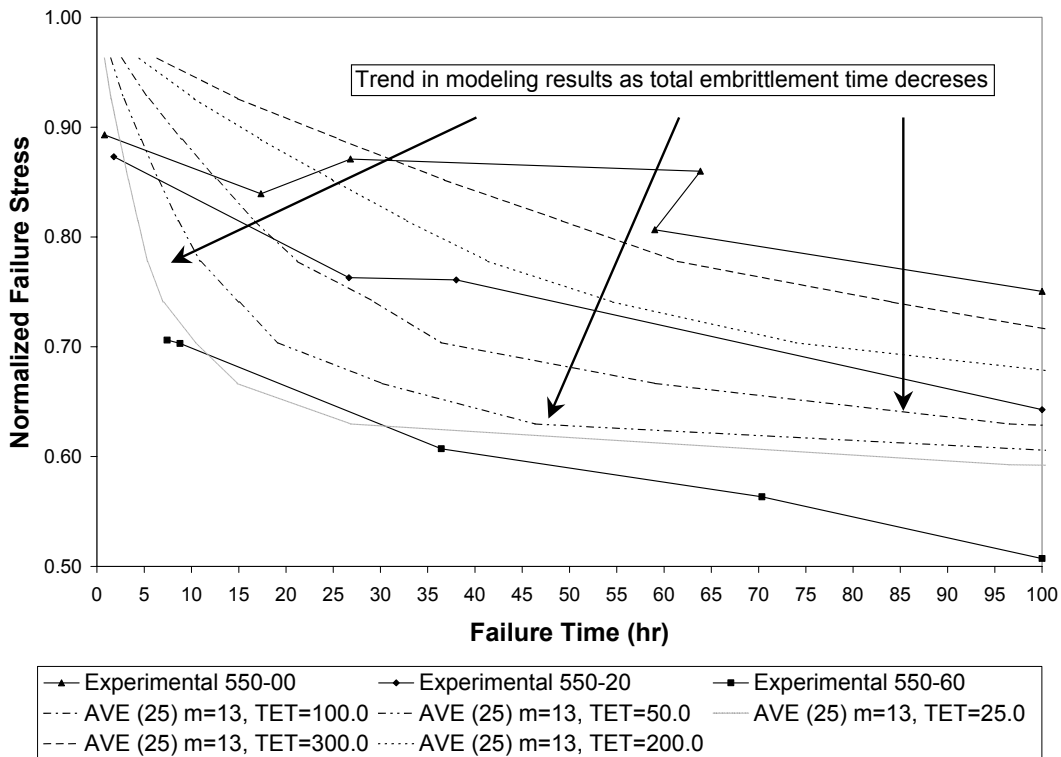
Figure 107: Effects of Embrittlement Time on Modeling Results at 550°C
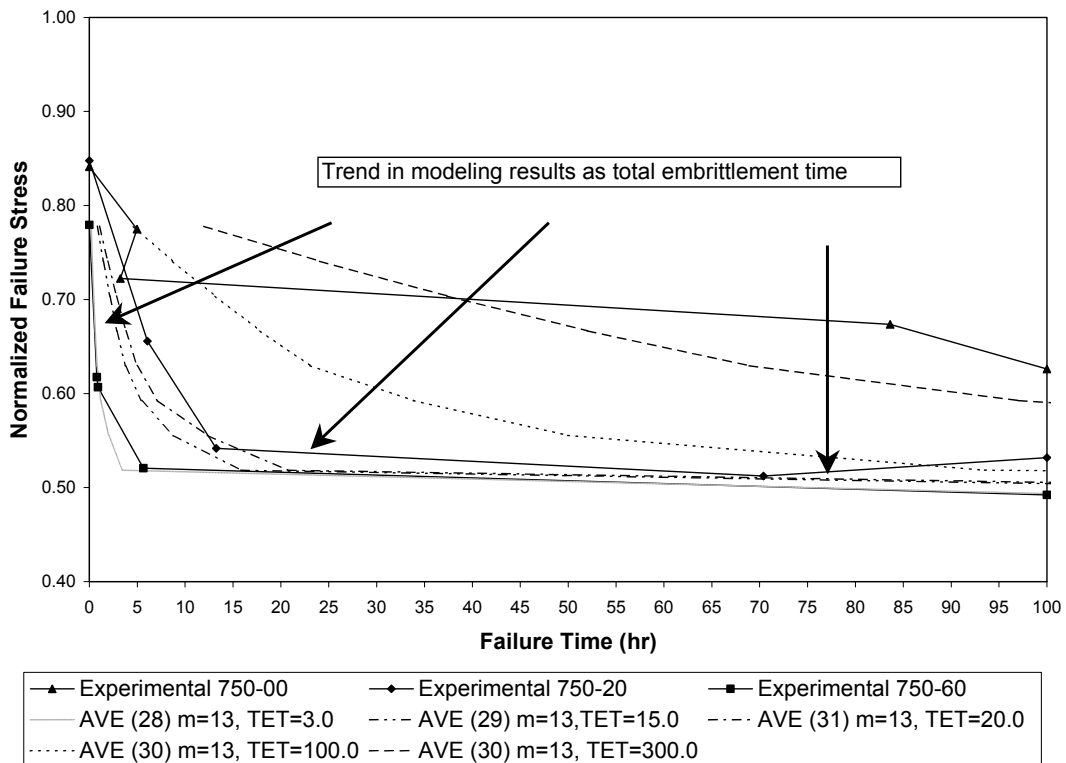
Figure 108: Effects of Embrittlement Time on Modeling Results at 750°C

There are several differences between the model developed by Morscher and Cawley [17] that is presented in Appendix A and the model developed in the present study. The previous model predicted the life of the HN/BN/SiC and Syl/BN/SiC CMCs at 815°C, whereas this study models the life of the Syl-iBN/BN/SiC CMC at intermediate temperatures between 550-750°C while taking into account moisture content levels of 0.0, 0.2, and 0.6 atm pH_2O. The previous model did not update the crack opening length as fibers failed, whereas this model incorporates an updated crack opening length in the fiber strength equations as fibers fail. The previous model assumed that when one embrittled fiber failed all other embrittled fibers in the whole cross-section failed, whereas this model assumes an embrittled fiber failure only causes the other embrittled fibers in the tow to fail. The previous model is a probabilistic model based on fiber theory, whereas this model is a Monte Carlo-type model based on similar fiber theory. The previous model does not take into account the load carried by the fibers that fail in the stress transfer region, whereas this model will distribute the load in the stress transfer length and thus accounts for the appropriate relationship between load and failure. The following discussion addresses

each of these differences between the previous modeling effort and the modeling effort of this research.

The Syl-iBN/BN/SiC system was chosen for two main reasons. The Syl-iBN fiber preforms were donated for this research by NASA Glenn Research Center because little data has been collected on CMCs with this type of fiber for the test conditions investigated in this research. As shown earlier, a lot of work has been done on the HN/BN/SiC. The SiC matrix and BN interphase were chosen because the SiC/SiC system is the CMC system best suited for combustor applications and BN is currently the interphase of choice for SiC/SiC composites.

As mentioned above and presented in Chapter V, Morscher and Cawley [17] developed a technique for generating an equation for fiber strength degradation based on time and at 815°C. The present modeling effort modified their techniques for the temperature range of 550-750°C and generated equations that are functions of both time and temperature instead of time only. The fiber strength degradation can now be determined by knowing the time and temperature for the intermediate temperature range.

The model presented in Chapter V uses Marshall et al [68] theory to calculate the crack opening as does the previous model. However, the previous model calculated the crack opening and used the same value during a simulation. The crack opening is dependent on material properties and on fiber volume fraction, which will change as fibers fail. Therefore, it is appropriate to recalculate it as time progresses and as fibers fail. The present model incorporated the crack opening length into the strength equations so that at every time step throughout the model the effect of a changing crack opening length due to fiber failures is taken into account.

The probabilistic approach of the previous model combined the probabilities of failure for all embrittled fibers. When the probability reached 1.0, an embrittled fiber failure was guaranteed and it was assumed that all other embrittled fibers failed as well. This was due to strong bonding between embrittled fibers. This assumption means that after the entire crack is embrittled, the specimen fails when the next fiber fails, thus reducing the strength of the specimen to the strength of the weakest fiber. The model in this research assumes that only the embrittled fibers

170

in the tow of the failing fiber simultaneously fail. The end results are similar because the distribution of fiber strengths was such that the stress transferred to the fibers in other tows usually resulted in an embrittled fiber failing from one of those tows, thus failing all embrittled fibers in that tow, etc. So the difference in the models would be at the early stages of the model where there are fewer embrittled fibers in the tows.

The model presented in this research failed both embrittled fibers and pristine fibers. If a pristine fiber failed, the percentage of load the fiber still supported through interfacial shear was calculated. If an embrittled fiber failed, the fiber did not support any load. The previous model only calculated embrittled fiber failures and used the composite failure theory of Curtin et al [21] to check for composite failure. The model presented in this research compared individual fiber strengths with the applied stress on them until all fibers failed based on individual fiber failure mechanisms.

A parameter sensitivity analysis looked at variation in the key parameters of the model. The amount of the variation represented realistic variation in CMC properties. Variation in the number of through-the-thickness cracks showed that the stress rupture curve converges as the number of cracks increases. However, little fidelity in the curve was gained beyond 10 cracks. Variation in the Weibull parameter, m, defined the overall shape of the curve. As it increased, the intercept of the initial portion of the stress rupture curve was decreased and the bottom part of the curve was raised. Variation in the modulus of elasticity of the composite, E_c, and modulus of elasticity of the fiber, E_f, had little effect on the stress rupture curve. This was expected since the individual fiber strengths are predominantly governed by the fiber strength in the stress transfer region, which is not a function of E_c or E_f.

If a relationship can be developed for this CMC system that shows the dependence of the number of through-the-thickness matrix cracks on E_m, then the effects of a changing E_c could be seen in this model. Variation in the interfacial shear stress ratio, τ ratio, had slight effects on the stress rupture curve. Variation in various strengths, σ_{ultRT}, σ_{ult}, and σ_o had significant effects on the stress rupture curve. A small ±5% variation in σ_{ultRT} and σ_{ult} and a ±10% linear variation in σ_o

171

captured nearly all the experimental data scatter in both cases. In all parameter variation

analyses, the 550°C model was slightly more sensitive than the 750°C.

Although most of the modeling results from the parameter sensitivity analysis in Chapter

V captured the experimental data by using realistic variations to the parameters, none of the

variations created trends in the modeling data that matched the trends in the experimental data.

By changing the total embrittlement time, the model developed in this research accurately

predicted the stress rupture behavior of the Syl-iBN/BN/SiC CMC system at intermediate

temperature under humid conditions. This research shows that the embrittlement time is a

function of pH$_2$O and the effects of moisture can be modeled using the proposed model and

varying the total embrittlement time.

VII.   Summary and Conclusions

This research combined experimental and analytical techniques to answer important questions concerning how moisture affects the constituent materials of the Syl-iBN/BN/SiC CMC system and the resulting strength degradation as a function of time, intermediate temperature, and moisture content level. Monotonic tensile tests at room temperature were conducted to gather material property data and provide fracture surfaces using FESEM. These fracture surface images showed normal CMC failure mechanisms and were used as baseline images. Monotonic test in various environments were conducted to investigate the effect of temperature and moisture on the material properties and the provide fracture surfaces for FESEM analysis and comparison to the baseline fracture surface images. Stress rupture tests in the various environments were conducted to gather strength reduction data and to provide fractures surfaces to compare with the baseline fracture surface and to investigate how the embrittlement phenomenon changes with respect to time, temperature, and moisture content.

The results of the experimental portion of this research led to a new approach to modeling CMC failure. This model, with an accompanying parameter sensitivity analysis, gives a better understanding of CMC failure due to embrittlement at intermediate temperature under humid conditions and can predict the effects of embrittlement. This research provided insight for the Air Force Research Laboratory and the civilian turbine engine community. The understanding of the moisture and intermediate temperature effects on the stress rupture life will lead to better designs of engine components that meet Air Force and civilian needs. The contributions of this research have also shed light on future research that needs to be done. The research presented here is an introduction into the moisture effects at intermediate temperatures. To completely understand how the environmental affects on the performance of new CMC materials used in the combustion environment of a turbine engine, more research must be done.

Environmental Embrittlement of CMCs

Prior to this research several studies investigated the stress rupture behavior of the Nic/SiC and HN/SiC CMC systems at intermediate and high temperatures. The studies at intermediate temperatures showed a dramatic reduction in the strength for these systems and identified embrittlement as the detrimental cause of strength degradation and poor performance of the CMC material. The applied stress caused through-the-thickness cracks which, added to the network of pores throughout the material, allowed the environment into the interior of the material causing embrittlement.   Embrittlement occurred at intermediate temperatures due to the pesting of load bearing fibers caused by the oxidation of the BN interphase by the O_2 and the reaction of the oxidation by-products with the trace amounts of H_2O in the ambient testing environment.

The previous state of the art understanding of this phenomenon was that is was a gaseous diffusion controlled process occurring at the outside edge of the specimen first and then moving towards the center of the specimen. The temperature, the amount of reactants, the consumption rate of the reactants, and the type of material controlled the diffusion of the embrittlement through the crack. This process has been described as a "picture frame" phenomenon where the center has pristine fibers and the outside edge has embrittled fibers. Embrittlement changed the failure mechanism of the embrittled fibers such that the fibers that pested together failed when the weakest fiber failed. The effect of moisture was known to be one step in the embrittlement phenomenon, but the effect of changing the amount of moisture on the strength of the CMC was unknown. None of the previous studies attempted to quantify the effects of moisture at intermediate temperatures.

This research focused on an area of interest that has not previously been studied; intermediate temperature and moisture effects on the strength degradation of the Syl-iBN/BN/SiC CMC system, which is the state of the art SiC/SiC CMC system. It investigated the effects of the following environmental conditions: 550^oC and 750^oC with controlled moisture levels of 0.0, 0.2, and 0.6 atm pH_2O at each temperature. The research combined experimental and analytical

work that quantified and modeled the effects of the different environments on the stress rupture life of the Syl-iBN/BN/SiC CMC material.

Using FESEM this research showed that both the amount of moisture and the temperature of the environment have deleterious effects on the strength of the Syl-iBN/BN/SiC CMC in the intermediate temperature range by speeding up the embrittlement process of a CMC by pesting the loading bearing fibers in a through-the-thickness crack. It showed that as temperature increased and/or the moisture content increased, there was more evidence of embrittlement. The amount of embrittlement was a function of time for a given environment, thus explaining the increase in strength degradation.

When comparing the FESEM images for the 550°C and 750°C results with similar moisture content, the amount of embrittlement observed at 0.0 atm pH_2O was similar for each temperature, however, at 0.6 atm pH_2O there was more embrittlement at 750°C. In fact, the worst case scenario was the 750°C with 0.6 atm pH_2O. At 550°C, there was increasing and consistent degradation with increasing moisture content. However, at 750°C, although the degradation increased with moisture content and was larger than the 550°C cases, the magnitude of the normalized strength degradation converged as moisture content increased. This was evident in the normalized (stress rupture failure stress divided by the room temperature ultimate strength) 100-hour strengths, that is, 75%, 65% and 51% for the 550°C with 0, 0.2, or 0.6 atm pH_2O cases, respectively, and 67%, 51%, and 49% for the 750°C with similar moisture content, respectively. Embrittlement at 550°C was more dependent on moisture content than at 750°C. At 550°C the rupture life of the specimen was reduced over the entire 100-hour test time as the moisture content is increased. At 750°C the stress rupture curves converged quickly to approximately 50% of the room temperature ultimate strength. Also, the embrittlement phenomenon was surface chemistry kinetics controlled at these temperatures resulting in the embrittlement occurring randomly over the entire fracture surface. This was attributed to a transition from gaseous diffusion controlled embrittlement to surface chemistry kinetics controlled embrittlement

The analysis of the experimental results led to a new approach of modeling CMC failure. Unique strength equations for individual fibers in the presence of a through-the-thickness crack were developed that started with analytical equations developed by Morscher and Cawley [17] and were based on material properties, specimen specifications, loading conditions, and environmental effects on the failure mechanisms of fibers in a CMC system seen in this research as well as previous research. The individual fiber performance was then related to the overall CMC performance. The formulation of the model includes the fundamentals of cracking effects, material properties, specimen properties, individual fiber characteristics, strength degradation, and embrittlement effects. The parameters representing these physical characteristics of CMC failure were crack opening length, slip transfer length, crack spacing interfacial shear stress, modulus of elasticity of the constituents, number of fibers, number of tows, volume fraction of fibers, fiber radius, Weibull distribution of strength among fibers, strength reduction due to the manufacturing process, strength reduction as a function of time and temperature, and the total embrittlement time of a crack surface. Using the FESEM analysis mentioned above it was determined that the amount of moisture and temperature of the environment control the time it takes to completely embrittle a fracture plane. The affects of moisture and temperature were incorporated in the model through this parameter. Temperature was also incorporated into the model through the time degradation of the fiber reference strength.

This research studied and analyzed the effects of parameter variation on the stress rupture simulation. Variations were used that represented realistic scatter due to the nature of CMC materials. This parameter sensitivity analysis gave credibility to the model and showed that CMC failure could be modeled by modeling individual fibers and the effect they have on each other. It showed that the ultimate strength at room temperature, the ultimate strength in the testing environments, and the reference strength of the fibers are the most sensitive parameters. This is important because the room temperature ultimate strength of the material is subjected to a significant amount of scatter and the ultimate strength in the testing environment and the reference strength of the fiber are the parameter most affected by the environment. This understanding will help designers develop better materials for future applications.

Future Work

The work presented here established that moisture and intermediate temperature caused the pesting of load bearing tows to occur faster resulting in severe strength degradation as a function of time, temperature, and moisture. This research is an important step in studying the effects of moisture. However, more work needs to be done to quantify the effects and determine a relationship between degradation of strength to temperature and moisture content level. The temperature effects on the fiber strength degradation have been established. Additional data would be useful to investigate if the temperature has an effect on the crack formation and propagation through the matrix material. This research showed that the stress rupture life is only slightly sensitive to the number of cracks in the specimen. However, the assumption was made that the cracks formed and propagated instantaneously at the start of the loading. It would be beneficial to gain an understanding on how the crack formation and propagation affects the fiber strengths and the embrittlement process and if moisture affects crack formation and propagation.

The effect of moisture content level on the embrittlement phenomenon at a particular temperature needs to be understood more thoroughly. Investigating one or two particular environments, tests could be designed to collect the necessary data to determine if there exists a critical pH_2O at a given temperature such that above this pH_2O the effects are not distinguishable. This information would be important to turbine engine designers.

Also, future work should focus on a potential transition time that may exist between when a pristine fiber starts to embrittle and when the embrittlement is detrimental to the fiber (i.e. the pesting causes neighboring fibers to fail when any embrittled fiber in the bunch fails). This is important to understand because the failure of an embrittled fiber results in the failure of all fibers pested to it regardless of their strengths, thus, reducing the embrittled region to a monolithic ceramic with the strength of the weakest fiber. The embrittlement kinetics needs to be investigated to gain an understanding of this potential transition.

Appendix A

Larson-Miller Plots

Integration of the differential form of the Arrhenius equation leads to steady state creep strain by discarding the constant of integration:

$$d\varepsilon = A(\sigma)e^{\frac{-Q}{RT}}dt$$

65

$$\varepsilon = A(\sigma)te^{\frac{-Q}{RT}}$$

66

where

$\varepsilon \equiv$ strain
$A(\sigma) \equiv$ material dependent function of stress
$t \equiv$ time (hr)

This suggests that at a given stress the creep strains form a unique curve if plotted versus the quantity θ, called the temperature-compensated time:

$$\theta = te^{\frac{-Q}{RT}}$$

67

To develop the Larson-Miller Parameter, take the logarithm to the base ten of both sides of Equation 66 and rearrange:

$$\frac{\log_{10} e}{R}\frac{Q}{T} = \log t - \log \theta$$

68

The Larson-Miller Parameter, P_{LM}, is then defined as all none time and temperature dependent terms:

$$P_{LM} = \frac{\log_{10} e}{R} Q \tag{69}$$

$$P_{LM} = T(\log t - \log \theta) \tag{70}$$

Moisture Content

For the air, the volume of heated air at atmospheric pressure can be related to the volume of air under heated conditions using the ideal gas equation of state:

$$nR = \frac{P_i V_i}{T_i} \tag{71}$$

where

$n \equiv$ number of moles
$R \equiv$ universal gas constant (0.082061 l•atm/mol•K)
$P_i \equiv$ pressure at i (atm)
$V_i \equiv$ volume at i (l)
$T_i \equiv$ temperature at i (K)

Since R is constant and n and P are the same before and after heating, the volume of the air in the heating chamber can be related to the volume of the input air in the following way:

$$\frac{V_{in}}{T_{in}} = \frac{V_A}{T_A} \tag{72}$$

where

$V_{in} \equiv$ volume of the input air
$T_{in} \equiv$ temperature of the input air
$V_A \equiv$ volume of air in the heating chamber
$T_A \equiv$ temperature of air in the heating chamber

Solve for the volume of the heating chamber air:

$$V_A = \frac{V_{in} T_A}{T_{in}} \tag{73}$$

179

To calculate the volume rate of steam, or water vapor rate, multiply the input water flow rate by the specific volume of steam at the test temperature. The total volume rate, V_T, is the sum of the water vapor volume rate, V_w, and the air volume rate, V_A:

$$V_T = V_A + V_W \qquad\qquad \textbf{74}$$

Next, calculate the molar rate of water, n_w, by dividing the mass rate of water by the molecular weight of water:

$$n_w = \frac{x\ grams}{min} \frac{mol}{18\ grams} = \frac{x\ mol}{18\ min} \qquad\qquad \textbf{75}$$

Calculate the partial pressure of water, pH_2O, in atm using the Ideal Gas Law:

$$p = \frac{n_w RT}{V_T} \qquad\qquad \textbf{76}$$

Crack Opening Length (Marshall et al [69])

Start with the assumption that the applied stress, σ_a, is equivalent to the sum of the stress on all fibers:

$$\sigma_a = Tf \qquad\qquad \textbf{77}$$

where

$T \equiv$ stress (MPa)
$f \equiv$ number of fibers

Assuming the matrix strain and the fibers strain are equivalent at some plane AA' (see Figure 109 which shows a diagram of a single fiber bridging a crack opening); the traction will have the following relation:

$$\frac{T_m}{E_m} = \frac{T_f}{E_f} \qquad\qquad \textbf{78}$$

where

$T_m \equiv$ stress on the matrix (MPa)
$T_f \equiv$ stress on the fiber (MPa)
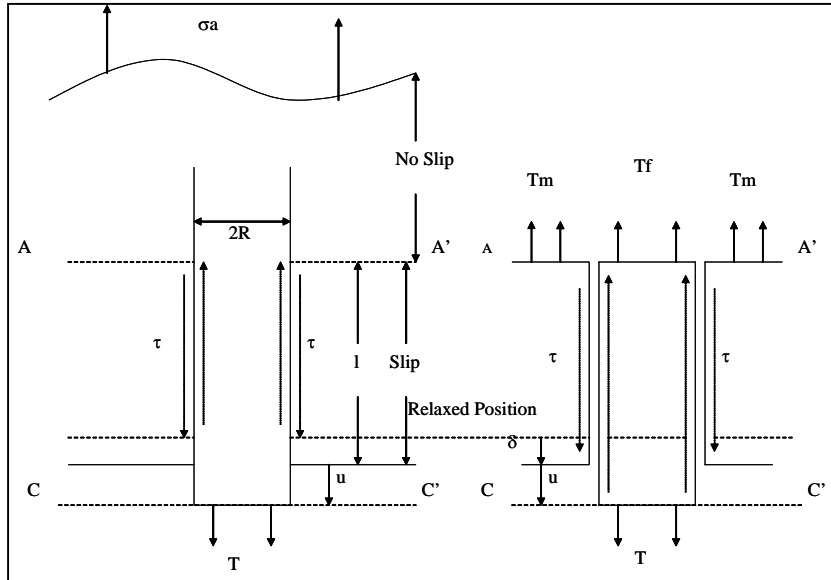
Figure 109: Bridged Crack Opening Diagram [69]

Sum the forces on the matrix:

$$T_m A_m = 2\pi R l \tau$$

79

where

$A_m \equiv$ area of matrix (m^2)
$R \equiv$ fiber radius (m)
$l \equiv$ fiber length (m)

Sum the forces on the fiber:

$$TA_f = 2\pi R l \tau + T_f A_f$$

80

where

$A_f \equiv$ Area of fiber (m^2)

Calculate the extension δ/l:

$$\frac{\delta}{l} = \frac{\pi R l \tau}{A_m E_m}$$

81

Calculate the extension (δ+u)/l:

$$\frac{(\delta + u)}{l} = \frac{T_f}{E_f} + \frac{\pi R l \tau}{A_f E_f}$$

Combine Equations 77, 78, and 79 and simplify:

$$TA_f = 2\pi R l \tau + \frac{E_f}{E_m} \frac{2\pi R l \tau}{A_m} \cdot A_f$$

$$T = \frac{2l\tau}{R} + \frac{E_f}{E_m} \frac{2\pi R l \tau}{A_m} = \frac{2l\tau}{R}\left(1 + \frac{E_f}{E_m} \frac{\pi R^2 l}{lA_m}\right)$$

$$T = \frac{2l\tau}{R}\left(1 + \frac{E_f}{E_m} \frac{V_f}{V_m}\right)$$

Combine Equations 77, 78, 80, and 81 and simplify:

$$\frac{u_o}{l} = \frac{T_f}{E_f} + \frac{\pi R l \tau}{A_f E_f} - \frac{\pi R l \tau}{A_m E_m} = \frac{T_f}{E_f} + \frac{\pi R l \tau}{A_f E_f} - \frac{T_f}{2E_f} = \frac{l\tau}{RE_f}\left(1 + \frac{T_f R}{2l\tau}\right)$$

$$\frac{u_o}{l} = \frac{l\tau}{RE_f}\left(1 + \frac{E_f}{E_m} \frac{V_f}{V_m}\right)$$

$$l^2 = \frac{u_o RE_f}{\tau\left(1 + \frac{E_f V_f}{E_m V_m}\right)}$$

Combine Equations 85 and 88 and simplify:

$$T = \frac{2\tau}{R}\left(1 + \frac{E_f}{E_m} \frac{V_f}{V_m}\right)\left(\frac{u_o RE_f}{\tau\left(1 + \frac{E_f V_f}{E_m V_m}\right)}\right)^{\frac{1}{2}}$$

$$T = 2\left[\frac{u_o E_f \tau \left(1 + \frac{E_f V_f}{E_m V_m}\right)}{R}\right]^{\frac{1}{2}}$$ **90**

Combine Equation 74 and 90, using u = 2u$_o$, and solve for u:

$$\sigma_a = 2\left[\frac{\frac{u}{2} E_f \tau \left(1 + \frac{E_f V_f}{E_m V_m}\right)}{R}\right]^{\frac{1}{2}} f$$ **91**

$$\sigma_{f,c}^2 = \left[\frac{2u E_f \tau \left(1 + \frac{E_f V_f}{E_m V_m}\right)}{R}\right]$$ **92**

$$u = \frac{\sigma_{f,c}^2 R}{2\tau_T E_f \left(1 + \frac{E_f f}{E_m (1 - f)}\right)}$$ **93**

Strength Reduction Factor

Continuing with the formulations of Curtin [22] and Curtin et al [21], Morscher and Cawley [17] found an analytical solution for this strength reduction factor. Curtin et at [21] found the ultimate strength of a CMC to be:

$$\sigma_{ult} = f\sigma_c \left[\frac{2(m+1)}{m(m+2)}\right]^{\frac{1}{m+1}} \left[\frac{m+1}{m+2}\right]$$ **94**

$$\sigma_c = \left(\sigma_o^m \cdot \tau \cdot \frac{L_o}{R}\right)^{\frac{1}{(m+1)}}$$ **95**

Substituting Equation 95 into Equation 94, Morscher [10] solved for σ_o for a composite fiber:

$$\sigma_{o\,composite} = \left[\frac{m(m+2)R}{2(m+1)\tau_{ult}L_o} \left(\frac{m+2}{m+1} \frac{\sigma_{ult}}{f_{init}} \right)^{m+1} \right]^{\frac{1}{m}}$$

96

where

$\tau_{ult} \equiv$ interfacial shear stress during ultimate strength test (MPa)

Yun and DiCarlo [27] found that the σ_o for the as-produced SiC fibers used in this research is 2800 MPa. Therefore the strength reduction factor becomes:

$$SR = \frac{\left[\frac{m(m+2)R}{2(m+1)\tau_{ult}L_o} \left(\frac{m+2}{m+1} \frac{\sigma_{ult}}{f_{init}} \right)^{m+1} \right]^{\frac{1}{m}}}{2800}$$

97

Previous Study

Their formulation is as follows:

The stress on a fiber in a bridged matrix crack, σf, is defined as:

$$\sigma_f = \frac{\sigma}{f}$$

98

where

$\sigma \equiv$ applied stress on the CMC specimen (MPa)
$f \equiv$ fiber volume fraction in the loading direction

Fiber failure follows a Weibull distribution that can be used to determine the probability of failure, $P(\sigma, L)$:

$$P(\sigma, L) = 1 - e^{-\Phi}$$

99

where

$L \equiv$ length of fiber (m)
$\Phi \equiv$ fraction of failed fibers

Φ can be determined by:

$$\Phi = \frac{L}{L_o}\left(\frac{\sigma_f}{\sigma_o}\right)^m$$

where

$L_o \equiv$ reference length of fiber (m)
$\sigma_o \equiv$ reference stress of the fiber (MPa)
$m \equiv$ Weibull parameter

The adoption of the formulation of Curtin's [22] characteristic stress, σ_c, and characteristic gauge length, δ_c, proved useful:

$$\sigma_c = \left(\frac{\sigma_o^m \tau L_o}{R}\right)^{\frac{1}{m+1}} ; \delta_c = \frac{R\sigma_c}{\tau}$$

101

$$\Phi(\sigma_c, \delta_c) = 1$$

102

where

$\tau \equiv$ interfacial shear stress (MPa)
$R \equiv$ radius of the fiber (m)

In the crack opening region the effective gauge length or fiber length, L, is simply the crack opening, u. Therefore, the fraction of fibers that fail in the crack opening region, Φ_u, is:

$$\Phi_u = \left(\frac{u}{L_o}\right)\left(\frac{\sigma_f}{\sigma_o}\right)^m$$

103

The crack opening, u, was solved using the formulation by Marshall et al [69] presented earlier:

$$u = \frac{\sigma^2 R}{4\tau f^2 E_f\left(1 + \frac{E_f f}{E_m(1-f)}\right)}$$

104

where

$E_f \equiv$ modulus of elasticity of the fiber (GPa)
$E_m \equiv$ modulus of elasticity of the matrix (GPa)

In the stress transfer region, z, the stress on the fiber varies along the fiber because of load transfer between the fiber and the matrix caused by friction. Based on Equation 12, other researchers [10,21,23] made an assumption that the far field stress on the fibers is zero for the case when z is equal to twice

the fiber slip length, $\delta/2$. This is a reasonable assumption since the contribution to Φ from the low far field fiber stress, $\sim 0.2\ \sigma_{f,c}$, is negligible [10]. Therefore, δ can be approximated by:

$$\delta = \frac{\sigma_{f,c}R}{\tau}$$ **105**

Solving Equation 12 using Equation 105 gives fraction of failed fibers in the stress transfer region. The formulation is as follows:

Assume z is twice the slip length:

$$z = 2 \cdot \frac{\delta}{2} = \delta$$ **106**

Define $\sigma(x)$ as the stress along the fiber:

$$\sigma(x) = \sigma_{f,c} - \frac{2 \cdot \tau}{R} \cdot x$$ **107**

Substitute Equations 106 and 107 into Equation 12 and simplify:

$$\Phi_z = \frac{1}{\sigma_o^m \cdot L_o} \int_0^{\delta} \left(\sigma_{f,c} - \frac{2 \cdot \tau}{R} \cdot x \right)^m dx$$ **108**

Define:

$$a = \sigma_{f,c} - \frac{2 \cdot \tau}{R} \cdot x$$ **109**

$$dx = -\frac{R}{2 \cdot \tau} da$$ **110**

Substitute Equations 109 and 110 into Equation 108, integrate, and simplify:

$$\Phi_z = \frac{-R}{\sigma_o^m \cdot L_o \cdot 2 \cdot \tau} \int_0^{\delta} (a)^m da$$ **111**

$$\Phi_z = \frac{-R}{\sigma_o^m \cdot L_o \cdot 2 \cdot \tau} \left[\frac{1}{m+1} \cdot \left(a(\delta)^{m+1} - a(0)^{m+1} \right) \right]$$

<div align="right">112</div>

$$\Phi_z = \frac{-R}{\sigma_o^m \cdot L_o \cdot 2 \cdot \tau \cdot (m+1)} \cdot \left(\left(\sigma_{f,c} - \frac{2 \cdot \tau}{R} \cdot \delta \right)^{m+1} - \left(\sigma_{f,c} \right)^{m+1} \right)$$

<div align="right">113</div>

Substitute Equations 13 and 105 and simplify:

<div align="right">114</div>

$$\Phi_z = \frac{-R}{\sigma_o^m \cdot L_o \cdot 2 \cdot \tau \cdot (m+1)} \cdot \left(\left(\sigma_{f,c} - \frac{2 \cdot \tau}{R} \cdot \delta \right)^{m+1} - \left(\sigma_{f,c} \right)^{m+1} \right)$$

$$\Phi_z = \frac{-1}{\sigma_c^{m+1} \cdot 2 \cdot (m+1)} \cdot \left(-2 \cdot \left(\sigma_{f,c} \right)^{m+1} \right)$$

<div align="right">115</div>

$$\Phi_z = \frac{\left(\dfrac{\sigma_{f,c}}{\sigma_c} \right)^{m+1}}{(m+1)}$$

<div align="right">116</div>

The total fraction of fiber failure is the sum of Equations 103 and 116 simplifying with Equation 101:

$$\Phi_{t,T} = \frac{K_\Phi}{\sigma_{o(t,T)}^m}$$

<div align="right">117</div>

$$K_\Phi = \left(\frac{\sigma_f^m}{L_o} \right) \left(\frac{\delta}{m+1} + u \right)$$

Using the data in Figure 18 the depth of embrittlement can be determined as:

$$x = C_{ox} t^{\frac{1}{2}}$$

<div align="right">118</div>

Using the data in Figure 7 the fiber strength as a function of time at 815°C can be determined as:

<div align="right">119</div>

$$\sigma_{o(t,T)} = C_f t^{-\frac{1}{n}}$$

<div align="center">187</div>

The fibers experience a strength reduction due to processing and manufacturing. The composite failure criterion of Curtin et al [21] was used:

$$\sigma_{ult} = \sigma_c \left[\frac{2(m+2)}{m(m+1)} \right]^{\frac{1}{m+1}} \left[\frac{m+1}{m+2} \right]$$

120

where

$\sigma_{ult} \equiv$ ultimate strength of the specimen (MPa)

The ultimate strength of the fibers in the composite can be estimated by solving for σ_o from Equations 120 and 101.

$$\sigma_{o(composite)} = \left[\frac{m(m+2)}{2(m+1)} \frac{R}{\tau L_o} \left(\frac{m+2}{m+1} \sigma_{ult} \right)^{m+1} \right]^{\frac{1}{m}}$$

121

where

$\sigma_{o(composite)} \equiv$ reference strength of a fiber in a composite (MPa)

The strength reduction is Equation 121 divided by the room temperature reference strength of 2800 MPa [27]. Applying this to Equation 119:

$$\sigma_{o(t,T)} = \frac{\sigma_{o(composite)}}{\sigma_{o(RT)}} C_f t^{-\frac{1}{n}} = C_{frupture} t^{-\frac{1}{n}}$$

122

The fraction of fiber failure as a function of depth of embrittlement is generated by substituting Equation 122 into Equation 117 and converting Equation 118 as function of x:

$$\Phi_{t,T} = \frac{K_\Phi}{C_{frupture}^m} \left(\frac{x}{C_{ox}} \right)^{\frac{2m}{n}}$$

123

Knowing some fibers will fail prior to becoming embrittled the fraction of fiber failure after they are embrittled is determined:

$$\Phi_{emb} = \Phi_{t\max} - \Phi_t = \frac{K_\Phi}{C_{frupture}^m C_{ox}^{\frac{2m}{n}}}\left(x_{\max}^{\frac{2m}{n}} - x^{\frac{2m}{n}}\right)$$

124

The number of embrittled fiber failures before total embrittlement can be determined by the product of the number of fibers per unit thickness, N_x, and the integration of Φ_{emb} over the maximum depth of embrittlement:

$$N_{femb}^{t<temb} = N_x \int_o^{x_{\max}} \Phi_{emb}dx = \frac{N_x K_\Phi}{C_{frupture}^m C_{ox}^{\frac{2m}{n}}} x_{\max}^{\left(\frac{2m}{n}+1\right)}\left(1 - \frac{1}{\frac{2m}{n}+1}\right)$$

125

The number of embrittled fiber failures after total embrittlement time assuming no embrittled fibers fail prior is determined by:

$$N_{femb}^{t>temb} = N_{femb}^{t<temb} + N_f\left(\Phi_t - \Phi_{temb}\right) = N_{femb}^{t<temb} + N_f \frac{K_\Phi}{C_{frupture}^m}\times\left(t^{\frac{m}{n}} - t_{emb}^{\frac{m}{n}}\right)$$

126

When an embrittled fiber fails all embrittled fibers fail due to the strong bond between embrittled fibers. The remaining pristine fibers are checked against the ultimate strength criteria of Curtin et al [21]:

$$\sigma_{ult} = \sigma_c e^{\frac{1}{m+1}}$$

127

The stress on the remaining pristine fibers, σ_{ffail}, is determined by:

$$\sigma_{ffail} = \frac{\sigma_f}{1 - f_{emb}} ; f_{emb} = \frac{2x_{tffail}}{b}$$

128

where

$f_{emb} \equiv$ fraction of fiber that have been embrittled

To account for multiple cracks, multiply the number of embrittled failures with a single crack by the number of cracks. The model was run for two regimes of rupture behavior: (a) oxidation kinetics controlled rupture and (b) single fiber failure controlled failure.

Bibliography

1. K.M. Prewo and J.J. Brennan, "High Strength Silicon Carbide Fiber Reinforced Glass Matrix Composites," *J. Mater. Sci.*, **15** [2] 463-68 (1980).

2. D.B. Marshall and A.G. Evans, "Failure Mechanisms in Ceramic-Fiber/Ceramic-Matrix Composites," *J. Am. Ceram. Soc.*, **68** [5] 225-231 (1985).

3. D. Brewer, "HSR/EPM combustor materials development program," *Mater. Sci. Eng.*, A261 284-291 (1999).

4. Photo provided by R.L. Sikorski. Air Force Research Laboratory, Wright Patterson Air Force Base, OH. Email Correspondence. December 2000.

5. Recreated and modified by Mike Bruggeman from J.D. Mattingly, <u>Elements of Gas Turbine Propulsion</u>, McGraw-Hill, Inc, New York, 1996.

6. R.G. McNally. Chief Propulsion Branch, Turbine Engine Division, Propulsion Directorate, Air Force Research Laboratory, Wright Patterson Air Force Base, OH. Personal Correspondence. December 2003.

7. J.J. Brennan, "Interfacial Characterization of Glass and Glass-Ceramic Matrix/Nicalon SiC Fiber Composites," *Mater. Sci. Res.*, **20**, 546-60 (1986).

8. R.F. Cooper and K. Chyung, "Structure and Chemistry of Fiber-Reinforced Ceramics," *J. Mater. Sci.*, **22**, 3148-60 (1987).

9. H. Cao, E. Bischoff, O. Sbaizero, M. Ruhle, A.G. Evans, D.B. Marshall, and J.J. Brennan, "Effect of Interfaces on the properties of Fiber-Reinforced Ceramics," *J. Amer. Ceram. Soc.*, **73** [6] 1691-99 (1990).

10. G.N. Morscher, "Intermediate Temperature Stress Rupture of Woven SiC Fiber, BN Interphase, SiC Matrix Composites in Air," Ph.D. Dissertation, Case Western Reserve University (January 2000).

11. N.S. Jacobson, S. Farmer, A. Moore, and H. Sayir, "High Temperature Oxidation Behavior of Boron Nitride Part I: Monolithic BN," *J. Am. Ceram. Soc.* **82** [2] 393-8 (1999).

12. N.S. Jacobson, G.N. Morscher, D.R. Bryant, and R.E. Tressler, "High Temperature Oxidation of Boron Nitride Part II: BN Layers in Composites," *J. Am. Ceram. Soc.* **82** [6] 1473-82 (1999).

13. F.E. Heredia, J.C. McNulty, F.W. Zok, and A.G. Evans, "Oxidation Embrittlement Probe for Ceramic-Matrix Composites," *J. Am. Ceram. Soc.*, **78** [8] 2097-100 (1995).

14. E.J. Opila and R.E. Hann Jr., "Paralinear Oxidation of CVD SiC in Water Vapor," *J. Am. Ceram. Soc.*, **80** [1] 197-205 (1997).

15. N.S. Jacobson, "Corrossion of Silicon-Based Ceramics in Combustion Environments," *J. Am. Ceram. Soc.*, **76** [1] 3-28 (1993).

16.   G.N. Morscher. Senior Research Associate, Ohio Aerospace Institute, NASA Glenn Research Center, Cleveland OH. Personal Correspondence. 05 Nov 03.

17.   G.N. Morscher and J.D. Cawley, "Intermediate Temperature Strength Degradation in SiC/SiC Composites," J. European Ceramic Society, vol. 22, no. 14-15, pp. 2777-2788 (2002).

18.   K.K. Chawla, Ceramic Matrix Composites, Chapman and Hall, London, 1993.

19.   B. Budiansky, J.W. Hutchinson, and A.G. Evans, "Matrix Fracture in Fiber-Reinforced Ceramics," *J. Mech. Phys. Solids*, **34** [2] 167-189 (1986).

20.   S. Danchaivijit and D.K. Shetty, "Matrix Cracking in Ceramic-Matrix Composites," *J. Am. Ceram. Soc.*, **76** [10] 2497-504 (1993).

21.   W.A. Curtin, B. K. Ahn, and N. Tekeda, "Modeling Brittle and Tough Stress-Strain Behavior in Unidirectional Ceramic Matrix Composites," *Acta Mater.*, **46**, 3409 (1998).

22.   W.A. Curtin, "Theory of Mechanical Properties of Ceramic-Matrix Composites," *J. Am. Ceram. Soc.*, **74**, 2837 (1991).

23.   H. Cao and M. D. Thouless, "Tensile Tests of Ceramic-Matrix Composites: Theory and Experiment," *J. Am. Ceram Soc.*, **73**, 2091 (1990).

24.   J.A. DiCarlo, "Creep Limitations of Current Polycrystalline Ceramic Fibers," *Comp. Sci. and Tech.*, **51**, 213-222, (1992)

25.   J.A. DiCarlo and H.M. Yun, "Factors Controlling Stress-Rupture of Fiber-Reinforced Ceramic Composites," 12th International Conference on Composite Materials, Paris, France, 5-9 July 1999.

26.   N.E. Dowling, Mechanical Behavior of Materials: Engineering Methods for Deformation, Fracture, and Fatigue, Second Edition, Prentice Hall, 1999.

27.   H.M. Yun and J.A. DiCarlo, "Time/Temperature Dependent Tensile Strength of SiC and Al2O3-Based Fibers," pp. 17-26 in Ceramic Transactions, vol. 74, Advances in Ceramic-Matrix Composites III. Edited by N.P. Bansal and J.P. Singh. American Ceramic Society, Westerville, OH (1996).

28.   H.M. Yun and J.A. DiCarlo, "Thermo-mechanical Properties of Ceramic Fibers for Structural Ceramic Matrix Composites." Proceedings of CIMTEC '02, Florence, Italy (2002).

29.   L.P. Zawada. Senior Materials Research Engineer, Air Force Research Laratory, Materials and Manufacturing Directorate, Wright-Patterson Air Force Base OH. Personal Correspondence. 01 Oct 03.

30.   Committee on Advanced Fibers for High-Temperature Ceramic Composites, National Materials Advisory Board, Commission on Engineering and Technical Systems, National Research Council, Ceramic Fibers and Coatings: Advanced Materials for the Twenty-First Century, National Academy Press, Washington D.C., 1998 and 2000.

31.   L.P. Zawada. Senior Materials Research Engineer, Air Force Research Laboratory, Materials and Manufacturing Directorate, Wright-Patterson Air Force Base OH. Email Correspondence. 01 Feb 04.

32. K.L. More, E. Lara-Curzio, P. Tortorelli, A. Szweda, D. Carruthers, and M. Steware, "Evaluating the High-Temperature Stability of an Oxide/Oxide Composite Material at High Water Vapor Pressure," *Ceramic Eng and Science Proceedings*, In print 2004.

33. United States Patent Application: 20030207155, "Hybrid Ceramic Material Composed of Insulating and Structural Ceramic Layers", 06 Nov 2003.

34. A.G. Evans and D.B. Marshall, "Overview No. 85: The Mechanical Behavior of Ceramic Matrix Composites," *Acta Matall*, **37** [10] 2567-2583 (1989).

35. L. Filipuzzi, G. Camus, R. Naslain, and J. Thebault, "Oxidation Mechanisms and Kinetics of 1D-SiC/C/SiC Composite Materials: I, An Experimental Approach," *J. Am. Ceram. Soc.*, **77** [2] 459-466 (1994).

36. A.J. Eckel, J.D. Cawley, and T.A. Parthasarthy, "Oxidation Kinetics of a Continuous Carbon Phase in a Nonreactive Matrix," *J. Am. Ceram. Soc.*, **78** [4] 972-80 (1995).

37. J.D. Cawley, "Effect of Interphase Carbon Thickness on Environmental Resistance of Continuous Fiber-Reinforced Ceramic Matrix Composites," pp. 377-84 in Ceramic Transactions, Vol. 58, *High-Temperature Ceramic-Matrix Composites II*, Edited by A.G. Evans and R. Naslain. American Ceramic Society, Westrerville, OH (1995).

38. K.S. Goto, K.H. Han, and G.R. St. Pierre, "A Review on Oxidation Kinetics of Carbon Fiber/Carbon Matrix Composites at High Temperature," *Transaction of Iron and Steel Institute in Japan*, Vol. 26, 597-603 (1986).

39. United States Patent: 4,642,271, "BN Coating of Ceramic Fibers for Ceramic Fiber Composites", 10 Feb 87.

40. B.W. Sheldon, E.Y. Sun, S.R. Nutt, J.J. Brennan, "Oxidation of BN-Coated SiC Fibers in Ceramic Matrix Composites," *J. Am. Ceram. Soc.*, **79** [2] 539-43 (1996).

41. Linus U.J.T. Ogbuji, "A Pervasive Mode of Oxidation Degradation in a SiC-SiC Composite", *J. Am. Ceram. Soc.*, **81** [11] 2777-84 (1998).

42. H.T. Lin and P.F. Becher, "Stress-Temperature-Lifetime Response of Nicalon Fiber-Reinforced SiC Composites in Air,"; pp. 128-41 in *ASTM Symposium of Thermal and Mechanical Test Methods and Behavior of Continuous-Fiber Ceramic Composites*, ASTM STP 1309, Eds. M.G. Jenkins, S.T. Gonczy, E. Lara-Curzio, N.E. Ashbaugh, and L.P. Zawada (1997).

43. H.T. Lin, P.F. Becher, and P.F. Tortorelli, "Elevated Temperature Static Fatigue of a Nicalon Fiber-Reinforced SiC Composite," in the MRS Symposium Proceedings, Vol. 365, Ceramic Matrix Composites/Advanced High-Temperature Structural Materials, Materials Research Society, Pittsburg, Pennsylvania, pp. 435-440 (1995).

44. E. Lara-Curzio, M.K. Ferber, and P.F. Tortorelli, "Interface Oxidation and Stress-Rupture of NicalonTM/SiC CVCCs at Intermediate Temperatures," Key Engineering Materials Vols. 127-131, Trans Tech Publications, Switzerland, pp. 1069-1082 (1997).

45. E. Lara-Curzio, "Stress-Rupture of Nicalon/SiC Continuous Fiber Ceramic Matrix Composites in Air at 950°C," *J. Am. Ceram. Soc.*, **80** [12] 3268-72 (1997).

46.   P. Lipetzky, N.S. Stoloff, and G.J. Dvorak, "Atmospheric Effects on High-Temperature Lifetime of Ceramic Composites," *Ceram. Eng. Sci. Proc.*, **18** [4] 355-362 (1997).

47.   T.E. Steyer, F.W. Zok, and D.P. Walls, "Stress Rupture of an Enhanced Nicalon™/SiC Composite at Intermediate Temperatures," *J. Am. Ceram. Soc.* **81** [8] 2140-46 (1998).

48.   M.J. Verilli, A.M. Calomino, and D.N. Brewer, "Creep-rupture Behavior of a Nicalon/SiC Composite," Thermal and Mechanical Test Methods and Behavior of Continuous-Fiber Ceramic Composites, ASTM STP 1309, eds. M.G. Jenkins, S.T. Gonczy, E. Lara-Curzio, N.E. Ashbaugh, and L. Zawada, ASTM pp. 158-175 (1997).

49.   E.Y. Sun, H.T. Lin, and J.J. Brennan, "Intermediate-Temperature Environmental Effects on Boron Nitride-Coated Silicon Carbide-Fiber-Reinforced Glass-Ceramic Composites," *J. Am. Ceram. Soc.*, **80** [3] 609-14 (1997).

50.   G.N. Morscher, "Tensile Stress Rupture of SiC_f/SiC_m Minicomposites with Carbon and Boron Nitride Interphases at Elevated Temperatures in Air," *J. Am. Ceram. Soc.*, **80** [8] 2029-42 (1997).

51.   H.T. Lin and P.F. Becher, "Effect of Coating on Lifetime of Nicalon Fiber-Silicon Carbide Composites in Air," *Mater. Sci. Eng.*, A231 143-150 (1997).

52.   W.H. Glime and J.D. Cawley, "Stress Concentration Due to Fiber-Matrix Fusion in Ceramic Matrix Composites," *J. Am. Ceram. Soc.* **81** 2597-604 (1998).

53.   J. Martínez-Fernández and G.N. Morscher, "Room and Elevated Temperature Tensile Properties of Single Tow Hi-Nicalon, Carbon Interphase, CVI SiC Matrix Minicomposites," *J. European Ceram. Soc.*, **20** 2627-2636 (2000).

54.   G.N. Morscher, "The Effect of Static and Cyclic Tensile Stress and Temperature on Failure for Precracked Hi-Nicalon/BN/CVD SiC Minicomposites in Air," *Ceram. Eng. Sci. Pro*c., (1997).

55.   G.N. Morscher, J. Hurst, and D. Brewer, "Intermediate-Temperature Stress Rupture of a Woven Hi-Nicalon, BN-Interphase, Sic-Matrix Composite in Air," *J. Am. Ceram. Soc.*, **83** [6] 1441-49 (2000).

56.   R.C. Robinson and J.L Smialek, "SiC Recession Caused by SiO2 Scale Volatility under Combustor Conditions: I, Experimental Results and Empirical Model," *J. Am. Ceram. Soc.*, **82** [7] 1817-25 (1999).

57.   Recreated and modified by Mike Bruggeman from Ref **13**.

58.   National Institute of Standards and Technology, "NIST Chemical Webbook," http://webbook.nist.gov/chemistry/ January 2004.

59.   C.G. Cofer and J. Economy, "Oxidative and Hydrolytic Stability of Boron Nitride – A New Approach to Improving the Oxidation Resistance of Carbonaceous Structures," *Carbon*, **33** [4] 389-95 (1995).

60.   T.A. Parthasarathy. Contractor, Air Force Research Laboratory, Materials and Manufacturing Directorate, Wright-Patterson Air Force Base OH. Email Correspondence to L.P. Zawada. 03 Feb 04.

61. G.N. Morscher, D.R. Bryant, and R.E. Tressler, "Environmental Durability of BN-Based Interphases (for SiC_f/SiC_m Composites) in H_2O Containing Atmosphere at Intermediate Temperatures," *Ceram. Eng. Sci. Proc.*, **18** [3] 525-534 (1997).

62. A.J. Eckel, J.D. Cawley, and T.A. Parthasarthy, "Oxidation Kinetics of a Continuous Carbon Phase in a Nonreactive Matrix," *J. Am. Ceram. Soc.*, **78** [4] 972-80 (1995).

63. N.S. Jacobson, S. Farmer, A. Moore, and H. Sayir, "High Temperature Oxidation Behavior of Boron Nitride Part I: Monolithic BN," *J. Am. Ceram. Soc.* **82** [2] 393-8 (1999).

64. N.S. Jacobson, G.N. Morscher, D.R. Bryant, and R.E. Tressler, "High Temperature Oxidation of Boron Nitride Part II: BN Layers in Composites," *J. Am. Ceram. Soc.* **82** [6] 1473-82 (1999).

65. M.C. Halbig, D.N. Brewer, and A.J. Eckel, "Degradation of Continuous Fiber Ceramic Matrix Composites Under Constant Load Conditions," NASA/TM 2000-209681 (2000).

66. G.N. Morscher, "Intermediate Temperature Stress Rupture of Woven SiC Fiber, BN Interphase, SiC Matrix Composites in Air," Ph.D. Dissertation, Case Western Reserve University (January 2000).

67. F.E. Heredia, J.C. McNulty, F.W. Zok, and A.G. Evans," Oxidation Embrittlement Probe for Ceramic-Matrix Composites," J. Am. Ceram. Soc., **78** [8] 2097-100 (1995).

68. L.S. Sigl and A.G. Evans, "Effects of Residual Stress and Frictional Sliding on Cracking and Pull-out in Brittle Matrix Composites," *Mechanics of Material*, **8** 1-12 (1989).

69. D.B. Marshall, B.N. Cox, and A.G. Evans, "The Mechanics of Matrix Cracking in Brittle-Matrix Fiber Composites." *Acta metal.*, **33**, 2013-2021 (1985).

70. J.W. Hutchinson and H.M. Jensen, "Models for Fiber Debonding and Pullout in Brittle Composites with Friction," *Mech. Mater.,* **9**, 139-63 (1990).

71. Apparatus used in this research was a modified design based on a NASA Glenn Research Center design by Marc Freedman.

72. G.N. Morscher, "Modal Acoustic Emission of Damage Accumulation in a Woven SiC/SiC Composite," *Comp. Sci. Tech.*, **59**, 687-697 (1999).

73. W.A. Curtin. Professor, Brown University, Providence RI. Personal Correspondence. February 2000.

74. N. Iyengar and W. A. Curtin, "Time-Dependent Failure In Fiber-Reinforced Composites By Fiber Degradation," *Acta Mater.*, **45**, 1489 (1997).

75. S.J. Zhou and W.A. Curtin, "Failure of Fiber Composites: A Lattice Green Function Model," *Acta Metall. Mater* **43** [8] 3093-3104 (1995).

76. M. Ibnabdeljalil and W.A. Curtin, "Strength and Reliability of fiber-Reinforced Composites: Localized Load-Sharing and Associated Size Effects," *Int.J. Solids Structures*, **34** [21] 2649-2668 (1997).

77. W.G. Vincenti and C.H. Kruger, Jr., Introduction to Physical Gas Dynamics, John Wiley and Sons, Inc., New York, 1965.

1. REPORT DATE *(DD-MM-YYYY)* March 2005	**2. REPORT TYPE** **Doctoral Dissertation**	**3. DATES COVERED** *(From – To)* Dec 1998 – Mar 2005

4. TITLE AND SUBTITLE Tensile Stress Rupture Behavior Of A Woven Ceramic Matrix Composite In Humid Environments At Intermediate Temperature	**5a. CONTRACT NUMBER**
	5b. GRANT NUMBER
	5c. PROGRAM ELEMENT NUMBER
6. AUTHOR(S) LaRochelle, Kevin, J., Major, USAF	**5d. PROJECT NUMBER**
	5e. TASK NUMBER
	5f. WORK UNIT NUMBER

7. PERFORMING ORGANIZATION NAMES(S) AND ADDRESS(S) Air Force Institute of Technology Graduate School of Engineering and Management (AFIT/EN) 2950 Hobson Way WPAFB OH 45433-7765	**8. PERFORMING ORGANIZATION REPORT NUMBER** AFIT/DS/ENY/05-01

9. SPONSORING/MONITORING AGENCY NAME(S) AND ADDRESS(ES) AFRL/PRTP Attn: Ruth Sikorski, DR-II, Aero Engineer 1950 Fifth Street WPAFB OH 45433-7251 DSN: 785-7268	**10. SPONSOR/MONITOR'S ACRONYM(S)**
	11. SPONSOR/MONITOR'S REPORT NUMBER(S)

12. DISTRIBUTION/AVAILABILITY STATEMENT
        APPROVED FOR PUBLIC RELEASE; DISTRIBUTION UNLIMITED.

13. SUPPLEMENTARY NOTES

14. ABSTRACT
Stress rupture tests on the Sylramic[TM] fiber with an in-situ layer of boron nitride, boron nitride interphase, and SiC matrix ceramic matrix composite were performed at 550°C and 750°C with 0.0, 0.2, or 0.6 atm partial pressure of water vapor, pH_2O. The 550°C, 100-hr strengths were 75%, 65% and 51% of the monotonic room temperature tensile strength, respectively. At 750°C, the strengths were 67%, 51%, and 49%, respectively. Field Emission Scanning Electron Microscopy analysis estimated the total embrittlement times for 550°C with 0.0, 0.2, and 0.6 atm pH_2O were > 63 hrs, > 38 hrs, and between 8 and 71 hrs, respectively. Corresponding estimated embrittlement times for the 750°C were > 83 hrs, between 13 and 71 hrs, and between 1 and 6 hrs. A time-dependent, phenomenological, Monte Carlo-type failure model was developed and simulated total embrittlement times that were within the experimentally determined range for all cases. Variation in the room temperature ultimate strength, the elevated temperature ultimate strength, and the fiber reference strength affected the model the most. Variation in the modulus of elasticity of the matrix and fiber affected it the least. Stress rupture strength degradation increases with temperature, moisture content level, and exposure time.

15. SUBJECT TERMS
Silicon Carbide, Ceramic Matrix Composite, Moisture, Stress Rupture, Embrittlement, Intermediate Temperature

16. SECURITY CLASSIFICATION OF:			**17. LIMITATION OF ABSTRACT**	**18. NUMBER OF PAGES**	**19a. NAME OF RESPONSIBLE PERSON** Dr. Shankar Mall, ENY
REPORT U	**ABSTRACT** U	**c. THIS PAGE** U	**UU**	208	**19b. TELEPHONE NUMBER** *(Include area code)* (937) 255-3636, ext 4587; e-mail: Shankar.Mall@afit.edu

Standard Form 298 (Rev: 8-98)
Prescribed by ANSI Std. Z39-18